

# MATTER AND RADIATION IN THE STRONG MAGNETIC FIELDS OF NEUTRON STARS

A Dissertation

Presented to the Faculty of the Graduate School

of Cornell University

in Partial Fulfillment of the Requirements for the Degree of

Doctor of Philosophy

by

Zachary James Medin

August 2008

© 2008 Zachary James Medin  
ALL RIGHTS RESERVED

# MATTER AND RADIATION IN THE STRONG MAGNETIC FIELDS OF NEUTRON STARS

Zachary James Medin, Ph.D.

Cornell University 2008

Recent observations of the radiation from highly magnetized neutron stars have provided a wealth of information on these objects, but they have also raised many new questions. We study various aspects of the surfaces and magnetospheres of neutron stars, including the cohesive properties and condensation of the stellar surface, formation of magnetosphere acceleration zones, and the initiation and propagation of electron-positron cascades through the magnetosphere.

We present calculations of the electronic structure of matter in strong magnetic fields ranging from  $B = 10^{12}$  G to  $2 \times 10^{15}$  G, appropriate for observed magnetic neutron stars. Our calculations are based on the density functional theory. We find that condensed matter surfaces composed of hydrogen, helium, and carbon are all bound relative to individual atoms for  $B = 10^{12}$  G or higher. Condensed iron surfaces, however, are only significantly bound for  $B \gtrsim 10^{14}$  G. We also present Hartree–Fock calculations of the polarization-dependent photoionization cross sections of the He atom in strong magnetic fields ranging from  $10^{12}$  G to  $10^{14}$  G.

We investigate several important astrophysical implications of our calculations of the cohesive property of magnetic condensed matter. We find that for sufficiently strong magnetic fields and/or low temperatures, the neutron star surface may be in a condensed state with little gas or plasma above it; such surface condensation may lead to the formation of a charge-depleted acceleration zone (“vacuum gap”)

in the magnetosphere above the stellar polar cap. We quantitatively determine the conditions for surface condensation and vacuum gap formation in magnetic neutron stars. We find that condensation can occur if the thermal energy  $kT$  of the neutron star surface is less than about 8% of its cohesive energy  $Q_s$ , and that a vacuum gap can form if  $kT$  is less than about 4% of  $Q_s$ .

We study the conditions for the onset of pair cascades in the magnetospheres of neutron stars and the related pulsar death line/boundary. We also present Monte Carlo simulations of the full pair cascade from onset to completion. Our calculations generalize previous works to the superstrong field regime. We find that curvature radiation is a viable mechanism for the initiation of pair cascades, but that resonant and nonresonant inverse Compton scatterings are not. Additionally, we obtain the final photon spectra and pair energy distribution functions of the cascade and find significant differences between their nature in high-field neutron stars and in moderate-field neutron stars.

## BIOGRAPHICAL SKETCH

Zach Medin was born in Owatonna, Minnesota in 1980, to Gary and Roxanne Medin. In 1981 his first sister, Ashley, was born. In 1982 he moved with his family to New Brighton, Minnesota, where he spent the best 16 years of his life. In 1983 his second sister, Brie, was born, and from that point on women were the dominant force in his life. He took an early interest in astronomy, spending hours of his grade school years looking through books about the planets and stars.

In 1998, through a stroke of good luck, Zach was accepted into the California Institute of Technology, so he packed up and moved off to Pasadena, California. While it was difficult for him to leave his family and home, he soon grew to love the place and met a lot of people there who would become lifelong friends.

After graduating from Caltech in 2002 with a major in Physics, Zach followed his roommate to Cornell University in Ithaca, New York, where he began his career as a graduate student in astrophysics. Graduate school was hard work, but he still managed to find time to enjoy the finer things in life, like board games, volleyball, and good food. In 2003 Zach met the love of his life, Roxana Candia Rojas. They were married in Lima, Peru, on July 26, 2008.

Zach will receive his Ph.D. in August, 2008 and then move to Montreal, Canada to begin postdoctoral work at the University of McGill.

A mi esposa, Roxana

## ACKNOWLEDGEMENTS

First and foremost I would like to thank my thesis advisor, Dong Lai. Dong has been a constant source of good ideas and reality checks throughout my graduate career, and has continued to push me to excel academically and research-wise. I can truly say that none of this work would have been possible without him. I would also like to thank my collaborator Sasha Potekhin and my special committee members Jim Cordes, Phil Nicholson, and Ira Wasserman, for helping me write parts of this thesis. I am grateful as well for the support I received from Director of Graduate Studies Jim Bell and from astronomy faculty member Dave Chernoff.

My family has been a wonderful source of comfort and motivation throughout my college and graduate school years. I would like to thank my mom for always keeping me on task, my dad for convincing me that my work is interesting to non-astronomers, and my sisters for showing me the lighter side of life and for supporting me no matter what I've done. I would like to thank my grandparents for sending me cards on my birthday and my uncles and aunts for the good food on Thanksgiving and Christmas. También quiero dar las gracias a mi nueva familia en el Perú y Ithaca, por su hospitalidad y las clases de español.

I would like to thank my friends, old and new, for trying to keep me from graduating: Tim W., Jarrod, Ralph, Robin, Merrett, Kenny, Charlie, Pilar, Dave T., Andy, Paul, Stefan, Dave B., Taner, Ali, Matt, Akiko, Wynn, Francois, Abdul, Ruxandra, Wen, Marc, Tim M., Ryan Y., Marko, Will, Travis, Tristan, Danny, Marc F., Shannon, and of course Ryan G., my roommate of eight years.

Finally, a special thanks goes to my best friend and wife, Roxana, for her patience and positive attitude throughout my time in graduate school. Roxana: You have given me so much happiness. Te amo mucho, and I look forward to spending the rest of my life with you!

# TABLE OF CONTENTS

Biographical Sketch . . . . .	iii
Dedication . . . . .	iv
Acknowledgements . . . . .	v
Table of Contents . . . . .	vi
List of Tables . . . . .	ix
List of Figures . . . . .	x
<b>1 Overview</b>	<b>1</b>
<b>2 Density-functional-theory calculations of matter in strong magnetic fields: Atoms and molecules</b>	<b>5</b>
2.1 Introduction . . . . .	5
2.1.1 Previous works . . . . .	7
2.1.2 Plan of this chapter . . . . .	9
2.2 Basic scaling relations for atoms and molecules in strong magnetic fields . . . . .	11
2.2.1 Atoms . . . . .	11
2.2.2 Molecules . . . . .	13
2.3 Density-functional calculations: Methods and equations . . . . .	15
2.4 Results . . . . .	21
2.4.1 Hydrogen . . . . .	24
2.4.2 Helium . . . . .	25
2.4.3 Carbon . . . . .	30
2.4.4 Iron . . . . .	34
2.5 Conclusions . . . . .	39
<b>3 Density-functional-theory calculations of matter in strong magnetic fields: Infinite chains and condensed matter</b>	<b>40</b>
3.1 Introduction . . . . .	40
3.2 Basic scaling relations for linear chains and 3D condensed matter in strong magnetic fields . . . . .	44
3.3 Density-functional-theory calculations of 1D chains: Methods and equations . . . . .	47
3.3.1 Basic equations and concepts . . . . .	48
3.3.2 The electron band structure shape and occupations . . . . .	55
3.3.3 The complex longitudinal wave functions . . . . .	58
3.4 Results: One-dimensional chains . . . . .	64
3.4.1 Hydrogen . . . . .	68
3.4.2 Helium . . . . .	69
3.4.3 Carbon . . . . .	74
3.4.4 Iron . . . . .	78
3.5 Calculations of three-dimensional condensed matter . . . . .	83



3.5.1	Method . . . . .	90
3.5.2	Results: 3D condensed matter . . . . .	94
3.6	Discussions . . . . .	97
<b>4</b>	<b>Radiative transitions of the helium atom in highly magnetized neutron star atmospheres</b>	<b>101</b>
4.1	Introduction . . . . .	101
4.2	Bound states and singly-ionized states of helium atoms in strong magnetic fields . . . . .	106
4.2.1	Bound states of the helium atom . . . . .	106
4.2.2	Continuum states of the helium atom . . . . .	109
4.3	Radiative transitions . . . . .	111
4.3.1	Bound-bound transitions . . . . .	113
4.3.2	Photoionization . . . . .	115
4.4	Results . . . . .	123
4.4.1	Fitting Formula . . . . .	123
4.5	Finite nucleus mass effects . . . . .	125
4.5.1	Non-moving helium atom . . . . .	132
4.5.2	Moving helium atom . . . . .	133
4.6	Conclusion . . . . .	137
<b>5</b>	<b>Condensed surfaces of magnetic neutron stars, thermal surface emission, and particle acceleration above pulsar polar caps</b>	<b>139</b>
5.1	Introduction . . . . .	139
5.2	Cohesive properties of condensed matter in strong magnetic fields . . . . .	142
5.3	Condensation of neutron star surfaces in strong magnetic fields . . . . .	146
5.4	Polar vacuum gap accelerators in pulsars and magnetars . . . . .	155
5.4.1	Particle emission from condensed neutron star surfaces . . . . .	159
5.4.2	Conditions for gap formation . . . . .	164
5.5	Discussion . . . . .	166
<b>6</b>	<b>Pair cascades in pulsar magnetospheres: polar gap accelerators and the pulsar death line/boundary</b>	<b>169</b>
6.1	Introduction . . . . .	169
6.2	Vacuum gap accelerators . . . . .	172
6.2.1	Acceleration potential . . . . .	172
6.2.2	Requirements for gap breakdown . . . . .	174
6.2.3	Pair production . . . . .	174
6.2.4	Photon emission multiplicity and the pulsar death boundary . . . . .	175
6.3	Space-charge-limited flow (SCLF) accelerators . . . . .	188
6.3.1	Acceleration potential . . . . .	188
6.3.2	Requirements for gap breakdown . . . . .	190
6.3.3	Pair production . . . . .	190
6.3.4	Photon emission multiplicity and the pulsar death boundary . . . . .	191

6.4	Discussion . . . . .	204
<b>7</b>	<b>Pair cascades in pulsar magnetospheres: plasma distributions and photon spectra</b>	<b>207</b>
7.1	Introduction . . . . .	207
7.2	Acceleration models for the primary particle . . . . .	210
7.3	Simulation of the pair cascade: Physics ingredients and methods . .	213
7.3.1	Propagation and photon emission of the primary electron . .	217
7.3.2	Photon propagation, pair production, and splitting . . . . .	221
7.3.3	Propagation and photon emission of the secondary electrons and positrons . . . . .	227
7.3.4	Cascades initiated by a primary photon . . . . .	230
7.4	Results . . . . .	231
7.4.1	Photon-initiated cascades . . . . .	231
7.4.2	Electron-initiated cascades . . . . .	235
7.4.3	Photon splitting . . . . .	245
7.4.4	Inverse Compton scattering (ICS) . . . . .	248
7.5	Discussions . . . . .	248
<b>A</b>	<b>Chapter 2 appendix</b>	<b>254</b>
A.1	Numerical method . . . . .	254
A.1.1	Evaluating the integrals in the Kohn-Sham equations . . . .	254
A.1.2	Solving the differential equations and total energy . . . . .	256
A.2	Correlation energy . . . . .	257
<b>B</b>	<b>Chapter 3 appendix</b>	<b>260</b>
B.1	Technical details and numerical method . . . . .	260
B.1.1	Evaluating the integrals in the Kohn-Sham equations . . . .	260
B.1.2	Evaluating the integrals in the calculation of 3D condensed matter . . . . .	261
B.1.3	Solving the differential equations and the total energy self-consistently . . . . .	263
<b>C</b>	<b>Chapter 6 appendix</b>	<b>266</b>
C.1	Maximum potential drop for an oblique rotator . . . . .	266
C.2	Scattering rate calculation . . . . .	270
<b>D</b>	<b>Chapter 7 appendix</b>	<b>271</b>
D.1	Resonant inverse Compton scattering . . . . .	271
D.2	Photon attenuation and the optical depth for pair production . . .	273
D.3	Electron levels . . . . .	276

## LIST OF TABLES

2.1	Ground-state energies of hydrogen molecules . . . . .	26
2.2	Fit of the ground-state energies of hydrogen molecules . . . . .	27
2.3	Ground-state energies of helium molecules . . . . .	28
2.4	Fit of the ground-state energies of helium molecules . . . . .	29
2.5	Ground-state energies of carbon molecules . . . . .	31
2.6	Ground-state energies of ionized carbon atoms . . . . .	32
2.7	Fit of the ground-state energies of carbon atoms . . . . .	32
2.8	Ground-state energies of iron molecules . . . . .	36
2.9	Ground-state energies of ionized iron atoms . . . . .	37
2.10	Fit of the ground-state energies of iron atoms . . . . .	38
3.1	The ground-state energy of 1D infinite chains of hydrogen . . . . .	70
3.2	The ground-state energy of 1D infinite chains of helium . . . . .	75
3.3	The ground-state energy of 1D infinite chains of carbon . . . . .	79
3.4	The ground-state energy of 1D infinite iron chains . . . . .	84
3.5	The energy difference between the 3D condensed matter and 1D chain for carbon and iron . . . . .	95
4.1	Bound-bound transitions $ a\rangle \rightarrow  b\rangle$ . . . . .	120
4.2	Bound-free transitions $ b\rangle \rightarrow  f\rangle$ . . . . .	121
7.1	Final photon and electron energies and numbers . . . . .	246

## LIST OF FIGURES

2.1	The formation of $H_2$ . . . . .	14
2.2	Molecular energy versus ion separation for hydrogen molecules . . .	25
2.3	Longitudinal wave functions for selected electron orbitals of $He_8$ . .	29
2.4	Longitudinal wave functions for selected electron orbitals of $C_5$ . .	33
2.5	Molecular energy versus ion separation for $Fe_2$ and $Fe_3$ molecules .	35
2.6	Molecular energy per versus ion separation for various configura- tions of electrons in the $Fe_2$ molecule . . . . .	38
3.1	The electron band structure . . . . .	57
3.2	The shapes of the longitudinal wave functions of electrons in dif- ferent bands . . . . .	59
3.3	The longitudinal wave function for the $(m, \nu, k) = (0, 0, \pi/2a)$ elec- tron orbital of $C_\infty$ . . . . .	61
3.4	The longitudinal wave function for the $(m, \nu, k) = (0, 1, \pi/2a)$ elec- tron orbital of $Fe_\infty$ . . . . .	62
3.5	The magnitudes of the longitudinal wave functions for selected elec- tron orbitals of $C_\infty$ . . . . .	63
3.6	The electron energy of the $(m, \nu) = (0, 0)$ band for the carbon infinite chain . . . . .	65
3.7	The electron energy of the $(m, \nu) = (0, 0)$ band for the iron infinite chain . . . . .	66
3.8	The energies of H molecules and infinite chain versus ion separation	71
3.9	The molecular energy for the $H_N$ molecule as a function of $N$ . . .	72
3.10	The occupation numbers of each $m$ level of hydrogen infinite chains	73
3.11	The molecular energy for the $He_N$ molecule as a function of $N$ . . .	76
3.12	The occupation numbers of each $m$ level of infinite He chains . . .	77
3.13	The molecular energy for the $C_N$ molecule as a function of $N$ . . .	80
3.14	The occupation numbers of each $m$ level of infinite C chains . . . .	81
3.15	The density distribution of electrons in the iron infinite chain, as a function of $\rho$ . . . . .	85
3.16	The density distribution of electrons in the iron infinite chain, as a function of $z$ . . . . .	86
3.17	The energy as a function of the ion separation for an infinite Fe chain	87
3.18	The molecular energy for the $Fe_N$ molecule as a function of $N$ . . .	88
3.19	The occupation numbers of each $m$ level of infinite Fe chains . . . .	89
3.20	The body-centered tetragonal structure of the lattice . . . . .	90
3.21	The energy of 3D condensed matter relative to 1D chain as a func- tion of $R$ , for carbon . . . . .	95
3.22	The cohesive energy as a function of $B$ , for H, He, C, and Fe infinite chains and 3D condensed matter . . . . .	96
4.1	Partial cross sections versus final ionized electron energy . . . . .	118

4.2	Total cross section $\sigma_0$ versus photon energy for helium photoionization, at $10^{12}$ G . . . . .	126
4.3	Total cross section $\sigma_0$ versus photon energy for helium photoionization, at $10^{14}$ G . . . . .	127
4.4	Total cross section $\sigma_+$ versus photon energy for helium photoionization, at $10^{12}$ G . . . . .	128
4.5	Total cross section $\sigma_-$ versus photon energy for helium photoionization, at $10^{12}$ G . . . . .	129
4.6	Total cross section $\sigma_+$ versus photon energy for helium photoionization, at $10^{14}$ G . . . . .	130
4.7	Total cross section $\sigma_-$ versus photon energy for helium photoionization, at $10^{14}$ G . . . . .	131
5.1	Cohesive energy and molecular dissociation energy for helium . . .	146
5.2	Cohesive energy and molecular dissociation energy for carbon . . .	147
5.3	Cohesive energy and molecular dissociation energy for iron . . . .	148
5.4	The electron work function . . . . .	149
5.5	Density of iron vapor in phase equilibrium with the condensed iron surface . . . . .	156
5.6	Density of carbon vapor in phase equilibrium with the condensed carbon surface . . . . .	157
5.7	The condition for the formation of a vacuum gap above condensed neutron star surfaces . . . . .	165
6.1	Pulsar death boundaries for the CR and resonant ICS gap breakdown mechanisms . . . . .	178
6.2	The pulsar death boundaries when the resonant ICS mechanism is most important for initiating a cascade, as a function of $B/B_Q$ . .	185
6.3	Death boundaries for the SCLF model . . . . .	198
6.4	The pulsar death boundaries for the SCLF model, when the resonant ICS mechanism is most important for initiating a cascade, as a function of $B/B_Q$ . . . . .	199
6.5	The pulsar death boundaries for the SCLF model, when the non-resonant ICS mechanism is most important for initiating a cascade, as a function of $B/B_Q$ . . . . .	203
7.1	SCLF Lorentz factor contours for CR, RICS, and NRICS . . . . .	211
7.2	The magnetosphere pair cascade . . . . .	214
7.3	The photon emission angle . . . . .	220
7.4	The angle between the photon and the magnetic field . . . . .	223
7.5	Attenuation for both photon splitting and pair production . . . . .	225
7.6	Final photon spectra and plasma distributions of photon-initiated cascades, for $B_{12} = 1$ . . . . .	233

7.7	Spectra of successive generations of $e^+e^-$ pairs and photons, for photon-initiated cascades . . . . .	234
7.8	Final photon spectra and plasma distributions of photon-initiated cascades, for $B = B_Q$ . . . . .	236
7.9	Photon spectra at various magnetic field strengths . . . . .	237
7.10	Pair plasma distributions at various magnetic field strengths . . . .	238
7.11	Photon spectra and plasma distributions for various stellar periods	239
7.12	Photon energy distribution $\epsilon'$ at different heights above the star . .	240
7.13	Photon and electron number distributions as a function of radius .	242
7.14	Photon spectra and plasma distributions at different heights above the star for $\gamma_0 = 2 \times 10^7$ . . . . .	243
7.15	Photon spectra and plasma distributions at different heights above the star for $\gamma_0 = 5 \times 10^7$ . . . . .	244
7.16	Final electron/positron multiplicity as a function of $\gamma_0$ . . . . .	245
7.17	The effect of photon splitting on the final photon spectra and plasma distributions . . . . .	247
7.18	The effect of resonant inverse Compton scattering on the final photon spectra and plasma distributions . . . . .	249
7.19	The observed phase-averaged gamma ray spectrum for PSR B1055-52252	
B.1	Flowchart of our procedure for finding $f_{m\nu k}(z)$ , $\varepsilon_{m\nu}(k)$ , and $\sigma_{m\nu}$ self-consistently. . . . .	264
C.1	The polar gap structure . . . . .	267
C.2	Potential along the $\hat{x}$ direction for an oblique rotator . . . . .	269
D.1	Simplified picture of the ICS effect on the electron . . . . .	272
D.2	The optical depth to reach the second threshold for pair production	275

## CHAPTER 1

### OVERVIEW

This thesis contains three parts dealing with various aspects of matter and radiation in highly magnetized neutron stars: on the properties of matter in strong magnetic fields (Part I), on the formation of condensed matter on the surface of a neutron star and a charge-depleted acceleration zone in the magnetosphere above the stellar polar cap (Part II), and on the physics of pair cascades in neutron star magnetospheres (Part III).

Part I consists of Chapters 2–4. In Chapters 2 and 3 we present calculations of the electronic structure of matter in strong magnetic fields ranging from  $B = 10^{12}$  G to  $2 \times 10^{15}$  G, appropriate for observed magnetic neutron stars. At these field strengths, the magnetic forces on the electrons dominate over the Coulomb forces, and to a good approximation the electrons are confined to the ground Landau level. Our calculations are based on the density functional theory, and use a local magnetic exchange-correlation function appropriate in the strong field regime. The band structures of electrons in different Landau orbitals are computed self-consistently. Numerical results of the ground-state energies for atoms and molecules are given in Chapter 2 for  $H_N$  (up to  $N = 10$ ),  $He_N$  (up to  $N = 8$ ),  $C_N$  (up to  $N = 5$ ), and  $Fe_N$  (up to  $N = 3$ ), as well as for various ionized atoms. Numerical results of the ground-state energies and electron work functions for one-dimensional chains are given in Chapter 3 for  $H_\infty$ ,  $He_\infty$ ,  $C_\infty$ , and  $Fe_\infty$ . Fitting formulae for the  $B$ -dependence of the energies are also given in both cases. In general, as  $N$  increases, the binding energy per atom in a molecule,  $|\mathcal{E}_N|/N$ , increases and approaches the energy per cell of the corresponding infinite chain. For all the field strengths considered in these two chapters, hydrogen, helium, and

carbon molecules and chains are found to be bound relative to individual atoms (although for  $B$  less than a few  $\times 10^{12}$  G, carbon molecules and chains are very weakly bound relative to individual atoms). Iron molecules are not bound at  $B \lesssim 10^{13}$  G, but become energetically more favorable than individual atoms at larger field strengths; similarly, iron chains are significantly bound for  $B \gtrsim 10^{14}$  G and are weakly bound if at all at  $B \lesssim 10^{13}$  G. In Chapter 3 we also study the cohesive property of three-dimensional condensed matter of H, He, C, and Fe at zero pressure, constructed from interacting chains in a body-centered tetragonal lattice. Such three-dimensional condensed matter is found to be bound relative to individual atoms, with the cohesive energy increasing rapidly with increasing  $B$ .

In Chapter 4 we present Hartree–Fock calculations of the polarization-dependent photoionization cross sections of the He atom in strong magnetic fields ranging from  $10^{12}$  G to  $10^{14}$  G. We are motivated by recent observations of thermally emitting isolated neutron stars, which revealed spectral features that could be interpreted as radiative transitions of He in a magnetized neutron star atmosphere. Convenient fitting formulae for the cross sections are given as well as related oscillator strengths for various bound-bound transitions. The effects of finite nucleus mass on the radiative absorption cross sections are examined using perturbation theory.

Part II consists of Chapter 5. In Chapter 5 we investigate several important astrophysical implications of our calculations of the cohesive property of magnetic condensed matter (Chapters 2 and 3). These calculations suggest that for sufficiently strong magnetic fields and/or low temperatures, the neutron star surface may be in a condensed state with little gas or plasma above it. Such surface condensation can significantly affect the thermal emission from isolated neutron stars, and may lead to the formation of a charge-depleted acceleration zone (“vac-



uum gap”) in the magnetosphere above the stellar polar cap. In this chapter we quantitatively determine the conditions for surface condensation and vacuum gap formation in magnetic neutron stars. We find that condensation can occur if the thermal energy  $kT$  of the neutron star surface is less than about 8% of its cohesive energy  $Q_s$ , and that a vacuum gap can form if  $\boldsymbol{\Omega} \cdot \mathbf{B}_p < 0$  (i.e., the neutron star’s rotation axis and magnetic moment point in opposite directions) and  $kT$  is less than about 4% of  $Q_s$ . For example, at  $B = 3 \times 10^{14}$  G, a condensed Fe surface forms when  $T \lesssim 10^7$  K and a vacuum gap forms when  $T \lesssim 5 \times 10^6$  K. Thus, vacuum gap accelerators may exist for some neutron stars. We discuss the implications of our results for the recent observations of neutron star thermal radiation as well as for the detection/non-detection of radio emission from high-B pulsars and magnetars.

Part III consists of Chapters 6 and 7. In Chapter 6 we study the conditions for the onset of pair cascading in the magnetospheres of neutron stars, motivated by the important role these cascades play in the emission of coherent radio waves from pulsars. To initiate the cascade an acceleration region is required; we consider acceleration zones formed either by complete charge depletion directly above the polar cap due to surface condensation, as described in Chapter 5 (a Ruderman-Sutherland type “vacuum gap”), or by partial charge depletion over a more extended region due to relativistic frame dragging (a type of “space-charge-limited-flow” gap). Our calculations of the condition of cascade-induced gap breakdown and the related pulsar death line/boundary generalize previous works to the super-strong field regime. Photon emission by accelerating electrons and positrons due to both curvature radiation and resonant/nonresonant inverse Compton scattering are considered; we find that inverse Compton scatterings do not produce a sufficient number of high energy photons in the gap (despite the fact that resonantly upscattered photons can immediately produce pairs for  $B \gtrsim 1.6 \times 10^{14}$  G) and

thus do not lead to pair cascades for most neutron star parameters.

In Chapter 7 we present simulations of the full pair cascade from onset to completion, for various neutron star parameters (spin, magnetic field strength and geometry, and temperature). The initial strength of the cascade (peak energy and number of particles) is estimated from our analysis of the acceleration region (Chapter 6). Our calculations of the final photon spectra and pair plasma distributions for the pair cascade generalize previous works to the superstrong field regime (both photon splitting and low-Landau-level pair creation are considered). We find that when curvature radiation is the dominant mechanism for photon emission in the gap, the pulsar death lines/boundaries derived in Chapter 6 and in other works are good indicators of the strength of the cascade (e.g., if the neutron star lies on the “alive” side of the death boundary it will have a very strong cascade); when inverse Compton scattering (resonant or not) is the dominant photon emission mechanism, most neutron stars will have very weak cascades regardless of the death boundary.

CHAPTER 2

**DENSITY-FUNCTIONAL-THEORY CALCULATIONS OF  
MATTER IN STRONG MAGNETIC FIELDS: ATOMS AND  
MOLECULES**

## **2.1 Introduction**

Neutron stars (NSs) are endowed with magnetic fields far beyond the reach of terrestrial laboratories (Mészáros 1992; Reisenegger 2005; Harding & Lai 2006). Most of the  $\sim 1600$  known radio pulsars have surface magnetic fields in the range of  $10^{11} - 10^{13}$  G, as inferred from their measured spin periods and period derivatives and the assumption that the spindown is due to magnetic dipole radiation. A smaller population of older, millisecond pulsars have  $B \sim 10^8 - 10^9$  G. For about a dozen accreting neutron stars in binary systems, electron cyclotron features have been detected, implying surface fields of  $B \sim 10^{12} - 10^{13}$  G. An important development in astrophysics in the last decade centered on the so-called anomalous x-ray pulsars and soft gamma repeaters (Woods & Thompson 2005): there has been mounting observational evidence in recent years that supports the idea that these are magnetars, neutron stars whose radiations are powered by superstrong magnetic fields of order  $10^{14} - 10^{15}$  G or higher (Duncan & Thompson 1992; Thompson & Duncan 1995, 1996). By contrast, the highest static magnetic field currently produced in a terrestrial laboratory is  $5 \times 10^5$  G; transient fields approaching  $10^9$  G have recently been generated during high-intensity laser interactions with dense plasmas (Wagner et al. 2004).

It is well-known that the properties of matter can be drastically modified by strong magnetic fields found on neutron star surfaces. The natural atomic unit for

the magnetic field strength,  $B_0$ , is set by equating the electron cyclotron energy  $\hbar\omega_{Be} = \hbar(eB/m_e c) = 11.577 B_{12}$  keV, where  $B_{12} = B/(10^{12} \text{ G})$ , to the characteristic atomic energy  $e^2/a_0 = 2 \times 13.6$  eV (where  $a_0$  is the Bohr radius):

$$B_0 = \frac{m_e^2 c^3}{\hbar^3} = 2.3505 \times 10^9 \text{ G}. \quad (2.1)$$

For  $b = B/B_0 \gtrsim 1$ , the usual perturbative treatment of the magnetic effects on matter (e.g., Zeeman splitting of atomic energy levels) does not apply. Instead, in the transverse direction (perpendicular to the field) the Coulomb forces act as a perturbation to the magnetic forces, and the electrons in an atom settle into the ground Landau level. Because of the extreme confinement of the electrons in the transverse direction, the Coulomb force becomes much more effective in binding the electrons along the magnetic field direction. The atom attains a cylindrical structure. Moreover, it is possible for these elongated atoms to form molecular chains by covalent bonding along the field direction. Interactions between the linear chains can then lead to the formation of three-dimensional condensed matter (Ruderman 1974; Ruder et al. 1994; Lai 2001).

Our main motivation for studying matter in such strong magnetic fields arises from the importance of understanding neutron star surface layers, which play a key role in many neutron star processes and observed phenomena. Theoretical models of pulsar and magnetar magnetospheres depend on the cohesive properties of the surface matter in strong magnetic fields (Ruderman & Sutherland 1975; Arons & Scharlemann 1979; Usov & Melrose 1996; Harding & Muslimov 1998; Beloborodov & Thompson 2007). For example, depending on the cohesive energy of the surface matter, an acceleration zone (“polar gap”) above the polar cap of a pulsar may or may not form. More importantly, the surface layer directly mediates the thermal radiations from neutron stars. The advent of x-ray telescopes in recent years has made detailed study of neutron star surface emission a reality. Such

study can potentially provide invaluable information on the physical properties and evolution of NSs: equation of state at supernuclear densities, superfluidity, cooling history, magnetic field, surface composition, different NS populations, etc. (see, e.g., Yakovlev & Pethick 2004). More than two dozen isolated neutron stars (including radio pulsars, radio-quiet neutron stars and magnetars) have clearly detected thermal surface emission (Kaspi et al. 2006; Haberl 2005; Harding & Lai 2006). While some neutron stars show featureless spectra, absorption lines or features have been detected in half a dozen or so systems (Haberl 2005). Indeed, many of the observed neutron stars have sufficiently low surface temperatures and/or high magnetic fields, such that bound atoms or molecules are expected to be present in their atmospheres (Lai & Salpeter 1997; Potekhin et al. 1999; Ho & Lai 2003; Potekhin et al. 2004). It is even possible that the atmosphere is condensed into a solid or liquid form from which radiation directly emerges (Lai & Salpeter 1997; van Adelsberg et al. 2005; Lai 2001). Thus, in order to properly interpret various observations of neutron stars, it is crucial to have a detailed understanding of the properties of atoms, molecules and condensed matter in strong magnetic fields ( $B \sim 10^{11}$ - $10^{16}$  G).

### 2.1.1 Previous works

H and He atoms at almost all field strengths have been well studied (Ruder et al. 1994; Jones et al. 1999; Al-Hujaj & Schmelcher 2003a), including the nontrivial effect associated with the center-of-mass motion of a H atom (Potekhin 1998). Neuhauser et al. (1987) presented numerical results for several atoms up to  $Z = 26$  (Fe) at  $B \sim 10^{12}$  G based on calculations using a one-dimensional Hartree-Fock method (see also Mori & Hailey 2002 for  $Z$  up to 10). Some results [based on

a two-dimensional (2D) mesh Hartree-Fock method] for atoms (up to  $Z = 10$ ) at the field strengths  $B/B_0 = 0.5 - 10^4$  are also available (Ivanov & Schmelcher 2000; Al-Hujaj & Schmelcher 2004a,b). The Hartree-Fock method is approximate because electron correlations are neglected. Due to their mutual repulsion, any pair of electrons tend to be more distant from each other than the Hartree-Fock wave function would indicate. In zero-field, this correlation effect is especially pronounced for the spin-singlet states of electrons for which the spatial wave function is symmetrical. In strong magnetic fields ( $B \gg B_0$ ), the electron spins (in the ground state) are all aligned antiparallel to the magnetic field, and the multielectron spatial wave function is antisymmetric with respect to the interchange of two electrons. Thus the error in the Hartree-Fock approach is expected to be less than the 1% accuracy characteristic of zero-field Hartree-Fock calculations (Neuhauser et al. 1987; Schmelcher et al. 1999). Other calculations of heavy atoms in strong magnetic fields include Thomas-Fermi type statistical models (Fushiki et al. 1992; Lieb et al. 1994a,b) and density functional theory (Jones 1985, 1986; Kössl et al. 1988; Relovsky & Ruder 1996). The Thomas-Fermi type models are useful in establishing asymptotic scaling relations, but are not adequate for obtaining accurate binding and excitation energies. The density functional theory can potentially give results as accurate as the Hartree-Fock method after proper calibration is made (Vignale & Rasolt 1987, 1988).

Quantitative results for the energies of hydrogen molecules  $H_N$  with  $N = 2, 3, 4, 5$  in a wide range of field strengths ( $B \gg B_0$ ) were obtained (based on the Hartree-Fock method) by Lai et al. (Lai et al. 1992; Lai 2001) and molecular excitations were studied in Lai & Salpeter (1996); Schmelcher et al. (2001) (more complete references can be found in Lai 2001). Quantum Monte Carlo calculations of  $H_2$  in strong magnetic fields have been performed (Ortiz et al. 1995). Some

numerical results of  $\text{He}_2$  for various field strengths are also available (Lai 2001). Hartree-Fock results of diatomic molecules (from  $\text{H}_2$  up to  $\text{C}_2$ ) and several larger molecules (up to  $\text{H}_5$  and  $\text{He}_4$ ) at  $B/B_0 = 1000$  are given in Demeur et al. (1994).

### 2.1.2 Plan of this chapter

In this chapter and Chapter 3, we develop a density-functional-theory calculation of the ground-state energy of matter for a wide range of magnetic field strengths, from  $10^{12}$  G (typical of radio pulsars) to  $2 \times 10^{15}$  G (magnetar fields). We consider H, He, C, and Fe, which represent the most likely composition of the outermost layer of neutron stars (e.g., Harding & Lai 2006). The present chapter focuses on atoms (and related ions) and small molecules. Because of additional complications related to the treatment of band structure, calculations of infinite molecular chains and condensed matter are presented in Medin & Lai (2006a).

Our calculations are based on density functional theory (Hohenberg & Kohn 1964; Kohn & Sham 1965; Jones & Gunnarsson 1989). As mentioned above, the Hartree-Fock method is expected to be highly accurate, particularly in the strong field regime where the electron spins are aligned with each other. In this regime the density functional method is not as accurate, due to the lack of an exact correlation function for electrons in strong magnetic fields. However, in dealing with systems with many electrons, the Hartree-Fock method becomes increasingly impractical as the magnetic field increases, since more and more Landau orbitals (even though electrons remain in the ground Landau level) are occupied and keeping track of the direct and exchange interactions between electrons in various orbitals becomes computationally rather tedious. Our density-functional calculations allow us to obtain the energies of atoms and small molecules and the energy of condensed

matter using the same method, thus providing reliable cohesive energy of condensed surface of magnetic neutron stars, a main goal of our study. Compared to previous density-functional-theory calculations (Jones 1985, 1986; Kössl et al. 1988; Relovsky & Ruder 1996), we use an improved exchange-correlation function for highly magnetized electron gases, we calibrate our density functional code with previous results (when available) based on other methods, and (for calculations of condensed matter) adopt a more accurate treatment of the band structure. Moreover, our calculations extend to the magnetar-like field regime ( $B \sim 10^{15}$  G).

Note that in this chapter we neglect the motions of the nuclei, due to electron-nucleus interactions or finite temperatures. The center-of-mass motions of the atoms and molecules induce the motional Stark effect, which can change the internal structure of the bound states (see, e.g., Lai 2001; Potekhin 1998). Such issues are beyond the scope of this chapter.

After summarizing the approximate scaling relations for atoms and molecules in strong magnetic fields in Section 2.2, we describe our method in Section 2.3 and present numerical results in Section 2.4. Some technical details are given in Appendix A.

This chapter is based on the published paper by Medin & Lai 2006 [Medin Z., Lai D., 2006, Physical Review A, 74, 062507; ©2006. The American Physical Society. All rights reserved]. It is reprinted here with minor changes, based on rights retained by the author.



## 2.2 Basic scaling relations for atoms and molecules in strong magnetic fields

### 2.2.1 Atoms

First consider a hydrogenic atom (with one electron and nuclear charge  $Z$ ). In a strong magnetic field with  $b = B/B_0 \gg Z^2$ , the electron is confined to the ground Landau level (“adiabatic approximation”), and the Coulomb potential can be treated as a perturbation. The energy spectrum is specified by two quantum numbers,  $(m, \nu)$ , where  $m = 0, 1, 2, \dots$  measures the mean transverse separation between the electron and the nucleus ( $-m$  is also known as the magnetic quantum number), while  $\nu$  specifies the number of nodes in the  $z$  wave function. There are two distinct types of states in the energy spectrum  $\mathcal{E}_{m\nu}$ . The “tightly bound” states have no node in their  $z$  wave functions ( $\nu = 0$ ). The transverse size of the atom in the  $(m, 0)$  state is  $L_\perp \sim \rho_m = (2m + 1)^{1/2} \rho_0$ , with  $\rho_0 = (\hbar c / eB)^{1/2} = b^{-1/2}$  (in atomic units).<sup>1</sup> For  $\rho_m \ll 1$ , the atom is elongated with  $L_z \gg L_\perp$ . We can estimate the longitudinal size  $L_z$  by minimizing the energy,  $\mathcal{E} \sim L_z^{-2} - ZL_z^{-1} \ln(L_z/L_\perp)$  (where the first term is the kinetic energy and the second term is the Coulomb energy), giving

$$L_z \sim \left( Z \ln \frac{1}{Z \rho_m} \right)^{-1}. \quad (2.2)$$

The energy is given by

$$\mathcal{E}_{m0} \sim -Z^2 \left[ \ln \frac{1}{Z^2} \left( \frac{b}{2m + 1} \right) \right]^2 \quad (2.3)$$

for  $b \gg (2m + 1)Z^2$ . Another type of state of the atom has nodes in the  $z$  wave functions ( $\nu > 0$ ). These states are “weakly bound”, and have energies given by

---

<sup>1</sup>Unless otherwise specified, we use atomic units, in which length is in  $a_0$  (Bohr radius), mass in  $m_e$ , energy in  $e^2/a_0 = 2$  Ry, and field strength in units of  $B_0$ .

$\mathcal{E}_{m\nu} \simeq -Z^2 n^{-2}$  Ry, where  $n$  is the integer part of  $(\nu + 1)/2$ . The sizes of the wave functions are  $\rho_m$  perpendicular to the field and  $L_z \sim \nu^2/Z$  along the field (see Lai 2001 and references therein for more details).

A multielectron atom (with the number of electrons  $N_e$  and the charge of the nucleus  $Z$ ) can be constructed by placing electrons at the lowest available energy levels of a hydrogenic atom. The lowest levels to be filled are the tightly bound states with  $\nu = 0$ . When  $a_0/Z \gg \sqrt{2N_e - 1}\rho_0$ , i.e.,  $b \gg 2Z^2 N_e$ , all electrons settle into the tightly bound levels with  $m = 0, 1, 2, \dots, N_e - 1$ . The energy of the atom is approximately given by the sum of all the eigenvalues of Eq. (2.3). Accordingly, we obtain an asymptotic expression for  $N_e \gg 1$  (Kadomtsev & Kudryavtsev 1971):

$$\mathcal{E} \sim -Z^2 N_e \left( \ln \frac{b}{2Z^2 N_e} \right)^2. \quad (2.4)$$

For intermediate-strong fields (but still strong enough to ignore Landau excitations),  $Z^2 N_e^{-2/3} \ll b \ll 2Z^2 N_e$ , many  $\nu > 0$  states of the inner Landau orbitals (states with relatively small  $m$ ) are populated by the electrons. In this regime a Thomas-Fermi type model for the atom is appropriate, i.e., the electrons can be treated as a one-dimensional Fermi gas in a more or less spherical atomic cell (see, e.g., Kadomtsev 1970; Mueller, Rau, & Spruch 1971). The electrons occupy the ground Landau level, with the  $z$  momentum up to the Fermi momentum  $p_F \sim n/b$ , where  $n$  is the number density of electrons inside the atom (recall that the degeneracy of a Landau level is  $eB/hc \sim b$ ). The kinetic energy of electrons per unit volume is  $\varepsilon_k \sim b p_F^3 \sim n^3/b^2$ , and the total kinetic energy is  $\mathcal{E}_k \sim R^3 n^3/b^2 \sim N_e^3/(b^2 R^6)$ , where  $R$  is the radius of the atom. The potential energy is  $\mathcal{E}_p \sim -ZN_e/R$  (for  $N_e \lesssim Z$ ). Therefore the total energy of the atom can be written as  $\mathcal{E} \sim N_e^3/(b^2 R^6) - ZN_e/R$ . Minimizing  $\mathcal{E}$  with respect to  $R$  yields

$$R \sim (N_e^2/Z)^{1/5} b^{-2/5}, \quad \mathcal{E} \sim -(Z^2 N_e)^{3/5} b^{2/5}. \quad (2.5)$$

For these relations to be valid, the electrons must stay in the ground Landau level; this requires  $Z/R \ll \hbar\omega_{Be} = b$ , which corresponds to  $b \gg Z^2 N_e^{-2/3}$ .

### 2.2.2 Molecules

In a strong magnetic field, the mechanism of forming molecules is quite different from the zero-field case (Ruderman 1974; Lai et al. 1992). Consider hydrogen as an example. The spin of the electron in a H atom is aligned antiparallel to the magnetic field (flipping the spin would cost  $\hbar\omega_{Be}$ ), therefore two H atoms in their ground states ( $m = 0$ ) do not bind together according to the exclusion principle. Instead, one H atom has to be excited to the  $m = 1$  state. The two H atoms, one in the ground state ( $m = 0$ ), another in the  $m = 1$  state then form the ground state of the  $H_2$  molecule by covalent bonding. Since the activation energy for exciting an electron in the H atom from the Landau orbital  $m$  to  $(m + 1)$  is small, the resulting  $H_2$  molecule is stable. Similarly, more atoms can be added to form  $H_3$ ,  $H_4$ , .... The size of the  $H_2$  molecule is comparable to that of the H atom. The interatomic separation  $a$  and the dissociation energy  $D$  of the  $H_2$  molecule scale approximately as  $a \sim (\ln b)^{-1}$  and  $D \sim (\ln b)^2$ , although  $D$  is numerically smaller than the ionization energy of the H atom. (See Fig. 2.2.2 for a sketch of the formation of  $H_2$ .)

Consider the molecule  $Z_N$ , formed out of  $N$  neutral atoms  $Z$  (each with  $Z$  electrons and nuclear charge  $Z$ ). For sufficiently large  $b$  (see below), the electrons occupy the Landau orbitals with  $m = 0, 1, 2, \dots, NZ - 1$ , and the transverse size of the molecule is  $L_\perp \sim (NZ/b)^{1/2}$ . Let  $a$  be the atomic spacing and  $L_z \sim Na$  the size of the molecule in the  $z$  direction. The energy per “atom” in the molecule,  $\mathcal{E} = \mathcal{E}_N/N$ , can be written as  $\mathcal{E} \sim Z(Na)^{-2} - (Z^2/a)l$ , where  $l \sim \ln(a/L_\perp)$ .

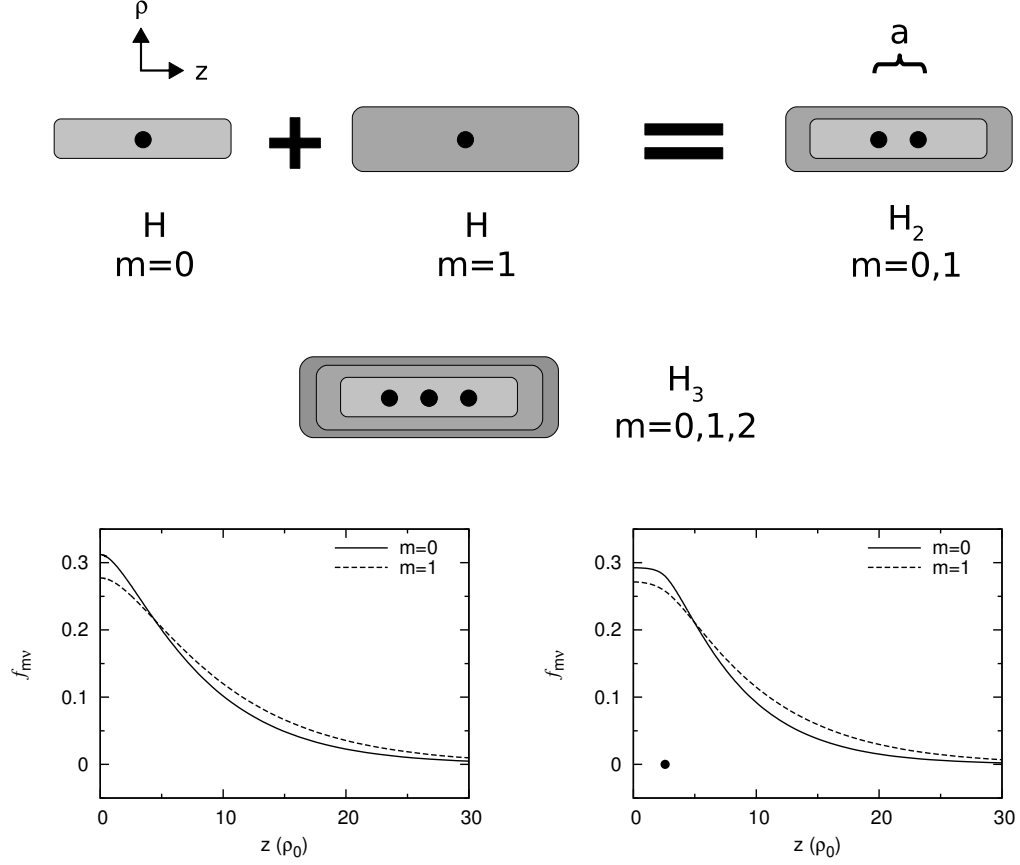


Figure 2.1: Upper panel: A schematic diagram showing the formation of the ground-state  $H_2$  molecule. The ground state of  $H_3$  is shown as well. Lower panels: Longitudinal wave functions for the electron orbitals of the ground state ( $m = 0$ ) and first excited state ( $m = 1$ ) of  $H$  at  $B_{12} = 1$  (left panel); and of the ground state ( $m = 0, 1$ ) of  $H_2$  at  $B_{12} = 1$ , at equilibrium ion separation (right panel). Only the  $z \geq 0$  region is shown. Wave functions are symmetric about  $z = 0$ . For the panel depicting  $H_2$  wave functions, the filled circle denotes the ion location.

Variation of  $\mathcal{E}$  with respect to  $a$  gives

$$a \sim (ZN^2l)^{-1}, \quad \mathcal{E} \sim -Z^3N^2l^2, \quad \text{with } l \sim \ln\left(\frac{b}{N^5Z^3}\right). \quad (2.6)$$

This above scaling behavior is valid for  $1 \ll N \ll N_s$ . The “critical saturation number”  $N_s$  is reached when  $a \sim L_\perp$ , or when (Lai et al. 1992)

$$N_s \sim \left(\frac{b}{Z^3}\right)^{1/5}. \quad (2.7)$$

Beyond  $N_s$ , it becomes energetically more favorable for the electrons to settle into the inner Landau orbitals (with smaller  $m$ ) with nodes in their longitudinal wave functions (i.e.,  $\nu \neq 0$ ). For  $N \gtrsim N_s$ , the energy per atom asymptotes to a value  $\mathcal{E} \sim -Z^{9/5}b^{2/5}$ , and size of the atom scales as  $L_\perp \sim a \sim Z^{1/5}b^{-2/5}$ , independent of  $N$  — the molecule essentially becomes one-dimensional condensed matter.

The scaling relations derived above are obviously crude — they are expected to be valid only in the asymptotic limit,  $\ln(b/Z^3) \gg 1$ . For realistic neutron stars, this limit is not quite reached. Thus these scaling results should only serve as a guide to the energies of various molecules. For a given field strength, it is not clear from the above analysis whether the  $Z_N$  molecule is bound relative to individual atoms. To answer this question requires quantitative calculations.

### 2.3 Density-functional calculations: Methods and equations

Our calculations will be based on the “adiabatic approximation,” in which all electrons are assumed to lie in the ground Landau level. For atoms or molecules with nucleus charge number  $Z$ , this is an excellent approximation for  $b \gg Z^2$ .

Even under more relaxed condition,  $b \gg Z^{4/3}$  (assuming the number of electrons in each atom is  $N_e \sim Z$ ) this approximation is expected to yield a reasonable total energy of the system and accurate results for the energy difference between different atoms and molecules; a quantitative evaluation of this approximation in this regime is beyond the scope of this chapter (but see Ivanov & Schmelcher 2000; Al-Hujaj & Schmelcher 2004a,b).

In the adiabatic approximation, the one-electron wave function (“orbital”) can be separated into a transverse (perpendicular to the external magnetic field) component and a longitudinal (along the magnetic field) component:

$$\Psi_{m\nu}(\mathbf{r}) = W_m(\mathbf{r}_\perp) f_{m\nu}(z). \quad (2.8)$$

Here  $W_m$  is the ground-state Landau wave function (Landau & Lifshitz 1977) given by

$$W_m(\mathbf{r}_\perp) = \frac{1}{\rho_0 \sqrt{2\pi m!}} \left( \frac{\rho}{\sqrt{2}\rho_0} \right)^m \exp\left( \frac{-\rho^2}{4\rho_0^2} \right) \exp(-im\phi), \quad (2.9)$$

where  $\rho_0 = (\hbar c/eB)^{1/2}$  is the cyclotron radius (or magnetic length), and  $f_{m\nu}$  is the longitudinal wave function which must be solved numerically. We normalize  $f_{m\nu}$  over all space:

$$\int_{-\infty}^{\infty} dz |f_{m\nu}(z)|^2 = 1, \quad (2.10)$$

so that  $\int d\mathbf{r} |\Psi_{m\nu}(\mathbf{r})|^2 = 1$ . The density distribution of electrons in the atom or molecule is

$$n(\mathbf{r}) = \sum_{m\nu} |\Psi_{m\nu}(\mathbf{r})|^2 = \sum_{m\nu} |f_{m\nu}(z)|^2 |W_m|^2(\rho), \quad (2.11)$$

where the sum is over all the electrons in the atom or molecule, with each electron occupying an  $(m\nu)$  orbital. The notation  $|W_m|^2(\rho) = |W_m(\mathbf{r}_\perp)|^2$  is used here because  $W_m$  is a function of  $\rho$  and  $\phi$  but  $|W_m|^2$  is a function only of  $\rho$ .

In an external magnetic field, the Hamiltonian of a free electron is

$$\hat{H} = \frac{1}{2m_e} \left( \mathbf{p} + \frac{e}{c} \mathbf{A} \right)^2 + \frac{\hbar e B}{2m_e c} \sigma_z, \quad (2.12)$$

where  $\mathbf{A} = \frac{1}{2} \mathbf{B} \times \mathbf{r}$  is the vector potential of the external magnetic field and  $\sigma_z$  is the  $z$  component Pauli spin matrix. For electrons in Landau levels, with their spins aligned parallel/antiparallel to the magnetic field, the Hamiltonian becomes

$$\hat{H} = \frac{\hat{p}_z^2}{2m_e} + \left( n_L + \frac{1}{2} \right) \hbar \omega_{Be} \pm \frac{1}{2} \hbar \omega_{Be}, \quad (2.13)$$

where  $n_L = 0, 1, 2, \dots$  is the Landau level index; for electrons in the ground Landau level, with their spins aligned antiparallel to the magnetic field (so  $n_L = 0$  and  $\sigma_z \rightarrow -1$ ),

$$\hat{H} = \frac{\hat{p}_z^2}{2m_e}. \quad (2.14)$$

The total Hamiltonian for the atom or molecule then becomes

$$\hat{H} = \sum_i \frac{\hat{p}_{z,i}^2}{2m_e} + V, \quad (2.15)$$

where the sum is over all electrons and  $V$  is the total potential energy of the atom or molecule. From this we can derive the total energy of the system.

Note that we use nonrelativistic quantum mechanics in our calculations, even when  $\hbar \omega_{Be} \gtrsim m_e c^2$  or  $B \gtrsim B_Q = B_0 / \alpha^2 = 4.414 \times 10^{13}$  G (where  $\alpha = e^2 / (\hbar c)$  is the fine structure constant). This is valid for two reasons: (i) The free-electron energy in relativistic theory is

$$\mathcal{E} = \left[ c^2 p_z^2 + m_e^2 c^4 \left( 1 + 2n_L \frac{B}{B_Q} \right) \right]^{1/2}. \quad (2.16)$$

For electrons in the ground Landau level ( $n_L = 0$ ), Eq. (2.16) reduces to  $\mathcal{E} \simeq m_e c^2 + p_z^2 / (2m_e)$  for  $p_z c \ll m_e c^2$ ; the electron remains nonrelativistic in the  $z$  direction as long as the electron energy is much less than  $m_e c^2$ ; (ii) Eq. (2.9)

indicates that the shape of Landau transverse wave function is independent of particle mass, and thus Eq. (2.9) is valid in the relativistic theory. Our calculations assume that the longitudinal motion of the electron is nonrelativistic. This is valid at all field strengths and for all elements considered with the exception of iron at  $B \gtrsim 10^{15}$  G. Even at  $B = 2 \times 10^{15}$  G (the highest field considered in this chapter), however, we find that the most-bound electron in any Fe atom or molecule has a longitudinal kinetic energy of only  $\sim 0.2m_e c^2$  and only the three most-bound electrons have longitudinal kinetic energies  $\gtrsim 0.1m_e c^2$ . Thus relativistic corrections are small in the field strengths considered in this chapter. Moreover, we expect our results for the relative energies between Fe atoms and molecules to be much more accurate than the absolute energies of either the atoms or the molecules.

Consider the molecule  $Z_N$ , consisting of  $N$  atoms, each with an ion of charge  $Z$  and  $Z$  electrons. In the lowest-energy state of the system, the ions are aligned along the magnetic field. The spacing between ions,  $a$ , is chosen to be constant across the molecule. In the density functional theory, the total energy of the system can be represented as a functional of the total electron density  $n(\mathbf{r})$ :

$$\mathcal{E}[n] = \mathcal{E}_K[n] + \mathcal{E}_{eZ}[n] + \mathcal{E}_{\text{dir}}[n] + \mathcal{E}_{\text{exc}}[n] + \mathcal{E}_{ZZ}[n]. \quad (2.17)$$

Here  $\mathcal{E}_K[n]$  is the kinetic energy of a system of noninteracting electrons, and  $\mathcal{E}_{eZ}$ ,  $\mathcal{E}_{\text{dir}}$ , and  $\mathcal{E}_{ZZ}$  are the electron-ion Coulomb energy, the direct electron-electron interaction energy, and the ion-ion interaction energy, respectively,

$$\mathcal{E}_{eZ}[n] = -\sum_{j=1}^N Z e^2 \int d\mathbf{r} \frac{n(\mathbf{r})}{|\mathbf{r} - \mathbf{z}_j|}, \quad (2.18)$$

$$\mathcal{E}_{\text{dir}}[n] = \frac{e^2}{2} \iint d\mathbf{r} d\mathbf{r}' \frac{n(\mathbf{r})n(\mathbf{r}')}{|\mathbf{r} - \mathbf{r}'|}, \quad (2.19)$$

$$\mathcal{E}_{ZZ}[n] = \sum_{j=1}^{N-1} (N-j) \frac{Z^2 e^2}{ja}. \quad (2.20)$$



The location of the ions in the above equations is represented by the set  $\{\mathbf{z}_j\}$ , with

$$\mathbf{z}_j = (2j - N - 1)\frac{a}{2}\hat{\mathbf{z}}. \quad (2.21)$$

The term  $\mathcal{E}_{\text{exc}}$  represents exchange-correlation energy. In the local approximation,

$$\mathcal{E}_{\text{exc}}[n] = \int d\mathbf{r} n(\mathbf{r}) \varepsilon_{\text{exc}}(n), \quad (2.22)$$

where  $\varepsilon_{\text{exc}}(n) = \varepsilon_{\text{ex}}(n) + \varepsilon_{\text{corr}}(n)$  is the exchange and correlation energy per electron in a uniform electron gas of density  $n$ . For electrons in the ground Landau level, the (Hartree-Fock) exchange energy can be written as follows (Danz & Glasser 1971):

$$\varepsilon_{\text{ex}}(n) = -\pi e^2 \rho_0^2 n F(t), \quad (2.23)$$

where the dimensionless function  $F(t)$  is

$$F(t) = 4 \int_0^\infty dx \left[ \tan^{-1} \left( \frac{1}{x} \right) - \frac{x}{2} \ln \left( 1 + \frac{1}{x^2} \right) \right] e^{-4tx^2}, \quad (2.24)$$

and

$$t = \left( \frac{n}{n_B} \right)^2 = 2\pi^4 \rho_0^6 n^2, \quad (2.25)$$

[ $n_B = (\sqrt{2}\pi^2 \rho_0^3)^{-1}$  is the density above which the higher Landau levels start to be filled in a uniform electron gas]. For small  $t$ ,  $F(t)$  can be expanded as follows (Fushiki et al. 1989):

$$F(t) \simeq 3 - \gamma - \ln 4t + \frac{2t}{3} \left( \frac{13}{6} - \gamma - \ln 4t \right) + \frac{8t^2}{15} \left( \frac{67}{30} - \gamma - \ln 4t \right) + \mathcal{O}(t^3 \ln t), \quad (2.26)$$

where  $\gamma = 0.5772 \dots$  is Euler's constant. We have found that the condition  $t \ll 1$  is well satisfied everywhere for almost all molecules in our calculations. The notable exceptions are the carbon molecules at  $B = 10^{12}$  G and the iron molecules at  $B = 10^{13}$  G, which have  $t \lesssim 1$  near the center of the molecule. These molecules are expected to have higher  $t$  values than the other molecules in our calculations, as they have large  $Z$  and low  $B$ .<sup>2</sup>

---

<sup>2</sup>For the uniform gas model,  $t \propto Z^{6/5} N_e^{-2/5} B^{-3/5}$ .

The correlation energy of uniform electron gas in strong magnetic fields has not be calculated in general, except in the regime  $t \ll 1$  and Fermi wavenumber  $k_F = 2\pi^2 \rho_0^2 n \gg 1$  [or  $n \gg (2\pi^3 \rho_0^2 a_0)^{-1}$ ]. Skudlarski and Vignale (1993) use the random-phase approximation to find a numerical fit for the correlation energy in this regime (see also Steinberg & Ortner 1998):

$$\varepsilon_{\text{corr}} = -\frac{e^2}{\rho_0} [0.595(t/b)^{1/8}(1 - 1.009t^{1/8})]. \quad (2.27)$$

In the absence of an “exact” correlation energy density we employ this strong-field-limit expression. Fortunately, because we are concerned mostly with finding energy changes between different states of atoms and molecules, the correlation energy term does not have to be exact. The presence or the form of the correlation term has a modest effect on the atomic and molecular energies calculated but has very little effect on the energy difference between them (see Appendix A.2 for more details on various forms of the correlation energy and comparisons).

Variation of the total energy with respect to the total electron density,  $\delta\mathcal{E}[n]/\delta n = 0$ , leads to the Kohn-Sham equations:

$$\left[ -\frac{\hbar^2}{2m_e} \nabla^2 + V_{\text{eff}}(\mathbf{r}) \right] \Psi_{m\nu}(\mathbf{r}) = \varepsilon_{m\nu} \Psi_{m\nu}(\mathbf{r}), \quad (2.28)$$

where

$$V_{\text{eff}}(\mathbf{r}) = -\sum_{j=1}^N \frac{Ze^2}{|\mathbf{r} - \mathbf{z}_j|} + e^2 \int d\mathbf{r}' \frac{n(\mathbf{r}')}{|\mathbf{r} - \mathbf{r}'|} + \mu_{\text{exc}}(n), \quad (2.29)$$

with

$$\mu_{\text{exc}}(n) = \frac{\partial(n\varepsilon_{\text{exc}})}{\partial n}. \quad (2.30)$$

Averaging the Kohn-Sham equations over the transverse wave function yields a set of one-dimensional equations:

$$\begin{aligned} \left( -\frac{\hbar^2}{2m_e} \frac{d^2}{dz^2} - \sum_{j=1}^N Ze^2 \int d\mathbf{r}_\perp \frac{|W_m|^2(\rho)}{|\mathbf{r} - \mathbf{z}_j|} + e^2 \iint d\mathbf{r}_\perp d\mathbf{r}' \frac{|W_m|^2(\rho) n(\mathbf{r}')}{|\mathbf{r} - \mathbf{r}'|} \right. \\ \left. + \int d\mathbf{r}_\perp |W_m|^2(\rho) \mu_{\text{exc}}(n) \right) f_{m\nu}(z) = \varepsilon_{m\nu} f_{m\nu}(z). \end{aligned} \quad (2.31)$$

These equations are solved self-consistently to find the eigenvalue  $\varepsilon_{m\nu}$  and the longitudinal wave function  $f_{m\nu}(z)$  for each orbital occupied by the  $N$  electrons. Once these are known, the total energy of the system can be calculated using

$$\begin{aligned} \mathcal{E}[n] = & \sum_{m\nu} \varepsilon_{m\nu} - \frac{e^2}{2} \iint d\mathbf{r} d\mathbf{r}' \frac{n(\mathbf{r})n(\mathbf{r}')}{|\mathbf{r} - \mathbf{r}'|} \\ & + \int d\mathbf{r} n(\mathbf{r}) [\varepsilon_{\text{exc}}(n) - \mu_{\text{exc}}(n)] + \sum_{j=1}^{N-1} (N-j) \frac{Z^2 e^2}{ja}. \end{aligned} \quad (2.32)$$

Details of our method used in computing the various integrals and solving the above equations are given in Appendix A.1.

Note that for a given system, the occupations of electrons in different  $(m\nu)$  orbitals are not known *a priori*, and must be determined as part of the procedure of finding the minimum energy state of the system. In our calculation, we first guess  $n_0, n_1, n_2, \dots$ , the number of electrons in the  $\nu = 0, 1, 2, \dots$  orbitals, respectively (e.g., the electrons in the  $\nu = 0$  orbitals have  $m = 0, 1, 2, \dots, n_0 - 1$ ). Note that  $n_0 + n_1 + n_2 + \dots = NZ$ . We find the energy of the system for this particular set of electron occupations. We then vary the electron occupations and repeat the calculation until the true minimum energy state is found. Obviously, in the case of molecules, we must vary the ion spacing  $a$  to determine the equilibrium separation and the the ground-state energy of the molecule. Graphical examples of how the ground state is chosen are given in Section 2.4.

## 2.4 Results

In this section we present our results for the parallel configuration of  $\text{H}_N$  (up to  $N = 10$ ),  $\text{He}_N$  (up to  $N = 8$ ),  $\text{C}_N$  (up to  $N = 5$ ), and  $\text{Fe}_N$  (up to  $N = 3$ ) at various magnetic field strengths between  $B = 10^{12}$  G and  $2 \times 10^{15}$  G. For

each molecule (or atom), data is given in tabular form on the molecule’s ground-state energy, the equilibrium separation of the ions in the molecule, and its orbital structure (electron occupation numbers  $n_0, n_1, n_2, \dots$ ). In some cases the first-excited-state energies are given as well, when the ground-state and first-excited-state energies are similar in value. We also provide the ground-state energies for selected ionization states of C and Fe atoms; among other uses, these quantities are needed for determining the ion emission from a condensed neutron star surface (Medin & Lai 2006a). All of the energies presented in this section are calculated to better than 0.1% numerical accuracy (see Appendix A.1).

For each of the molecules and ions presented in this section we provide numerical scaling relations for the ground-state energy as a function of magnetic field, in the form of a scaling exponent  $\beta$  with  $\mathcal{E}_N \propto B_{12}^\beta$ . We have provided this information to give readers easy access to energy values for fields in between those listed in the tables. The ground-state energy is generally not well fit by a constant  $\beta$  over the entire magnetic field range covered by this work, so we have provided  $\beta$  values over several different magnetic field ranges. Note that the theoretical value  $\beta = 2/5$  (see Section 2.2) is approached only in certain asymptotic limits.

We discuss here briefly a few trends in the data: All of the molecules listed in the following tables are bound. The  $\text{Fe}_2$  and  $\text{Fe}_3$  molecules at  $B_{12} = 5$  are not bound, so we have not listed them here, but we have listed the Fe atom at this field strength for comparison with other works. All of the bound molecules listed below have ground-state energies per atom that decrease monotonically with increasing  $N$ , with the exception of  $\text{H}_N$  at  $B_{12} = 1$ , which has a slight upward glitch in energy at  $\text{H}_4$  (see Table 2.1). Additionally, these energies approach asymptotic values for large  $N$  — the molecule essentially becomes one-dimensional condensed matter

(Medin & Lai 2006a). The equilibrium ion separations also approach asymptotic values for large  $N$ , but there is no strong trend in the direction of approach: sometimes the equilibrium ion separations increase with increasing  $N$ , sometimes they decrease, and sometimes they oscillate back and forth.

In general, we find that for a given molecule (e.g.,  $\text{Fe}_3$ ), the number of electrons in  $\nu > 0$  states decreases as the magnetic field increases. This is because the characteristic transverse size  $\rho_0 \propto B^{-1/2}$  decreases, so the electrons prefer to stay in the  $\nu = 0$  states. For a given field strength, as the number of electrons in the system  $NN_e$  increases (e.g., from  $\text{Fe}_2$  to  $\text{Fe}_3$ ), more electrons start to occupy the  $\nu > 0$  states since the average electron-nucleus separation  $\rho_m \propto (2m + 1)^{1/2} B^{-1/2}$  becomes too large for large  $m$ . For large enough  $N$  the value of  $n_0$ , the number of electrons in  $\nu = 0$  states, levels off, approaching its infinite chain value (see Medin & Lai 2006a). Similar trends happen with  $n_1$ ,  $n_2$ , etc., though much more slowly.

There are two ways that we have checked the validity of our results by comparison with other works. First, we have repeated several of our atomic and molecular calculations using the correlation energy expression empirically determined by Jones (1985):

$$\varepsilon_{\text{corr}} = -\frac{e^2}{\rho_0}(0.0096 \ln \rho_0^3 n + 0.122). \quad (2.33)$$

The results we then obtain for the atomic ground-state energies agree with those of Jones (1985, 1986). For example, for Fe at  $B_{12} = 5$  we find an atomic energy of  $-108.05$  eV and Jones gives an energy of  $-108.18$  eV. The molecular ground-state energies per atom are of course not the same as those for the infinite chain from Jones's work, but they are comparable, particularly for the large molecules. For example, we find for  $\text{He}_8$  at  $B_{12} = 5$  that the energy per atom is  $-1242$  eV and Jones finds for  $\text{He}_\infty$  that the energy per cell is  $-1260$  eV. (See Appendix A.2 for a

brief discussion of why in our calculations we chose to use the Skudlarski-Vignale correlation energy expression over that of Jones.)

Second, we have compared our hydrogen, helium, and carbon molecule results to those of Demeur et al. (1994); Lai et al. (1992). Because these works use the Hartree-Fock method, we cannot compare absolute ground-state energies with theirs, but we can compare energy differences. We find fair agreement, though the Hartree-Fock results are consistently smaller. Some of these comparisons are presented in the following subsections.

### 2.4.1 Hydrogen

Our numerical results for H are given in Table 2.1 and Table 2.2. Note that at  $B_{12} = 1$ ,  $H_4$  is less bound than  $H_3$ , and thus  $\mathcal{E} = \mathcal{E}_N/N$  is not a necessarily a monotonically decreasing function of  $N$  at this field strength. For the  $H_4$  molecule, two configurations,  $(n_0, n_1) = (4, 0)$  and  $(3, 1)$ , have very similar equilibrium energies (see Fig. 2.2), although the equilibrium ion separations are different. The real ground state may therefore be a “mixture” of the two configurations; such a state would presumably give a lower ground-state energy for  $H_4$ , and make the energy trend monotonic.

Hartree-Fock results for H molecules are given in (Lai et al. 1992). For  $H_2$ ,  $H_3$ , and  $H_4$ , the energies (per atom) are, respectively:  $-184.3$ ,  $-188.7$ ,  $-185.0$  eV at  $B_{12} = 1$ ;  $-383.9$ ,  $-418.8$ ,  $-432.9$  eV at  $B_{12} = 10$ ; and  $-729.3$ ,  $-847.4$ ,  $-915.0$  eV at  $B_{12} = 100$ . Thus, our density-functional-theory calculation tends to overestimate the energy  $|\mathcal{E}|$  by about 10%. Note that the Hartree-Fock results also reveal a non-monotonic behavior of  $\mathcal{E}$  at  $N = 4$  for  $B_{12} = 1$ , in agreement with our

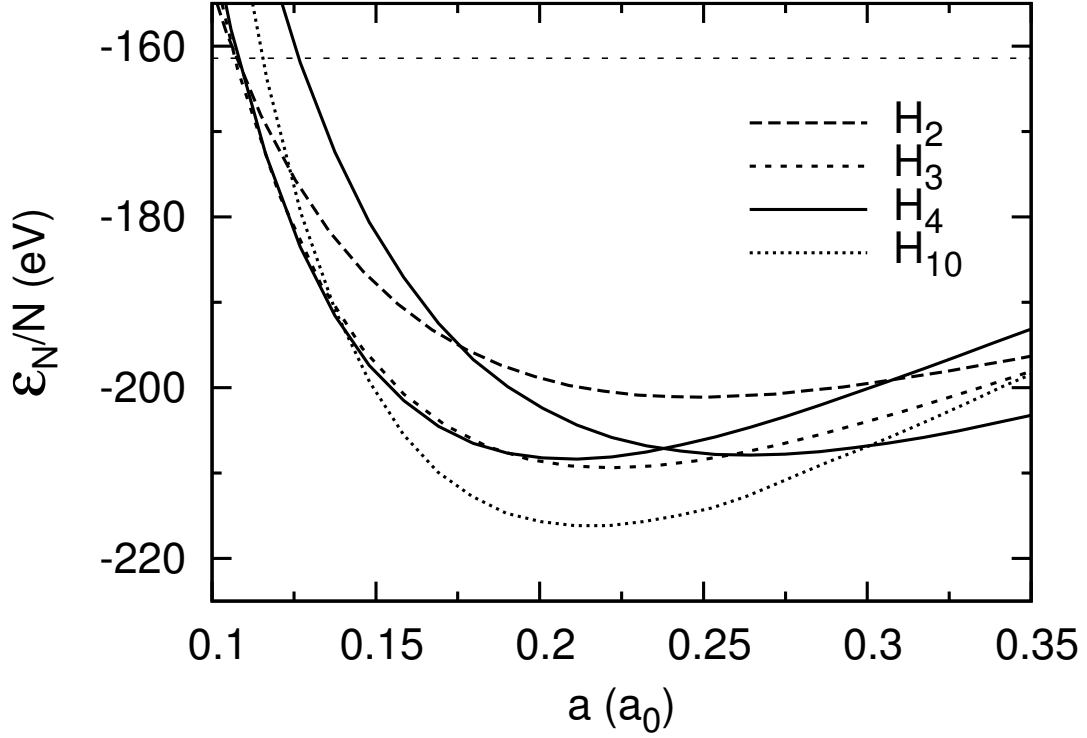


Figure 2.2: Molecular energy per atom versus ion separation for various hydrogen molecules at  $B_{12} = 1$ . The energy of the H atom is shown as a horizontal line at  $-161.4$  eV. The two lowest-energy configurations of  $H_4$  have nearly the same minimum energy, so the curves for both configurations are shown here.

density-functional result. Demeur et al. (1994) calculated the energies of  $H_2$ – $H_5$  at  $B_{12} = 2.35$ ; their results exhibit similar trends.

### 2.4.2 Helium

Our numerical results for He are given in Table 2.3 and Table 2.4.

The energies (per atom) of He and  $He_2$  based on Hartree-Fock calculations (Lai 2001) are, respectively:  $-575.5$ ,  $-601.2$  eV at  $B_{12} = 1$ ;  $-1178$ ,  $-1364$  eV at  $B_{12} = 10$ ;  $-2193$ ,  $-2799$  eV at  $B_{12} = 100$ ; and  $-3742$ ,  $-5021$  eV at  $B_{12} = 1000$ . At  $B_{12} = 2.35$ , Demeur et al. (1994) find that the energies (per atom) of He,  $He_2$ ,

Table 2.1: Ground-state energies, ion separations, and electron configurations of hydrogen molecules, over a range of magnetic field strengths. In some cases the first-excited-state energies are also listed. Energies are given in units of eV, separations in units of  $a_0$  (the Bohr radius). For molecules ( $H_N$ ) the energy per atom is given,  $\mathcal{E} = \mathcal{E}_N/N$ . All of the H and  $H_2$  molecules listed here have electrons only in the  $\nu = 0$  states. For the  $H_3$  and larger molecules here, however, the molecular structure is more complicated, and is designated by the notation  $(n_0, n_1, \dots)$ , where  $n_0$  is the number of electrons in the  $\nu = 0$  orbitals,  $n_1$  is the number of electrons in the  $\nu = 1$  orbitals, etc.

$B_{12}$	H $\mathcal{E}$	H <sub>2</sub> $\mathcal{E}$ $a$		H <sub>3</sub> $\mathcal{E}$ $a$ $(n_0, n_1)$			H <sub>4</sub> $\mathcal{E}$ $a$ $(n_0, n_1)$			H <sub>5</sub> $\mathcal{E}$ $a$ $(n_0, n_1)$		
1	-161.4	-201.1	0.25	-209.4	0.22	(3,0)	-208.4	0.21	(4,0)	-213.8	0.23	(4,1)
				-191.1	0.34	(2,1)	-207.9	0.26	(3,1)	-203.1	0.200	(5,0)
10	-309.5	-425.8	0.125	-469.0	0.106	(3,0)	-488.1	0.096	(4,0)	-493.5	0.090	(5,0)
										-478.9	0.112	(4,1)
100	-540.3	-829.5	0.071	-961.2	0.057	(3,0)	-1044.5	0.049	(4,0)	-1095.5	0.044	(5,0)
1000	-869.6	-1540.5	0.044	-1818.0	0.033	(3,0)	-2049	0.028	(4,0)	-2222	0.024	(5,0)

$B_{12}$	H <sub>6</sub> $\mathcal{E}$ $a$ $(n_0, n_1)$			H <sub>8</sub> $\mathcal{E}$ $a$ $(n_0, n_1, n_2)$			H <sub>10</sub> $\mathcal{E}$ $a$ $(n_0, n_1, n_2)$		
1	-214.1	0.23	(4,2)	-215.8	0.23	(5,2,1)	-216.2	0.22	(6,3,1)
	-213.4	0.21	(5,1)	-215.3	0.25	(4,3,1)	-216.0	0.23	(5,3,2)
10	-496.5	0.101	(5,1)	-507.1	0.095	(8,2,0)	-509.3	0.091	(7,3,0)
	-490.8	0.86	(6,0)	-504.1	0.089	(7,1,0)	-506.8	0.087	(8,2,0)
100	-1125.0	0.041	(6,0)	-1143.0	0.038	(8,0,0)	-1169.5	0.038	(9,1,0)
				-1139.5	0.043	(7,1,0)	-1164.0	0.042	(8,2,0)
1000	-2351	0.22	(6,0)	-2518	0.0190	(8,0,0)	-2600	0.0170	(10,0,0)
							-2542	0.0200	(9,1,0)



Table 2.2: Fit of the ground-state energies of hydrogen molecules to the scaling relation  $\mathcal{E} \propto B_{12}^\beta$ . The scaling exponent  $\beta$  is fit for each molecule  $H_N$  over three magnetic field ranges:  $B_{12} = 1 - 10$ ,  $10 - 100$ , and  $100 - 1000$ .

$B_{12}$	$\beta$							
	H	H <sub>2</sub>	H <sub>3</sub>	H <sub>4</sub>	H <sub>5</sub>	H <sub>6</sub>	H <sub>8</sub>	H <sub>10</sub>
1-10	0.283	0.326	0.350	0.370	0.363	0.365	0.371	0.372
10-100	0.242	0.290	0.312	0.330	0.346	0.355	0.353	0.361
100-1000	0.207	0.269	0.277	0.293	0.307	0.320	0.343	0.347

He<sub>3</sub>, and He<sub>4</sub> are, respectively:  $-753.4$ ,  $-812.6$ ,  $-796.1$ ,  $-805.1$  eV. Using our scaling relations, we find for that same field that the energies of He, He<sub>2</sub>, He<sub>3</sub>, and He<sub>5</sub> (we do not have an He<sub>4</sub> result) are:  $-791$ ,  $-871$ ,  $-889$ ,  $-901$  eV. Thus, our density-functional theory calculation tends to overestimate the energy  $|\mathcal{E}|$  by about 10%.

Figure 2.3 gives some examples of the longitudinal electron wave functions. One wave function of each node type in the molecule ( $\nu = 0$  to 3) is represented. Note that on the atomic scale each wave function is nodeless in nature; that is, there are no nodes at the ions, only in between ions. This is not surprising when one considers that all of the electrons in atomic helium at this field strength are nodeless. The entire molecular wave function can be thought of as a string of atomic wave functions, one around each ion, each modified by some phase factor to give the overall nodal nature of the wave function. Indeed, for atoms at field strengths that are low enough to allow  $\nu > 0$  states, we find that their corresponding molecules have electron wave functions with nodes at the ions. Atomic Fe at  $B_{12} = 10$ , for example, has an electron wave function with one node at the ion, and Fe<sub>2</sub> at  $B_{12} = 10$  has an electron wave function with a node at each ion.

Table 2.3: Ground-state energies, ion separations, and electron configurations of helium molecules, over a range of magnetic field strengths. In some cases the first-excited-state energies are also listed. Energies are given in units of eV, separations in units of  $a_0$  (the Bohr radius). For molecules ( $\text{He}_N$ ) the energy per atom is given,  $\mathcal{E} = \mathcal{E}_N/N$ . All of the He and  $\text{He}_2$  molecules listed here have electrons only in the  $\nu = 0$  states. For the  $\text{He}_3$  and larger molecules here, however, the molecular structure is more complicated, and is designated by the notation  $(n_0, n_1, \dots)$ , where  $n_0$  is the number of electrons in the  $\nu = 0$  orbitals,  $n_1$  is the number of electrons in the  $\nu = 1$  orbitals, etc.

$B_{12}$	He $\mathcal{E}$	He <sub>2</sub> $\mathcal{E}$ $a$		He <sub>3</sub> $\mathcal{E}$ $a$ $(n_0, n_1)$			He <sub>5</sub> $\mathcal{E}$ $a$ $(n_0, n_1, n_2)$			He <sub>8</sub> $\mathcal{E}$ $a$ $(n_0, n_1, n_2, n_3)$		
1	-603.5	-641.2	0.25	-647.3	0.28	(5,1)	-653.1	0.29	(6,3,1)	-656.7	0.28	(7,5,3,1)
				-633.0	0.32	(4,2)	-649.4	0.28	(7,2,1)	-656.5	0.27	(8,5,2,1)
10	-1252.0	-1462.0	0.115	-1520.0	0.105	(6,0)	-1553.5	0.110	(8,2,0)	-1574.5	0.110	(10,5,1,0)
				-1462.0	0.125	(5,1)	-1547.5	0.105	(9,1,0)	-1574.0	0.105	(11,4,1,0)
100	-2385	-3039	0.060	-3370	0.050	(6,0)	-3573	0.044	(10,0,0)	-3694	0.045	(13,3,0,0)
				-3140	0.054	(5,1)	-3543	0.049	(9,1,0)	-3690	0.043	(14,2,0,0)
1000	-4222	-5787	0.036	-6803	0.028	(6,0)	-7887	0.022	(10,0,0)	-8406	0.0200	(15,1,0,0)
										-8357	0.0180	(16,0,0,0)

Table 2.4: Fit of the ground-state energies of helium molecules to the scaling relation  $\mathcal{E} \propto B_{12}^\beta$ . The scaling exponent  $\beta$  is fit for each molecule  $\text{He}_N$  over three magnetic field ranges:  $B_{12} = 1 - 10$ ,  $10 - 100$ , and  $100 - 1000$ .

$B_{12}$	$\beta$				
	He	He <sub>2</sub>	He <sub>3</sub>	He <sub>5</sub>	He <sub>8</sub>
1-10	0.317	0.358	0.371	0.376	0.380
10-100	0.280	0.318	0.346	0.362	0.370
100-1000	0.248	0.280	0.305	0.344	0.357

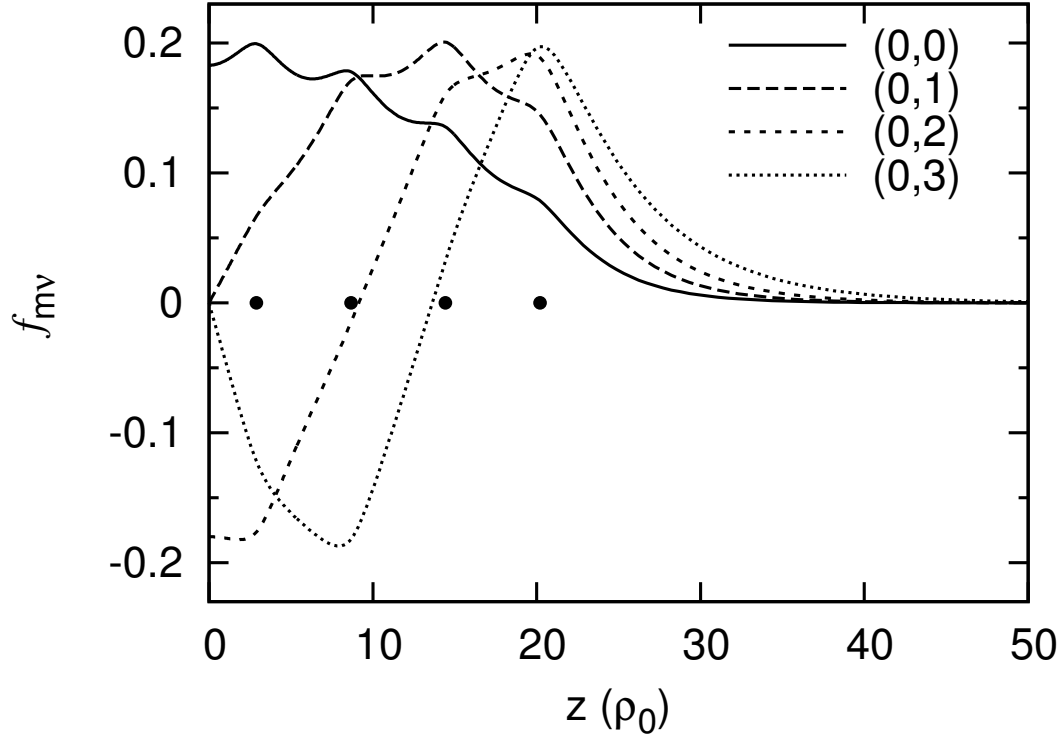


Figure 2.3: Longitudinal wave functions for selected electron orbitals of  $\text{He}_8$  at  $B_{12} = 1$ , at the equilibrium ion separation. Different orbitals are labeled by  $(m, \nu)$ . Only the  $z \geq 0$  region is shown. Wave functions with even  $\nu$  are symmetric about  $z = 0$ , and those with odd  $\nu$  are antisymmetric about  $z = 0$ . The filled circles denote the ion locations.

### 2.4.3 Carbon

Our numerical results for C are given in Table 2.5, Table 2.6, and Table 2.7.

The only previous result of C molecules is that by Demeur et al. (1994), who calculated  $C_2$  only at  $B_{12} = 2.35$ . At this field strength, our calculation shows that  $C_2$  is bound relative to C atom ( $\mathcal{E} = -5994, -6017$  eV for C,  $C_2$ ), whereas Demeur et al. find no binding ( $\mathcal{E} = -5770, -5749$  eV for C,  $C_2$ ). Thus our result differs qualitatively from (Demeur et al. 1994). We also disagree on the ground-state occupation at this field strength: we find  $(n_0, n_1) = (9, 3)$  while Demeur et al. find  $(n_0, n_1) = (7, 5)$ . We suggest that if Demeur et al. used the occupation  $(n_0, n_1) = (9, 3)$  they would obtain a lower-energy for  $C_2$ , though whether  $C_2$  would then be bound remains uncertain. Since the numerical accuracy of our computation is 0.1% of the total energy (thus, about 6 eV for  $B_{12} = 2.35$ ), our results for  $B_{12} \lesssim$  a few should be treated with caution.

Figure 2.4 gives some examples of the longitudinal electron wave functions. One wave function of each node type in the molecule ( $\nu = 0$  to 4) is represented. Note that on the atomic scale each wave function is nodeless in nature (as is the case for the wave functions in Fig. 2.3). The exception to this is at the central ion, where due to symmetry considerations the antisymmetric wave functions must have nodes. [The nodes for  $(m, \nu) = (0, 2)$  are near, but not at, the ions  $j = 2$  and  $j = 4$ . This is incidental.]

Table 2.5: Ground-state energies, ion separations, and electron configurations of carbon molecules, over a range of magnetic field strengths. In some cases the first-excited-state energies are also listed. Energies are given in units of eV, separations in units of  $a_0$  (the Bohr radius). For molecules ( $C_N$ ) the energy per atom is given,  $\mathcal{E} = \mathcal{E}_N/N$ . All of the C atoms listed here have electrons only in the  $\nu = 0$  orbitals. For the  $C_2$  and larger molecules here, however, the molecular structure is more complicated, and is designated by the notation  $(n_0, n_1, \dots)$ , where  $n_0$  is the number of electrons in the  $\nu = 0$  orbitals,  $n_1$  is the number of electrons in the  $\nu = 1$  orbitals, etc.

$B_{12}$	C	$C_2$			$C_3$		
	$\mathcal{E}$	$\mathcal{E}$	$a$	$(n_0, n_1)$	$\mathcal{E}$	$a$	$(n_0, n_1, n_2)$
1	-4341	-4351	0.53	(8,4)	-4356	0.52	(9,6,3)
		-4349	0.46	(9,3)	-4354	0.50	(10,5,3)
10	-10075	-10215	0.150	(11,1)	-10255	0.175	(13,4,1)
		-10200	0.180	(10,2)	-10240	0.185	(14,3,1)
100	-21360	-23550	0.054	(12,0)	-24060	0.055	(17,1,0)
					-23960	0.058	(16,2,0)
1000	-41330	-50760	0.027	(12,0)	-54870	0.024	(18,0,0)

$B_{12}$	$C_4$			$C_5$		
	$\mathcal{E}$	$a$	$(n_0, n_1, n_2, n_3)$	$\mathcal{E}$	$a$	$(n_0, n_1, n_2, n_3, n_4)$
1	-4356	0.52	(10,7,4,3)	-4358	0.48	(11,8,6,3,2)
	-4354	0.56	(9,7,5,3)	-4357	0.47	(12,8,5,3,2)
10	-10255	0.180	(15,6,2,1)	-10275	0.150	(18,8,3,1)
	-10250	0.185	(14,7,2,1)	-10270	0.155	(17,9,3,1)
100	-24350	0.054	(21,3,0,0)	-24470	0.057	(23,6,1,0,0)
	-24300	0.056	(20,4,0,0)	-24460	0.056	(24,5,1,0,0)
1000	-56500	0.024	(23,1,0,0)	-57640	0.022	(28,2,0,0,0)
	-56190	0.022	(24,0,0,0)	-57520	0.023	(27,3,0,0,0)

Table 2.6: Ground-state energies of ionized carbon atoms over a range of magnetic field strengths. Energies are given in units of eV. For these field strengths, the electron configuration of C atoms is such that all of their electrons lie in the  $\nu = 0$  orbitals; therefore the ionized atoms have all electrons in the  $\nu = 0$  orbitals as well. The ionization state is designated by the notation, “C $^{n+}$ ,” where  $n$  is the number of electrons that have been removed from the atom. The entry “C $^{5+}$ ,” for example, is a carbon nucleus plus one electron.

$B_{12}$	C	C $^{+}$	C $^{2+}$	C $^{3+}$	C $^{4+}$	C $^{5+}$
1	-4341	-4167	-3868	-3411	-2739	-1738.0
10	-10075	-9644	-8917	-7814	-6213	-3877
100	-21360	-20370	-18730	-16300	-12815	-7851
1000	-41330	-39210	-35830	-30920	-24040	-14425

Table 2.7: Fit of the ground-state energies of neutral and ionized carbon atoms and carbon molecules to the scaling relation  $\mathcal{E} \propto B_{12}^{\beta}$ . The scaling exponent  $\beta$  is fit over three magnetic field ranges:  $B_{12} = 1 - 10$ ,  $10 - 100$ , and  $100 - 1000$ .

$B_{12}$	$\beta$							
	C $^{5+}$	C $^{4+}$	C $^{+}$	C	C $_2$	C $_3$	C $_4$	C $_5$
1-10	0.348	0.356	0.364	0.366	0.371	0.372	0.372	0.372
10-100	0.306	0.314	0.325	0.326	0.363	0.370	0.376	0.377
100-1000	0.264	0.273	0.284	0.287	0.334	0.358	0.366	0.372

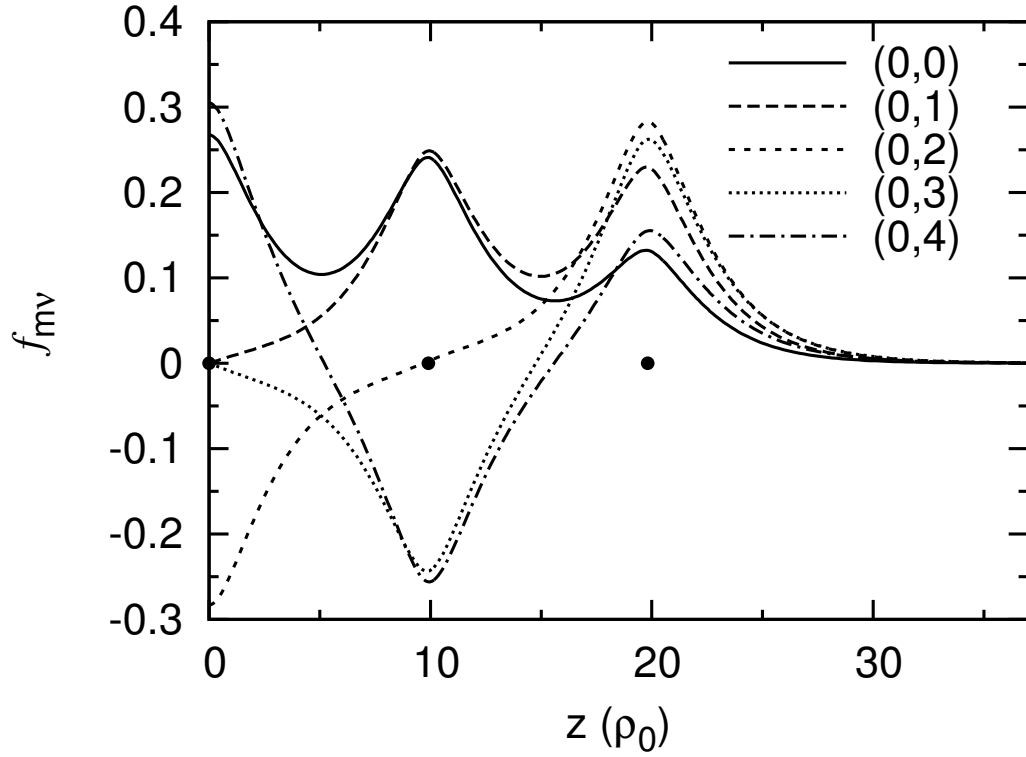


Figure 2.4: Longitudinal wave functions for selected electron orbitals of  $C_5$  at  $B_{12} = 1$ , at the equilibrium ion separation. Different orbitals are labeled by  $(m, \nu)$ . Only the  $z \geq 0$  region is shown. Wave functions with even  $\nu$  are symmetric about  $z = 0$ , and those with odd  $\nu$  are antisymmetric about  $z = 0$ . The filled circles denote the ion locations.

### 2.4.4 Iron

Our numerical results for Fe are given in Table 2.8, Table 2.9, and Table 2.10. The energy curves for  $B_{12} = 500$  are shown in Fig. 2.5, and some results for  $B_{12} = 100$  are shown in Fig. 2.6.

There is no previous quantitative calculation of Fe molecules in strong magnetic fields that we are aware of. The most relevant work is that of Abrahams & Shapiro (1991), who use a Thomas-Fermi type model to calculate Fe and  $\text{Fe}_2$  energies for magnetic fields up to  $B_{12} = 30$ . Unfortunately, a comparison of our results with those of this work is not very useful, as Thomas-Fermi models are known to give inaccurate energies and in particular large overestimates of binding and cohesive energies. As an example, from Abrahams & Shapiro (1991) the energy difference between Fe and  $\text{Fe}_2$  at  $B_{12} = 30$  is 1.7 keV, which is twice as large as our result at  $B_{12} = 100$ .

In Table 2.8 we have not provided results for the  $\text{Fe}_2$  and  $\text{Fe}_3$  molecules at  $B_{12} = 5$ , as these molecules are not bound relative to the Fe atom. We have not provided results for the  $\text{Fe}_3$  molecule at  $B_{12} = 10$  because the energy difference (per atom) between  $\text{Fe}_3$  and the Fe atom at this field strength is smaller than the error in our calculation, 0.1% of  $|\mathcal{E}|$  or 140 eV. The energy difference (per atom) between the  $\text{Fe}_2$  molecule and the Fe atom at  $B_{12} = 10$  is also smaller than the error in our calculation (indeed, the difference should be less than that between  $\text{Fe}_3$  and Fe at this field strength), but we have redone the calculation using more grid and integration points such that the energy values reported here for these two molecules are accurate numerically to 0.01% (see Appendix A.1). At this accuracy, our results indicate that  $\text{Fe}_2$  is bound over Fe at  $B_{12} = 10$  with a energy difference per atom of 30 eV.



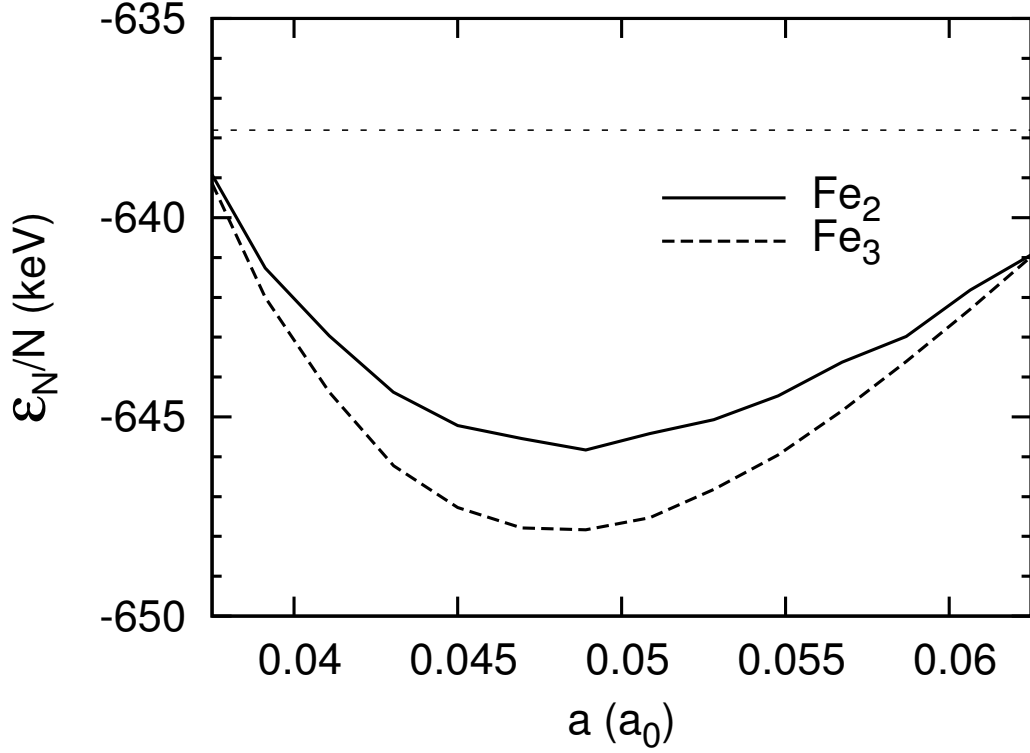


Figure 2.5: Molecular energy per atom versus ion separation for  $\text{Fe}_2$  and  $\text{Fe}_3$  molecules at  $B_{12} = 500$ . The energy of the Fe atom is shown as a horizontal line at  $-637.8$  keV.

Figure 2.6 illustrates how the ground-state electron configuration is found for each molecule. The configuration with the lowest equilibrium energy is chosen as the ground-state configuration. In the case depicted in Fig. 2.6,  $\text{Fe}_2$  at  $B_{12} = 100$ , there are actually two such configurations. Within the error of our calculation, we cannot say which one represents the ground state. Note that the systematic error seen in the minimization curves of the various  $\text{Fe}_2$  configurations is much smaller than our target 0.1% error for the total energy (the sinusoidal error in the figure has an amplitude of  $\approx 30$  eV, or around 0.01% of the total energy).

Table 2.8: Ground-state energies, ion separations, and electron configurations of iron molecules, over a range of magnetic field strengths. In some cases the first-excited-state energies are also listed. Energies are given in units of keV, separations in units of  $a_0$  (the Bohr radius). For molecules ( $\text{Fe}_N$ ) the energy per atom is given,  $\mathcal{E} = \mathcal{E}_N/N$ . The electron configuration is designated by the notation  $(n_0, n_1, \dots)$ , where  $n_0$  is the number of electrons in the  $\nu = 0$  orbitals,  $n_1$  is the number of electrons in the  $\nu = 1$  orbitals, etc. Note that no information is listed for the  $\text{Fe}_2$  and  $\text{Fe}_3$  molecules at  $B_{12} = 5$ , as we have found that these molecules are not bound at this field strength. Also note that there are two lowest-energy states for  $\text{Fe}_2$  at  $B_{12} = 100$ ; within the error of our calculation, the two states have the same minimum energies.

$B_{12}$	Fe		Fe <sub>2</sub>			Fe <sub>3</sub>		
	$\mathcal{E}$	$(n_0, n_1)$	$\mathcal{E}$	$a$	$(n_0, n_1)$	$\mathcal{E}$	$a$	$(n_0, n_1, n_2)$
5	-107.20	(24,2)	-	-	-	-	-	-
10	-142.15	(25,1)	-142.18	0.30	(32,19,1)	-	-	-
100	-354.0	(26,0)	-354.9	0.107	(39,13)	-355.2	0.107	(47,21,10)
			-354.9	0.103	(40,12)	-355.1	0.108	(46,22,10)
500	-637.8	(26,0)	-645.7	0.048	(45,7)	-648.1	0.048	(58,16,4)
			-645.4	0.050	(44,8)	-648.0	0.050	(57,16,5)
1000	-810.6	(26,0)	-828.8	0.035	(47,5)	-834.1	0.035	(62,13,3)
			-828.4	0.034	(48,4)	-834.0	0.036	(61,14,3)
2000	-1021.5	(26,0)	-1061.0	0.025	(49,3)	-1073.0	0.025	(67,10,1)
			-1056.0	0.023	(50,2)	-1072.5	0.025	(66,11,1)

Table 2.9: Ground-state energies of ionized iron atoms over a range of magnetic field strengths. Energies are given in units of keV. For  $B_{12} \geq 100$ , the electron configuration of Fe atoms is such that all of their electrons lie in the  $\nu = 0$  orbitals; therefore for these field strengths the ionized atoms have all electrons in the  $\nu = 0$  orbitals as well. The ionization state is designated by the notation, “Fe $^{n+}$ ,” where  $n$  is the number of electrons that have been removed from the atom. The entry “Fe $^{25+}$ ,” for example, is an iron nucleus plus one electron.

$B_{12}$	Fe	Fe $^{+}$	Fe $^{2+}$	Fe $^{3+}$	Fe $^{4+}$	Fe $^{5+}$	Fe $^{10+}$	Fe $^{15+}$	Fe $^{20+}$	Fe $^{25+}$
100	-354.0	-352.8	-351.2	-349.0	-346.4	-343.2	-318.3	-273.8	-199.65	-59.01
500	-637.8	-635.3	-632.0	-627.8	-622.7	-616.6	-569.4	-486.5	-350.2	-99.48
1000	-810.6	-807.2	-802.8	-797.2	-790.7	-782.5	-715.8	-602.0	-439.6	-122.70
2000	-1021.5	-1016.0	-1008.5	-999.8	-989.1	-976.7	-905.4	-768.6	-546.8	-150.10

Table 2.10: Fit of the ground-state energies of neutral and ionized iron atoms and iron molecules to the scaling relation  $\mathcal{E} \propto B_{12}^\beta$ . The scaling exponent  $\beta$  is fit over three magnetic field ranges:  $B_{12} = 100 - 500$ ,  $500 - 1000$ , and  $1000 - 2000$ .

$B_{12}$	$\beta$						
	Fe <sup>25+</sup>	Fe <sup>20+</sup>	Fe <sup>10+</sup>	Fe <sup>+</sup>	Fe	Fe <sub>2</sub>	Fe <sub>3</sub>
100-500	0.324	0.349	0.361	0.365	0.366	0.372	0.374
500-1000	0.303	0.328	0.330	0.345	0.346	0.359	0.364
1000-2000	0.291	0.315	0.339	0.332	0.334	0.358	0.363

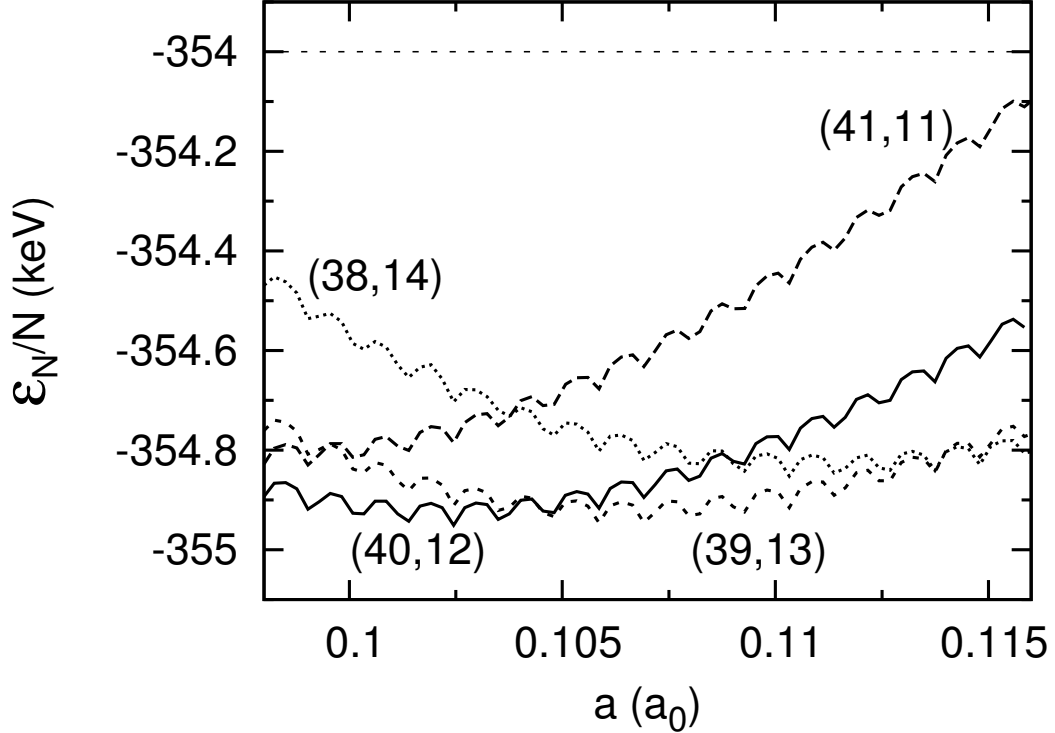


Figure 2.6: Molecular energy per atom versus ion separation for various configurations of electrons in the Fe<sub>2</sub> molecule at  $B_{12} = 100$ . The configurations are labeled using the notation  $(n_0, n_1)$ , where  $n_0$  is the number of electrons with  $\nu = 0$  and  $n_1$  is the number with  $\nu = 1$ . The energy of the Fe atom is shown as a horizontal line at  $-354.0$  keV. The states “(40, 12)” and “(39, 13)” have the lowest equilibrium energies of all possible configurations and within the numerical accuracy of our calculation have the same equilibrium energies. The wavy structure of the curves gives an indication of the numerical accuracy of our code. Note that states with electrons in the  $\nu = 2$  orbitals [for example,  $(39, 12, 1)$ ] have energies higher than the atomic energy and are therefore unbound.

## 2.5 Conclusions

We have presented density-functional-theory calculations of the ground-state energies of various atoms and molecular chains ( $H_N$  up to  $N = 10$ ,  $He_N$  up to  $N = 8$ ,  $C_N$  up to  $N = 5$ , and  $Fe_N$  up to  $N = 3$ ) in strong magnetic fields ranging from  $B = 10^{12}$  G to  $2 \times 10^{15}$  G. These atoms and molecules may be present in the surface layers of magnetized neutron stars, such as radio pulsars and magnetars. While previous results (based on Hartree-Fock or density-functional-theory calculations) are available for some small molecules at selected field strengths (e.g., Lai et al. 1992; Lai 2001; Demeur et al. 1994) many other systems (e.g., larger C molecules and Fe molecules) are also computed in this chapter. We have made an effort to present our numerical results systematically, including fitting formulae for the  $B$ -dependence of the energies. Comparison with previous results (when available) show that our density-functional calculations tend to overestimate the binding energy  $|\mathcal{E}_N|$  by about 10%. Since it is advantageous to use the density functional theory to study systems containing large number of electrons (e.g., condensed matter; see 3), it would be useful to find ways to improve upon this accuracy.

At  $B_{12} \geq 1$ , hydrogen, helium, and carbon molecules are all more energetically favorable than their atomic counterparts (although for carbon, the relative binding between the atom and molecule is rather small), but iron is not. Iron molecules start to become bound at  $B_{12} \gtrsim 10$ , and are not decidedly more favorable than isolated atoms until about  $B_{12} = 100$ .

For the bound molecules considered here, the ground-state energy per atom approaches an asymptotic value as  $N$  gets large. The molecule then essentially becomes a one-dimensional infinite chain. We will study such condensed matter in Chapter 3.

CHAPTER 3

**DENSITY-FUNCTIONAL-THEORY CALCULATIONS OF  
MATTER IN STRONG MAGNETIC FIELDS: INFINITE CHAINS  
AND CONDENSED MATTER**

### 3.1 Introduction

Young neutron stars (ages  $\lesssim 10^7$  years) are observed to have surface magnetic fields in the range of  $10^{11}$ - $10^{15}$  G (Mészáros 1992; Reisenegger 2005; Woods & Thompson 2005; Harding & Lai 2006), far beyond the reach of terrestrial laboratories (Wagner et al. 2004). It is well known that the properties of matter can be drastically modified by such strong magnetic fields. The natural atomic unit for the magnetic field strength,  $B_0$ , is set by equating the electron cyclotron energy  $\hbar\omega_{Be} = \hbar(eB/m_e c) = 11.577 B_{12}$  keV, where  $B_{12} = B/(10^{12}$  G), to the characteristic atomic energy  $e^2/a_0 = 2 \times 13.6$  eV (where  $a_0$  is the Bohr radius):

$$B_0 = \frac{m_e^2 c^3}{\hbar^3} = 2.3505 \times 10^9 \text{ G}. \quad (3.1)$$

For  $b = B/B_0 \gtrsim 1$ , the usual perturbative treatment of the magnetic effects on matter (e.g., Zeeman splitting of atomic energy levels) does not apply. Instead, in the transverse direction (perpendicular to the field) the Coulomb forces act as a perturbation to the magnetic forces, and the electrons in an atom settle into the ground Landau level. Because of the extreme confinement of the electrons in the transverse direction, the Coulomb force becomes much more effective in binding the electrons along the magnetic field direction. The atom attains a cylindrical structure. Moreover, it is possible for these elongated atoms to form molecular chains by covalent bonding along the field direction. Interactions between the

linear chains can then lead to the formation of three-dimensional condensed matter (Ruderman 1974; Ruder et al. 1994; Lai 2001).

This chapter is the second in a series where we present calculations of matter in strong magnetic fields using density functional theory. In Chapter 2, we studied various atoms and molecules in magnetic fields ranging from  $10^{12}$  G to  $2 \times 10^{15}$  G for H, He, C, and Fe, representative of the most likely neutron star surface compositions. Numerical results and fitting formulae of the ground-state energies were given for  $H_N$  (up to  $N = 10$ ),  $He_N$  (up to  $N = 8$ ),  $C_N$  (up to  $N = 5$ ), and  $Fe_N$  (up to  $N = 3$ ), as well as for various ionized atoms. It was found that as  $B$  increases, molecules become increasingly more bound relative to individual atoms, and that the binding energy per atom in a molecule,  $|\mathcal{E}_N|/N$ , generally increases and approaches a constant value with increasing  $N$ . In this chapter, we present density-functional-theory calculations of infinite chains of H, He, C, and Fe. Our goal is to obtain the cohesive energy of such one-dimensional (1D) condensed matter relative to individual atoms for a wide range of field strengths. We also carry out approximate calculations of the relative binding energy between 1D chains and three-dimensional (3D) condensed matter at zero pressure.

The cohesive property of matter in strong magnetic fields is a fundamental quantity characterizing magnetized neutron star surface layers, which play a key role in many neutron star processes and observed phenomena. The cohesive energy refers to the energy required to pull an atom out of the bulk condensed matter at zero pressure. Theoretical models of pulsar and magnetar magnetospheres depend on the cohesive properties of the surface matter in strong magnetic fields (Ruderman & Sutherland 1975; Arons & Scharlemann 1979; Usov & Melrose 1996; Harding & Muslimov 1998; Beloborodov & Thompson 2007; Gil et al. 2003). For

example, depending on the cohesive energy of the surface matter, an acceleration zone (“polar gap”) above the polar cap of a pulsar may or may not form, and this will affect pulsar radio emission and other high-energy emission processes. Also, while a hot or warm neutron star most certainly has a gaseous atmosphere that mediates its thermal emission, condensation of the stellar surface may occur at sufficiently low temperatures (Lai & Salpeter 1997; Lai 2001). For example, radiation from a bare condensed surface (with no atmosphere above it) has been invoked to explain the nearly perfect blackbody emission spectra observed in some nearby isolated neutron stars (Burwitz et al 2003; Mori & Ruderman 2003; van Adelsberg et al. 2005; Turolla et al. 2004; Perez-Azorin et al. 2006). However, whether surface condensation actually occurs depends on the cohesive energy of the surface matter.

There have been few quantitative studies of infinite chains and zero-pressure condensed matter in strong magnetic fields. Earlier variational calculations (Flowers et al. 1977; Müller 1984) as well as calculations based on Thomas-Fermi type statistical models (Abrahams & Shapiro 1991; Fushiki et al. 1992; Lieb et al. 1994a,b), while useful in establishing scaling relations and providing approximate energies of the atoms and the condensed matter, are not adequate for obtaining reliable energy differences (cohesive energies). Quantitative results for the energies of infinite chains of hydrogen molecules  $H_\infty$  in a wide range of field strengths ( $B \gg B_0$ ) were presented in both Lai et al. (1992) (using the Hartree-Fock method with the plane-wave approximation; see also Lai (2001) for some results of  $He_\infty$ ) and Relovsky & Ruder (1996) (using density functional theory). For heavier elements such as C and Fe, the cohesive energies of 1D chains have only been calculated at a few magnetic field strengths in the range of  $B = 10^{12}$ - $10^{13}$  G, using Hartree-Fock models (Neuhauser et al. 1987) and density functional theory (Jones 1985). There were discrepancies between the results of these works, and some



(e.g., Neuhauser et al. 1987) adopted a crude treatment for the band structure (see Section 3.3.3). An approximate calculation of 3D condensed matter based on density functional theory was presented in Jones (1986).

Our calculations of atoms and small molecules (Chapter 2) and of infinite chains and condensed matter (this chapter) are based on density functional theory (Hohenberg & Kohn 1964; Kohn & Sham 1965; Vignale & Rasolt 1987, 1988; Jones & Gunnarsson 1989). In the strong field regime where the electron spins are aligned with each other, the Hartree-Fock method is expected to be highly accurate (Neuhauser et al. 1987; Schmelcher et al. 1999). However, in dealing with systems with many electrons, it becomes increasingly impractical as the magnetic field increases, since more and more Landau orbitals (even though electrons remain in the ground Landau level) are occupied and keeping track of the direct and exchange interactions between electrons in various orbitals becomes computationally rather tedious. Our density-functional calculations allow us to obtain the energies of atoms and small molecules and the energy of condensed matter using the same method, thus providing reliable cohesive energy values for condensed surfaces of magnetic neutron stars, a main goal of our study. Compared to previous density-functional theory calculations (Jones 1985, 1986; Kössl et al. 1988; Relovsky & Ruder 1996), we use an improved exchange-correlation function appropriate for highly magnetized electron gases, we calibrate our density-functional code with previous results (when available) based on other methods, and (for calculations of condensed matter) adopt a more accurate treatment of the band structure. Moreover, our calculations extend to the magnetar-like field regime ( $B \sim 10^{15}$  G).

This chapter is organized as follows. After briefly summarizing the approximate scaling relations for linear chains and condensed matter in strong magnetic fields

in Section 3.2, we describe our method and the basic equations in Section 3.3. Numerical results (tables and fitting formulae) for linear chains are presented in Section 3.4. In Section 3.5 we describe our approximate calculation and results for the relative energy between 1D chain and 3D condensed matter. We conclude in Section 3.6. Some technical details are given Appendix B.

This chapter is based on the published paper by Medin & Lai 2006 [Medin Z., Lai D., 2006, Physical Review A, 74, 062508; ©2006. The American Physical Society. All rights reserved]. It is reprinted here with minor changes, based on rights retained by the author.

## 3.2 Basic scaling relations for linear chains and 3D condensed matter in strong magnetic fields

The simplest model for the linear chain is to treat it as a uniform cylinder of electrons, with ions aligned along the magnetic field axis. The radius of the cylinder is  $R$  and the length of a unit cell is  $a$  (which is also the atomic spacing along the  $z$  axis). The electrons lie in the ground Landau level, but can occupy different Landau orbitals with the radius of guiding center  $\rho_m = (2m + 1)^{1/2} \rho_0$ , where  $m = 0, 1, 2, \dots, m_{\max}$  and  $\rho_0 = (\hbar c / eB)^{1/2} = b^{-1/2}$  (in atomic units).<sup>1</sup> The maximum Landau orbital number  $m_{\max}$  is set by  $\rho_{m_{\max}} = R$ , giving  $m_{\max} \simeq \pi R^2 eB / (\hbar c) = R^2 b / 2$  (this is the Landau degeneracy in area  $\pi R^2$ ). For a uniform electron density  $n = Z / (\pi R^2 a)$ , the Fermi wave number (along  $z$ )  $k_F$  is determined from  $n = b k_F / (2\pi^2)$ , and the kinetic energy of the electrons in a cell is  $\mathcal{E}_k = (Z/3) \varepsilon'_F$ , with

---

<sup>1</sup>Unless otherwise specified, we use atomic units, in which the length in  $a_0$  (Bohr radius), mass in  $m_e$ , energy in  $e^2/a_0 = 2$  Ry, and magnetic field strength in units of  $B_0$ .

$\varepsilon'_F = k_F^2/2$  the Fermi kinetic energy. The total energy per atom (unit cell) in the chain can be written as (Ruderman 1971, 1974)

$$\mathcal{E}_\infty = \frac{2\pi^2 Z^3}{3b^2 R^4 a^2} - \frac{Z^2}{a} \left[ \ln \frac{2a}{R} - \left( \gamma - \frac{5}{8} \right) \right], \quad (3.2)$$

where  $\gamma = 0.5772 \dots$  is Euler's constant. In Eq. (3.2), the first term is the electron kinetic energy  $\mathcal{E}_k$  and the second term is the (direct) Coulomb energy (the Madelung energy for the one-dimensional uniform lattice). Minimizing  $\mathcal{E}_\infty$  with respect to  $R$  and  $a$  gives

$$\begin{aligned} R &= 1.65 Z^{1/5} b^{-2/5}, & a/R &= 2.14, \\ \mathcal{E}_\infty &= -0.354 Z^{9/5} b^{2/5}. \end{aligned} \quad (3.3)$$

Note that the energy (3.2) can be written as  $\mathcal{E}_\infty = -ZV_0 + (Z/3)\varepsilon'_F$ , where  $V_0$  is the depth of the potential well relative to the continuum. In equilibrium  $\mathcal{E}_\infty = -5\mathcal{E}_k = -(5/3)Z\varepsilon'_F$ , and thus  $V_0 = 2\varepsilon'_F$ . The Fermi level energy of the electrons in the chain relative to the continuum is then  $\varepsilon_F = \varepsilon'_F - V_0 = -\varepsilon'_F = 3\mathcal{E}_\infty/(5Z)$ , i.e.,

$$\varepsilon_F(1D) = -0.212 Z^{4/5} b^{2/5} \text{ a.u.} = -65.1 Z^{4/5} B_{12}^{2/5} \text{ eV}. \quad (3.4)$$

Alternatively, if we identify the number of electrons in a cell,  $N_e$ , as an independent variable, we find  $R = 1.65 (N_e^2/Z)^{1/5} b^{-2/5}$  and  $\mathcal{E}_\infty = -0.354 (Z^2 N_e)^{3/5} b^{2/5}$ . The chemical potential (which includes potential energy) of electrons in the chain is simply  $\mu = \varepsilon_F = \partial \mathcal{E}_\infty / \partial N_e$ , in agreement with Eq. (3.4). The electron work function is  $W = |\varepsilon_F|$ .

A linear 1D chain naturally attracts neighboring chains through the quadrupole-quadrupole interaction. By placing parallel chains close together (with spacing of order  $b^{-2/5}$ ), we obtain three-dimensional condensed matter (e.g., a body-centered tetragonal lattice) (Ruderman 1971).

The binding energy of the 3D condensed matter at zero pressure can be estimated using the uniform electron gas model. Consider a Wigner-Seitz cell with radius  $r_i = Z^{1/3}r_s$  ( $r_s$  is the mean electron spacing); the mean number density of electrons is  $n = Z/(4\pi r_i^3/3)$ . When the Fermi energy  $p_F^2/(2m_e)$  is less than the electron cyclotron energy  $\hbar\omega_{Be}$ , or when the electron number density satisfies  $n \leq n_B = (\sqrt{2}\pi^2\rho_0^3)^{-1} = 0.0716 b^{3/2}$  (or  $r_i \geq r_{iB} = 1.49 Z^{1/3}b^{-1/2}$ ), the electrons only occupy the ground Landau level. The energy per cell can be written

$$\mathcal{E}_s(r_i) = \frac{3\pi^2 Z^3}{8b^2 r_i^6} - \frac{0.9Z^2}{r_i}, \quad (3.5)$$

where the first term is the kinetic energy and the second term is the Coulomb energy. For a zero-pressure condensed matter, we require  $d\mathcal{E}_s/dr_i = 0$ , and the equilibrium  $r_i$  and energy are then given by

$$r_i \simeq 1.90 Z^{1/5} b^{-2/5}, \quad (3.6)$$

$$\mathcal{E}_s \simeq -0.395 Z^{9/5} b^{2/5}. \quad (3.7)$$

The corresponding zero-pressure condensation density is

$$\rho_s \simeq 561 A Z^{-3/5} B_{12}^{6/5} \text{ g cm}^{-3}. \quad (3.8)$$

The electron Fermi level energy is

$$\varepsilon_F(3D) = \frac{3}{5Z} \mathcal{E}_s = -0.237 Z^{4/5} b^{2/5} \text{ a.u.} = -72.7 Z^{4/5} B_{12}^{2/5} \text{ eV}. \quad (3.9)$$

The uniform electron gas model can be improved by incorporating the Coulomb exchange energy and Thomas-Fermi correction due to nonuniformity of the electron gas (Lai 2001; Fushiki et al. 1989).

Although the simple uniform electron gas model and its Thomas-Fermi type extensions give a reasonable estimate for the binding energy for the condensed

state, they are not adequate for determining the cohesive property of the condensed matter. Also, as we shall see, Eq. (3.4) or Eq. (3.9) does not give a good scaling relation for the electron work function when detailed electron energy levels (bands) in the condensed matter are taken into account. The cohesive energy  $Q_s = \mathcal{E}_a - \mathcal{E}_s$  is the difference between the atomic ground-state energy  $\mathcal{E}_a$  and the condensed matter energy per cell  $\mathcal{E}_s$ . In principle, a three-dimensional electronic band structure calculation is needed to solve this problem. However, for sufficiently strong magnetic fields, such that  $a_0/Z \gg \sqrt{2Z+1}\rho_0$  or  $B_{12} \gg 100 (Z/26)^3$ , a linear 1D chain is expected to be strongly bound relative to individual atoms (i.e., the cohesive energy of the chain,  $Q_\infty = \mathcal{E}_a - \mathcal{E}_\infty$ , is significantly positive) (Lai 2001). For such strong fields, the binding of 3D condensed matter results mainly from the covalent bond along the magnetic axis, rather than from chain-chain interactions; in another word, the energy difference  $|\Delta\mathcal{E}_s| = |\mathcal{E}_s - \mathcal{E}_\infty|$  is small compared to  $Q_\infty$ . In the magnetic field regime where  $Q_\infty$  is small or even negative, chain-chain interactions are important in deciding whether 3D condensed matter is bound relative to individual atoms. In this chapter we will concentrate on calculating  $\mathcal{E}_\infty$  and  $Q_\infty$  for linear chains (Sections 3 and 4). In Section 5 we shall quantify the magnitude of  $\Delta\mathcal{E}_s$  for different elements and field strengths.

### 3.3 Density-functional-theory calculations of 1D chains:

#### Methods and equations

Our calculations of 1D infinite chains are based on density functional theory, which is well established in the strong magnetic field regime ( $B \gg B_0$ ) of interest here (Vignale & Rasolt 1987, 1988). Extensive comparisons of our density-functional-

theory results for atoms and finite molecules with previous results (when available) based on different methods were given in Chapter 2; such comparisons established the validity and calibrate the systematic error of our approach. As we discuss below, for infinite chains considered in the present chapter, it is important to calculate the band structure of electrons (for different Landau orbitals) self-consistently, rather than using certain approximate *ansätze* as adopted in some previous works (Neuhauser et al. 1987).

### 3.3.1 Basic equations and concepts

Our calculations will be based on the “adiabatic approximation,” in which all electrons are assumed to lie in the ground Landau level. For elements with nuclear charge number  $Z$ , this is an excellent approximation for  $b \gg Z^2$ . Even under the more relaxed condition  $b \gg Z^{4/3}$ , this approximation is expected to yield a reasonable total energy and accurate results for the energy difference between different electronic systems (atoms and chains) (see Chapter 2). Also, we use nonrelativistic quantum mechanics in our calculations, even when  $\hbar\omega_{Be} \gtrsim m_e c^2$  or  $B \gtrsim B_Q = B_0/\alpha^2 = 4.414 \times 10^{13}$  G (where  $\alpha = e^2/(\hbar c)$  is the fine structure constant). As discussed in Chapter 2, this is accurate as long as the electrons stay in the ground Landau level.

In a 1D chain, the ions form a periodic lattice along the magnetic field axis. The number of cells (“atoms”) in the chain is  $N \rightarrow \infty$  and the ions are equally spaced with lattice spacing  $a$ . In the adiabatic approximation, the one-electron wave function (“orbital”) can be separated into a transverse (perpendicular to the external magnetic field) component and a longitudinal (along the magnetic field)

component:

$$\Psi_{m\nu k}(\mathbf{r}) = \frac{1}{\sqrt{N}} W_m(\mathbf{r}_\perp) f_{m\nu k}(z). \quad (3.10)$$

Here  $W_m$  is the ground-state Landau wave function (Landau & Lifshitz 1977) given by

$$W_m(\mathbf{r}_\perp) = \frac{1}{\rho_0 \sqrt{2\pi m!}} \left( \frac{\rho}{\sqrt{2}\rho_0} \right)^m \exp\left(\frac{-\rho^2}{4\rho_0^2}\right) \exp(-im\phi), \quad (3.11)$$

which is normalized as  $\int d^2\mathbf{r}_\perp |W_m|^2 = 1$ . The longitudinal wave function  $f_{m\nu k}$  must be solved numerically, and we choose to normalize it over a unit cell of the lattice:

$$\int_{-a/2}^{a/2} |f_{m\nu k}(z)|^2 dz = 1, \quad (3.12)$$

so that normalization of  $\Psi_{m\nu k}$  is  $\int d^3\mathbf{r} |\Psi_{m\nu k}|^2 = 1$  (here and henceforth, the general integral sign  $\int d^3\mathbf{r}$  refers to integration over the whole chain, with  $z$  from  $-Na/2$  to  $Na/2$ ). The index  $\nu = 0, 1, 2, \dots$  labels the different bands of the electron (see below), rather than the number of nodes in the longitudinal wave function as in the atom or molecule case.

The quantum number  $k$  is not present for atoms or finite molecules, but enters here because of the periodic nature of the electrons in the longitudinal direction. By Bloch's theorem, the electrons satisfy the periodicity condition

$$f_{m\nu k}(z + a) = e^{ika} f_{m\nu k}(z), \quad (3.13)$$

and  $k$  is the Bloch wave number. Note that the longitudinal wave functions are periodic in  $k$  with period  $\Delta k = 2\pi/a$ ; i.e.,  $f_{m\nu, k+K}(z) = f_{m\nu k}(z)$  with  $K$  being any reciprocal vector (number, in one dimension) of the lattice,  $K = 2\pi n/a$  ( $n$  is an integer). Because of this, to ensure that each wave function  $f_{m\nu k}$  is unique, we restrict  $k$  to the first Brillouin zone,  $k \in [-\pi/a, \pi/a]$ . The electrons fill each  $(m\nu)$  band, with spacing  $\Delta k = \pi/(Na)$ , and thus the maximum number of electrons in a given band is  $N$  (out of the total  $ZN$  electrons in the chain). In another word, the number of electrons per unit cell in each  $(m\nu)$  band is  $\sigma_{m\nu} \leq 1$  (see Section 3.3.2).

The density distribution of electrons in the chain is given by

$$n(\mathbf{r}) = \sum_{m\nu k} |\Psi_{m\nu k}(\mathbf{r})|^2 = \frac{a}{2\pi} \sum_{m\nu} |W_m|^2(\rho) \int_{I_{m\nu}} dk |f_{m\nu k}(z)|^2, \quad (3.14)$$

where the sum/integral is over all electron states, each electron occupying an  $(m\nu k)$  orbital. The notation  $|W_m|^2(\rho) = |W_m(\mathbf{r}_\perp)|^2$  is used here because  $W_m$  is a function of  $\rho$  and  $\phi$  but  $|W_m|^2$  is a function of  $\rho$  only. The notation  $\int_{I_{m\nu}}$  in the  $k$  integral refers to the fact that the region of integration depends on the  $(m\nu)$  level; we will discuss this interval and electron occupations in Section 3.3.2. To simplify the appearance of the electron density expression, we define the function

$$\bar{f}_{m\nu}(z) = \sqrt{\frac{a}{2\pi} \int_{I_{m\nu}} dk |f_{m\nu k}(z)|^2}, \quad (3.15)$$

so that

$$n(\mathbf{r}) = \sum_{m\nu} |W_m|^2(\rho) \bar{f}_{m\nu}^2(z). \quad (3.16)$$

In an external magnetic field, the Hamiltonian of a free electron is

$$\hat{H} = \frac{1}{2m_e} \left( \mathbf{p} + \frac{e}{c} \mathbf{A} \right)^2 + \frac{\hbar e B}{2m_e c} \sigma_z, \quad (3.17)$$

where  $\mathbf{A} = \frac{1}{2} \mathbf{B} \times \mathbf{r}$  is the vector potential of the external magnetic field and  $\sigma_z$  is the  $z$ -component Pauli spin matrix. For electrons in Landau levels, with their spins aligned parallel/antiparallel to the magnetic field, the Hamiltonian becomes

$$\hat{H} = \frac{\hat{p}_z^2}{2m_e} + \left( n_L + \frac{1}{2} \right) \hbar \omega_{Be} \pm \frac{1}{2} \hbar \omega_{Be}, \quad (3.18)$$

where  $n_L = 0, 1, 2, \dots$  is the Landau level index; for electrons in the ground Landau level, with their spins aligned antiparallel to the magnetic field (so  $n_L = 0$  and  $\sigma_z \rightarrow -1$ ),

$$\hat{H} = \frac{\hat{p}_z^2}{2m_e}. \quad (3.19)$$

The total Hamiltonian for the atom or molecule then becomes

$$\hat{H} = \sum_i \frac{\hat{p}_{z,i}^2}{2m_e} + V, \quad (3.20)$$



where the sum is over all electrons and  $V$  is the total potential energy of the atom or molecule.

In the density functional formalism, the total energy per cell of the chain is expressed as a functional of the total electron density  $n(\mathbf{r})$ :

$$\mathcal{E}[n] = \mathcal{E}_K[n] + \mathcal{E}_{eZ}[n] + \mathcal{E}_{\text{dir}}[n] + \mathcal{E}_{\text{exc}}[n] + \mathcal{E}_{ZZ}[n]. \quad (3.21)$$

Here  $\mathcal{E}_K[n]$  is the kinetic energy of the system of non-interacting electrons, and  $\mathcal{E}_{eZ}$ ,  $\mathcal{E}_{\text{dir}}$  and  $\mathcal{E}_{ZZ}$  are the electron-ion Coulomb energy, the direct electron-electron interaction energy and the ion-ion interaction energy, respectively:

$$\mathcal{E}_{eZ}[n] = - \sum_{j=-N/2}^{N/2} Z e^2 \int_{|z| < a/2} d\mathbf{r} \frac{n(\mathbf{r})}{|\mathbf{r} - \mathbf{z}_j|}, \quad (3.22)$$

$$\mathcal{E}_{\text{dir}}[n] = \frac{e^2}{2} \iint_{|z| < a/2} d\mathbf{r} d\mathbf{r}' \frac{n(\mathbf{r})n(\mathbf{r}')}{|\mathbf{r} - \mathbf{r}'|}, \quad (3.23)$$

$$\mathcal{E}_{ZZ}[n] = \sum_{j=1}^{N/2} \frac{Z^2 e^2}{ja}. \quad (3.24)$$

The location of the ions in the above equations is represented by the set  $\{\mathbf{z}_j\}$ , with

$$\mathbf{z}_j = ja\hat{\mathbf{z}}, \quad j = (-N/2), (-N/2 + 1), \dots, 0, \dots, N/2. \quad (3.25)$$

The term  $\mathcal{E}_{\text{exc}}$  represents the exchange-correlation energy. In the local approximation,

$$\mathcal{E}_{\text{exc}}[n] = \int_{|z| < a/2} d\mathbf{r} n(\mathbf{r}) \varepsilon_{\text{exc}}(n), \quad (3.26)$$

where  $\varepsilon_{\text{exc}}(n) = \varepsilon_{\text{ex}}(n) + \varepsilon_{\text{corr}}(n)$  is the exchange and correlation energy per electron in a uniform electron gas of density  $n$ . For electrons in the ground Landau level, the (Hartree-Fock) exchange energy can be written as (Danz & Glasser 1971)

$$\varepsilon_{\text{ex}}(n) = -\pi e^2 \rho_0^2 n F(t), \quad (3.27)$$

where the dimensionless function  $F(t)$  is

$$F(t) = 4 \int_0^\infty dx \left[ \tan^{-1} \left( \frac{1}{x} \right) - \frac{x}{2} \ln \left( 1 + \frac{1}{x^2} \right) \right] e^{-4tx^2}, \quad (3.28)$$

and

$$t = \left(\frac{n}{n_B}\right)^2 = 2\pi^4 \rho_0^6 n^2, \quad (3.29)$$

$[n_B = (\sqrt{2}\pi^2 \rho_0^3)^{-1}]$  is the density above which the higher Landau levels start to be filled in a uniform electron gas]. For small  $t$ ,  $F(t)$  can be expanded as (Fushiki et al. 1989)

$$F(t) \simeq 3 - \gamma - \ln 4t + \frac{2t}{3} \left( \frac{13}{6} - \gamma - \ln 4t \right) + \frac{8t^2}{15} \left( \frac{67}{30} - \gamma - \ln 4t \right) + \mathcal{O}(t^3 \ln t), \quad (3.30)$$

where  $\gamma = 0.5772\dots$  is Euler's constant. We have found that the condition  $t \ll 1$  is well satisfied everywhere for almost all infinite chains in our calculations. The notable exceptions are the carbon chains at  $B = 10^{12}$  G and the iron chains at  $B \leq 10^{13}$  G, which have  $t \lesssim 1$  near the center of each cell. These chains are expected to have higher  $t$  values than the other chains in our calculations, as they have large  $Z$  and low  $B$ <sup>2</sup>.

The correlation energy of uniform electron gas in strong magnetic fields has not been calculated in general, except in the regime  $t \ll 1$  and Fermi wave number  $k_F = 2\pi^2 \rho_0^2 n \gg 1$  [or  $n \gg (2\pi^3 \rho_0^2 a_0)^{-1}$ ]. Skudlarski and Vignale (1993) use the random-phase approximation to find a numerical fit for the correlation energy in this regime (see also Steinberg & Ortner 1998):

$$\varepsilon_{\text{corr}} = -\frac{e^2}{\rho_0} [0.595(t/b)^{1/8} (1 - 1.009t^{1/8})]. \quad (3.31)$$

In the absence of an “exact” correlation energy density we employ this strong-field-limit expression. Fortunately, because we are concerned mostly with finding the energy difference between atoms and chains, the correlation energy term does not have to be exact. The presence or the form of the correlation term has a modest effect on the atomic and chain energies calculated but has very little effect on the

---

<sup>2</sup>For the uniform gas model,  $t \propto Z^{4/5} B^{-3/5}$ .

energy difference between them (see Chapter 2 for more details on various forms of the correlation energy and comparisons).

Variation of the total energy with respect to the electron density,  $\delta\mathcal{E}[n]/\delta n = 0$ , leads to the Kohn-Sham equation:

$$\left[ -\frac{\hbar^2}{2m_e} \nabla^2 + V_{\text{eff}}(\mathbf{r}) \right] \Psi_{m\nu k}(\mathbf{r}) = \varepsilon_{m\nu}(k) \Psi_{m\nu k}(\mathbf{r}), \quad (3.32)$$

where

$$V_{\text{eff}}(\mathbf{r}) = - \sum_{j=-N/2}^{N/2} \frac{Ze^2}{|\mathbf{r} - \mathbf{z}_j|} + e^2 \int d\mathbf{r}' \frac{n(\mathbf{r}')}{|\mathbf{r} - \mathbf{r}'|} + \mu_{\text{exc}}(n), \quad (3.33)$$

with

$$\mu_{\text{exc}}(n) = \frac{\partial(n\varepsilon_{\text{exc}})}{\partial n}. \quad (3.34)$$

Averaging the Kohn-Sham equation over the transverse wave function yields a set of one-dimensional equations:

$$\left[ -\frac{\hbar^2}{2m_e} \frac{d^2}{dz^2} + \bar{V}_{\text{eff}}(z) \right] f_{m\nu k}(z) = \varepsilon_{m\nu}(k) f_{m\nu k}(z). \quad (3.35)$$

where

$$\begin{aligned} \bar{V}_{\text{eff}}(z) = & -Ze^2 \sum_{j=-N/2}^{N/2} \int d\mathbf{r}_{\perp} \frac{|W_m|^2(\rho)}{|\mathbf{r} - \mathbf{z}_j|} + e^2 \iint d\mathbf{r}_{\perp} d\mathbf{r}' \frac{|W_m|^2(\rho) n(\mathbf{r}')}{|\mathbf{r} - \mathbf{r}'|} \\ & + \int d\mathbf{r}_{\perp} |W_m|^2(\rho) \mu_{\text{exc}}(n). \end{aligned} \quad (3.36)$$

This set of equations are solved self-consistently to find the eigenvalue  $\varepsilon_{m\nu}(k)$  and the longitudinal wave function  $f_{m\nu k}(z)$  for each orbital occupied by the electrons. Once these are known, the total energy per cell of the infinite chain can be calculated using

$$\begin{aligned} \mathcal{E}_{\infty} = & \frac{a}{2\pi} \sum_{m\nu} \int_{I_{m\nu}} dk \varepsilon_{m\nu}(k) - \frac{e^2}{2} \iint_{|z| < a/2} d\mathbf{r} d\mathbf{r}' \frac{n(\mathbf{r})n(\mathbf{r}')}{|\mathbf{r} - \mathbf{r}'|} \\ & + \int_{|z| < a/2} d\mathbf{r} n(\mathbf{r}) [\varepsilon_{\text{exc}}(n) - \mu_{\text{exc}}(n)] + \sum_{j=1}^{N/2} \frac{Z^2 e^2}{ja}, \end{aligned} \quad (3.37)$$

where the interval  $I_{m\nu}$  is the same as in the electron density expression, Eq. (3.16).

Note that the electron-ion, direct electron-electron, and ion-ion interaction energy terms given above formally diverge for  $N \rightarrow \infty$ . These terms must be properly combined to yield a finite net potential energy. Note that for an electron in the “primary” unit cell ( $-a/2 \leq z \leq a/2$ ), the potential generated by a distant cell (centered at  $z_j = ja$ ) can be well approximated by the quadrupole potential:

$$V_Q(\rho, z; ja) = \frac{3e^2}{2} \frac{Q_{zz}}{|ja|^5} (2z^2 - \rho^2), \quad (3.38)$$

where  $Q_{zz}$  is the quadrupole moment of a unit cell

$$Q_{zz} = \int_{|z| < a/2} d\mathbf{r} (2z^2 - \rho^2) n(\rho, z). \quad (3.39)$$

The Coulomb (quadrupole-quadrupole) energy between the primary cell and the distant cell is simply

$$\mathcal{E}_{QQ}(ja) = \int_{|z| < a/2} d\mathbf{r} n(\mathbf{r}) V_Q(\rho, z; ja) = \frac{3e^2}{2} \frac{Q_{zz}^2}{|ja|^5}. \quad (3.40)$$

In our calculations, we treat distant cells with  $|j| > N_Q$  using the quadrupole approximation, while treating the nearby cells ( $|j| \leq N_Q$ ) exactly. Thus the (averaged) effective potential, Eq. (3.36), becomes

$$\begin{aligned} \bar{V}_{\text{eff}}(z) = & -Ze^2 \sum_{j=-N_Q}^{N_Q} \int d\mathbf{r}_\perp \frac{|W_m|^2(\rho)}{|\mathbf{r} - \mathbf{z}_j|} \\ & + e^2 \iint_{|z'| < a(N_Q+1/2)} d\mathbf{r}_\perp d\mathbf{r}' \frac{|W_m|^2(\rho) n(\mathbf{r}')}{|\mathbf{r} - \mathbf{r}'|} + \int d\mathbf{r}_\perp |W_m|^2(\rho) \mu_{\text{exc}}(n) \\ & + \left( \sum_{j=N_Q+1}^{\infty} \frac{1}{j^5} \right) \frac{3e^2 Q_{zz}}{a^5} \int d\mathbf{r}_\perp |W_m|^2(\rho) (2z^2 - \rho^2). \end{aligned} \quad (3.41)$$

The total energy per unit cell [see Eq. (3.37)] is given by

$$\begin{aligned} \mathcal{E}_\infty = & \frac{a}{2\pi} \sum_{m\nu} \int_{I_{m\nu}} dk \varepsilon_{m\nu}(k) - \frac{e^2}{2} \iint_{|z| < a/2, |z'| < a(N_Q+1/2)} d\mathbf{r} d\mathbf{r}' \frac{n(\mathbf{r}) n(\mathbf{r}')}{|\mathbf{r} - \mathbf{r}'|} \\ & + \int_{|z| < a/2} d\mathbf{r} n(\mathbf{r}) [\varepsilon_{\text{exc}}(n) - \mu_{\text{exc}}(n)] \\ & + \sum_{j=1}^{N_Q} \frac{Z^2 e^2}{ja} - \left( \sum_{j=N_Q+1}^{\infty} \frac{1}{j^5} \right) \frac{3e^2}{2} \frac{Q_{zz}^2}{a^5}. \end{aligned} \quad (3.42)$$

In practice, we have found that accurate results are obtained for the energy of the chain even with  $N_Q = 1$  (i.e., only the primary cell and its nearest neighbors are treated exactly and more distant cells are treated using quadrupole approximation).

Details of our method used in computing the various integrals above and solving the Kohn-Sham equations self-consistently are given in Appendix B.

### 3.3.2 The electron band structure shape and occupations

As discussed above, the electron orbitals in the chain are specified by three quantum numbers:  $m, \nu, k$ . While  $m, \nu$  are discrete,  $k$  is continuous. In the ground state, the electrons will occupy the  $(m\nu k)$  orbitals with the lowest energy eigenvalues  $\varepsilon_{m\nu}(k)$ . To determine the electron occupations and the total chain energy, it is necessary to calculate the  $\varepsilon_{m\nu}(k)$  energy curves. Here we discuss the qualitative property of these energy curves (i.e., the electron band structure) using the theory of one-dimensional periodic potentials (see, e.g., Ashcroft & Mermin 1976).

Like the wave functions, the energy curves are periodic, with  $\varepsilon_{m\nu}(k + K) = \varepsilon_{m\nu}(k)$ , where  $K$  is  $2\pi/a$  multiplied by any integer. The energy curves are also symmetric about the Bragg “planes” (“points” in 1D) of the reciprocal lattice,  $\varepsilon_{m\nu}(K - k) = \varepsilon_{m\nu}(k)$ . Thus we can determine the entire band structure of the electrons by calculating it between any two Bragg points. Since we have chosen to limit our calculation to the first Brillouin zone  $k \in [-\pi/a, \pi/a]$ , we only need to consider the domain  $k \in [0, \pi/a]$ .

For a given  $m$ , the energy curves lie in bands which do not overlap and increase in energy with increasing  $\nu$  (see Fig. 3.1). These bands are bounded by the energy

values at the Bragg points, such that in each band the energy increases/decreases monotonically between the two points. The direction of this growth alternates with  $\nu$ : For the  $\nu = 0$  band, the energy is at a minimum for  $k = 0$  and increases to a local maximum at  $k = \pi/a$ ; for the  $\nu = 1$  band, the energy curve is at a minimum for  $k = \pi/a$  and grows to a maximum at  $k = 0$ , etc. These properties are depicted in Fig. 3.1.

Also shown in the figure is the Fermi level energy  $\varepsilon_F$  of the electrons in the infinite chain. The electrons occupy all orbitals  $(m\nu k)$  with energy less than  $\varepsilon_F$ . For each  $(m\nu)$  band, we define the occupation parameter  $\sigma_{m\nu}$ , which gives the number of electrons that occupy this band per unit cell [i.e., the number of electrons that occupy the  $(m\nu)$  band in the whole chain is  $\sigma_{m\nu}N$ ]. Since the maximum possible number of electrons in each  $(m\nu)$  band is  $N$ , we have  $\sigma_{m\nu} \leq 1$ . Because there are  $ZN$  electrons total in the chain, these occupation numbers are subject to the constraint

$$\sum_{m\nu} \sigma_{m\nu} = Z. \quad (3.43)$$

It is also useful to define for each  $(m\nu)$  level the Fermi wave number  $k_F^{m\nu}$ , such that the electrons fill up all allowed orbitals between the minimum-energy Bragg point ( $k = 0$  for even  $\nu$  and  $k = \pi/a$  for odd  $\nu$ ) and  $k_F^{m\nu}$ . The occupied  $k$ 's are therefore

$$k \in \left[0, \sigma_{m\nu} \frac{\pi}{a}\right] \equiv [0, k_F^{m\nu}] \quad (3.44)$$

for even  $\nu$ , and

$$k \in \left[(1 - \sigma_{m\nu}) \frac{\pi}{a}, \frac{\pi}{a}\right] \equiv \left[k_F^{m\nu}, \frac{\pi}{a}\right] \quad (3.45)$$

for odd  $\nu$ , plus the corresponding reflection about the Bragg point  $k = 0$ . For a completely filled band (as illustrated in Fig. 3.1 for the  $\nu = 0$  band),  $\sigma_{m\nu} = 1$  and  $k_F^{m\nu} = \pi/a$  (for  $\nu = \text{even}$ ) or 0 (for  $\nu = \text{odd}$ ); for a partially filled band (the  $\nu = 1$

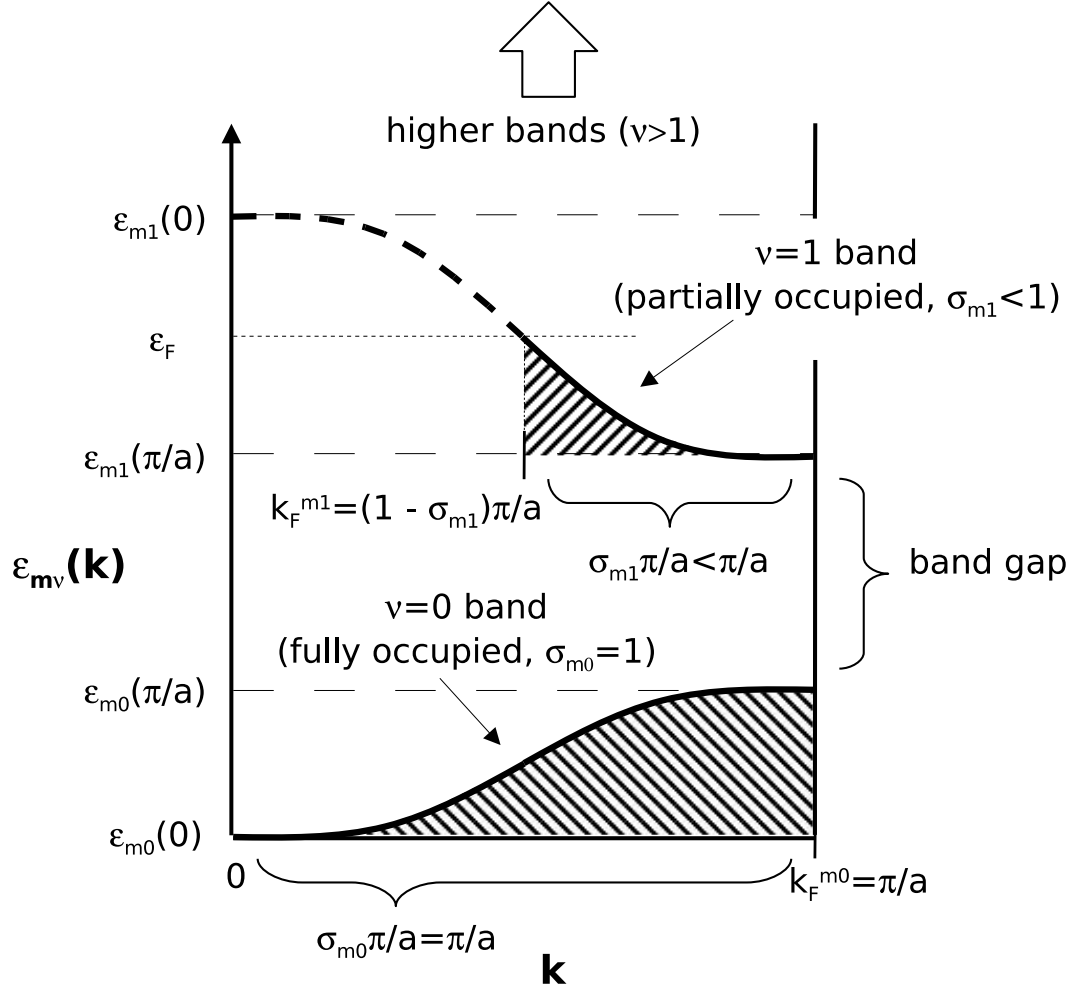


Figure 3.1: A schematic diagram showing the electron band structure for a particular  $m$  value. In this example, the first band ( $\nu = 0$ ) is fully occupied ( $\sigma_{m0} = 1$ ) while the second band ( $\nu = 1$ ) is partially filled ( $\sigma_{m1} < 1$ ).

band in Fig. 3.1),

$$\varepsilon_{m\nu}(k_F^{m\nu}) = \varepsilon_F. \quad (3.46)$$

With the allowed  $k$  values specified, the  $k$  integration domain in Eqs. (3.14), (3.15), (3.37) and (3.42) is given by

$$\int_{I_{m\nu}} dk \Rightarrow \begin{cases} 2 \int_0^{k_F^{m\nu}} dk, & \nu \text{ even}, \\ 2 \int_{k_F^{m\nu}}^{\pi/a} dk, & \nu \text{ odd}. \end{cases} \quad (3.47)$$

Note that the Fermi level energy  $\varepsilon_F$  and various occupation numbers  $\sigma_{m\nu}$  must be calculated self-consistently. In principle, they should be determined by minimizing the total energy with respect to  $\sigma_{m\nu}$  subject to the constraint Eq. (3.43), i.e.,

$$\frac{\delta}{\delta \sigma_{m\nu}} \left[ \mathcal{E}[n; \sigma_{m\nu}] - \varepsilon_F \left( \sum_{m\nu} \sigma_{m\nu} - Z \right) \right] = 0. \quad (3.48)$$

Since

$$\frac{\partial n(\mathbf{r})}{\partial \sigma_{m\nu}} = \pm \frac{\pi}{a} \frac{\partial n(\mathbf{r})}{\partial k_F^{m\nu}} = |W_m|^2(\rho) |f_{m\nu k_F^{m\nu}}(z)|^2, \quad (3.49)$$

Eq. (3.48) yields

$$\left[ -\frac{\hbar^2}{2m_e} \frac{d^2}{dz^2} + \bar{V}_{\text{eff}}(z) \right] f_{m\nu k_F^{m\nu}}(z) = \varepsilon_F f_{m\nu k_F^{m\nu}}(z). \quad (3.50)$$

Comparing this to Eq. (3.35), we find  $\varepsilon_{m\nu}(k_F^{m\nu}) = \varepsilon_F$ , which is Eq. (3.46). This shows that using Eq. (3.46) to find  $\varepsilon_F$  minimizes the total energy of the system.

### 3.3.3 The complex longitudinal wave functions

The longitudinal electron wave function  $f_{m\nu k}(z)$  satisfies the Kohn-Sham equations (3.35) subject to the periodicity condition Eq. (3.13), or equivalently, the cell boundary condition

$$f_{m\nu k}(a/2) = e^{ika} f_{m\nu k}(-a/2). \quad (3.51)$$



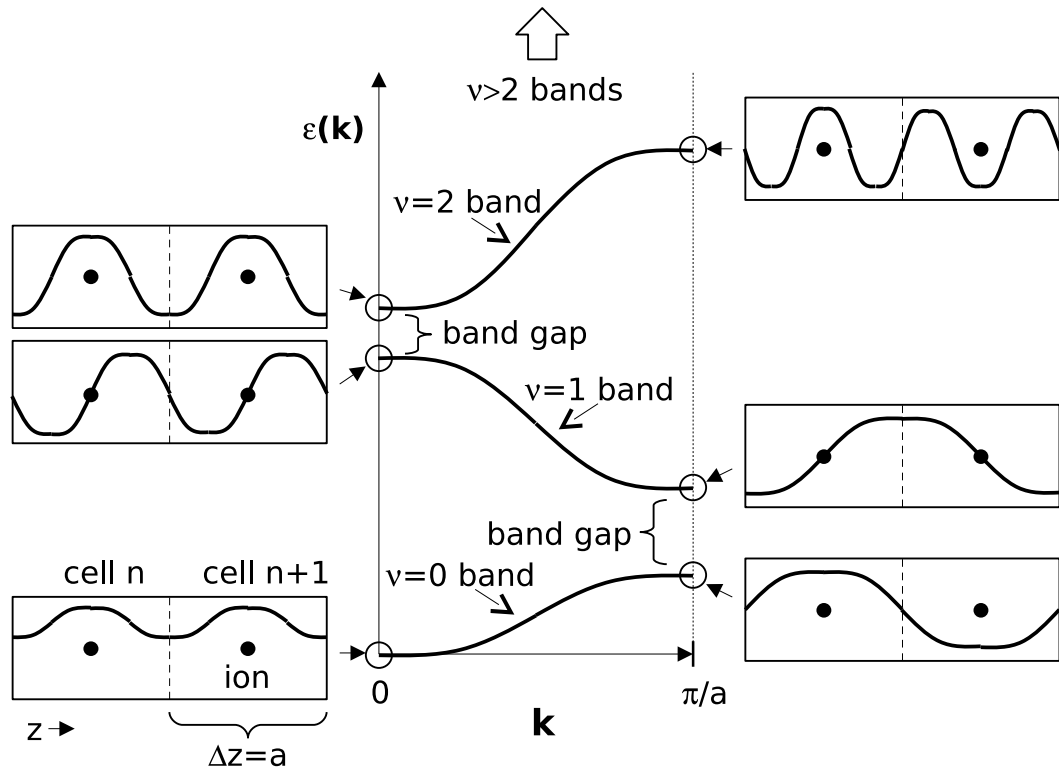


Figure 3.2: A schematic diagram showing the shapes of the longitudinal wave functions of electrons in different bands at  $k = 0$  and  $k = \pi/a$ .

Since the electron density distribution  $n(\mathbf{r})$  is periodic across each cell and symmetric about each ion, the following boundary condition is also useful:

$$|f_{m\nu k}(z)|'|_{z=a/2} = |f_{m\nu k}(z)|'|_{z=-a/2} = 0. \quad (3.52)$$

Due to the complex boundary condition Eq. (3.51), the wave function  $f_{m\nu k}$  is complex for general  $k$ 's. The exceptions are  $k = 0$  and  $k = \pi/a$ : For  $k = 0$ , the boundary condition becomes  $f_{m\nu k}(a/2) = f_{m\nu k}(-a/2)$ , and for  $k = \pi/a$  we have  $f_{m\nu k}(a/2) = -f_{m\nu k}(-a/2)$ . Thus for  $k = 0$  and  $\pi/a$ , we can choose the longitudinal wave functions to be real. The general shapes of these wave functions (for different bands) are sketched out in Fig. 3.2. We see that at the Bragg points, between the two states with the same number of nodes, the one that is more concentrated near the ion has lower energy than the other state; this difference gives rise to the band gap. The  $k = 0, \pi/a$  eigenvalues  $\varepsilon_{m\nu}$  and eigenfunctions can be calculated in the domain  $0 < z < a/2$  with the boundary condition  $f_{m\nu k}(0) = 0$  or  $f'_{m\nu k}(0) = 0$ .

The electron wave functions for general  $k$ 's are more difficult to compute as they have complex boundary conditions. Our procedure for calculating these wave functions and their corresponding electron energies is as follows: For each energy band ( $m\nu$ ), the electron eigenstates at  $k = 0$  and  $k = \pi/a$  are first found (see above). For every energy between  $\varepsilon_{m\nu}(k = 0)$  and  $\varepsilon_{m\nu}(k = \pi/a)$ , we find the wave function that solves the Kohn-Sham equation while satisfying the symmetric/periodic density condition Eq. (3.52). More precisely, we choose  $f = 1$  (up to a normalization constant) and guess  $f' = i g$  (where  $g$  is a real number) at  $z = a/2$  (thus  $|f|' = 0$  is satisfied at  $z = a/2$ ), and then integrate the Kohn-Sham equation to  $z = -a/2$ ; we adjust  $g$  so that  $|f|' = 0$  is satisfied at  $z = -a/2$ . Example wave functions for general  $k$ 's are shown in Figs. 3.3–3.5. Once the wave function is obtained, we determine its  $k$  value from the Bloch boundary condition Eq. (3.51).

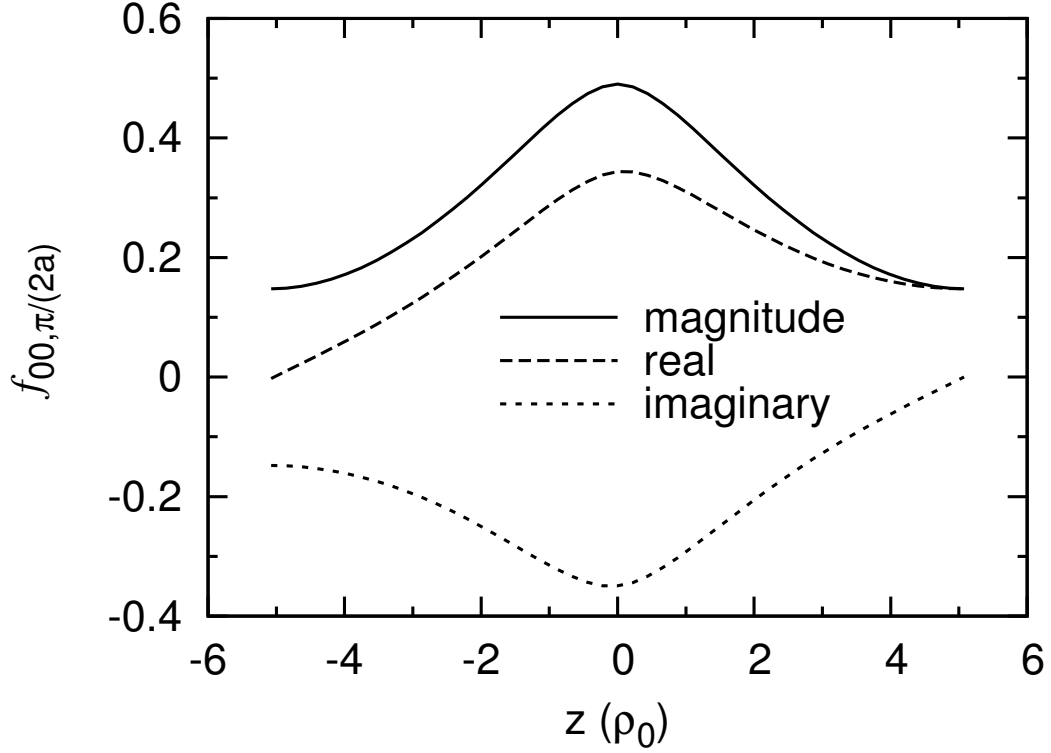


Figure 3.3: The longitudinal wave function for the  $(m, \nu, k) = (0, 0, \pi/2a)$  electron orbital of the carbon infinite chain at  $B_{12} = 1$ . The real and imaginary parts of the wave function are shown, as well as the magnitude  $|f_{m\nu k}|$ .

Through this method we find  $\varepsilon_{m\nu}(k)$  as a function of  $k$  for each  $(m\nu)$  band.

Some examples of our computed  $\varepsilon_{m\nu}(k)$  are shown in Figs. 3.6 and 3.7. To show that our calculations are consistent with theoretical models, we have included several model fits for the electron energy curves: the tight-binding fit in Fig. 3.6, which has the form

$$\varepsilon_{m\nu}(k) \simeq c_1 + c_2 \cos(ka) \quad (3.53)$$

[see Ashcroft & Mermin 1976, Eq. (10.19)], and the weak-periodic-potential fit in Fig. 3.7, which has the form

$$\varepsilon_{m\nu}(k) \simeq c_1 + \frac{1}{2}[k^2/2 + (2\pi/a - k)^2/2] - \frac{1}{2}\{[(2\pi/a - k)^2/2 - k^2/2]^2 + c_2^2\}^{1/2} \quad (3.54)$$

[see Ashcroft & Mermin 1976, Eq. (9.26)]. The constants  $c_1$  and  $c_2$  in the for-

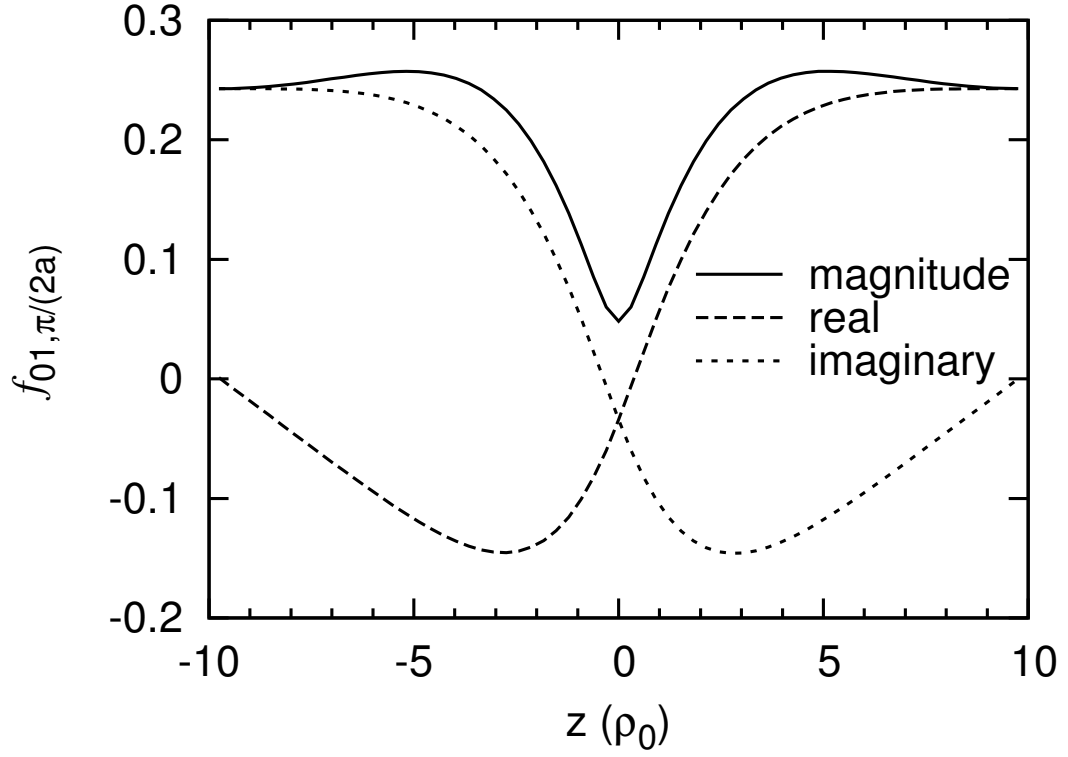


Figure 3.4: The longitudinal wave function for the  $(m, \nu, k) = (0, 1, \pi/2a)$  electron orbital of the iron infinite chain at  $B_{12} = 10$ . The real and imaginary parts of the wave function are shown, as well as the magnitude  $|f_{m\nu k}|$ .

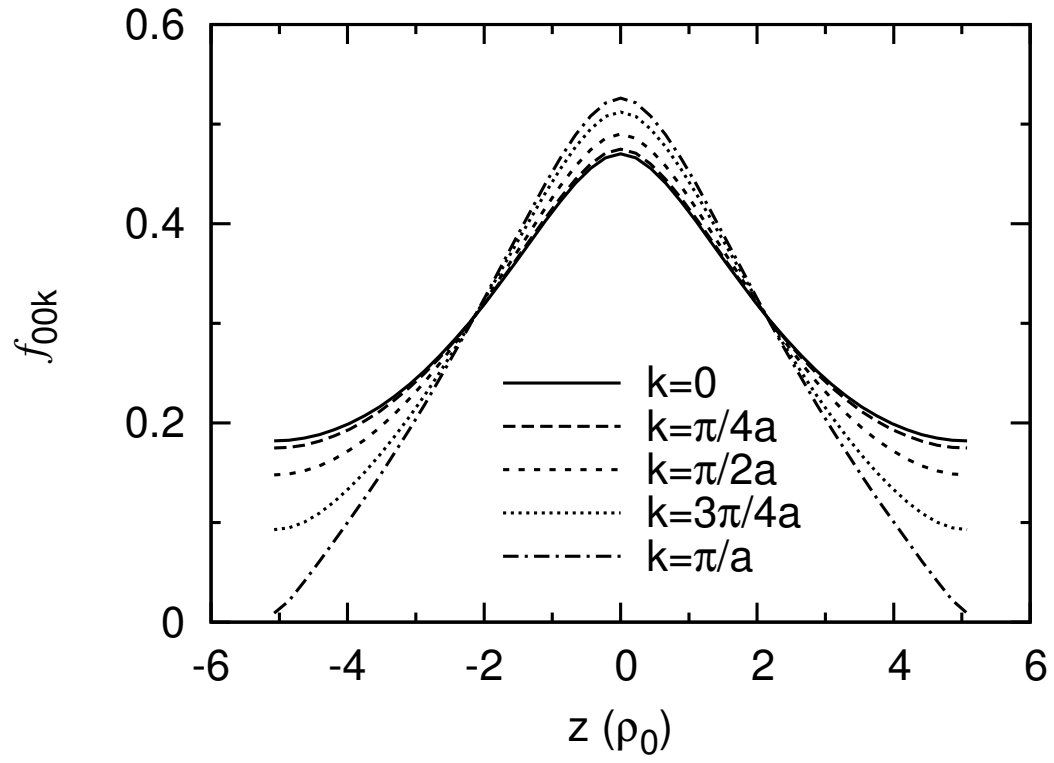


Figure 3.5: The magnitudes of the longitudinal wave functions for selected electron orbitals [with  $(m, \nu) = (0, 0)$ ] of the carbon infinite chain at  $B_{12} = 1$ .

mulas are fit to the two endpoints of the energy curves,  $\varepsilon_{m\nu}(0)$  and  $\varepsilon_{m\nu}(\pi/a)$ . The tight-binding model fits well for the most-tightly-bound electron bands in our calculations, while the weak-periodic-potential model fits well for all of the other bands. Note that for  $k \ll \pi/a$ , the electron energy can be approximately fit by  $\varepsilon_{m\nu}(k) = \varepsilon_{m\nu}(0) + k^2/2$ , as would be the case if the wave functions were of the form  $f_{m\nu}(z)e^{ikz}$  — this is the ansatz adopted by Neuhauser et al. (1987) in their Hartree-Fock calculations. But obviously for larger  $k$ , this is a rather bad approximation. We suggest that approximate treatment in the band structure may account for a large part of the discrepancies among cohesive energy results in previous works. For example, the disagreement between Jones (1985) [where  $\varepsilon_{m\nu}(k)$  was calculated for a few values of  $k$  and then fit to a simple expression] and Neuhauser et al. (1987) (where a  $k^2$  dependence for the electron energy was assumed) on whether or not carbon is bound at  $B_{12} = 5$  is due to the band structure model, not to the fact the former used the density functional theory while the latter used the Hartree-Fock method.

### 3.4 Results: One-dimensional chains

In this section we present our results for hydrogen, helium, carbon, and iron infinite chains at various magnetic field strengths between  $B = 10^{12}$  G and  $2 \times 10^{15}$  G. For each chain, data is given in tabular form for the ground-state energy (per unit cell)  $\mathcal{E}_\infty$ , the equilibrium ion separation  $a$ , and the electron Fermi level energy  $\varepsilon_F$  (the electron work function is  $W = |\varepsilon_F|$ ). We provide relevant information for the electron occupations in different bands, such as the number of Landau orbitals and the number of fully occupied bands (see below for specific elements). We also give the ground-state energy of the corresponding atom,  $\mathcal{E}_a$ , so that the cohesive energy

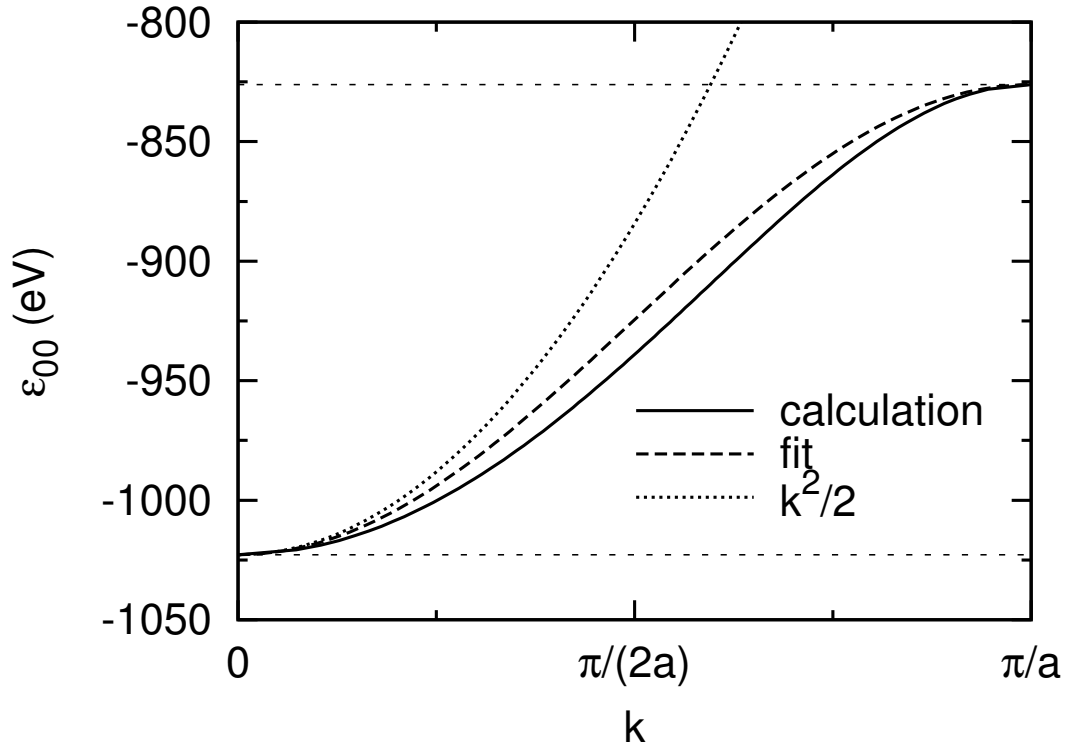


Figure 3.6: The electron energy of the  $(m, \nu) = (0, 0)$  band for the carbon infinite chain at  $B_{12} = 1$ . The tight-binding model fit for this level is shown as a dashed line [see Eq. (3.53)], and the dotted line shows the free electron result  $\varepsilon_{00}(k) - \varepsilon_{00}(0) = k^2/2$ .

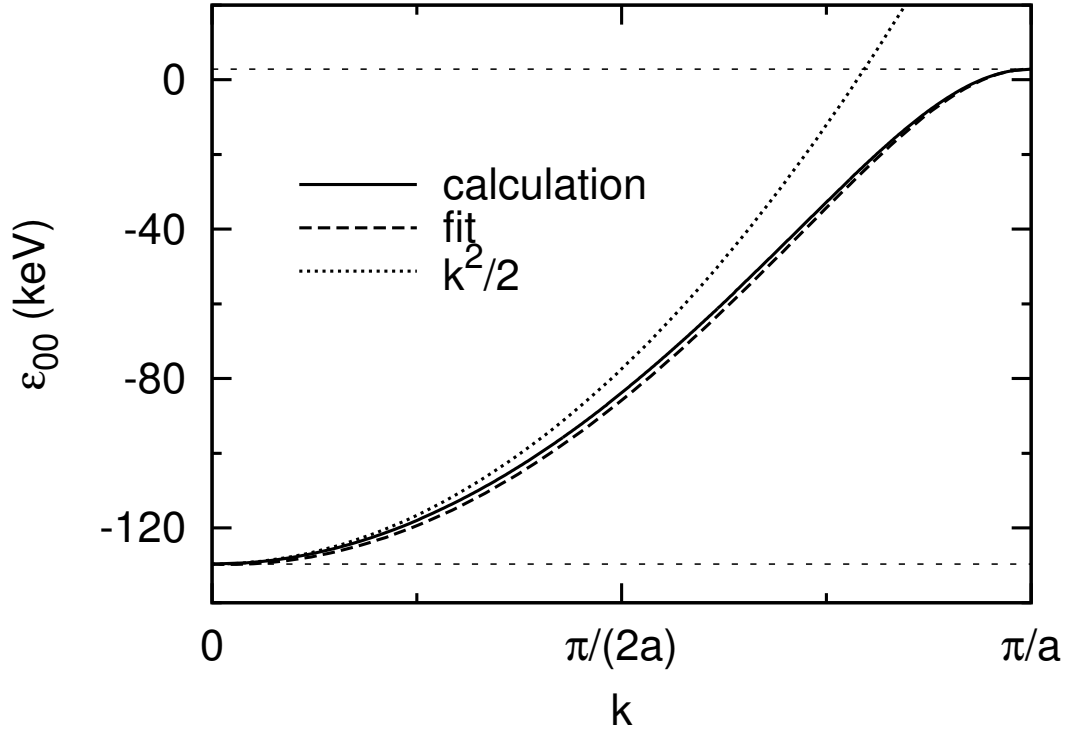


Figure 3.7: The electron energy of the  $(m, \nu) = (0, 0)$  band for the iron infinite chain at  $B_{12} = 2000$ . The weak-periodic-potential model fit for this level is shown as a dashed line [see Eq. (3.54)], and the dotted line shows the free electron result  $\varepsilon_{00}(k) - \varepsilon_{00}(0) = k^2/2$ .



of each chain can be obtained,  $Q_\infty = \mathcal{E}_a - \mathcal{E}_\infty$ .

For each chain and atom we provide numerical scaling relations for the ground-state energy and Fermi level energy as a function of the magnetic field, in the form of scaling exponents  $\beta$  and  $\gamma$ , with

$$\mathcal{E}_a, \mathcal{E}_\infty \propto B^\beta, \quad \varepsilon_F \propto B^\gamma. \quad (3.55)$$

We also give the rescaled, dimensionless energy  $\bar{\mathcal{E}}_\infty$ , and equilibrium ion separation  $\bar{a}$  defined by [see Eq. (3.3)]

$$\mathcal{E}_\infty \simeq \bar{\mathcal{E}}_\infty Z^{9/5} b^{2/5} \text{ a.u.}, \quad a \simeq \bar{a} Z^{1/5} b^{-2/5} \text{ a.u.} \quad (3.56)$$

We shall see that the scaling relations in Eq. (3.56) with  $\bar{\mathcal{E}}_\infty \simeq \text{const.}$  and  $\bar{a} \simeq \text{const.}$  represent a reasonable approximation to our numerical results, although such scaling formulae are not accurate enough for calculating the cohesive energy  $Q_\infty = \mathcal{E}_a - \mathcal{E}_\infty$ . However, Eq. (3.4) or Eq. (3.9) for the Fermi level energy based on the uniform gas model is not a good representation of our numerical results. In Chapter 2 we have shown that as  $N$  increases, the energy per atom in the  $\text{H}_N$  (or  $\text{He}_N$ ,  $\text{C}_N$ ,  $\text{Fe}_N$ ) molecule,  $\mathcal{E}_N/N$ , gradually approaches a constant value. The infinite chain ground-state energy  $\mathcal{E}_\infty$  found in the present chapter is consistent with the large- $N$  molecule ground-state energy limit  $\mathcal{E}_N/N$  obtained in Chapter 2 (see the related figures in the following subsections). Since finite molecules and infinite chains involve completely different treatments of the electron states, the consistency of  $\mathcal{E}_\infty$  and  $\mathcal{E}_N/N$  provides an important check of the validity of our calculations.

Other comparisons can be made between the infinite chains and finite molecules. For example, our results of ion separation  $a$  and scaling constant  $\beta$  are consistent between infinite chains and finite molecules. Also, we find that if the isolated atom

has electrons in  $\nu = 0$  and  $\nu = 1$  orbitals, then the corresponding infinite chain will have electrons in  $\nu = 0$  and  $\nu = 1$  bands; if the isolated atom only has electrons in  $\nu = 0$  orbitals, the corresponding infinite chain will have electrons only in  $\nu = 0$  bands.

We have compared our cohesive energy results with those of other work, whenever available. These comparisons are presented in the following subsections.

### 3.4.1 Hydrogen

Our numerical results for H are given in Table 3.1. Examples of the energy curves of various  $H_N$  molecules and  $H_\infty$  at  $B_{12} = 1$  are depicted in Fig. 3.8. The minimum of each energy curve determines the equilibrium ion separation in the molecule/chain. Figure 3.9 compares the molecular and infinite chain energies at various field strengths, and shows that as  $N$  increases, the energy per atom in the  $H_N$  molecule asymptotes to  $\mathcal{E}_\infty$ . Figure 3.10 gives the occupation number  $\sigma_{m0}$  of different Landau orbitals at various field strengths. Only the  $\nu = 0$  bands are occupied, none of these are completely filled ( $\sigma_{m0} < 1$ ), and the  $\nu \geq 1$  bands are empty ( $\sigma_{m1} = 0$ ). We see that as  $B$  increases, the electrons spread into more Landau orbitals, thus the number of  $m$  states occupied by the electrons ( $n_m$  in Table 3.1) increases. Approximately, since the chain radius  $R \propto b^{-2/5}$  and  $R \sim (2n_m - 1)^{1/2}/b^{1/2}$  (the electrons occupy the Landau orbitals with  $m = 0, 1, 2, \dots, n_m - 1$ ), we have  $n_m \propto b^{1/5}$ . Table 3.1 shows that for  $B_{12} \gtrsim 10$  our results for  $\mathcal{E}_\infty$  and  $a$  are well fit by

$$\mathcal{E}_\infty \simeq -529 B_{13}^{0.374} \text{ eV}, \quad a = 0.091 B_{13}^{-0.40} a_0 \quad (3.57)$$

[where  $B_{13} = B/(10^{13} \text{ G})$ ], similar to the scaling of Eq. (3.56). The electron work function  $W = |\varepsilon_F|$  does not scale as Eq. (3.4), but is a fraction of the ionization

energy of the H atom,  $|\mathcal{E}_a|$ . Note that  $|\mathcal{E}_a|$  is not well fit by a power law ( $\propto B^\beta$ ), but is well described by  $|\mathcal{E}_a| \propto (\ln b)^2$  (accurate fitting formulae for  $|\mathcal{E}_a|$  are given in, e.g., Ho & Lai 2003).

At  $B_{12} = 1, 10, 100$ , we find cohesive energies of  $Q_\infty = \mathcal{E}_a - \mathcal{E}_\infty = 59.6, 219.7, 712.7$  eV (see Table 3.1). At those same fields, Lai et al. (1992) find cohesive energies of 28.9, 141, 520 eV. At  $B_{12} = 0.94$ , Relovsky & Ruder (1996) find a cohesive energy of 47.1 eV. We expect our H calculation (and that of Relovsky & Ruder 1996) to overestimate the cohesive energy since an exchange-correlation functional is used in the chain calculation while none is required for the H atom. But we also expect the result obtained in Lai et al. (1992) to somewhat underestimate the cohesive energy since a uniform (longitudinal) electron density was assumed.

### 3.4.2 Helium

Our numerical results for He are given in Table 3.2. Figure 3.11 compares the molecular and infinite chain energies at various field strengths, and shows that as  $N$  increase, the energy per atom in the  $\text{He}_N$  molecule approaches  $\mathcal{E}_\infty$  for the infinite chain. Figure 3.12 gives occupation number  $\sigma_{m0}$  of different Landau orbitals at various field strengths. As in the case of H, only the  $\nu = 0$  bands are occupied, and the number of Landau states required ( $n_m$  in Table 3.2) increases with increasing  $B$ , with  $n_m \propto Z^{2/5} b^{1/5}$ . Table 3.2 shows that for  $B_{12} \gtrsim 10$ ,

$$\mathcal{E}_\infty \simeq -1252 B_{13}^{0.382} \text{ eV}, \quad a = 0.109 B_{13}^{-0.40} a_0, \quad (3.58)$$

similar to the scaling of Eq. (3.56). The electron work function  $W = |\varepsilon_F|$  does not scale as Eq. (3.4), but is a fraction of the ionization energy: Using a Hartree-Fock code (e.g., Lai et al. 1992) we find that at  $B_{12} = 1, 10, 100, 1000$  the He atomic

Table 3.1: The ground-state energy (per unit cell)  $\mathcal{E}_\infty$  (in units of eV), ion separation  $a$  (in units of Bohr radius  $a_0$ ), the number of occupied Landau levels  $n_m$ , and the Fermi level energy  $\varepsilon_F$  (in eV) of 1D infinite chains of hydrogen, over a range of magnetic field strengths. The ground-state energy of individual hydrogen atoms,  $\mathcal{E}_a$  (in units of eV), is also provided for reference. The dimensionless energy  $\bar{\mathcal{E}}_\infty$  and ion separation  $\bar{a}$  are calculated using Eq. (3.56). The scaling exponents  $\beta$  and  $\gamma$ , defined by  $\mathcal{E}_a$ ,  $\mathcal{E}_\infty \propto B^\beta$ , and  $\varepsilon_F \propto B^\gamma$ , are calculated over the three magnetic field ranges provided in the table:  $B_{12} = 1 - 10$ ,  $10 - 100$ ,  $100 - 1000$  (the exponent in the  $B_{12} = 1$  row corresponds to the fit over  $B_{12} = 1 - 10$ , etc.). The occupation of different  $(m\nu)$  bands is designated by the number  $n_m$ : the electrons occupy Landau orbitals with  $m = 0, 1, 2, \dots, n_m - 1$ , all in the  $\nu = 0$  band; see Fig. 3.10.

$B_{12}$	H		$H_\infty$							
	$\mathcal{E}_a$	$\beta$	$\mathcal{E}_\infty$	$\bar{\mathcal{E}}_\infty$	$\beta$	$a$	$\bar{a}$	$n_m$	$\varepsilon_F$	$\gamma$
1	-161.4	0.283	-221.0	-0.721	0.379	0.23	2.6	6	-85.0	0.28
10	-309.5	0.242	-529.2	-0.688	0.374	0.091	2.6	10	-165	0.27
100	-540.3	0.207	-1253.0	-0.648	0.374	0.037	2.6	16	-311	0.26
1000	-869.6	-	-2962	-0.610	-	0.0145	2.6	26	-571	-

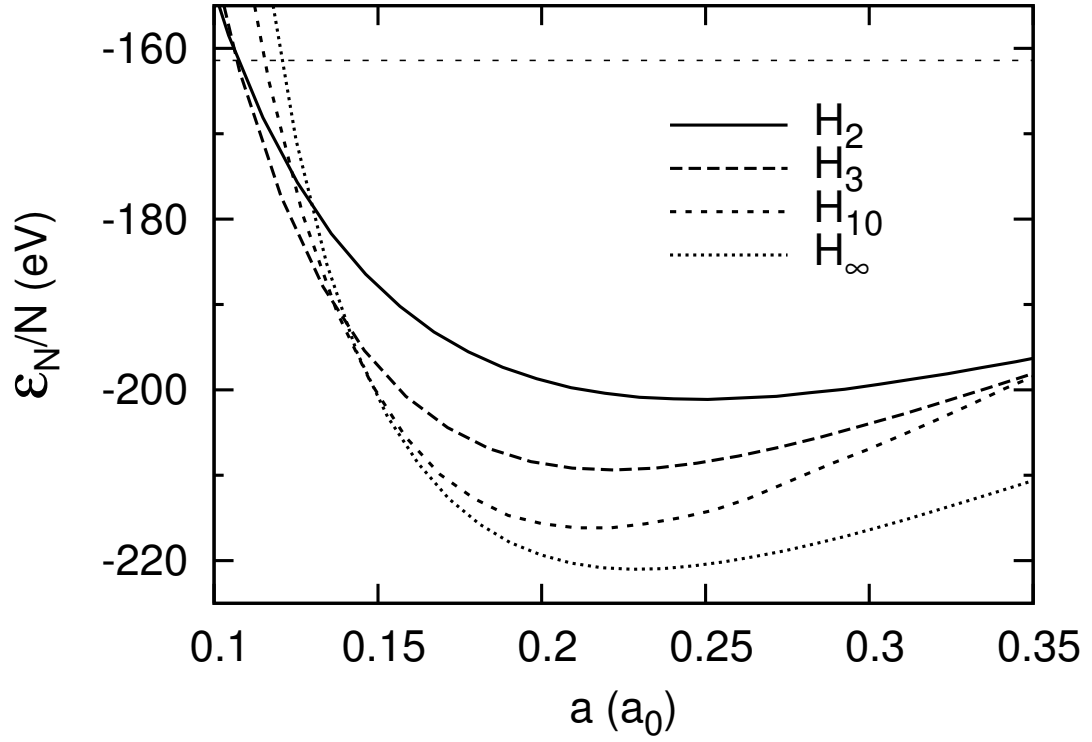


Figure 3.8: The energies (per atom or cell) of various H molecules and infinite chain as a function of ion separation  $a$  at  $B_{12} = 1$ . The results of finite molecules are based on Chapter 2. The energy of the H atom is shown as a horizontal line at  $-161.4$  eV.

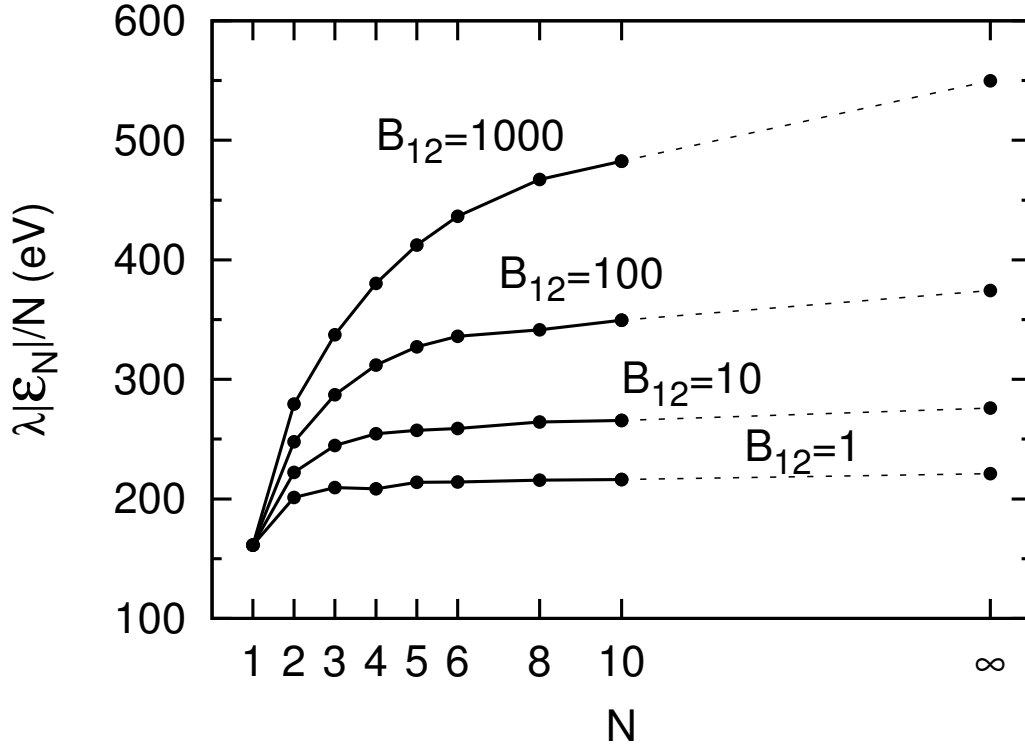


Figure 3.9: The molecular energy per atom,  $|\mathcal{E}_N|/N$ , for the  $H_N$  molecule, as a function of  $N$  at several different field strengths. The results of finite molecules are based on Chapter 2. As  $N$  increases,  $\mathcal{E}_N/N$  asymptotes to  $\mathcal{E}_\infty$ . To facilitate plotting, the values of  $|\mathcal{E}_1|$  (atom) at different magnetic field strengths are normalized to the value at  $B_{12} = 1$ , 161.4 eV. This means that  $\lambda = 1$  for  $B_{12} = 1$ ,  $\lambda = 161.4/309.5$  for  $B_{12} = 10$ ,  $\lambda = 161.4/540.3$  for  $B_{12} = 100$ , and  $\lambda = 161.4/869.6$  for  $B_{12} = 1000$ .

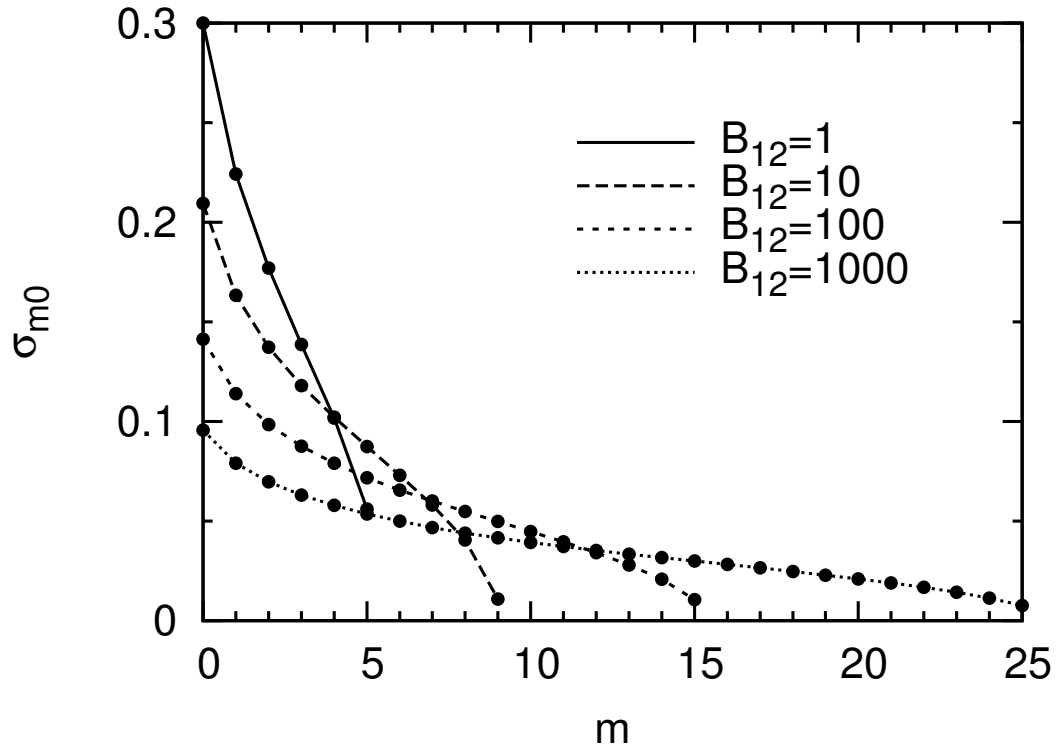


Figure 3.10: The occupation numbers of each  $m$  level of hydrogen infinite chains, for various magnetic field strengths. The data points are plotted over the curves to show the discrete nature of the  $m$  levels. Note that only the  $\nu = 0$  bands are occupied by the electrons.

energies are  $-575.5$ ,  $-1178.0$ ,  $-2193$ ,  $-3742$  eV. The  $\text{He}^+$  (i.e., once-ionized He) energies at these field strengths are  $-416.2$ ,  $-846.5$ ,  $-1562.0$ ,  $-2638$  eV. Therefore, the ionization energies of He at these field strengths are  $159.3$ ,  $331.5$ ,  $631$ , and  $1104$  eV, respectively.

At  $B_{12} = 1$ , we find a cohesive energy of  $58.9$  eV (see Table 3.2). At the same field, Neuhauser et al. (1987) (based on the Hartree-Fock model) find a cohesive energy of  $25$  eV, and Müller (1984) (based on variational methods) gives a cohesive energy of  $50$  eV. At  $B_{12} = 0.94$ , Relovsky & Ruder (1996) (based on density functional theory) find a cohesive energy of  $56.6$  eV. At  $B_{12} = 5$  Jones (1985) finds a cohesive energy of  $220$  eV, which is close to our value. That our results agree best with those of Relovsky & Ruder (1996); Jones (1985) is expected, as we used a similar method to find the ground-state atomic and chain energies. Similar to the finite He molecules (Chapter 2), we expect our density-functional-theory calculation to overestimate the cohesive energy, but we also expect the result of Neuhauser et al. (1987) to underestimate  $Q_\infty$ .

### 3.4.3 Carbon

Our numerical results for C are given in Table 3.3. Figure 3.13 compares molecular and infinite chain energies at various field strengths, showing that as  $N$  increase, the energy per atom in the  $\text{C}_N$  molecule approaches  $\mathcal{E}_\infty$  for the infinite chain. Figure 3.14 gives the occupation number  $\sigma_{m0}$  of different Landau orbitals at various field strengths. As in the case of H and He, only the  $\nu = 0$  bands are occupied, although for C at  $B_{12} = 1$ , the  $m = 0$  and  $m = 1$  bands (both with  $\nu = 0$ ) are fully occupied (thus  $n_f = 2$  in Table 3.3). The number of Landau states required ( $n_m$  in Table 3.3) increases with increasing  $B$ , approximately with  $n_m \propto Z^{2/5} b^{1/5}$ .



Table 3.2: The ground-state energy (per unit cell)  $\mathcal{E}_\infty$  (in units of eV), ion separation  $a$  (in units of Bohr radius  $a_0$ ), the number of occupied Landau levels  $n_m$ , and Fermi level energy  $\varepsilon_F$  (in eV) of 1D infinite chains of helium, over a range of magnetic field strengths. The ground-state energy of individual He atoms,  $\mathcal{E}_a$  (in units of eV), is also provided for reference (this is based on the density-functional-theory calculation of Medin & Lai 2006a). The dimensionless energy  $\bar{\mathcal{E}}_\infty$  and ion separation  $\bar{a}$  are calculated using Eq. (3.56). The scaling exponents  $\beta$  and  $\gamma$ , defined by  $\mathcal{E}_a$ ,  $\mathcal{E}_\infty \propto B^\beta$ , and  $\varepsilon_F \propto B^\gamma$ , are calculated over the three magnetic field ranges provided in the table:  $B_{12} = 1 - 10$ ,  $10 - 100$ ,  $100 - 1000$  (the exponent in the  $B_{12} = 1$  row corresponds to the fit over  $B_{12} = 1 - 10$ , etc.). The occupation of different  $(m\nu)$  bands is designated by the number  $n_m$ : the electrons occupy Landau orbitals with  $m = 0, 1, 2, \dots, n_m - 1$ , all in the  $\nu = 0$  band; see Fig. 3.12. Note that all of the He atoms here also have electrons only in the  $\nu = 0$  states.

$B_{12}$	He		He $_\infty$							
	$\mathcal{E}_a$	$\beta$	$\mathcal{E}_\infty$	$\bar{\mathcal{E}}_\infty$	$\beta$	$a$	$\bar{a}$	$n_m$	$\varepsilon_F$	$\gamma$
1	-603.5	0.317	-662.4	-0.621	0.385	0.28	2.7	9	-85.0	0.29
10	-1252.0	0.280	-1608.0	-0.600	0.382	0.109	2.7	14	-167	0.27
100	-2385	0.248	-3874	-0.575	0.382	0.043	2.7	23	-310	0.26
1000	-4222	-	-9329	-0.552	-	0.0175	2.7	39	-568	-

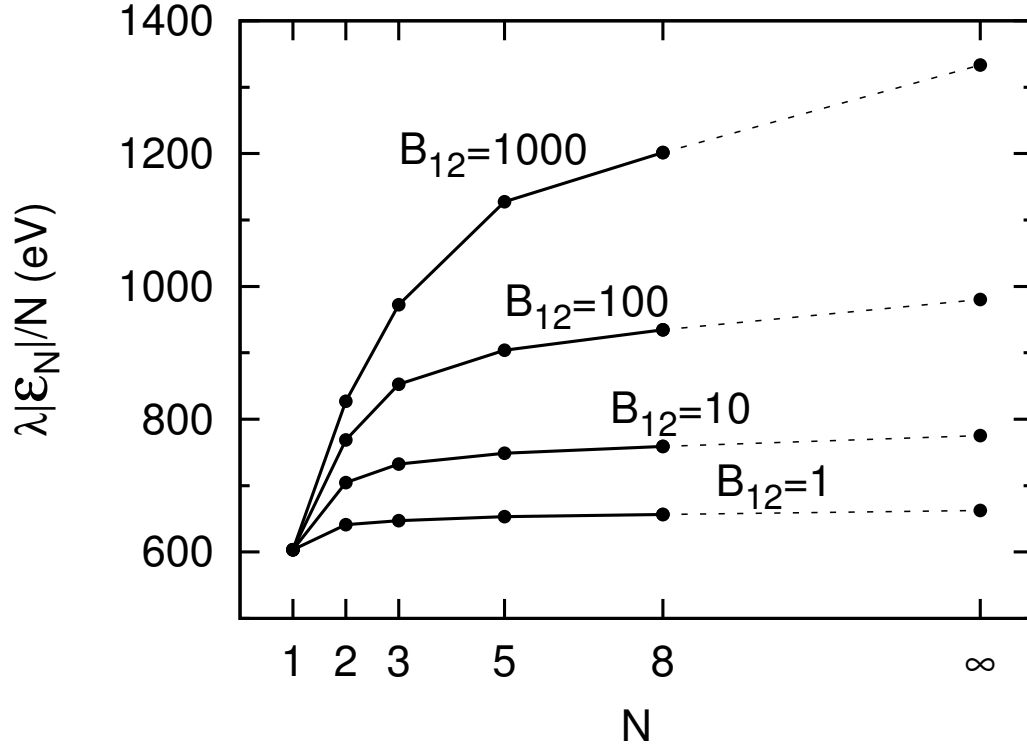


Figure 3.11: The molecular energy per atom,  $|\mathcal{E}_N|/N$ , for the  $\text{He}_N$  molecule, as a function of  $N$  at several different field strengths. The results of finite molecules are based on Chapter 2. As  $N$  increases,  $\mathcal{E}_N/N$  asymptotes to  $\mathcal{E}_\infty$ . To facilitate plotting, the values of  $|\mathcal{E}_1|$  (atom) at different magnetic field strengths are normalized to the value at  $B_{12} = 1$ , 603.5 eV. This means that  $\lambda = 1$  for  $B_{12} = 1$ ,  $\lambda = 603.5/1252.0$  for  $B_{12} = 10$ ,  $\lambda = 603.5/2385$  for  $B_{12} = 100$ , and  $\lambda = 603.5/4222$  for  $B_{12} = 1000$ .

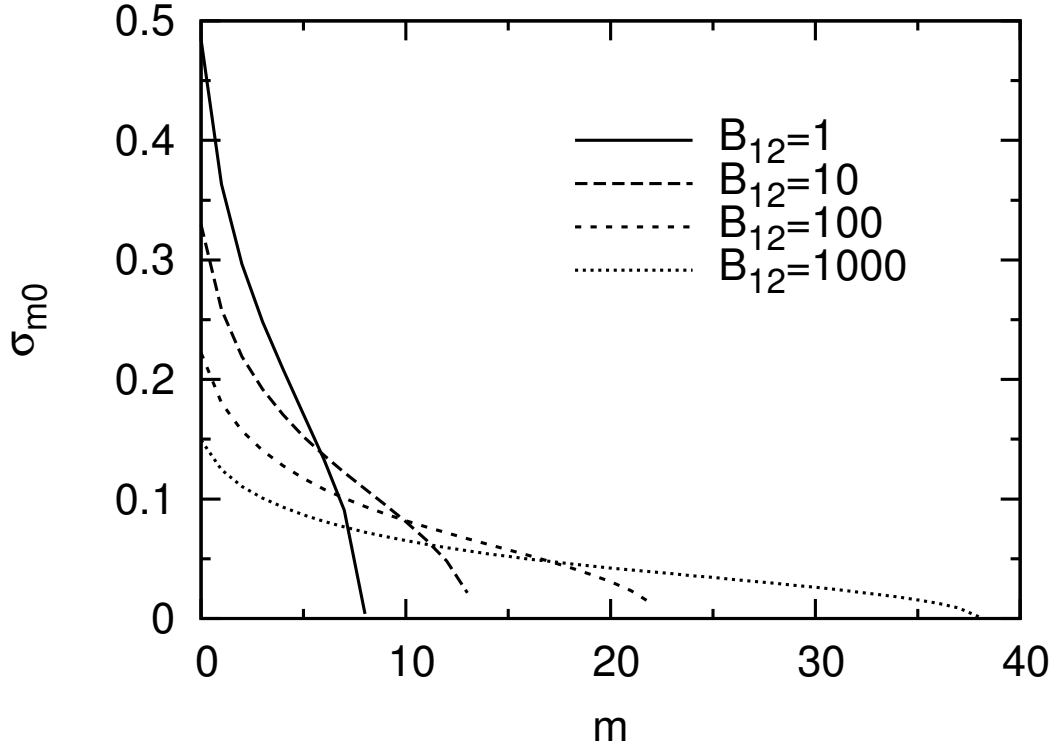


Figure 3.12: The occupation numbers of each  $m$  level of infinite He chains, for various magnetic field strengths. Only the  $\nu = 0$  bands are occupied by the electrons. Note that for  $B_{12} = 1$ , the  $m = 8$  orbital has a rather small occupation,  $\sigma_{80} \simeq 0.006$ ; if  $\varepsilon_F$  were slightly more negative, this orbital would be completely unoccupied.

Table 3.3 shows that for  $B_{12} \gtrsim 10$ ,

$$\mathcal{E}_\infty \simeq -10\,300\, B_{13}^{0.387} \text{ eV}, \quad a = 0.154\, B_{13}^{-0.43} a_0. \quad (3.59)$$

Note that these expressions are more approximate than for H and He. The electron work function  $W = |\varepsilon_F|$  does not scale as Eq. (3.4), but is a fraction of the ionization energy: from Chapter 2, the ionization energies of C at  $B_{12} = 1, 10, 100, 1000$  are 174, 430, 990, and 2120 eV, respectively.

At  $B_{12} = 10$ , we find a cohesive energy of 240 eV (see Table 3.3). At  $B_{12} = 8.5$ , Relovsky & Ruder (1996) give a cohesive energy of 240 eV. At  $B_{12} = 5$  Jones (1985) finds a cohesive energy of 100 eV; at the same field (using our scaling relations), we find a cohesive energy of 100 eV ( $\pm 30$  eV). Neuhauser et al. (1987), on the other hand, find that carbon is not bound at  $B_{12} = 1$  or 5. This is probably due to the approximate band structure ansatz adopted in Neuhauser et al. (1987) (see Section 3.3.3): for fully occupied bands, the approximation that  $\varepsilon_{m\nu}(k)$  increases as  $k^2/2$  is invalid and can lead to large error in the total energy of the chain.

### 3.4.4 Iron

Our numerical results for Fe are given in Table 3.4. The electron density profile at various field strengths is shown in Figs. 3.15 and 3.16. As the magnetic field increases the density goes up, for two reasons. First, the equilibrium ion separation decreases. Second, the electrons become more tightly bound to each ion, in both the  $\rho$  and  $z$  directions (the electrons move closer to each ion faster than the ions move closer to each other). It is interesting to note that the peak density at a given  $z$  is not necessarily along the central axis of the chain ( $\rho = 0$ ), but gradually moves outward with increasing  $z$ .

Table 3.3: The ground-state energy (per unit cell)  $\mathcal{E}_\infty$  (in units of eV), ion separation  $a$  (in units of Bohr radius  $a_0$ ), electron occupation numbers  $(n_m, n_f)$ , and Fermi level energy  $\varepsilon_F$  (in eV) of 1D infinite chains of carbon, over a range of magnetic field strengths. The ground-state energy of individual C atoms,  $\mathcal{E}_a$  (in units of eV), is also provided for reference (this is based on the density-functional-theory calculation of Medin & Lai 2006a). The dimensionless energy  $\bar{\mathcal{E}}_\infty$  and ion separation  $\bar{a}$  are calculated using Eq. (3.56). The scaling exponents  $\beta$  and  $\gamma$ , defined by  $\mathcal{E}_a$ ,  $\mathcal{E}_\infty \propto B^\beta$ , and  $\varepsilon_F \propto B^\gamma$ , are calculated over the three magnetic field ranges provided in the table:  $B_{12} = 1 - 10$ ,  $10 - 100$ ,  $100 - 1000$  (the exponent in the  $B_{12} = 1$  row corresponds to the fit over  $B_{12} = 1 - 10$ , etc.). The occupation of different  $(m\nu)$  bands is designated by the notation  $(n_m, n_f)$ : the electrons occupy Landau orbitals with  $m = 0, 1, 2, \dots, n_m - 1$ , all with  $\nu = 0$ ; the number of fully occupied ( $\sigma_{m\nu} = 1$ ) bands is denoted by  $n_f$ ; see Fig. 3.14. Note that all of the C atoms here also have electrons only in the  $\nu = 0$  states.

$B_{12}$	C		$C_\infty$							
	$\mathcal{E}_a$	$\beta$	$\mathcal{E}_\infty$	$\bar{\mathcal{E}}_\infty$	$\beta$	$a$	$\bar{a}$	$(n_m, n_f)$	$\varepsilon_F$	$\gamma$
1	-4341	0.366	-4367	-0.567	0.373	0.49	3.9	(12,2)	-92.8	0.27
10	-10075	0.326	-10315	-0.533	0.385	0.154	3.1	(23,0)	-173	0.25
100	-21360	0.287	-25040	-0.515	0.389	0.056	2.8	(41,0)	-306	0.25
1000	-41330	-	-61320	-0.502	-	0.022	2.7	(69,0)	-539	-

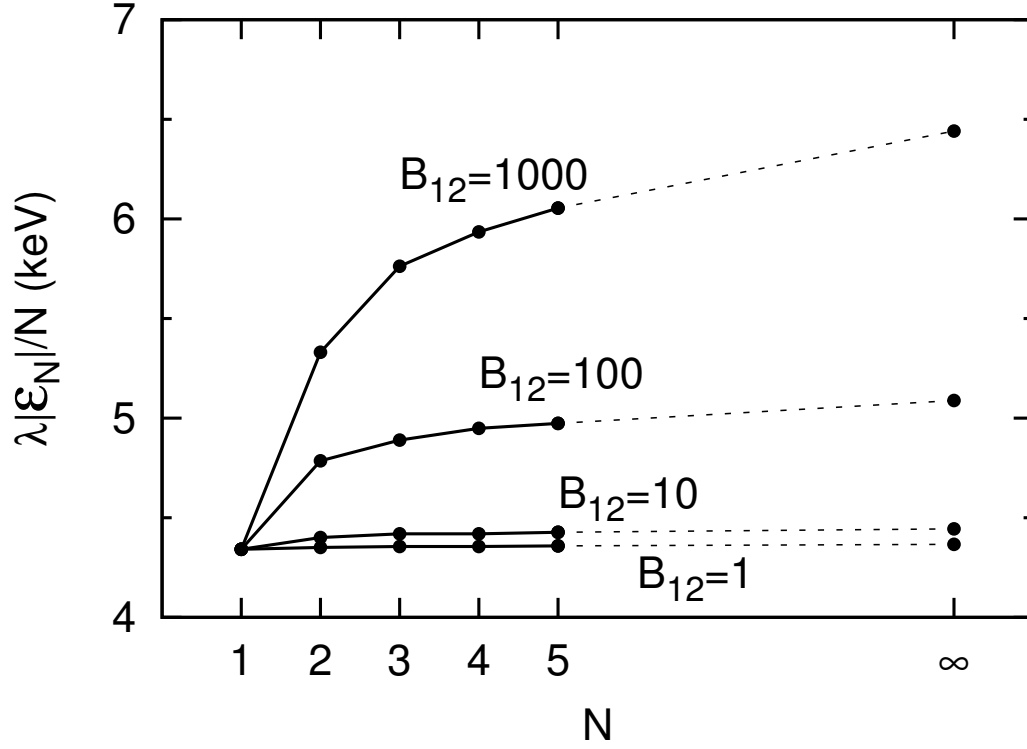


Figure 3.13: The molecular energy per atom,  $|\mathcal{E}_N|/N$ , for the  $C_N$  molecule, as a function of  $N$  at several different field strengths. The results of finite molecules are based on Chapter 2. As  $N$  increases,  $\mathcal{E}_N/N$  asymptotes to  $\mathcal{E}_\infty$ . To facilitate plotting, the values of  $|\mathcal{E}_1|$  (atom) at different magnetic field strengths are normalized to the value at  $B_{12} = 1$ , 4341 eV. This means that  $\lambda = 1$  for  $B_{12} = 1$ ,  $\lambda = 4341/10\,075$  for  $B_{12} = 10$ ,  $\lambda = 4341/21\,360$  for  $B_{12} = 100$ , and  $\lambda = 4341/41\,330$  for  $B_{12} = 1000$ .

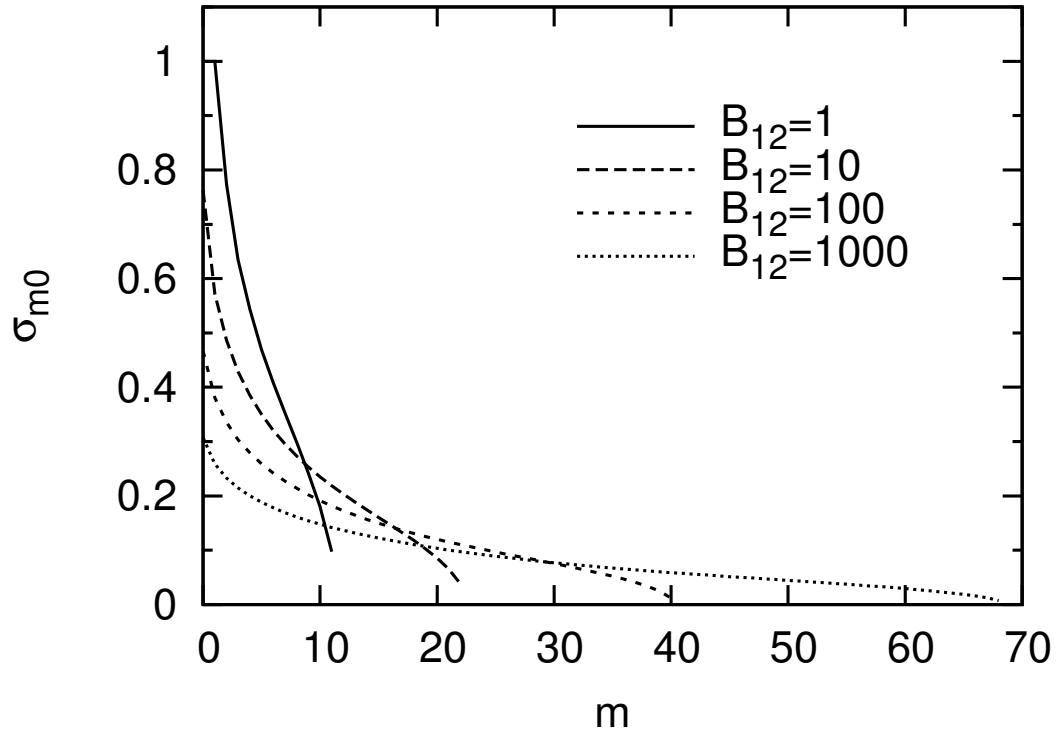


Figure 3.14: The occupation numbers of each  $m$  level of infinite C chains, for various magnetic field strengths. Only the  $\nu = 0$  bands are occupied by the electrons. Note that for  $B_{12} = 1$ , the  $m = 0$  and  $m = 1$  bands are completely filled.

The energy curves for  $\text{Fe}_2$ ,  $\text{Fe}_3$  (calculated in Chapter 2), and  $\text{Fe}_\infty$  at  $B_{12} = 500$  are shown in Fig. 3.17. Figure 3.18 compares the molecular and infinite chain energies at various field strengths, showing that as  $N$  increases, the energy per atom in the  $\text{Fe}_N$  molecule approaches  $\mathcal{E}_\infty$  for the infinite chain. Figure 3.19 gives the occupation number  $\sigma_{m\nu}$  of different bands at various field strengths. For  $B_{12} \gtrsim 100$ , only the  $\nu = 0$  bands are occupied; for such field strengths, the Fe atom also has all its electrons in the tightly bound  $\nu = 0$  states (see Table 3.4). At  $B_{12} = 100$ , the number of fully occupied bands is  $n_f^{(0)} = 7$  ( $m = 0, 1, 2, \dots, 6$ , all with  $\nu = 0$ ). As  $B$  increases, the electrons spread to more Landau orbitals, and the number of occupied  $m$ -states  $n_m^{(0)}$  increases, approximately as  $n_m^{(0)} \propto Z^{2/5} b^{1/5}$ . Note that at the highest field strength considered, the electrons occupy  $m = 0, 1, 2, \dots, 156$  — keeping track of all these Landau orbitals ( $n_m^{(0)} = 157$ ) is one of the more challenging aspects of our computation. Table 3.4 shows that for  $B_{12} \gtrsim 100$ ,

$$\mathcal{E}_\infty \simeq -356 B_{14}^{0.374} \text{ keV}, \quad a = 0.107 B_{14}^{-0.43} a_0 \quad (3.60)$$

[where  $B_{14} = B/(10^{14} \text{ G})$ ]. These scaling expressions are more approximate than for H and He. The electron work function  $W = |\varepsilon_F|$  does not scale as Eq. (3.4), but is a fraction of the ionization energy: from Chapter 2, the ionization energies of Fe at  $B_{12} = 100, 500, 1000, 2000$  are 1.2, 2.5, 3.4, and 5.5 keV, respectively.

Note that at  $B_{12} = 5$  and 10, the cohesive energy ( $Q_\infty = \mathcal{E}_a - \mathcal{E}_\infty$ ) of the iron chain is rather small compared to the absolute value of the ground-state energy of the atom ( $|\mathcal{E}_a|$ ) or chain ( $|\mathcal{E}_\infty|$ ). For these field strengths, our formal numerical result for the cohesive energy is at or smaller than the standard error of our computations (0.1% of  $|\mathcal{E}_a|$  or  $|\mathcal{E}_\infty|$ ), so we have redone the calculations using more grid and integration points such that the atomic and chain energies reported here for these field strengths are accurate to at least 0.02% of  $|\mathcal{E}_a|$  or  $|\mathcal{E}_\infty|$  (see Appendix B). Although these more-accurate cohesive energies are (barely) larger



than the error in our calculations, there are of course systematic errors introduced by using density functional theory which must be considered. It is very possible that a similar, full-band-structure calculation using Hartree-Fock theory would find no binding. In any case, for such “low” field strengths ( $B_{12} \lesssim 10$ ) the exact result of our one-dimensional calculation is not crucial, since in the three-dimensional condensed matter the additional cohesion resulting from chain-chain interactions dominates over  $Q_\infty$ , as we will show in Section 3.5.

At  $B_{12} = 5$ , Neuhauser et al. (1987) and Jones (1985) found that iron is not bound, while we find that it is barely bound. At  $B_{12} = 10$ , Jones (1986) calculated the cohesive energy for three-dimensional condensed matter, so we compare our results with those of Jones (1986) in Section 3.5. We have not found any quantitative calculations of cohesive energies for iron at field strengths larger than  $10^{13}$  G.

### 3.5 Calculations of three-dimensional condensed matter

For the magnetic field strengths considered in this chapter ( $B \gtrsim 10^{12}$  G), H and He infinite chains are significantly bound relative to individual atoms. Additional binding energy between 3D condensed matter and 1D chain is expected to be small (Lai et al. 1992) (see below). Thus the cohesive energy of the 3D condensed H or He,  $Q_s = \mathcal{E}_a - \mathcal{E}_s$  (where  $\mathcal{E}_s$  is the energy per cell in the 3D condensed matter), is close to  $Q_\infty = \mathcal{E}_a - \mathcal{E}_\infty$ , the cohesive energy of the 1D H or He chain. For C and Fe at relatively low magnetic fields (e.g., C at  $B_{12} \lesssim 10$  and Fe at  $B_{12} \lesssim 100$ ), 1D chains are not significantly bound relative to atoms and additional cohesion due to chain-chain interactions is important in determining the true cohesive energy of the 3D condensed matter. Indeed, for Fe at  $B_{12} = 5, 10$ , our calculations of 1D

Table 3.4: The ground-state energy (per unit cell)  $\mathcal{E}_\infty$  (in units of keV), ion separation  $a$  (in units of the Bohr radius  $a_0$ ), electron occupation numbers  $(n_m^{(0)}, n_f^{(0)}; n_m^{(1)}, n_f^{(1)})$ , and Fermi level energy  $\varepsilon_F$  (in eV) of 1D infinite iron chains, over a range of magnetic field strengths. The ground-state energy of individual Fe atoms,  $\mathcal{E}_a$  (in units of keV), is also provided for reference (this is based on the density-functional-theory calculation of Medin & Lai 2006a). The dimensionless energy  $\bar{\mathcal{E}}_\infty$  and ion separation  $\bar{a}$  are calculated using Eq. (3.56). The scaling exponents  $\beta$  and  $\gamma$ , defined by  $\mathcal{E}_a$ ,  $\mathcal{E}_\infty \propto B^\beta$ , and  $\varepsilon_F \propto B^\gamma$ , are calculated over the three magnetic field ranges provided in the table:  $B_{12} = 1 - 10$ ,  $10 - 100$ ,  $100 - 1000$  (the exponent in the  $B_{12} = 1$  row corresponds to the fit over  $B_{12} = 1 - 10$ , etc.). For atoms the electron configuration is specified by the notation  $(n_0, n_1)$  (with  $n_0 + n_1 = Z = 26$ ), where  $n_0$  is the number of electrons in the  $\nu = 0$  orbitals and  $n_1$  is the number of electrons in the  $\nu = 1$  orbitals. For infinite chains, the occupation of different  $(m\nu)$  bands is designated by the notation  $(n_m^{(0)}, n_f^{(0)}; n_m^{(1)}, n_f^{(1)})$ , where  $n_m^{(0)}$  is the total number of occupied  $\nu = 0$  orbitals (from  $m = 0$  to  $m = n_m^{(0)} - 1$ ), and  $n_m^{(1)}$  the corresponding number for the  $\nu = 1$  orbitals;  $n_f^{(0)}$  ( $n_f^{(1)}$ ) is the number of fully occupied ( $\sigma_{m\nu} = 1$ )  $\nu = 0$  ( $\nu = 1$ ) orbitals. Note that for  $B_{12} \gtrsim 100$ , only the  $\nu = 0$  states are occupied in the Fe atom, and only the  $\nu = 0$  bands are occupied in the Fe chain; see Fig. 3.19.

$B_{12}$	Fe			Fe $_\infty$							
	$\mathcal{E}_a$ (keV)	$(n_0, n_1)$	$\beta$	$\mathcal{E}_\infty$ (keV)	$\bar{\mathcal{E}}_\infty$	$\beta$	$a$	$\bar{a}$	$(n_m^{(0)}, n_f^{(0)}; n_m^{(1)}, n_f^{(1)})$	$\varepsilon_F$ (eV)	$\gamma$
5	-107.23	(24,2)	0.407	-107.31	0.522	0.407	0.42	4.7	(35,15;3,1)	-161	0.27
10	-142.15	(25,1)	0.396	-142.30	0.525	0.398	0.30	4.4	(42,13;2,0)	-194	0.30
100	-354.0	(26,0)	0.366	-355.8	0.522	0.376	0.107	4.0	(69,7)	-384	0.26
500	-637.8	(26,0)	0.346	-651.9	0.503	0.371	0.050	3.5	(105,2)	-583	0.12
1000	-810.6	(26,0)	0.334	-842.8	0.493	0.372	0.035	3.3	(130,1)	-635	0.12
2000	-1021.5	(26,0)	-	-1091.0	0.483	-	0.025	3.1	(157,0)	-690	-

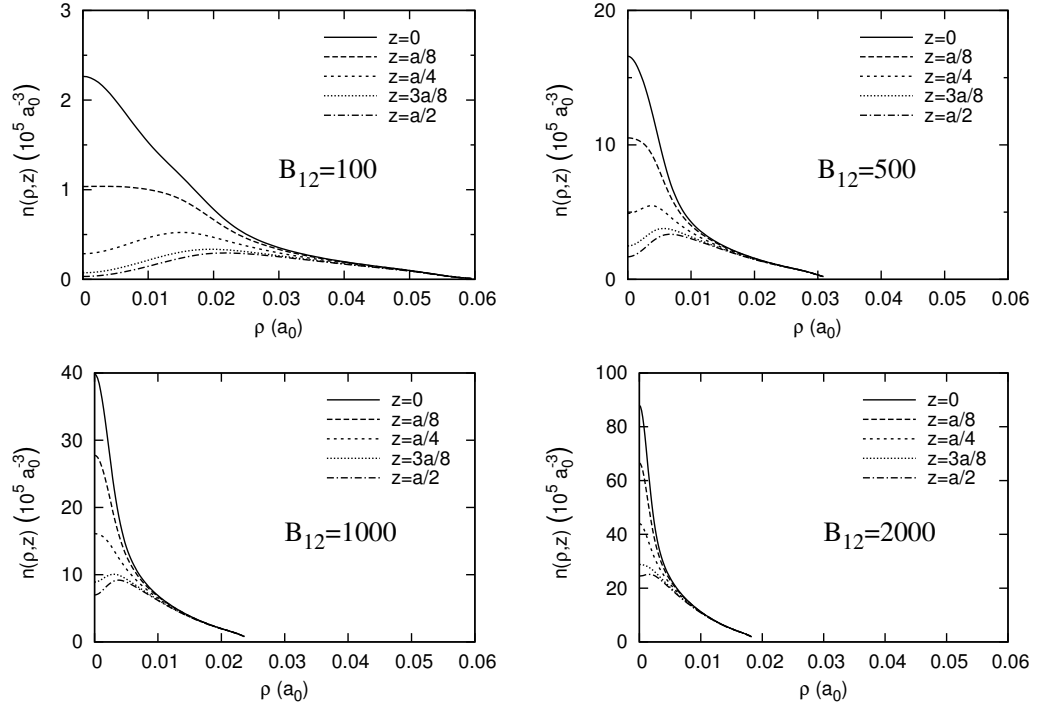


Figure 3.15: The density distribution of electrons in the iron infinite chain at four different magnetic field strengths (labeled on the graphs). The density is shown as a function of  $\rho$  for five equally spaced  $z$  points from the center of a cell ( $z = 0$ ) to the edge of that cell ( $z = a/2$ ).

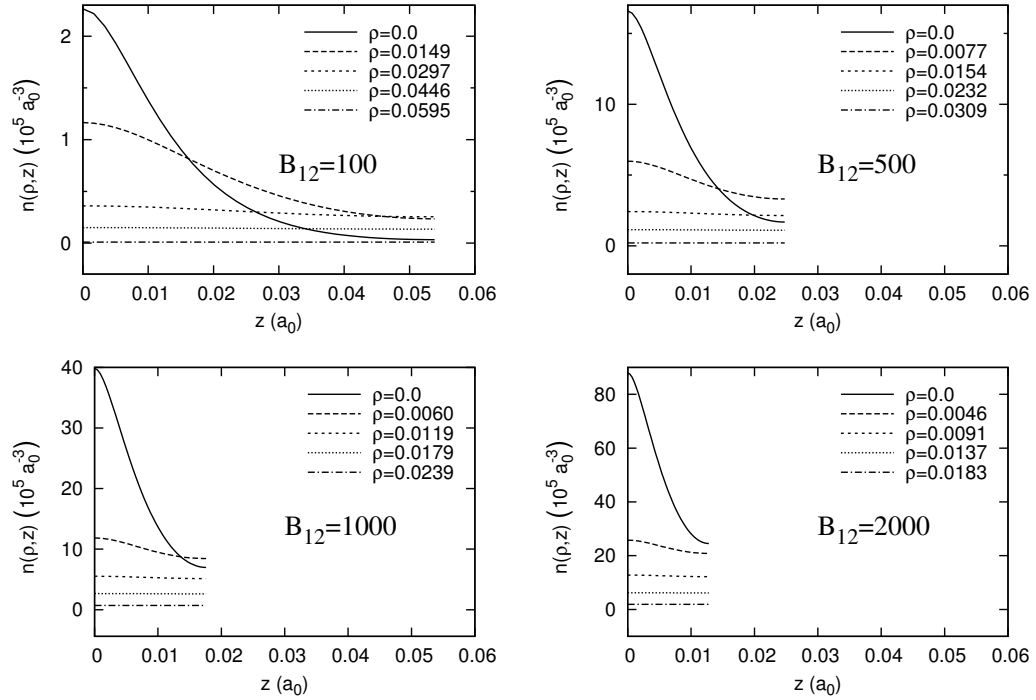


Figure 3.16: The density distribution of electrons in the iron infinite chain at four different magnetic field strengths (labeled on the graphs). The density is shown as a function of  $z$  for five equally spaced  $\rho$  points from the center of a cell ( $\rho = 0$ ) to the guiding center radius of the highest occupied  $m$  level ( $\rho = \rho_{m_{\max}}$ ). The  $\rho$  points are given in units of  $a_0$ .

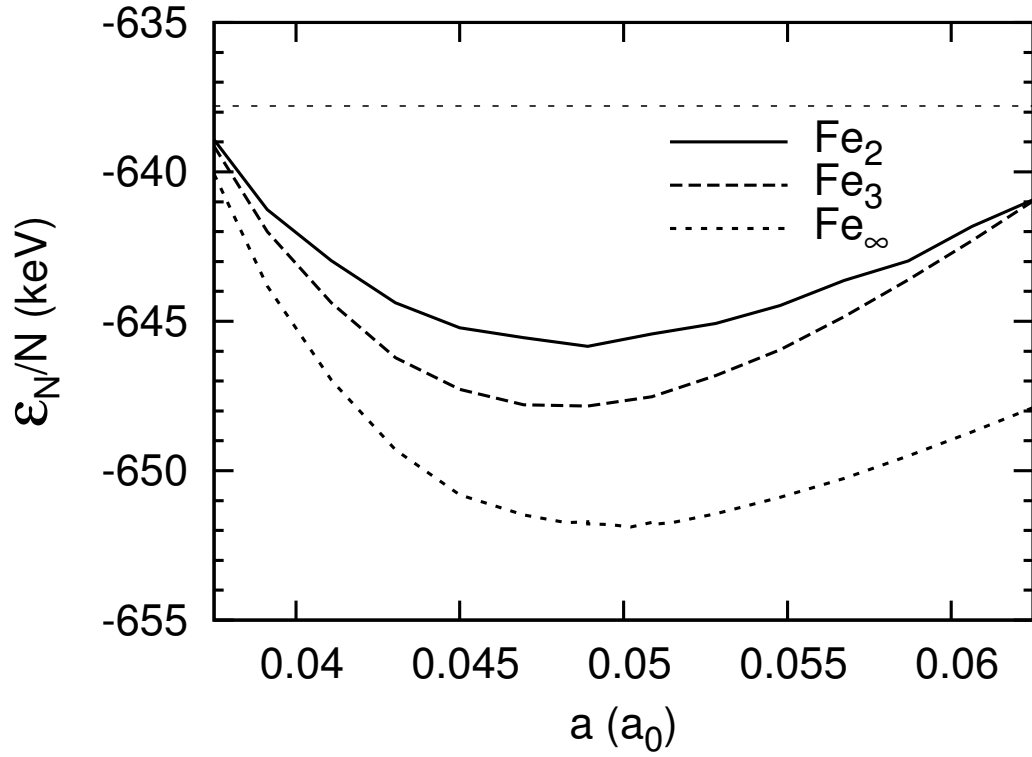


Figure 3.17: The energy per cell as a function of the ion separation for an infinite Fe chain at  $B_{12} = 500$ . The molecular energy per atom versus ion separation for the  $\text{Fe}_2$  and  $\text{Fe}_3$  molecules at the same field strength (based on calculations in Chapter 2) are also shown. The energy of the Fe atom is shown as a horizontal line at  $-637.8$  keV.

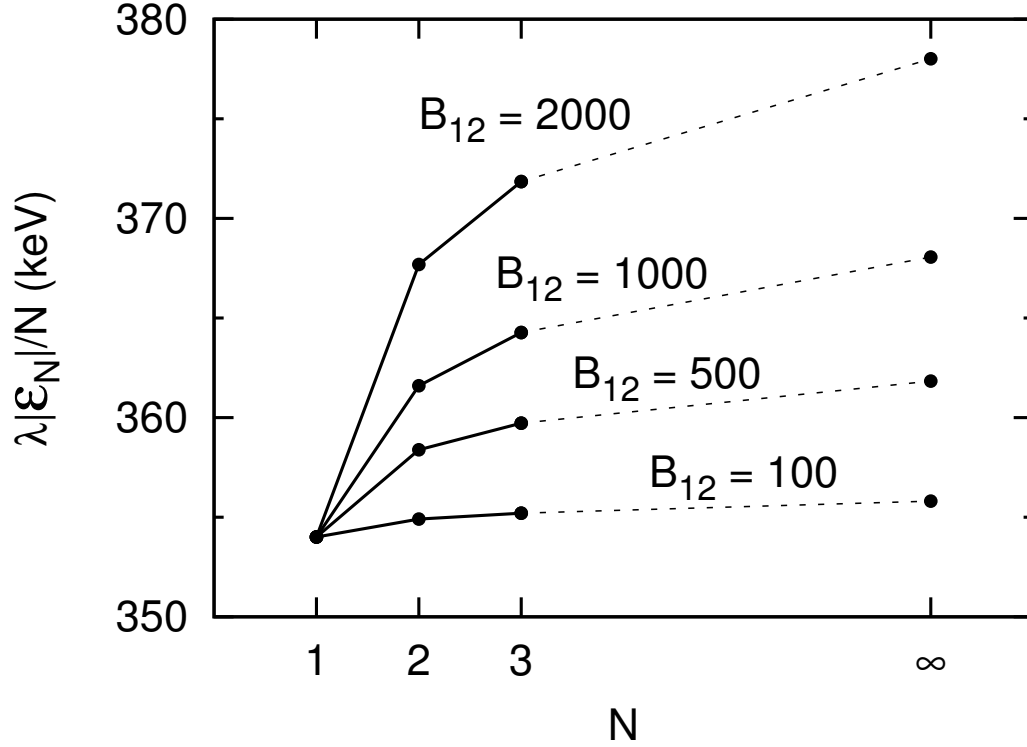


Figure 3.18: The molecular energy per atom,  $|\mathcal{E}_N|/N$ , for the  $\text{Fe}_N$  molecule, as a function of  $N$  at several different field strengths. The results of finite molecules are based on Chapter 2. As  $N$  increases,  $\mathcal{E}_N/N$  asymptotes to  $\mathcal{E}_\infty$ . To facilitate plotting, the values of  $|\mathcal{E}_1|$  (atom) at different magnetic field strengths are normalized to the value at  $B_{12} = 100$ , 354.0 keV. This means that  $\lambda = 1$  for  $B_{12} = 100$ ,  $\lambda = 354.0/637.8$  for  $B_{12} = 500$ ,  $\lambda = 354.0/810.6$  for  $B_{12} = 1000$ , and  $\lambda = 354.0/1021.5$  for  $B_{12} = 2000$ .

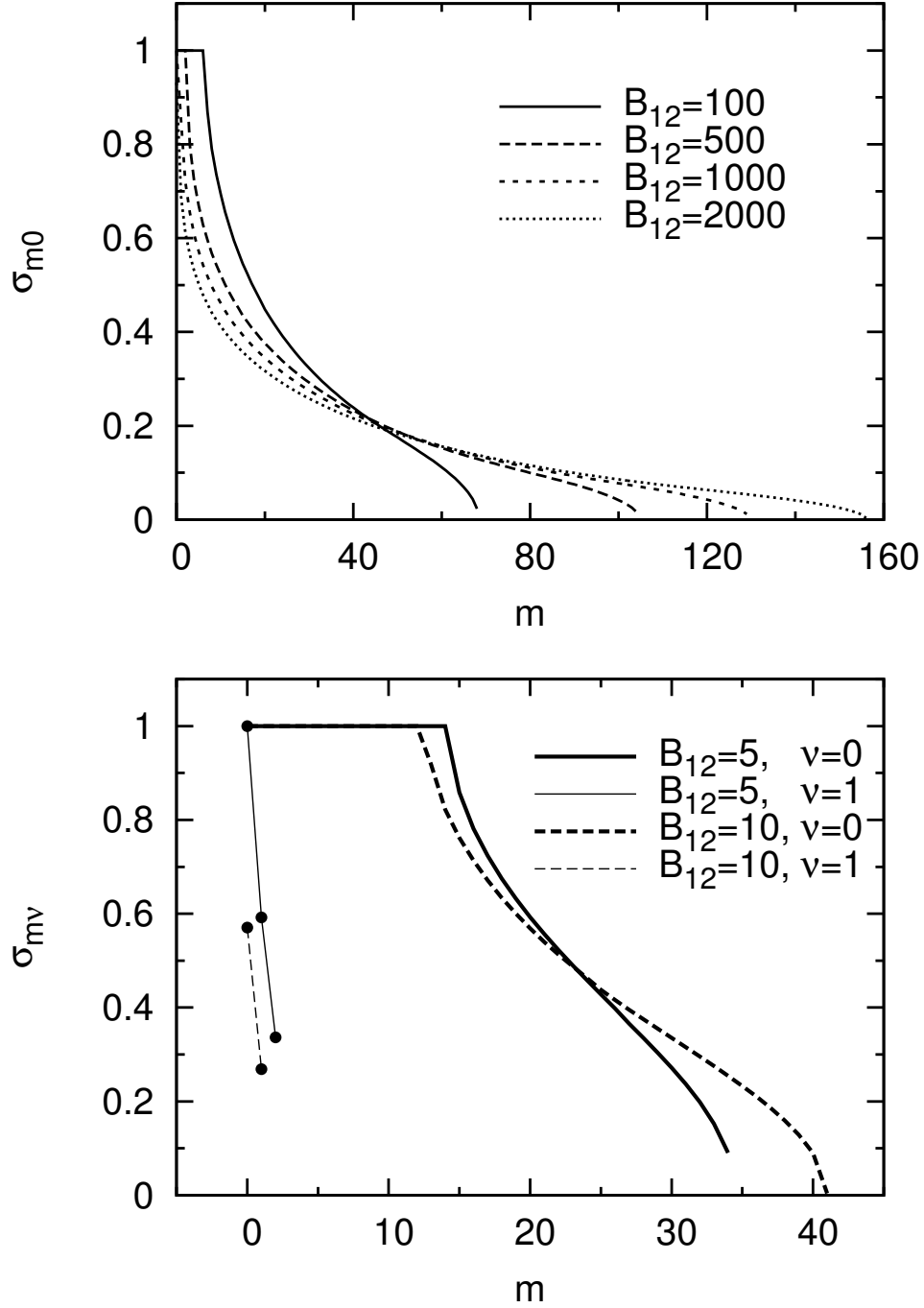


Figure 3.19: The occupation numbers of each  $m$  level of infinite Fe chains, for various magnetic field strengths. For  $B_{12} \gtrsim 100$ , only the  $\nu = 0$  bands are occupied by the electrons (upper panel). For  $B_{12} = 5$  and 10 the  $m$  levels with  $\nu = 1$  are shown with points as well as lines, since there are only a few such occupied levels (lower panel).

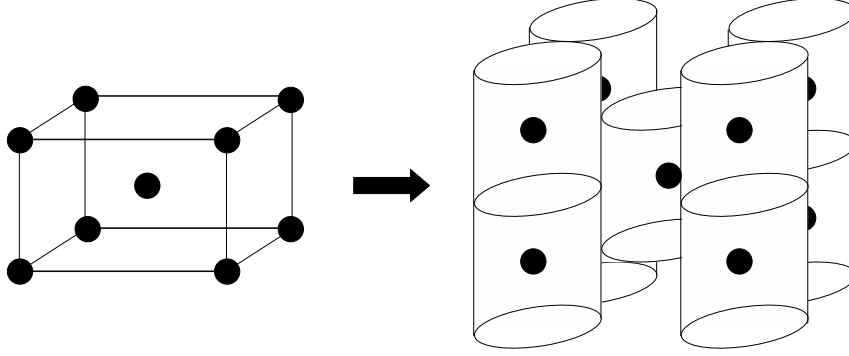


Figure 3.20: A schematic diagram showing the body-centered tetragonal structure of the lattice, with only the ions displayed (left panel) and with the ions and the surround electron orbitals displayed (right panel).

chains give such a small  $Q_\infty$  (see Table 3.4) that it is somewhat ambiguous as to whether the Fe condensed matter is truly bound relative to individual atoms. In these cases, calculations of 3D condensed matter is crucial (Jones 1986).

In this section, we present an approximate calculation of the relative binding energy between 3D condensed matter and 1D chains,  $\Delta\mathcal{E}_s = \mathcal{E}_s - \mathcal{E}_\infty$ .

### 3.5.1 Method

To form 3D condensed matter we place the infinite chains in parallel bundles along the magnetic field. We consider a body-centered tetragonal lattice structure; i.e., the chains are uniformly spaced over a grid in the  $xy$  plane (perpendicular to the magnetic axis), with every other chain in the grid shifted by half a cell ( $\Delta z = a/2$ ) in the  $z$  direction (see Fig. 3.20). The transverse separation between two nearest neighboring chains is denoted by  $2R$ , with  $R$  to be determined.



To calculate the ground-state energy of this 3D condensed matter, we assume that the electron density calculated for an individual 1D chain is not modified by chain-chain interactions, thus we do not solve for the full electron density in the 3D lattice self-consistently. In reality, for each Landau orbital the transverse wave function of an electron in the 3D lattice is no longer given by Eq. (3.11) (which is centered at one particular chain), but is given by a superposition of many such Landau wave functions centered at different lattice sites and satisfies the periodic (Bloch) boundary condition. The longitudinal wave function  $f_{m\nu k}(z)$  will be similarly modified. Our calculations show that the equilibrium separation ( $2R$ ) between chains is large enough that there is little overlap in the electron densities of any two chains, so we believe that our approximation is reasonable.

Using this approximation, the electron density in the 3D lattice is simply the sum of individual infinite chain electron densities:

$$n_{3D}(\mathbf{r}) = \sum_{ij} n(\mathbf{r} - \mathbf{r}_{ij}), \quad (3.61)$$

where  $n(\mathbf{r})$  are the electron density in the 1D chain (as calculated in Sections 3.3-3.4), the sum over  $ij$  spans all positive and negative integers, and

$$\mathbf{r}_{ij} = 2Ri \hat{\mathbf{x}} + 2Rj \hat{\mathbf{y}} + \frac{a}{2}[i, j] \hat{\mathbf{z}} \quad (3.62)$$

represents the location of the origin of each chain (the notation  $[i, j] = 1$  when  $i + j = \text{odd}$ , and  $[i, j] = 0$  when  $i + j = \text{even}$ ). In practice, the chain-chain overlap is so small that we only need to consider neighboring chains. The density at a point in the positive  $xyz$  octant of a 3D unit cell is approximately given by

$$n_{3D}(\mathbf{r}) \simeq n(\mathbf{r}) + n(\mathbf{r} - 2R\hat{\mathbf{x}} - a/2\hat{\mathbf{z}}) + n(\mathbf{r} - 2R\hat{\mathbf{y}} - a/2\hat{\mathbf{z}}) + n(\mathbf{r} - 2R\hat{\mathbf{x}} - 2R\hat{\mathbf{y}}). \quad (3.63)$$

The energy (per unit cell)  $\Delta\mathcal{E}_{3D}(R)$  of the 3D condensed matter relative to the 1D chain consists of the chain-chain interaction Coulomb energy  $\Delta\mathcal{E}_{\text{Coul}}$  and

the additional electron kinetic energy  $\Delta\mathcal{E}_K$  and exchange-correlation energy  $\Delta\mathcal{E}_{\text{exc}}$  due to the (slight) overlap of different chains. The dominant contribution to the Coulomb energy comes from the interaction between nearest-neighboring cells. For a given cell in the matter, each of the eight nearest-neighboring cells contributes an interaction energy of

$$\mathcal{E}_{\text{nn}} = \mathcal{E}_{eZ,\text{nn}} + \mathcal{E}_{\text{dir},\text{nn}} + \mathcal{E}_{ZZ,\text{nn}}, \quad (3.64)$$

where

$$\mathcal{E}_{eZ,\text{nn}} = -Ze^2 \int_{|z|<a/2} d\mathbf{r} \frac{n(\mathbf{r})}{|\mathbf{r} - \mathbf{r}_{\text{nn}}|}, \quad (3.65)$$

$$\mathcal{E}_{\text{dir},\text{nn}}[n] = \frac{e^2}{2} \iint_{|z|<a/2, |z'|<a/2} d\mathbf{r} d\mathbf{r}' \frac{n(\mathbf{r})n(\mathbf{r}')}{|\mathbf{r} - (\mathbf{r}' + \mathbf{r}_{\text{nn}})|} \quad (3.66)$$

$$\mathcal{E}_{ZZ,\text{nn}} = \frac{1}{2} \frac{Z^2 e^2}{|\mathbf{r}_{\text{nn}}|} = \frac{1}{2} \frac{Z^2 e^2}{\sqrt{(a/2)^2 + (2R)^2}}, \quad (3.67)$$

and  $\mathbf{r}_{\text{nn}}$  is the location of the ion in a nearest-neighboring cell, for example

$$\mathbf{r}_{\text{nn}} = 2R\hat{\mathbf{x}} + \frac{a}{2}\hat{\mathbf{z}}. \quad (3.68)$$

More distant cells contribute to the Coulomb energy through their quadrupole moments. The classical quadrupole-quadrupole interaction energy between two cells separated by a distance  $d$  is

$$\mathcal{E}_{QQ}(d, \theta) = \frac{3e^2}{16} \frac{Q_{zz}^2}{d^5} (3 - 30 \cos^2 \theta + 35 \cos^4 \theta), \quad (3.69)$$

where  $Q_{zz}$  is given by Eq. (3.39) and  $\theta$  is the angle between the line joining the two quadrupoles and the  $z$  axis. The total contribution from all nonneighboring cells to the Coulomb energy is then

$$\frac{1}{2} \sum_{(ijk)} \mathcal{E}_{QQ}(\mathbf{r}_{ijk}), \quad (3.70)$$

where

$$\mathbf{r}_{ijk} = \mathbf{r}_{ij} + a k \hat{\mathbf{z}}, \quad d = |\mathbf{r}_{ijk}|, \quad \cos \theta = \frac{k + [i, j]/2}{d/a}, \quad (3.71)$$

and the sum in Eq. (3.70) spans over all positive and negative integers except those corresponding to the nearest neighbors.

In the density functional theory, the kinetic and exchange-correlation energies depend entirely on the electron density. These energies differ in the 3D condensed matter from the 1D chain because the overall electron density  $n_{3D}(\mathbf{r})$  [see Eq. (3.61)] within each 3D cell is (slightly) larger than  $n(\mathbf{r})$  due to the overlap of the infinite chains. Since we do not solve for the electron density in the 3D condensed matter self-consistently, we calculate the kinetic energy difference using the local (Thomas-Fermi) approximation:

$$\Delta\mathcal{E}_K(R) = \int_{|z|<a/2; |x|,|y|<R} d\mathbf{r} n_{3D}(\mathbf{r}) \varepsilon_K(n_{3D}) - \int_{|z|<a/2} d\mathbf{r} n(\mathbf{r}) \varepsilon_K(n). \quad (3.72)$$

Here  $\varepsilon_K(n)$  is the (Thomas-Fermi) kinetic energy (per electron) for an electron gas at density  $n$ , and is given by (e.g., Lai 2001)

$$\varepsilon_K(n) = \frac{\hbar^2(2\pi^2\rho_0^2n)^2}{6m_e} = \frac{e^2}{3\rho_0} b^{1/2} t, \quad (3.73)$$

where  $t$  is given by Eq. (3.29). Note that the regions of integration in the  $xy$  direction are different for the two terms in Eq. (3.72), as in the 1D chain the unit cell extends over all  $\rho$  space, while in the 3D condensed matter the cell is restricted to  $x, y \in [-R, R]$ .

Similar to  $\Delta\mathcal{E}_K$ , in the local approximation, the change in exchange-correlation energy per unit cell is

$$\Delta\mathcal{E}_{\text{exc}}(R) = \int_{|z|<a/2; |x|,|y|<R} d\mathbf{r} n_{3D}(\mathbf{r}) \varepsilon_{\text{exc}}(n_{3D}) - \int_{|z|<a/2} d\mathbf{r} n(\mathbf{r}) \varepsilon_{\text{exc}}(n), \quad (3.74)$$

where  $\varepsilon_{\text{exc}}(n)$  is the exchange-correlation energy (per electron) at density  $n$  (see Section 3.3.1).

Combining the Coulomb energy, the kinetic energy, and the exchange-correlation energy, the total change in the energy per unit cell when 3D condensed matter is

formed from 1D infinite chains can be written

$$\Delta\mathcal{E}_{3D}(R) = \Delta\mathcal{E}_{\text{Coul}} + \Delta\mathcal{E}_K + \Delta\mathcal{E}_{\text{exc}}, \quad (3.75)$$

where

$$\Delta\mathcal{E}_{\text{Coul}}(R) = 8\mathcal{E}_{\text{nn}} + \frac{1}{2} \sum_{(ijk)} \mathcal{E}_{QQ}(\mathbf{r}_{ijk}). \quad (3.76)$$

We calculate  $\Delta\mathcal{E}_{3D}(R)$  as a function of  $R$  and locate the minimum to determine the equilibrium chain-chain separation  $2R$  and the equilibrium energy of the 3D condensed matter. Our method for evaluating various integrals is described in Appendix B.

### 3.5.2 Results: 3D condensed matter

Table 3.5 presents our numerical results for the equilibrium chain-chain separation  $2R = 2R_{\text{eq}}$  and the energy difference (per cell) between the 3D condensed matter and 1D chain,  $\Delta\mathcal{E}_s = \mathcal{E}_s - \mathcal{E}_{\infty} = \Delta\mathcal{E}_{3D}(R = R_{\text{eq}})$ , for C and Fe at various magnetic field strengths. A typical energy curve is shown in Fig. 3.21. We see that it is important to include the kinetic energy contribution  $\Delta\mathcal{E}_K$  to the 3D energy; without  $\Delta\mathcal{E}_K$ , the energy curve would not have a local minimum at a finite  $R$ .

A comparison of the  $R$  values in Table 3.5 with various iron chain electron densities in Fig. 3.15 shows that our assumption of small electron density overlap between chains is indeed a good approximation. The electron densities are slowly-varying at the overlapping region, so using the local (Thomas-Fermi) model to calculate the kinetic energy difference is also consistent with the results of our model. Our equilibrium  $R$  is within about 15% of the value predicted in the uniform cylinder model [see Eq. (3.3)].

Table 3.5: The energy difference (per unit cell) between the 3D condensed matter and 1D chain,  $\Delta\mathcal{E}_s = \mathcal{E}_s - \mathcal{E}_\infty$ , for carbon and iron over a range of magnetic field strengths. Energies are given in units of eV for C and keV for Fe. The equilibrium chain-chain separation is  $2R_{\text{eq}}$  (in units of the Bohr radius  $a_0$ ).

$B_{12}$	C		Fe	
	$\Delta\mathcal{E}_s$ (eV)	$R_{\text{eq}}$	$\Delta\mathcal{E}_s$ ( keV)	$R_{\text{eq}}$
1	-30	0.200		
5	-40	0.110	-0.6	0.150
10	-20	0.094	-0.6	0.115
100	-20	0.041	-2.2	0.054
500	-30	0.022	-2.1	0.025
1000	-10	0.017	-1.3	0.021

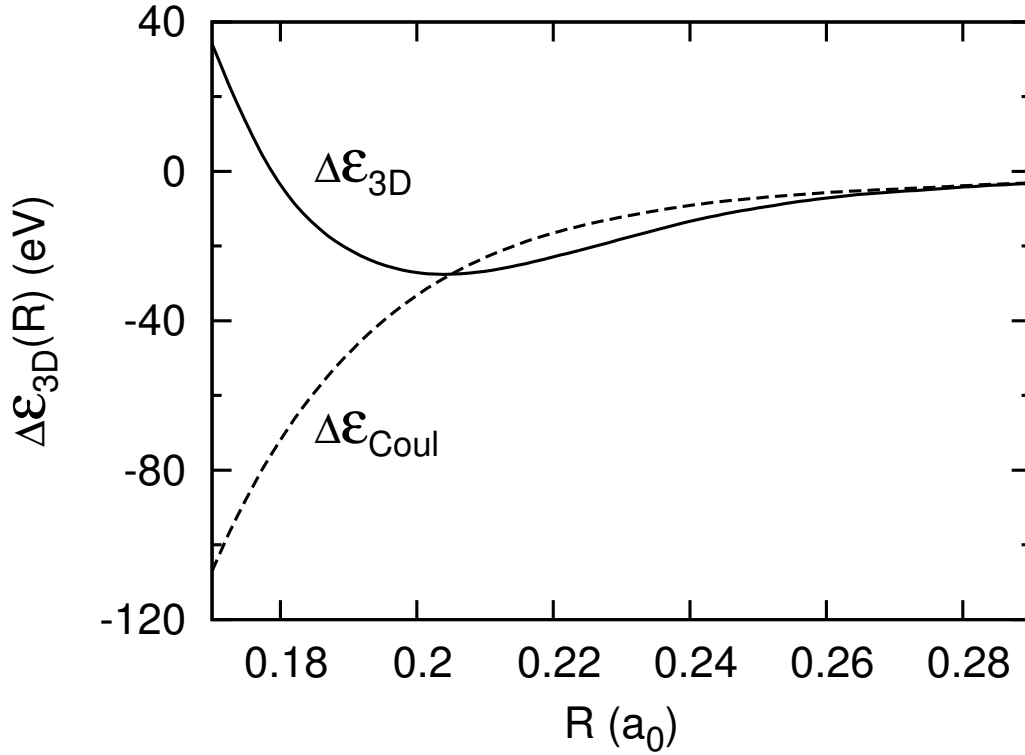


Figure 3.21: The energy (per cell) of 3D condensed matter relative to 1D chain as a function of  $R$ , for carbon at  $B_{12} = 1$ . The nearest-neighbor chain-chain separation in the 3D condensed matter is  $2R$ . The solid curve gives  $\Delta\mathcal{E}_{3D}(R)$  [Eq. (3.75)] and the dashed curve gives only the Coulomb energy  $\Delta\mathcal{E}_{\text{Coul}}$  [Eq. (3.76)].

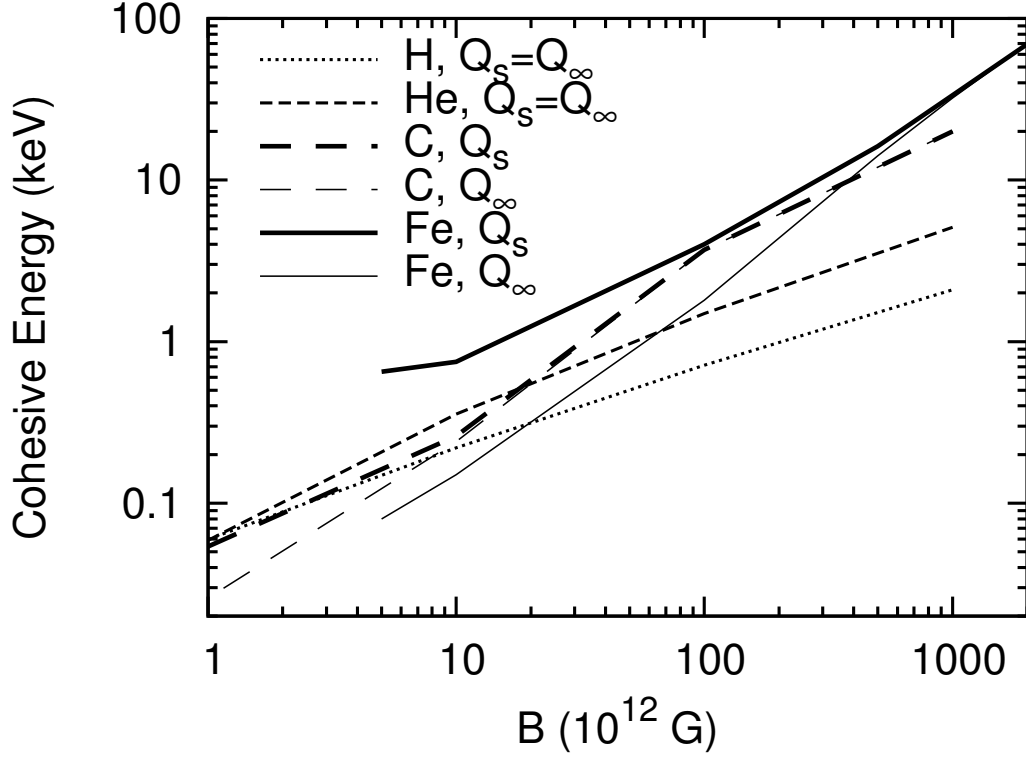


Figure 3.22: The cohesive energy as a function of  $B$ , for H (dotted line) and He (short-dashed line) infinite chains and C (long-dashed lines) and Fe (solid lines) infinite chains (lighter lines) and 3D condensed matter (heavier lines).

Given our results for  $\Delta\mathcal{E}_s$  and the cohesive energy of 1D chains,  $Q_\infty = \mathcal{E}_a - \mathcal{E}_\infty$ , we can obtain the cohesive energy of 3D condensed matter from

$$Q_s = \mathcal{E}_a - \mathcal{E}_s = \mathcal{E}_a - (\mathcal{E}_\infty + \Delta\mathcal{E}_s) = Q_\infty - \Delta\mathcal{E}_s. \quad (3.77)$$

For H and He, we find that  $|\Delta\mathcal{E}_s|$  is small compared to  $Q_\infty$  and thus  $Q_s \simeq Q_\infty$ . Figure 3.22 depicts  $Q_s$  and  $Q_\infty$  as a function of  $B$  for H, He, C, and Fe.

The only previous quantitative calculation of 3D condensed matter is that by Jones (1986), who finds cohesive energies of  $Q_s = 0.60, 0.92$  keV for iron at  $B_{12} = 5, 10$ . At these field strengths, our calculation (see Tables 3.4 and 3.5) gives  $Q_s = \mathcal{E}_a - \mathcal{E}_s = Q_\infty - \Delta\mathcal{E}_s = 0.08 + 0.6 \simeq 0.7$  keV and  $0.15 + 0.6 \simeq 0.75$  keV, respectively.

Note that our calculations and the results presented here assume that the ion spacing along the magnetic axis in 3D condensed matter,  $a$ , is the same as in the 1D chain. We have found that if both  $a$  and  $R$  are allowed to vary, the 3D condensed matter energy can be lowered slightly. This correction is most important for relatively low field strengths. For example, in the case of Fe at  $B_{12} = 10$ , if we increase  $a$  from the 1D chain value by 10%, then  $Q_\infty$  decreases by about 50 eV, but  $|\Delta\mathcal{E}_s|$  increases by about 200 eV, so that  $Q_s$  is increased to  $\sim 0.9$  keV. Given the approximate nature of our 3D calculations, we do not explore such refinement in detail in this chapter.

### 3.6 Discussions

Using density functional theory, we have carried out extensive calculations of the cohesive properties of 1D infinite chains and 3D zero-pressure condensed matter in strong magnetic fields. Our results, presented in various tables, figures, and fitting formulae, show that hydrogen, helium, and carbon infinite chains are all bound relative to individual atoms for magnetic fields  $B \geq 10^{12}$  G, but iron chains are not (significantly) bound until around  $B \sim 10^{14}$  G. For a given zero-pressure condensed matter system, the cohesion along the magnetic axis (chain axis) dominates over chain-chain interactions across the magnetic axis at sufficiently strong magnetic fields. But for relative low field strengths (e.g. Fe at  $B \lesssim 10^{14}$  G and C at  $B \lesssim$  a few  $\times 10^{12}$  G), chain-chain interactions play an important role in the cohesion of 3D condensed matter. Our calculations show that for the field strengths considered in this chapter ( $B \gtrsim 10^{12}$  G), 3D condensed H, He, C and Fe are all bound relative to individual atoms: For C, the cohesive energy  $Q_s = \mathcal{E}_a - \mathcal{E}_c$  ranges from  $\sim 50$  eV at  $B = 10^{12}$  G to 20 keV at  $10^{15}$  G; for Fe,  $Q_s$  ranges from  $\sim 0.8$  keV at  $10^{13}$  G to

33 keV at  $10^{15}$  G.

Our result for the 1D infinite chain energy (per cell),  $\mathcal{E}_\infty$ , is consistent with the energies of finite molecules obtained in Chapter 2 (Medin & Lai 2006a), where we showed that the binding energy (per atom) of the molecule,  $|\mathcal{E}_N|/N$  (where  $\mathcal{E}_N$  is the ground-state energy and  $N$  is the number of atoms in the molecule), increases with increasing  $N$ , and asymptotes to a constant value. The values of  $|\mathcal{E}_N|/N$  for various molecules obtained in Medin & Lai (2006a) are always less than  $|\mathcal{E}_\infty|$ . Since the electron energy levels in a finite molecule and those in an infinite chain are quite different (the former has discrete states while the latter has band structure), and the computations involved are also different, the consistency between the finite molecule results and 1D chain results provides an important check for the validity of our calculations.

It is not straightforward to assess the accuracy of our density-functional-theory calculations of infinite chains compared to the Hartree-Fock method. For finite molecules with small number of electrons, using the available Hartree-Fock results, we have found that density functional theory tends to overestimate the binding energy by about 10%, although this does not translate into an appreciable error in the molecular dissociation energy (Medin & Lai 2006a). For infinite chains, the only previous calculation using the Hartree-Fock method (Neuhauser et al. 1987) adopted an approximate treatment for the electron band structure (e.g., assuming that the electron energy increases as  $k^2/2$  as the Bloch wave number  $k$  increases), which, as we showed in this chapter (Section 3.3.3), likely resulted in appreciable error to the total chain energy. Since the cohesive energy  $Q_\infty$  of the chain involves the difference in the binding energy the 1D chain and the atom, and because of the statistical nature of density functional theory, we expect that our result



for  $Q_\infty$  is more accurate for heavy elements (C and Fe) than for light elements (H and He). We note that it is very difficult (perhaps impractical) to carry out *ab initio* Hartree-Fock calculations of infinite chains if no approximation is made about the electron band structure. This is especially the case in the superstrong magnetic field regime where many Landau orbitals are populated. For example, for the Fe chain at  $B = 10^{15}$  G, one must be dealing with 130 Landau orbitals (see Table 3.4), each with its own band structure — this would be a formidable task for any Hartree-Fock calculation.

We also note that our conclusion about 3D condensed matter is not based on fully self-consistent calculations and uses several approximations (Section 3.5). Although we have argued that the approximations we adopted are valid and our calculation gave reasonable values for the relative binding energies between 1D chains and 3D condensed matter, it would be desirable to carry out more definitive calculations of 3D condensed matter.

Our computed binding energies and equilibrium ion separations of infinite chains and condensed matter agree approximately with the simple scaling relations (e.g.,  $\mathcal{E}_\infty$  and  $a$  as a function of  $B$ ) derived from the uniform gas model (Section 3.2). We have provided more accurate fitting formulae which will allow one to obtain the cohesive energy at various field strengths. Our result for the electron work function ( $W = |\varepsilon_F|$ ), however, does not agree with the simple scaling relation derived for the uniform electron gas model. For example, we found that  $W$  scales more slowly with  $B$  ( $\gamma$  is significantly smaller than  $2/5$ ) and does not depend strongly on  $Z$  (as opposed to the  $Z^{4/5}$  dependence for the uniform gas model); see Tables 3.1–3.4. This “discrepancy” is understandable since, unlike the  $B = 0$  case, in strong magnetic fields the ionization of an atom and binding energy

of condensed matter can be very different in values and have different dependences on  $B$ : for sufficiently large  $B$ , the former scales roughly as  $(\ln b)$ , while the later scales as  $\sim b^{0.4}$ . Our computed electron work function is of order (and usually a fraction of) the ionization energy of the corresponding atom, which is generally much smaller than the estimate of  $W$  based on uniform gas model. We also found that the ionization energy of successively larger (finite) molecules (Medin & Lai 2006a) approaches our calculated work function for the infinite chain — thus we believe our result for  $W$  is reliable. Note that Jones (1986) also found that the work function  $W$  is almost independent of  $Z$ , but his  $W$  values scale as  $B^{0.5}$  and are much larger than our results for the same field strengths. His  $W$  values are also larger than the ionization energies of the corresponding atoms.

Our results for the cohesive energy and work function of condensed matter in strong magnetic fields have significant implications for the physical conditions of the outermost layers of magnetized neutron stars and the possible existence of “vacuum gap” accelerators in pulsars. We investigate these issues in Chapters 5 and 6.

## CHAPTER 4

# RADIATIVE TRANSITIONS OF THE HELIUM ATOM IN HIGHLY MAGNETIZED NEUTRON STAR ATMOSPHERES

### 4.1 Introduction

An important advance in neutron star astrophysics in the last few years has been the detection and detailed studies of surface emission from a large number of isolated neutron stars (NSs), including radio pulsars, magnetars, and radio-quiet NSs (e.g., Kaspi et al. 2006; Harding & Lai 2006). This was made possible by X-ray telescopes such as *Chandra* and *XMM-Newton*. Such studies can potentially provide invaluable information on the physical properties and evolution of NSs (e.g., equation of state at super-nuclear densities, cooling history, surface magnetic field and composition). Of great interest are the radio-quiet, thermally emitting NSs (e.g., Haberl 2006): they share the common property that their spectra appear to be entirely thermal, indicating that the emission arises directly from the NS surfaces, uncontaminated by magnetospheric emission. The true nature of these sources, however, is unclear at present: they could be young cooling NSs, or NSs kept hot by accretion from the ISM, or magnetar descendants. While some of these NSs (e.g., RX J1856.5–3754) have featureless X-ray spectra remarkably well described by blackbodies (e.g., Burwitz et al 2003) or by emission from a condensed surface covered by a thin atmosphere (Ho et al. 2007), a single or multiple absorption features at  $\mathcal{E} \simeq 0.2\text{--}1$  keV have been detected from several sources (see van Kerkwijk & Kaplan 2007): e.g., 1E 1207.4–5209 (0.7 and 1.4 keV, possibly also 2.1, 2.8 keV; Sanwal et al. 2002; De Luca et al. 2004; Mori et al. 2005), RX J1308.6+2127 (0.2–0.3 keV; Haberl et al. 2003), RX J1605.3+3249 (0.45 keV; van

Kerkwijk et al. 2004), RX J0720.4–3125 (0.27 keV; Haberl et al. 2006), and possibly RBS 1774 ( $\sim 0.7$  keV; Zane et al. 2005). The identifications of these features, however, remain uncertain, with suggestions ranging from proton cyclotron lines to atomic transitions of H, He, or mid-Z atoms in a strong magnetic field (see Sanwal et al. 2002; Ho & Lai 2004; Pavlov & Bezchastnov 2005; Mori & Ho 2007). Clearly, understanding these absorption lines is very important as it would lead to direct measurement of the NS surface magnetic fields and compositions, shedding light on the nature of these objects. Multiple lines also have the potential of constraining the mass-radius relation of NSs (through measurement of gravitational redshift).

Since the thermal radiation from a NS is mediated by its atmosphere (if  $T$  is sufficiently high so that the surface does not condense into a solid; see, e.g., van Adelsberg et al. 2005; Medin & Lai 2006b, 2007), detailed modelling of radiative transfer in magnetized NS atmospheres is important. The atmosphere composition of the NS is unknown *a priori*. Because of the efficient gravitational separation of light and heavy elements, a pure H atmosphere is expected even if a small amount of fallback or accretion occurs after NS formation. A pure He atmosphere results if H is completely burnt out, and a heavy-element (e.g., Fe) atmosphere may be possible if no fallback/accretion occurs. The atmosphere composition may also be affected by (slow) diffusive nuclear burning in the outer NS envelope (Chang, Arras & Bildsten 2004), as well as by the bombardment on the surface by fast particles from NS magnetospheres (e.g., Beloborodov & Thompson 2007). Fully ionized atmosphere models in various magnetic field regimes have been extensively studied (e.g., Shibano et al. 1992; Zane et al. 2001; Ho & Lai 2001), including the effect of vacuum polarization (see Ho & Lai 2003; Lai & Ho 2002, 2003; van Adelsberg & Lai 2006). Because a strong magnetic field greatly increases the binding energies of atoms, molecules, and other bound species (for a review, see Lai 2001), these

bound states may have appreciable abundances in the NS atmosphere, as guessed by Cohen, Lodenquai, & Ruderman (1970) and confirmed by calculations of Lai & Salpeter (1997) and Potekhin, Chabrier & Shibano (1999). Early considerations of partially ionized and strongly magnetized atmospheres (e.g., Rajagopal, Romani & Miller 1997) relied on oversimplified treatments of atomic physics and plasma thermodynamics (ionization equilibrium, equation of state, and nonideal plasma effects). Recently, a thermodynamically consistent equation of state and opacities for magnetized ( $B = 10^{12} - 10^{15}$  G), partially ionized H plasma have been obtained (Potekhin & Chabrier 2003, 2004), and the effect of bound atoms on the dielectric tensor of the plasma has also been studied (Potekhin et al. 2004). These improvements have been incorporated into partially ionized, magnetic NS atmosphere models (Ho et al. 2003, 2007; Potekhin et al. 2004, 2006). Mid- $Z$  element atmospheres for  $B \sim 10^{12} - 10^{13}$  G were recently studied by Mori & Ho (2007).

In this chapter we focus on He atoms and their radiative transitions in magnetic NS atmospheres. It is well known that for  $B \gg Z^2 B_0$ , where  $Z$  is the charge number of the nucleus and  $B_0 = e^3 m_e^2 / \hbar^3 c = 2.35 \times 10^9$  G, the binding energy of an atom is significantly increased over its zero-field value. In this *strong-field regime* the electrons are confined to the ground Landau level, and one may apply the *adiabatic approximation*, in which electron motions along and across the field are assumed to be decoupled from each other (see Sect. 4.2.1). Using this approximation in combination with the Hartree–Fock method (“1DHF approximation”), several groups calculated binding energies for the helium atom (Pröschel et al. 1982; Thurner et al. 1993) and also for some other atoms and molecules (Neuhauser, Langanke & Koonin 1986; Neuhauser, Koonin & Langanke 1987; Miller & Neuhauser 1991; Lai et al. 1992). Mori & Hailey (2002) developed a “multiconfigurational perturbative hybrid Hartree–Fock” approach, which is a perturbative improvement of the

1DHF method. Other methods of calculation include Thomas–Fermi-like models (e.g., Abrahams & Shapiro 1991), the density functional theory (e.g., Relovsky & Ruder 1996; Medin & Lai 2006a), variational methods (e.g., Müller 1984; Vincke & Baye 1989; Jones et al. 1999; Turbinder & Guevara 2006), and 2D Hartree–Fock mesh calculations (Ivanov 1994; Ivanov & Schmelcher 2000) which do not directly employ the adiabatic approximation.

In strong magnetic fields, the finite nuclear mass and center-of-mass motion affect the atomic structure in a nontrivial way (e.g., Lai 2001; see Sect. 4.5). The stronger  $B$  is, the more important the effects of finite nuclear mass are. Apart from the H atom, these effects have been calculated only for the He atom which *rests as a whole*, but has a moving nucleus (Al-Hujaj & Schmelcher 2003a,b), and for the  $\text{He}^+$  ion (Bezchastnov, Pavlov & Ventura 1998; Pavlov & Bezchastnov 2005).

There were relatively few publications devoted to radiative transitions of non-hydrogenic atoms in strong magnetic fields. Several authors (Miller & Neuhauser 1991; Thurner et al. 1993; Jones et al. 1999; Mori & Hailey 2002; Al-Hujaj & Schmelcher 2003b) calculated oscillator strengths for bound-bound transitions; Miller & Neuhauser (1991) presented also a few integrated bound-free oscillator strengths. Rajagopal et al. (1997) calculated opacities of strongly magnetized iron, using photoionization cross sections obtained by M. C. Miller (unpublished). To the best of our knowledge, there were no published calculations of polarization-dependent photoionization cross sections for the He atom in the strong-field regime, as well as the calculations of the atomic motion effect on the photoabsorption coefficients for He in this regime. Moreover, the subtle effect of exchange interaction involving free electrons and the possible role of two-electron transitions (see Sect. 4.3.2) were not discussed before.

In this chapter we perform detailed calculations of radiative transitions of the He atom using the 1DHF approximation. The total error introduced into our calculations by the use of these two approximations, the Hartree-Fock method and the adiabatic approximation, is of order 1% or less, as can be seen by the following considerations: The Hartree-Fock method is approximate because electron correlations are neglected. Due to their mutual repulsion, any pair of electrons tend to be more distant from each other than the Hartree-Fock wave function would indicate. In zero-field, this correlation effect is especially pronounced for the spin-singlet states of electrons for which the spatial wave function is symmetrical. In strong magnetic fields ( $B \gg B_0$ ), the electron spins (in the ground state) are all aligned antiparallel to the magnetic field, and the multielectron spatial wave function is antisymmetric with respect to the interchange of two electrons. Thus the error in the Hartree-Fock approach is expected to be less than the 1% accuracy characteristic of zero-field Hartree-Fock calculations (Neuhauser et al. 1987; Schmelcher, Ivanov & Becken 1999; for  $B = 0$  see Scrinzi 1998). The adiabatic approximation is also very accurate at  $B \gg Z^2 B_0$ . Indeed, a comparison of the ground-state energy values calculated here to those of Ivanov (1994) (who did not use the adiabatic approximation) shows an agreement to within 1% for  $B = 10^{12}$  G and to within 0.1% for  $B = 10^{13}$  G.

The chapter is organized as follows. Section 4.2 describes our calculations of the bound states and continuum states of the He atom, and section 4.3 contains relevant equations for radiative transitions. We present our numerical results and fitting formulae in section 4.4 and examine the effects of finite nucleus mass on the photoabsorption cross sections in section 4.5.

This chapter is based on the published paper by Medin, Lai, & Potekhin 2008

[Medin Z., Lai D., Potekhin A., 2008, Monthly Notices of the Royal Astronomical Society, 383, 161; ©2008. Blackwell Publishing. All rights reserved]. It is reprinted here with minor changes, based on rights retained by the author.

## 4.2 Bound states and singly-ionized states of helium atoms in strong magnetic fields

### 4.2.1 Bound states of the helium atom

To define the notation, we briefly describe 1DHF calculations for He atoms in strong magnetic fields. Each electron in the atom is described by a one-electron wave function (orbital). If the magnetic field is sufficiently strong (e.g.,  $B \gg 10^{10}$  G for He ground state), the motion of an electron perpendicular to the magnetic field lines is mainly governed by the Lorentz force, which is, on the average, stronger than the Coulomb force. In this case, the adiabatic approximation can be employed – i.e., the wave function can be separated into a transverse (perpendicular to the external magnetic field) component and a longitudinal (along the magnetic field) component:

$$\phi_{m\nu}(\mathbf{r}) = f_{m\nu}(z)W_m(\mathbf{r}_\perp). \quad (4.1)$$

Here  $W_m$  is the ground-state Landau wave function (e.g., Landau & Lifshitz 1977) given by

$$W_m(\mathbf{r}_\perp) = \frac{1}{\rho_0 \sqrt{2\pi m!}} \left( \frac{\rho}{\sqrt{2}\rho_0} \right)^m \exp \left( \frac{-\rho^2}{4\rho_0^2} \right) e^{-im\varphi}, \quad (4.2)$$

where  $(\rho, \varphi)$  are the polar coordinates of  $\mathbf{r}_\perp$ ,  $\rho_0 = (\hbar c/eB)^{1/2}$  is the magnetic length and  $f_{m\nu}$  is the longitudinal wave function which can be calculated numerically. The quantum number  $m$  ( $\geq 0$  for the considered ground Landau state) specifies the



*negative* of the  $z$ -projection of the electron orbital angular momentum. We restrict our consideration to electrons in the ground Landau level; for these electrons,  $m$  specifies also the (transverse) distance of the guiding center of the electron from the ion,  $\rho_m = (2m + 1)^{1/2}\rho_0$ . The quantum number  $\nu$  specifies the number of nodes in the longitudinal wave function. The spins of the electrons are taken to be aligned anti-parallel with the magnetic field, and so do not enter into any of our equations. In addition, we assume that the ion is completely stationary (the ‘infinite ion mass’ approximation). In general, the latter assumption is not necessary for the applicability of the adiabatic approximation (see, e.g., Potekhin 1994). The accuracy of the infinite ion mass approximation will be discussed in Sect. 4.5.

Note that we use non-relativistic quantum mechanics in our calculations, even when  $\hbar\omega_{Be} \gtrsim m_e c^2$  or  $B \gtrsim B_Q = B_0/\alpha^2 = 4.414 \times 10^{13}$  G (where  $\alpha = e^2/(\hbar c)$  is the fine structure constant). This is valid for two reasons: (i) The free-electron energy in relativistic theory is

$$\mathcal{E} = \left[ c^2 p_z^2 + m_e^2 c^4 \left( 1 + 2n_L \frac{B}{B_Q} \right) \right]^{1/2}. \quad (4.3)$$

For electrons in the ground Landau level ( $n_L = 0$ ), Eq. (4.3) reduces to  $\mathcal{E} \simeq m_e c^2 + p_z^2/(2m_e)$  for  $p_z c \ll m_e c^2$ ; the electron remains non-relativistic in the  $z$  direction as long as the electron energy is much less than  $m_e c^2$ ; (ii) it is well known (e.g., Sokolov & Ternov 1986) that Eq. (4.2) describes the transverse motion of an electron with  $n_L = 0$  at any field strength, and thus Eq. (4.2) is valid in the relativistic theory. Our calculations assume that the longitudinal motion of the electron is non-relativistic. This is valid for helium at all field strengths considered in this chapter. Thus relativistic corrections to our calculated electron wave functions, binding energies, and transition cross sections are all small. Our approximation is justified in part by Chen & Goldman (1992), who find that the

relativistic corrections to the binding energy of the hydrogen atom are of order  $\Delta\mathcal{E}/\mathcal{E} \sim 10^{-5.5} - 10^{-4.5}$  for the range of field strengths we are considering in this work ( $B = 10^{12} - 10^{14}$  G).

A bound state of the He atom, in which one electron occupies the  $(m_1\nu_1)$  orbital, and the other occupies the  $(m_2\nu_2)$  orbital, is denoted by  $|m_1\nu_1, m_2\nu_2\rangle = |W_{m_1}f_{m_1\nu_1}, W_{m_2}f_{m_2\nu_2}\rangle$  (clearly,  $|m_1\nu_1, m_2\nu_2\rangle = |m_2\nu_2, m_1\nu_1\rangle$ ). The two-electron wave function is

$$\begin{aligned} \Psi_{m_1\nu_1, m_2\nu_2}(\mathbf{r}_1, \mathbf{r}_2) = & \frac{1}{\sqrt{2}} [W_{m_1}(\mathbf{r}_{1\perp}) f_{m_1\nu_1}(z_1) \\ & \times W_{m_2}(\mathbf{r}_{2\perp}) f_{m_2\nu_2}(z_2) \\ & - W_{m_2}(\mathbf{r}_{1\perp}) f_{m_2\nu_2}(z_1) W_{m_1}(\mathbf{r}_{2\perp}) f_{m_1\nu_1}(z_2)] . \end{aligned} \quad (4.4)$$

The one-electron wave functions are found using Hartree–Fock theory, by varying the total energy with respect to the wave functions. The total energy is given by (see, e.g., Neuhauser et al. 1987):

$$\mathcal{E} = \mathcal{E}_K + \mathcal{E}_{eZ} + \mathcal{E}_{\text{dir}} + \mathcal{E}_{\text{exc}} , \quad (4.5)$$

where

$$\mathcal{E}_K = \frac{\hbar^2}{2m_e} \sum_{m\nu} \int dz |f'_{m\nu}(z)|^2 , \quad (4.6)$$

$$\mathcal{E}_{eZ} = -Ze^2 \sum_{m\nu} \int dz |f_{m\nu}(z)|^2 V_m(z) , \quad (4.7)$$

$$\begin{aligned} \mathcal{E}_{\text{dir}} = & \frac{e^2}{2} \sum_{m\nu, m'\nu'} \iint dz dz' |f_{m\nu}(z)|^2 |f_{m'\nu'}(z')|^2 \\ & \times D_{mm'}(z - z') , \end{aligned} \quad (4.8)$$

$$\begin{aligned} \mathcal{E}_{\text{exc}} = & -\frac{e^2}{2} \sum_{m\nu, m'\nu'} \iint dz dz' f_{m'\nu'}^*(z) f_{m\nu}(z) \\ & \times f_{m\nu}^*(z') f_{m'\nu'}(z') \mathcal{E}_{mm'}(z - z') ; \end{aligned} \quad (4.9)$$

and

$$V_m(z) = \int d\mathbf{r}_\perp \frac{|W_m(\mathbf{r}_\perp)|^2}{\mathbf{r}} , \quad (4.10)$$

$$D_{mm'}(z - z') = \iint d\mathbf{r}_\perp d\mathbf{r}'_\perp \frac{|W_m(\mathbf{r}_\perp)|^2 |W_{m'}(\mathbf{r}'_\perp)|^2}{|\mathbf{r}' - \mathbf{r}|}, \quad (4.11)$$

$$\begin{aligned} \mathcal{E}_{mm'}(z - z') &= \iint d\mathbf{r}_\perp d\mathbf{r}'_\perp \frac{1}{|\mathbf{r}' - \mathbf{r}|} \\ &\times W_{m'}^*(\mathbf{r}_\perp) W_m(\mathbf{r}_\perp) W_m^*(\mathbf{r}'_\perp) W_{m'}(\mathbf{r}'_\perp). \end{aligned} \quad (4.12)$$

Variation of Eq. (4.5) with respect to  $f_{m\nu}(z)$  yields

$$\begin{aligned} &\left[ -\frac{\hbar^2}{2m_e} \frac{d^2}{dz^2} - Ze^2 V_m(z) \right. \\ &\quad \left. + e^2 \sum_{m'\nu'} \int dz' |f_{m'\nu'}(z')|^2 D_{mm'}(z - z') - \varepsilon_{m\nu} \right] f_{m\nu}(z) \\ &= e^2 \sum_{m'\nu'} \int dz' f_{m\nu}^*(z') f_{m'\nu'}(z') \mathcal{E}_{mm'}(z - z') f_{m'\nu'}(z). \end{aligned} \quad (4.13)$$

In these equations, asterisks denote complex conjugates, and  $f'_{m\nu}(z) \equiv df_{m\nu}/dz$ . The wave functions  $f_{m\nu}(z)$  must satisfy appropriate boundary conditions, i.e.,  $f_{m\nu} \rightarrow 0$  as  $z \rightarrow \pm\infty$ , and must have the required symmetry [ $f_{m\nu}(z) = \pm f_{m\nu}(-z)$ ] and the required number of nodes ( $\nu$ ). The equations are solved iteratively until self-consistency is reached for each wave function  $f_{m\nu}$  and energy  $\varepsilon_{m\nu}$ . The total energy of the bound He state  $|m_1\nu_1, m_2\nu_2\rangle$  can then be found, using either Eq. (4.5) or

$$\mathcal{E} = \sum_{m\nu} \varepsilon_{m\nu} - \mathcal{E}_{\text{dir}} - \mathcal{E}_{\text{exc}}. \quad (4.14)$$

### 4.2.2 Continuum states of the helium atom

The He state in which one electron occupies the bound ( $m_3\nu_3$ ) orbital, and other occupies the continuum state ( $m_4k$ ) is denoted by  $|m_3\nu_3, m_4k\rangle = |W_{m_3}f_{m_3\nu_3}, W_{m_4}f_{m_4k}\rangle$ . The corresponding two-electron wave function is

$$\Psi_{m_3\nu_3, m_4k}(\mathbf{r}_1, \mathbf{r}_2) = \frac{1}{\sqrt{2}} [W_{m_3}(\mathbf{r}_{1\perp}) f_{m_3\nu_3}(z_1)$$

$$\begin{aligned} & \times W_{m_4}(\mathbf{r}_{2\perp}) f_{m_4 k}(z_2) \\ & - W_{m_4}(\mathbf{r}_{1\perp}) f_{m_4 k}(z_1) W_{m_3}(\mathbf{r}_{2\perp}) f_{m_3 \nu_3}(z_2) \Big]. \end{aligned} \quad (4.15)$$

Here  $f_{m_4 k}(z)$  is the longitudinal wave function of the continuum electron, and  $k$  is the  $z$ -wavenumber of the electron at  $|z| \rightarrow \infty$  (far away from the He nucleus).

We can use Hartree–Fock theory to solve for the ionized He states as we did for the bound He states. Since the continuum electron wave function  $f_{m_4 k}(z)$  is non-localized in  $z$ , while the bound electron wave function  $f_{m_3 \nu_3}(z)$  is localized around  $z = 0$ , it is a good approximation to neglect the continuum electron’s influence on the bound electron. We therefore solve for the bound electron orbital using the equation

$$\left[ -\frac{\hbar^2}{2m_e} \frac{d^2}{dz^2} - Ze^2 V_{m_3}(z) \right] f_{m_3 \nu_3}(z) = \varepsilon_{m_3 \nu_3} f_{m_3 \nu_3}(z). \quad (4.16)$$

The continuum electron, however, is influenced by the bound electron, and its longitudinal wave function is determined from

$$\begin{aligned} & \left[ -\frac{\hbar^2}{2m_e} \frac{d^2}{dz^2} - Ze^2 V_{m_4}(z) \right. \\ & \quad \left. + e^2 \int dz' |f_{m_3 \nu_3}(z')|^2 D_{m_3 m_4}(z - z') - \varepsilon_f \right] f_{m_4 k}(z) \\ & = e^2 \int dz' f_{m_4 k}^*(z') f_{m_3 \nu_3}(z') \mathcal{E}_{m_3 m_4}(z - z') f_{m_3 \nu_4}(z). \end{aligned} \quad (4.17)$$

where  $\varepsilon_f = \varepsilon_{m_4 k} = \hbar^2 k^2 / (2m_e)$ . Here, the bound electron orbital  $|m_3 \nu_3\rangle$  satisfies the same boundary conditions as discussed in Sect. 4.2.1. The shape of the free electron wave function is determined by the energy of the incoming photon and the direction the electron is emitted from the ion. We will discuss this boundary condition in the next section. The total energy of the ionized He state  $|m_3 \nu_3, m_4 k\rangle$  is simply

$$\mathcal{E} = \varepsilon_{m_3 \nu_3} + \varepsilon_f. \quad (4.18)$$

Note that the correction terms  $\mathcal{E}_{\text{dir}}$  and  $\mathcal{E}_{\text{exc}}$  that appear in Eq. (4.14) do not also appear in Eq. (4.18). The direct and exchange energies depend on the local overlap of the electron wave functions, but the non-localized nature of the free electron ensures that these terms are zero for the continuum states.

### 4.3 Radiative transitions

We will be considering transitions of helium atoms from two initial states: the ground state,  $|00, 10\rangle$ , and the first excited state,  $|00, 20\rangle$ .

In the approximation of an infinitely massive, pointlike nucleus, the Hamiltonian of the He atom in electromagnetic field is (see, e.g., Landau & Lifshitz 1977)

$$H = \sum_{j=1,2} \frac{1}{2m_e} \left( \mathbf{p}_j + \frac{e}{c} \mathbf{A}_{\text{tot}}(\mathbf{r}_j) \right)^2 - \sum_{j=1,2} \frac{2e^2}{r_j^2} + \frac{e^2}{|\mathbf{r}_1 - \mathbf{r}_2|}, \quad (4.19)$$

where  $\mathbf{p}_j = -i\hbar\nabla_j$  is the canonical momentum operator, acting on the  $j$ th electron,  $\mathbf{r}_j$  is the  $j$ th electron radius vector, measured from the nucleus, and  $\mathbf{A}_{\text{tot}}(\mathbf{r})$  is the vector potential of the field. In our case,  $\mathbf{A}_{\text{tot}}(\mathbf{r}) = \mathbf{A}_B(\mathbf{r}) + \mathbf{A}_{\text{em}}(\mathbf{r})$ , where  $\mathbf{A}_B(\mathbf{r})$  and  $\mathbf{A}_{\text{em}}(\mathbf{r})$  are vector potentials of the stationary magnetic field and electromagnetic wave, respectively. The interaction operator is  $H_{\text{int}} = H - H_0$ , where  $H_0$  is obtained from  $H$  by setting  $\mathbf{A}_{\text{em}}(\mathbf{r}) = 0$ . The unperturbed Hamiltonian  $H_0$  is responsible for the stationary states of He, discussed in Sect. 4.2. The vector potential and the wave functions may be subject to gauge transformations; the wave functions presented in Sect. 4.2 correspond to the cylindrical gauge  $\mathbf{A}_B(\mathbf{r}) = \frac{1}{2}\mathbf{B} \times \mathbf{r}$ . Neglecting non-linear (quadratic in  $A_{\text{em}}$ ) term, we have

$$H_{\text{int}} \approx \frac{e}{2m_e c} \sum_{j=1,2} [\pi_j \cdot \mathbf{A}_{\text{em}}(\mathbf{r}_j) + \mathbf{A}_{\text{em}}(\mathbf{r}_j) \cdot \pi_j], \quad (4.20)$$

where

$$\pi = \mathbf{p} + \frac{e}{c} \mathbf{A}_B(\mathbf{r}). \quad (4.21)$$

is the non-perturbed kinetic momentum operator:  $\pi = m_e \dot{\mathbf{r}} = m_e(i/\hbar)[H_0 \mathbf{r} - \mathbf{r} H_0]$ .

For a monochromatic wave of the form  $\mathbf{A}_{\text{em}}(\mathbf{r}) \propto \epsilon e^{i\mathbf{q}\cdot\mathbf{r}}$ , where  $\epsilon$  is the unit polarization vector, applying the Fermi's Golden Rule and assuming the transverse polarization ( $\epsilon \cdot \mathbf{q} = 0$ ), one obtains the following general formula for the cross section of absorption of radiation from a given initial state  $|a\rangle$  (see, e.g., Armstrong & Nicholls 1972):

$$\sigma(\omega, \epsilon) = \sum_b \frac{4\pi^2}{\omega c} \left| \epsilon \cdot \langle b | e^{i\mathbf{q}\cdot\mathbf{r}} \mathbf{j} | a \rangle \right|^2 \delta(\omega - \omega_{ba}), \quad (4.22)$$

where  $|b\rangle$  is the final state,  $\omega = qc$  is the photon frequency,  $\omega_{ba} = (\mathcal{E}_b - \mathcal{E}_a)/\hbar$ , and  $\mathbf{j}$  is the electric current operator. In our case,  $\mathbf{j} = (-e/m_e)(\pi_1 + \pi_2)$ .

We shall calculate the cross sections in the dipole approximation – i.e., drop  $e^{i\mathbf{q}\cdot\mathbf{r}}$  from Eq. (4.22). This approximation is sufficiently accurate for calculation of the total cross section as long as  $\hbar\omega \ll m_e c^2$  (cf., e.g., Potekhin & Pavlov 1993, 1997 for the case of H atom). In the dipole approximation, Eq. (4.22) can be written as

$$\sigma(\omega, \epsilon) = \sum_b \frac{2\pi^2 e^2}{m_e c} f_{ba} \delta(\omega - \omega_{ba}), \quad (4.23)$$

where

$$f_{ba} = \frac{2}{\hbar \omega_{ba} m_e} |\langle b | \epsilon \cdot \pi | a \rangle|^2 = \frac{2m_e \omega_{ba}}{\hbar} |\langle b | \epsilon \cdot \mathbf{r} | a \rangle|^2 \quad (4.24)$$

is the oscillator strength. In the second equality we have passed from the ‘velocity form’ to the ‘length form’ of the matrix element (cf., e.g., Chandrasekhar 1945). These representations are identical for the exact wave functions, but it is not so for approximate ones. In the adiabatic approximation, the length representation [i.e., the right-hand side of Eq. (4.24)] is preferable (see Potekhin & Pavlov 1993; Potekhin, Pavlov, & Ventura 1997).

To evaluate the matrix element, we decompose the unit polarization vector  $\epsilon$  into three cyclic components,

$$\epsilon = \epsilon_- \hat{\mathbf{e}}_+ + \epsilon_+ \hat{\mathbf{e}}_- + \epsilon_0 \hat{\mathbf{e}}_0, \quad (4.25)$$

with  $\hat{\mathbf{e}}_0 = \hat{\mathbf{e}}_z$  along the external magnetic field direction (the z-axis),  $\hat{\mathbf{e}}_{\pm} = (\hat{\mathbf{e}}_x \pm i\hat{\mathbf{e}}_y)/\sqrt{2}$ , and  $\epsilon_{\lambda} = \hat{\mathbf{e}}_{\lambda} \cdot \epsilon$  (with  $\lambda = \pm, 0$ ). Then we can write the cross section as the sum of three components,

$$\sigma(\omega, \epsilon) = \sigma_+(\omega) |\epsilon_+|^2 + \sigma_-(\omega) |\epsilon_-|^2 + \sigma_0(\omega) |\epsilon_0|^2, \quad (4.26)$$

where  $\sigma_{\lambda}$  has the same form as Eq. (4.23), with the corresponding oscillator strength given by

$$f_{ba}^{\lambda} = \frac{2m_e \omega_{ba} \rho_0^2}{\hbar} |M_{ba}|^2 = \frac{2\omega_{ba}}{\omega_{Be}} |M_{ba}|^2, \quad (4.27)$$

with

$$M_{ba} = \langle b | \hat{\mathbf{e}}_{\lambda}^* \cdot \bar{\mathbf{r}} | a \rangle, \quad (4.28)$$

where  $\bar{\mathbf{r}} = \mathbf{r}/\rho_0$  and  $\omega_{Be} = eB/(m_e c)$  is the electron cyclotron frequency.

### 4.3.1 Bound-bound transitions

Consider the electronic transition

$$\begin{aligned} |a\rangle &= |m\nu, m_2\nu_2\rangle = |W_m f_{m\nu}, W_{m_2} f_{m_2\nu_2}\rangle \\ \longrightarrow |b\rangle &= |m'\nu', m_2\nu_2\rangle = |W_{m'} g_{m'\nu'}, W_{m_2} g_{m_2\nu_2}\rangle. \end{aligned} \quad (4.29)$$

The selection rules for allowed transitions and the related matrix elements are

$$\begin{aligned} \sigma_0 : \quad \Delta m &= 0, \quad \Delta\nu = \text{odd}, \\ M_{ba} &= \langle g_{m\nu'} | \bar{z} | f_{m\nu} \rangle \langle g_{m_2\nu_2} | f_{m_2\nu_2} \rangle, \end{aligned} \quad (4.30)$$

$$\begin{aligned}\sigma_+ : \quad \Delta m = 1, \Delta \nu = \text{even}, \\ M_{ba} = \sqrt{m+1} \langle g_{m'\nu'} | f_{m\nu} \rangle \langle g_{m_2\nu_2} | f_{m_2\nu_2} \rangle,\end{aligned}\tag{4.31}$$

$$\begin{aligned}\sigma_- : \quad \Delta m = -1, \Delta \nu = \text{even}, \\ M_{ba} = \sqrt{m} \langle g_{m'\nu'} | f_{m\nu} \rangle \langle g_{m_2\nu_2} | f_{m_2\nu_2} \rangle,\end{aligned}\tag{4.32}$$

where  $\Delta m = m' - m$ ,  $\Delta \nu = \nu' - \nu$ . The oscillator strengths for bound-bound transitions from the states  $|00, 10\rangle$  and  $|00, 20\rangle$  are given in Table 4.1.

The selection rules (4.30)–(4.32) are exact in the dipole approximation. The selection rules in  $m$  follow from the conservation of the  $z$ -projection of total (for the photon and two electrons) angular momentum. Technically, in the adiabatic approximation, they follow from the properties of the Landau functions (e.g., Potekhin & Pavlov 1993). The selection rules in  $\nu$  follow from the fact that the functions  $g_{m'\nu'}$  and  $f_{m\nu}$  have the same parity for even  $\nu' - \nu$  and opposite parity for odd  $\nu' - \nu$ .

In addition to these selection rules, there are approximate selection rules which rely on the approximate orthogonality of functions  $g_{m'\nu'}$  and  $f_{m\nu}$  (for general  $\nu \neq \nu'$ ). Because of this approximate orthogonality, which holds better the larger  $B$  is, we have

$$\langle g_{m'\nu'} | f_{m\nu} \rangle \langle g_{m_2\nu_2} | f_{m_2\nu_2} \rangle = \delta_{\nu,\nu'} + \varepsilon,\tag{4.33}$$

where  $|\varepsilon| \ll 1$  and  $\varepsilon \rightarrow 0$  as  $\Delta \nu \rightarrow \pm\infty$ . Therefore, the oscillator strengths for transitions with  $\lambda = \pm$  and  $\Delta \nu = 2, 4, \dots$  are small compared to those with  $\Delta \nu = 0$ . The latter oscillator strengths can be approximated, according to Eqs. (4.27), (4.31), (4.32) and (4.33), by

$$f_{ba}^+ \approx 2(m+1) \omega_{ba} / \omega_{Be}, \quad f_{ba}^- \approx 2m \omega_{ba} / \omega_{Be}\tag{4.34}$$

( $\lambda = \Delta m = \pm 1$ ,  $\nu' = \nu$ ).



The same approximate orthogonality leads to the smallness of matrix elements for transitions of the type  $|m\nu, m_2\nu_2\rangle \longrightarrow |m'\nu', m_2\nu'_2\rangle$  with  $\nu'_2 \neq \nu_2$  for  $\lambda = \pm$  and the smallness of cross terms in the matrix elements of the form  $\langle g_{m_2\nu_2} | f_{m\nu} \rangle \langle g_{m'\nu'} | f_{m_2\nu_2} \rangle$  when  $m' = m_2$  (i.e., the so-called “one-electron jump rule”); we have therefore excluded such terms from the selection rule equations above [Eqs. (4.30)–(4.32)].

### 4.3.2 Photoionization

The bound-free absorption cross section for the transition from the bound state  $|b\rangle$  to the continuum state  $|f\rangle$  is given by Eq. (4.22) with obvious substitutions  $|a\rangle \rightarrow |b\rangle$ ,  $|b\rangle \rightarrow |f\rangle$ , and

$$\sum_f \rightarrow (L_z/2\pi) \int_{-\infty}^{\infty} dk, \quad (4.35)$$

where  $L_z$  is the normalization length of the continuum electron  $[\int_{-L_z/2}^{L_z/2} dz |g_{mk}(z)|^2 = 1]$  and  $k$  is the wave number of the outgoing electron (Sect. 4.2.2). Therefore we have

$$\begin{aligned} \sigma_{\text{bf}}(\omega, \epsilon) = \frac{2\pi e^2 L_z}{m_e c \hbar^2 \omega_{fb} k} \Big\{ & \left| \langle f_k | e^{i\mathbf{q}\cdot\mathbf{r}} \epsilon \cdot \pi | b \rangle \right|^2 \\ & + \left| \langle f_{-k} | e^{i\mathbf{q}\cdot\mathbf{r}} \epsilon \cdot \pi | b \rangle \right|^2 \Big\}, \end{aligned} \quad (4.36)$$

where  $k = \sqrt{2m_e \epsilon_f}/\hbar$  and  $|f_{\pm k}\rangle$  represents the final state where the free electron has wave number  $\pm k$  (here and hereafter we assume  $k > 0$ ). The asymptotic conditions for these outgoing free electrons are (cf., e.g., Potekhin et al. 1997)  $g_{mk}(z) \sim \exp[i\varphi_k(z)]$  at  $z \rightarrow \pm\infty$ , where  $\varphi_k(z) = |kz| + (ka_0)^{-1} \ln |kz|$  and  $a_0 = \hbar^2/m_e e^2$  is the Bohr radius. Since we do not care about direction of the outgoing electron, we can use for calculations a basis of symmetric and antisymmetric wave functions of the continuum – that is, in Eq. (4.36) we can replace

$\langle f_k |$  and  $\langle f_{-k} |$  by  $\langle f_{\text{even}} |$  and  $\langle f_{\text{odd}} |$ . The symmetric state  $|f_{\text{even}}\rangle$  is determined by the free electron boundary condition  $g'_{mk,\text{even}}(0) = 0$  and the antisymmetric state  $|f_{\text{odd}}\rangle$  is determined by  $g_{mk,\text{odd}}(0) = 0$ . Since the coefficients in Eq. (4.17) are real,  $g_{mk,\text{even}}(z)$  and  $g_{mk,\text{odd}}(z)$  can be chosen real. At  $z \rightarrow \pm\infty$ , they behave as  $g_{mk,(\text{even},\text{odd})}(z) \sim \sin[\varphi(z) + \text{constant}]$  (where the value of constant depends on all quantum numbers, including  $k$ ). We still have the normalization  $\int_{-L_z/2}^{L_z/2} dz |g_{mk,(\text{even},\text{odd})}(z)|^2 = 1$ .

Similar to bound-bound transitions, we can decompose the bound-free cross section into three components, Eq. (4.26). Thus, using the dipole approximation and the length form of the matrix elements, as discussed above, we have for  $(\lambda = \pm, 0)$ -components of the bound-free cross section

$$\begin{aligned} \sigma_{\text{bf},\lambda}(\omega) = \frac{3}{4} \sigma_{\text{Th}} \left( \frac{m_e c^2}{\hbar \omega} \right)^3 \sqrt{\frac{m_e c^2}{2\varepsilon_f}} \left( \frac{L_z a_0}{\rho_0^2} \right) \left( \frac{\omega \rho_0}{c} \right)^4 \\ \times |\langle f | \hat{\mathbf{e}}_\lambda^* \cdot \mathbf{r} | b \rangle|^2, \end{aligned} \quad (4.37)$$

where  $|f\rangle = |f_{\text{even}}\rangle$  or  $|f\rangle = |f_{\text{odd}}\rangle$  depending on the parity of the initial state and according to the selection rules, and  $\sigma_{\text{Th}} = (8\pi/3) (e^2/m_e c^2)^2$  is the Thomson cross section. The selection rules and related matrix elements for the bound-free transitions

$$\begin{aligned} |b\rangle = |m\nu, m_2\nu_2\rangle = |W_m f_{m\nu}, W_{m_2} f_{m_2\nu_2}\rangle \\ \longrightarrow |f\rangle = |m'k, m_2\nu_2\rangle = |W_{m'} g_{m'k}, W_{m_2} g_{m_2\nu_2}\rangle \end{aligned} \quad (4.38)$$

are similar to those for the bound-bound transitions [see Eqs. (4.30)–(4.32)]:

$$\begin{aligned} \sigma_0 : \quad \Delta m = 0, \Delta\nu = \text{odd}, \\ M_{fb} = \langle g_{mk} | \bar{z} | f_{m\nu} \rangle \langle g_{m_2\nu_2} | f_{m_2\nu_2} \rangle, \\ \sigma_+ : \quad \Delta m = 1, \Delta\nu = \text{even}, \end{aligned} \quad (4.39)$$

$$M_{fb} = \sqrt{m+1} (\langle g_{m'k} | f_{m\nu} \rangle \langle g_{m_2\nu_2} | f_{m_2\nu_2} \rangle - \delta_{m'\nu, m_2\nu_2} \langle g_{m_2\nu_2} | f_{m\nu} \rangle \langle g_{m'k} | f_{m_2\nu_2} \rangle), \quad (4.40)$$

$$\sigma_- : \quad \Delta m = -1, \quad \Delta \nu = \text{even},$$

$$M_{fb} = \sqrt{m} (\langle g_{m'k} | f_{m\nu} \rangle \langle g_{m_2\nu_2} | f_{m_2\nu_2} \rangle - \delta_{m'\nu, m_2\nu_2} \langle g_{m_2\nu_2} | f_{m\nu} \rangle \langle g_{m'k} | f_{m_2\nu_2} \rangle), \quad (4.41)$$

In this case, the condition  $\Delta \nu = \text{odd}$  means that  $g_{m'k}$  and  $f_{m\nu}$  must have opposite parity, and the condition  $\Delta \nu = \text{even}$  means that  $g_{m'k}$  and  $f_{m\nu}$  must have the same parity. The oscillator strengths for bound-free transitions from the states  $|00, 10\rangle$  and  $|00, 20\rangle$  are given in Table 4.2.

Note that in Eqs. (4.40) and (4.41), the second term in the matrix element (of the form  $\langle g_{m_2\nu_2} | f_{m\nu} \rangle \langle g_{m'k} | f_{m_2\nu_2} \rangle$ ) corresponds to transitions of both electrons. This appears to violate the “one-electron jump rule” and other approximate selection rules discussed in Sect. 4.3.1 [see Eq. (4.33)]. In fact, these approximate rules are not directly relevant for bound-free transitions, since the matrix elements involving a continuum state are always small:  $\langle g_{m'k} | f_{m\nu} \rangle \rightarrow 0$  as the normalization length  $L_z \rightarrow \infty$ . Rather, we use a different set of selection rules to determine which of these ‘small’ matrix elements are smaller than the rest. The first is that

$$\langle g_{m'k} | f_{m\nu} \rangle \langle g_{m_2\nu_2} | f_{m_2\nu_2} \rangle \gg \langle g_{m'k} | f_{m\nu} \rangle \langle g_{m_2\nu'_2} | f_{m_2\nu_2} \rangle, \quad (4.42)$$

when  $\nu'_2 \neq \nu_2$ . This selection rule is similar to the bound-bound transition case as  $\langle g_{m_2\nu'_2} | f_{m_2\nu_2} \rangle$  involves a bound electron transition, not a free electron transition. The second approximate selection rule that applies here is more complicated: terms of the form  $\langle g_{m'\nu} | f_{m\nu} \rangle \langle g_{m_2k} | f_{m_2\nu_2} \rangle$  are small, unless  $m' = m_2$  and  $\nu_2 = \nu$ . This exception for  $m' = m_2$  and  $\nu_2 = \nu$  is due to the exchange term in the differential equation for the free electron wave function [Eq. (4.17)], which strongly

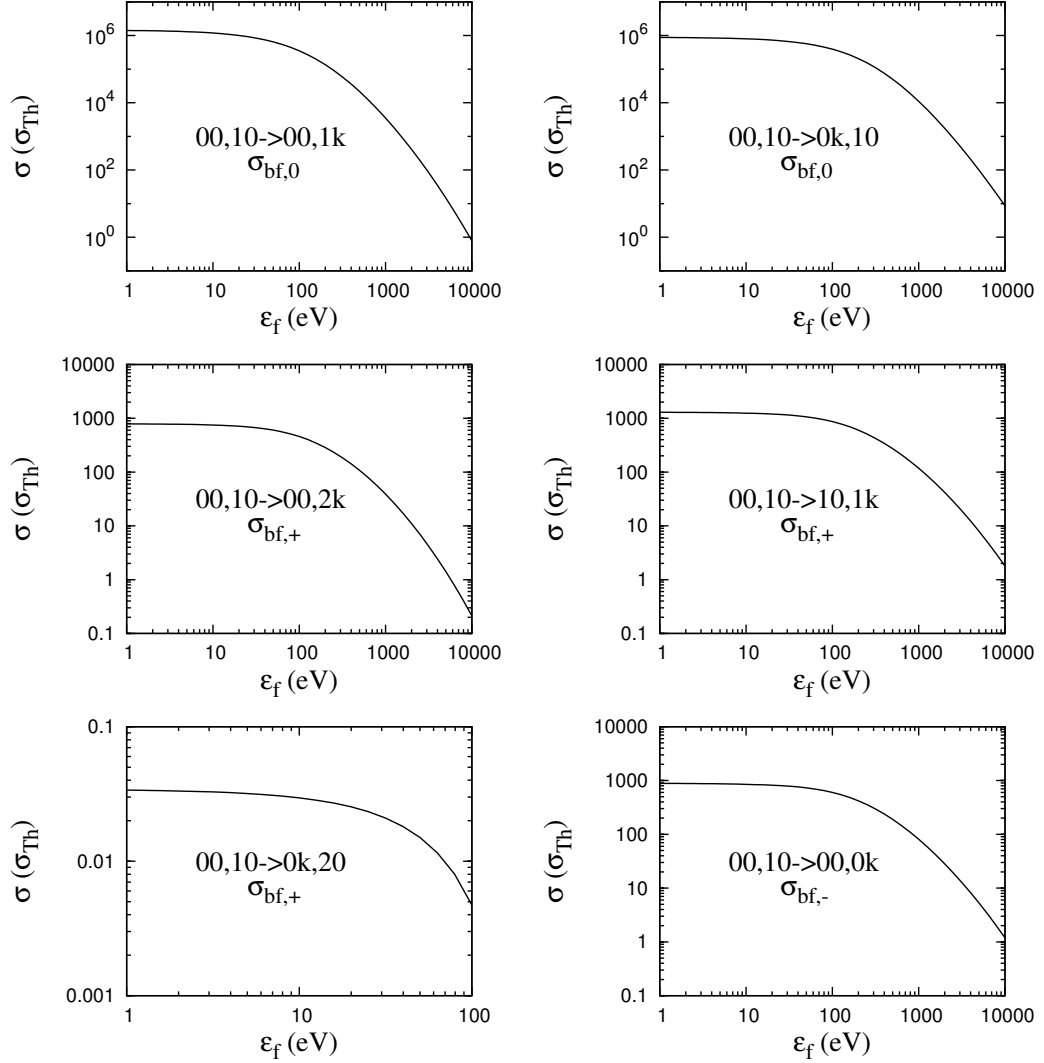


Figure 4.1: Partial cross sections  $\sigma_{(0,+,-)}$  versus final ionized electron energy for photoionization of the ground state helium atom ( $(m_1, m_2) = (1, 0)$ ). The field strength is  $10^{12}$  G. The transition  $|00, 10\rangle \rightarrow |0k, 20\rangle$  in the bottom left panel is an example of a ‘weak’ transition. We have ignored these transitions in our calculations of the total cross sections.

(anti)correlates the two final wave functions  $|g_{m'\nu}\rangle$  and  $|g_{m_2k}\rangle$ . If  $m' = m_2$  and  $\nu = \nu_2$ , then since  $\langle g_{m'\nu}|f_{m_2\nu_2}\rangle$  is not small (in fact, it is of order 1),  $\langle g_{m_2k}|f_{m_2\nu_2}\rangle$  will not be small but will be of the same order as other terms involving the free electron wave function. In particular, the second selection rule means, e.g., that the matrix element for the transition from  $|00, 10\rangle$  to  $|00, 0k\rangle$  is

$$M_{00,10\rightarrow 00,0k} = \langle g_{0k}|f_{10}\rangle\langle g_{00}|f_{00}\rangle - \langle g_{00}|f_{10}\rangle\langle g_{0k}|f_{00}\rangle, \quad (4.43)$$

where the second term is non-negligible, but that the matrix element for the transition from  $|00, 10\rangle$  to  $|0k, 20\rangle$ , which is

$$M_{00,10\rightarrow 0k,20} = \langle g_{20}|f_{10}\rangle\langle g_{0k}|f_{00}\rangle, \quad (4.44)$$

is small compared to the other matrix elements and can be ignored (see Fig. 4.1).

We make one final comment here about the effect of exchange interaction on the free electron state. If the exchange term [the right-hand side of Eq. (4.17)] is neglected in the calculation of the free electron wave function, then the cross terms (i.e., those involving two-electron transitions) in the matrix elements of Eqs. (4.40) and (4.41) are small and can be neglected. One then obtains approximate photoionization cross sections which are within a factor of two of the true values in most cases and much better for  $\sigma_0$  transitions. If the exchange term is included in Eq. (4.17) but the cross terms in the matrix elements are ignored, significant errors in the  $\sigma_{\pm}$  photoionization cross sections will result. To obtain reliable cross sections for all cases, both the exchange effect on the free electron and the contribution of two-electron transitions must be included.

Table 4.1: Bound-bound transitions  $|a\rangle \rightarrow |b\rangle$ : The photon energy  $\hbar\omega_{ba} = \mathcal{E}_b - \mathcal{E}_a$  (in eV) and the oscillator strength  $f_{ba}^\lambda$  for different polarization components  $\lambda$  [see Eq. (4.27)]. All transitions  $\Delta\nu \leq 1$  from the initial states  $|00, 10\rangle$  and  $|00, 20\rangle$  are listed, for several magnetic field strengths  $B_{12} = B/(10^{12} \text{ G})$ . The last two columns list the transition energies  $\hbar\omega_{ba}^*$  and oscillator strengths  $f_{ba}^*$ , corrected for the finite mass of the nucleus, according to Sect. 4.5.1.

$B_{12}$	$\sigma$	$ a\rangle$	$\rightarrow$	$ b\rangle$	$\hbar\omega_{ba}$	$f_{ba}$	$\hbar\omega_{ba}^*$	$f_{ba}^*$
1	0	$ 00, 10\rangle$	$\rightarrow$	$ 00, 11\rangle$	147.5	0.234	—	—
			$\rightarrow$	$ 10, 01\rangle$	271.8	0.124	—	—
			$\rightarrow$	$ 00, 20\rangle$	43.11	0.0147	44.70	0.0153
	0	$ 00, 20\rangle$	$\rightarrow$	$ 00, 21\rangle$	104.4	0.312	—	—
			$\rightarrow$	$ 20, 01\rangle$	277.7	0.115	—	—
			$\rightarrow$	$ 00, 30\rangle$	18.01	0.00930	19.60	0.0101
5	0	$ 00, 10\rangle$	$\rightarrow$	$ 00, 11\rangle$	256.2	0.127	—	—
			$\rightarrow$	$ 10, 01\rangle$	444.8	0.0603	—	—
			$\rightarrow$	$ 00, 20\rangle$	66.95	0.00459	74.89	0.00512
	0	$ 00, 20\rangle$	$\rightarrow$	$ 00, 21\rangle$	189.2	0.176	—	—
			$\rightarrow$	$ 20, 01\rangle$	455.0	0.0537	—	—
			$\rightarrow$	$ 00, 30\rangle$	28.94	0.00299	36.88	0.00381
10	0	$ 00, 10\rangle$	$\rightarrow$	$ 00, 11\rangle$	318.9	0.0974	—	—
			$\rightarrow$	$ 10, 01\rangle$	540.8	0.0457	—	—
			$\rightarrow$	$ 00, 20\rangle$	79.54	0.00273	95.42	0.00327
	0	$ 00, 20\rangle$	$\rightarrow$	$ 00, 21\rangle$	239.4	0.136	—	—
			$\rightarrow$	$ 20, 01\rangle$	553.3	0.0405	—	—
			$\rightarrow$	$ 00, 30\rangle$	34.84	0.00179	50.72	0.00261
50	0	$ 00, 10\rangle$	$\rightarrow$	$ 00, 11\rangle$	510.9	0.0557	—	—
			$\rightarrow$	$ 10, 01\rangle$	822.2	0.0266	—	—
			$\rightarrow$	$ 00, 20\rangle$	114.2	7.85e−4	193.6	0.00133
	0	$ 00, 20\rangle$	$\rightarrow$	$ 00, 21\rangle$	396.7	0.0776	—	—
			$\rightarrow$	$ 20, 01\rangle$	841.1	0.0235	—	—
			$\rightarrow$	$ 00, 30\rangle$	51.92	5.37e−4	131.3	0.00136
100	0	$ 00, 10\rangle$	$\rightarrow$	$ 00, 11\rangle$	616.4	0.0452	—	—
			$\rightarrow$	$ 10, 01\rangle$	971.4	0.0221	—	—
			$\rightarrow$	$ 00, 20\rangle$	131.4	4.52e−4	290.2	9.98e−4
	0	$ 00, 20\rangle$	$\rightarrow$	$ 00, 21\rangle$	485.0	0.0626	—	—
			$\rightarrow$	$ 20, 01\rangle$	993.4	0.0195	—	—
			$\rightarrow$	$ 00, 30\rangle$	60.57	3.13e−4	219.4	0.00114
	+		$\rightarrow$	$ 20, 10\rangle$	280.7	4.80e−4	439.5	7.51e−4

Table 4.2: Bound-free transitions  $|b\rangle \rightarrow |f\rangle$ : The threshold photon energy  $\hbar\omega_{\text{thr}}$  (in eV) and the fitting parameters  $\mathcal{A}$ ,  $\mathcal{B}$ , and  $\mathcal{C}$  used in the cross section fitting formulas [Eq. (4.48)]. All transitions from the initial states  $|00, 10\rangle$  and  $|00, 20\rangle$  are listed, for several magnetic field strengths  $B_{12} = B/(10^{12} \text{ G})$ .

$B_{12}$	$\sigma$	$ b\rangle$	$\rightarrow  f\rangle$	$m_i$	$\hbar\omega_{\text{thr}}$	$\mathcal{A}$	$\mathcal{B}$	$\mathcal{C}$
1	0	$ 00, 10\rangle$	$\rightarrow  00, 1k\rangle$	1	159.2	0.96	0.093	1.43e6
			$\rightarrow  10, 0k\rangle$	0	283.2	0.89	0.20	8.83e5
	+		$\rightarrow  00, 2k\rangle$	1	159.2	0.70	0.061	7.95e2
			$\rightarrow  10, 1k\rangle$	0	283.2	0.86	0.094	1.30e3
	−		$\rightarrow  00, 0k\rangle$	1	159.2	0.62	0.030	8.89e2
	0	$ 00, 20\rangle$	$\rightarrow  00, 2k\rangle$	2	116.0	1.00	0.062	1.78e6
			$\rightarrow  20, 0k\rangle$	0	289.2	0.88	0.22	8.71e5
	+		$\rightarrow  00, 3k\rangle$	2	116.0	0.66	0.038	3.94e2
			$\rightarrow  20, 1k\rangle$	0	289.2	0.54	0.14	6.48e2
	−		$\rightarrow  00, 1k\rangle$	2	116.0	0.62	0.029	5.82e2
5	0	$ 00, 10\rangle$	$\rightarrow  00, 1k\rangle$	1	268.2	0.86	0.061	8.39e5
			$\rightarrow  10, 0k\rangle$	0	456.4	0.69	0.16	4.60e5
	+		$\rightarrow  00, 2k\rangle$	1	268.2	0.68	0.036	1.14e2
			$\rightarrow  10, 1k\rangle$	0	456.4	0.83	0.057	1.93e2
	−		$\rightarrow  00, 0k\rangle$	1	268.2	0.60	0.020	1.36e2
	0	$ 00, 20\rangle$	$\rightarrow  00, 2k\rangle$	2	201.2	0.92	0.039	1.11e6
			$\rightarrow  20, 0k\rangle$	0	466.5	0.65	0.18	4.39e5
	+		$\rightarrow  00, 3k\rangle$	2	201.2	0.65	0.021	5.95e1
			$\rightarrow  20, 1k\rangle$	0	466.5	0.54	0.084	9.13e1
	−		$\rightarrow  00, 1k\rangle$	2	201.2	0.61	0.015	7.82e1
10	0	$ 00, 10\rangle$	$\rightarrow  00, 1k\rangle$	1	331.1	0.82	0.051	6.58e5
			$\rightarrow  10, 0k\rangle$	0	552.5	0.63	0.15	3.51e5
	+		$\rightarrow  00, 2k\rangle$	1	331.1	0.67	0.029	4.94e1
			$\rightarrow  10, 1k\rangle$	0	552.5	0.81	0.046	8.43e1
	−		$\rightarrow  00, 0k\rangle$	1	331.1	0.59	0.016	6.00e1
	0	$ 00, 20\rangle$	$\rightarrow  00, 2k\rangle$	2	251.6	0.88	0.033	8.77e5
			$\rightarrow  20, 0k\rangle$	0	564.9	0.59	0.16	3.31e5
	+		$\rightarrow  00, 3k\rangle$	2	251.6	0.64	0.017	2.64e1
			$\rightarrow  20, 1k\rangle$	0	564.9	0.53	0.069	3.97e1
	−		$\rightarrow  00, 1k\rangle$	2	251.6	0.61	0.012	3.25e1

Table 4.2: (continued)

$B_{12}$	$\sigma$	$ b\rangle$	$\rightarrow  f\rangle$	$m_i$	$\hbar\omega_{\text{thr}}$	$\mathcal{A}$	$\mathcal{B}$	$\mathcal{C}$
50	0	$ 00, 10\rangle$	$\rightarrow  00, 1k\rangle$	1	523.3	0.73	0.034	3.74e5
			$\rightarrow  10, 0k\rangle$	0	834.2	0.54	0.11	1.96e5
			$\rightarrow  00, 2k\rangle$	1	523.3	0.63	0.020	7.15e0
			$\rightarrow  10, 1k\rangle$	0	834.2	0.77	0.033	1.22e1
	-		$\rightarrow  00, 0k\rangle$	1	523.3	0.57	0.012	8.94e0
	0	$ 00, 20\rangle$	$\rightarrow  00, 2k\rangle$	2	409.1	0.79	0.021	5.02e5
			$\rightarrow  20, 0k\rangle$	0	853.0	0.50	0.13	1.83e5
			$\rightarrow  00, 3k\rangle$	2	409.1	0.62	0.0104	4.04e0
			$\rightarrow  20, 1k\rangle$	0	853.0	*0.52	0.052	5.88e0
	-		$\rightarrow  00, 1k\rangle$	2	409.1	0.59	0.0058	4.13e0
100	0	$ 00, 10\rangle$	$\rightarrow  00, 1k\rangle$	1	628.8	0.69	0.029	2.96e5
			$\rightarrow  10, 0k\rangle$	0	983.4	0.51	0.101	1.56e5
			$\rightarrow  00, 2k\rangle$	1	628.8	0.62	0.019	3.12e0
			$\rightarrow  10, 1k\rangle$	0	983.4	0.75	0.031	5.33e0
	-		$\rightarrow  00, 0k\rangle$	1	628.8	0.56	0.012	3.94e0
	0	$ 00, 20\rangle$	$\rightarrow  00, 2k\rangle$	2	498.0	0.75	0.018	3.96e5
			$\rightarrow  20, 0k\rangle$	0	1008	0.47	0.12	1.45e5
			$\rightarrow  00, 3k\rangle$	2	498.0	0.60	0.0092	1.81e0
			$\rightarrow  20, 1k\rangle$	0	1008	*0.50	0.050	2.60e0
	-		$\rightarrow  00, 1k\rangle$	2	498.0	0.58	0.0042	1.69e0



## 4.4 Results

Tables 4.1 and 4.2 give results for transitions of helium atoms from the ground state ( $|00, 10\rangle$ ) and the first excited state ( $|00, 20\rangle$ ). Table 4.1 gives results (photon energies and oscillator strengths) for all possible bound-bound transitions with  $\Delta\nu \leq 1$ , for the field strengths  $B_{12} = 1, 5, 10, 50, 100$ , where  $B_{12} = B/(10^{12} \text{ G})$ . Transitions  $|a\rangle \rightarrow |b\rangle$  for  $\lambda = -$  are not listed separately, being equivalent to transitions  $|b\rangle \rightarrow |a\rangle$  for  $\lambda = +$ . One can check that the oscillator strengths  $f_{ba}$  presented in Table 4.1 for  $\lambda = +$  are well described by the approximation (4.34).

Table 4.2 gives results (threshold photon energies and cross section fitting formulas, see below) for all possible bound-free transitions. Figure 4.1 shows partial cross section curves for all bound-free transitions from the ground state of helium for  $B_{12} = 1$ . The transition  $|00, 10\rangle \rightarrow |0k, 20\rangle$  is an example of a ‘weak’ transition, whose oscillator strength is small because of the approximate orthogonality of one-electron wave functions, as discussed at the end of Sect. 4.3.1. It is included in this figure to confirm the accuracy of our assumption. Figures 4.2 and 4.3 show total cross section curves for a photon polarized along the magnetic field, for  $B_{12} = 1$  and 100 respectively. Figures 4.4 and 4.5 show total cross sections for the circular polarizations,  $\lambda = \pm$ , for  $B_{12} = 1$ . Finally, Figs. 4.6 and 4.7 show total cross sections for  $\lambda = \pm$  and  $B_{12} = 100$ .

### 4.4.1 Fitting Formula

The high-energy cross section scaling relations from Potekhin & Pavlov (1993), which were derived for hydrogen photoionization in strong magnetic fields, also

hold for helium:

$$\sigma_{\text{bf},0} \propto \left( \frac{1}{\hbar\omega} \right)^{2m_i+9/2} \quad (4.45)$$

$$\sigma_{\text{bf},\pm} \propto \left( \frac{1}{\hbar\omega} \right)^{2m_i+7/2}, \quad (4.46)$$

where  $m_i$  is the  $m$  value of the initial electron that transitions to the free state. In addition, we use similar fitting formulae for our numerical cross sections:

$$\sigma_{\text{bf},0} \simeq \frac{\mathcal{C}}{(1 + \mathcal{A}y)^{2.5}(1 + \mathcal{B}(\sqrt{1+y} - 1))^{4(m_i+1)}} \sigma_{\text{Th}} \quad (4.47)$$

$$\sigma_{\text{bf},\pm} \simeq \frac{\mathcal{C}(1+y)}{(1 + \mathcal{A}y)^{2.5}(1 + \mathcal{B}(\sqrt{1+y} - 1))^{4(m_i+1)}} \sigma_{\text{Th}} \quad (4.48)$$

where  $y = \varepsilon_f/\hbar\omega_{\text{thr}}$  and  $\hbar\omega_{\text{thr}}$  is the threshold photon energy for photoionization. These formulas have been fit to the cross section curves with respect to the free electron energy  $\varepsilon_f$  in approximately the  $1-10^4$  eV range (the curves are fit up to  $10^5$  eV for strong magnetic fields  $B_{12} = 50-100$ , in order to obtain the appropriate high-energy factor). The data points to be fit are weighted proportional to their cross section values plus a slight weight toward low-energy values, according to the formula (error in  $\sigma$ )  $\propto \sigma \varepsilon_f^{0.25}$ .

Results for the three fitting parameters,  $\mathcal{A}$ ,  $\mathcal{B}$ , and  $\mathcal{C}$ , are given in Table 4.2 for various partial cross sections over a range of magnetic field strengths. For photoionization in strong magnetic fields ( $B_{12} \gtrsim 50$ ) the cross section curves we generate for the  $\sigma_+$  and  $\sigma_-$  transitions have a slight deficiency at low electron energies, such that the curves peak at  $\varepsilon_f \simeq 10$  eV, rather than at threshold as expected. These peaks do not represent a real effect, but rather reflect the limits on the accuracy of our code (the overlap of the wave function of the transitioning electron pre- and post-ionization is extremely small under these conditions). Because the cross section values are not correct at low energies, our fits are not as accurate for these curves. In Table 4.2 we have marked with a ‘\*’ those transitions

which are most inaccurately fit by our fitting formula, determined by cross section curves with low-energy dips greater than 5% of the threshold cross section value.

## 4.5 Finite nucleus mass effects

So far we have used the infinite ion mass approximation. In this section we shall evaluate the validity range of this approximation and suggest possible corrections.

It is convenient to use the coordinate system which contains the center-of-mass coordinate  $\mathbf{R}_{\text{cm}}$  and the relative coordinates  $\{\mathbf{r}_j\}$  of the electrons with respect to the nucleus. Using a suitable canonical transformation, the Hamiltonian  $H$  of an arbitrary atom or ion can be separated into three terms (Vincke & Baye 1988; Baye & Vincke 1990; Schmelcher & Cederbaum 1991):  $H_1$  which describes the motion of a free pseudo-particle with net charge  $Q$  and total mass  $M$  of the ion (atom), the coupling term  $H_2$  between the collective and internal motion, and  $H_3$  which describes the internal relative motion of the electrons and the nucleus.  $H_1$  and  $H_2$  are proportional to  $M^{-1}$ , so they vanish in the infinite mass approximation. It is important to note, however, that  $H_3$  (the only non-zero term in the infinite mass approximation) also contains a term that depends on  $M_0^{-1}$ , where  $M_0 \approx M$  is the mass of the nucleus. Thus, there are two kinds of non-trivial finite-mass effects: the effects due to  $H_1 + H_2$ , which can be interpreted as caused by the electric field induced in the co-moving reference frame, and the effects due to  $H_3$ , which arise irrespective of the atomic motion. Both kinds of effects have been included in calculations only for the H atom (Potekhin 1994; Potekhin & Pavlov 1997 and references therein) and  $\text{He}^+$  ion (Bezchastnov et al. 1998; Pavlov & Bezchastnov 2005). For the He atom, only the second kind of effects have been studied (Al-Hujaj

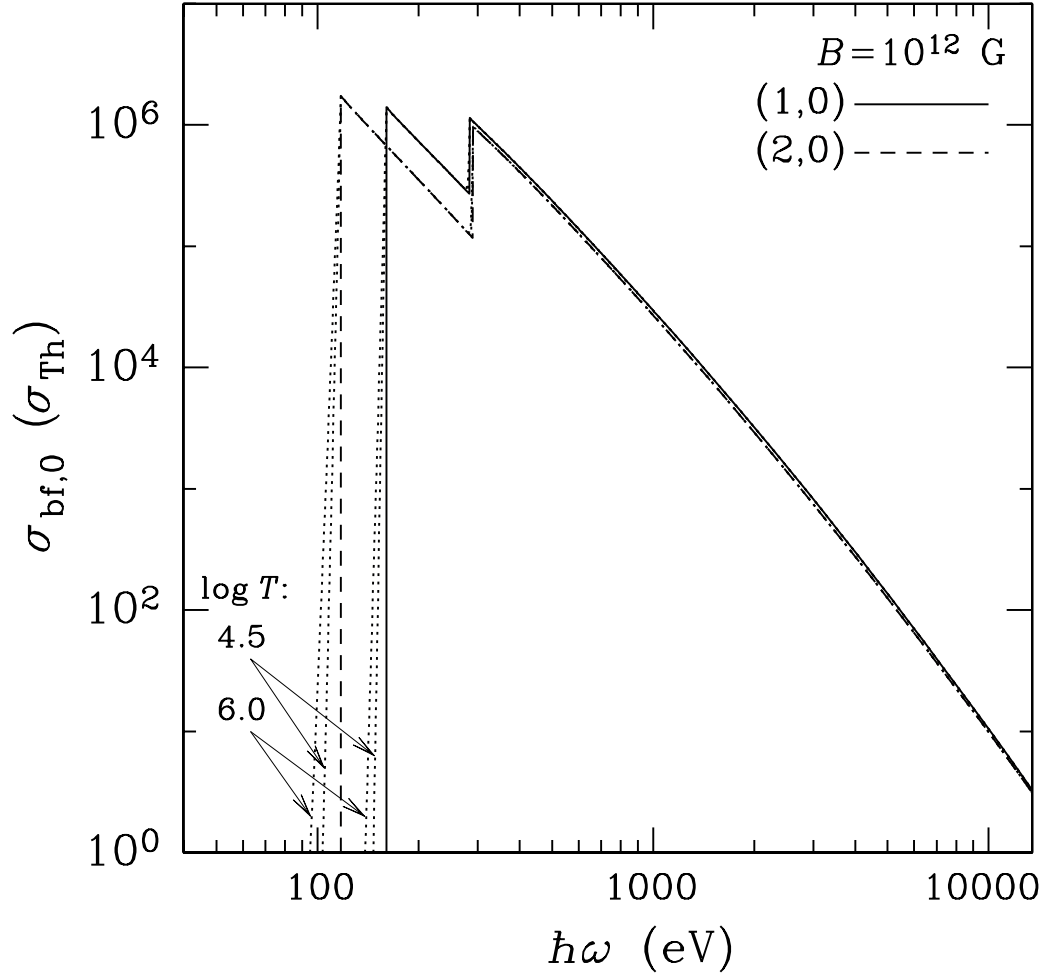


Figure 4.2: Total cross section  $\sigma_0$  versus photon energy for helium photoionization, from initial states  $(m_1, m_2) = (1, 0)$  (solid lines) and  $(2, 0)$  (dashed lines). The field strength is  $10^{12}$  G. The dotted lines extending from each cross section curve represent the effect of magnetic broadening on these cross sections, as approximated in Eq. (4.55), for  $T = 10^{4.5}$  K (steeper lines) and  $10^6$  K (flatter lines).

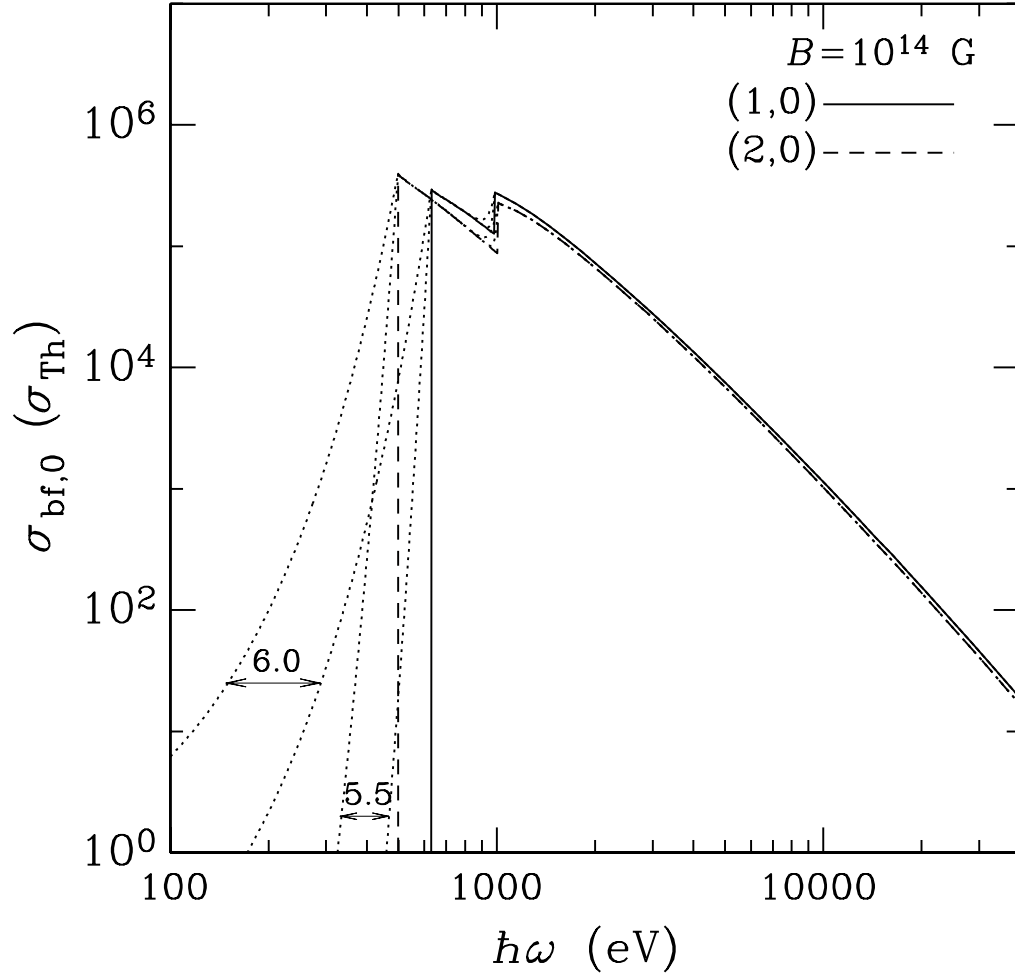


Figure 4.3: Total cross section  $\sigma_0$  versus photon energy for helium photoionization, from initial states  $(m_1, m_2) = (1, 0)$  (solid lines) and  $(2, 0)$  (dashed lines). The field strength is  $10^{14}$  G. The dotted lines extending from each cross section curve represent the effect of magnetic broadening on these cross sections, as approximated in Eq. (4.55), for  $T = 10^{5.5}$  K (steeper lines) and  $10^6$  K (flatter lines).

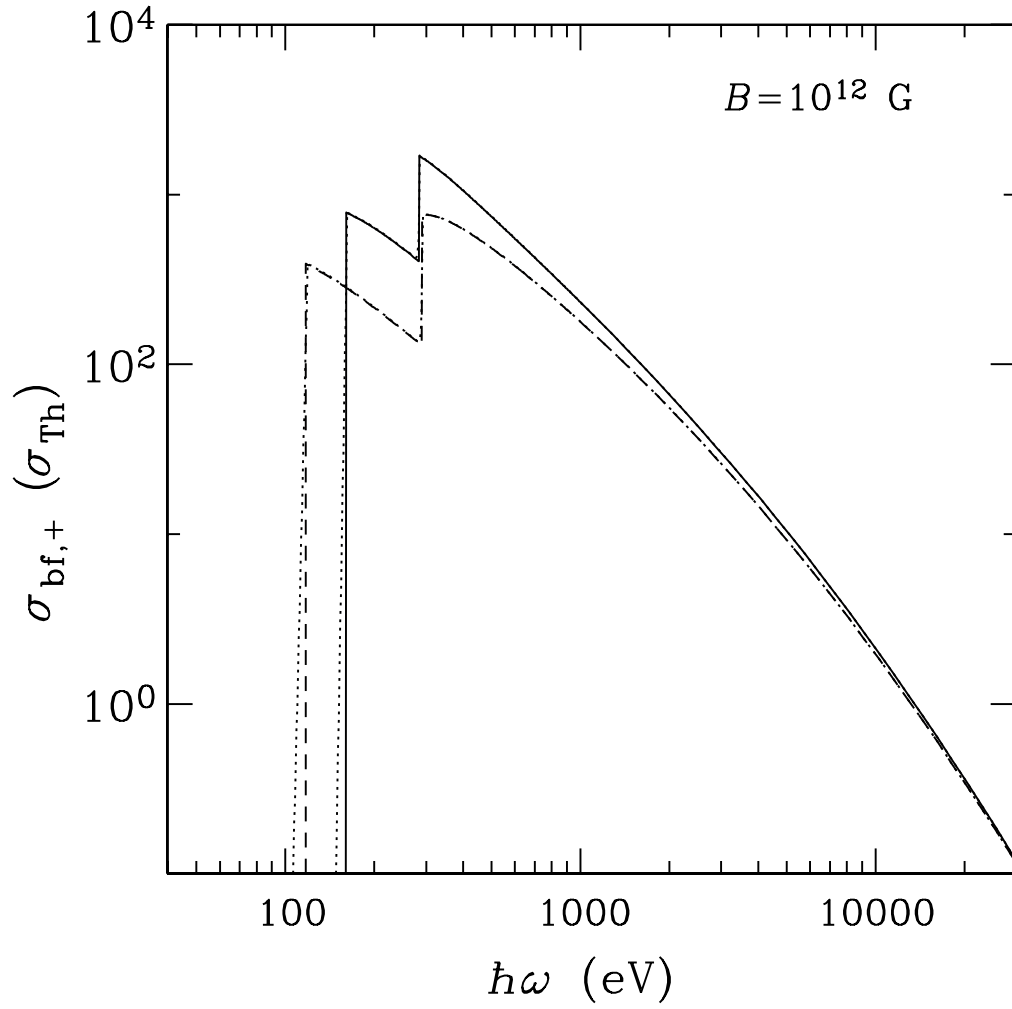


Figure 4.4: Total cross section  $\sigma_+$  versus photon energy for helium photoionization, from initial states  $(m_1, m_2) = (1, 0)$  (solid lines) and  $(2, 0)$  (dashed lines). The field strength is  $10^{12}$  G. The dotted lines extending from each cross section curve represent the effect of magnetic broadening on these cross sections, as approximated in Eq. (4.55), for  $T = 10^6$  K.

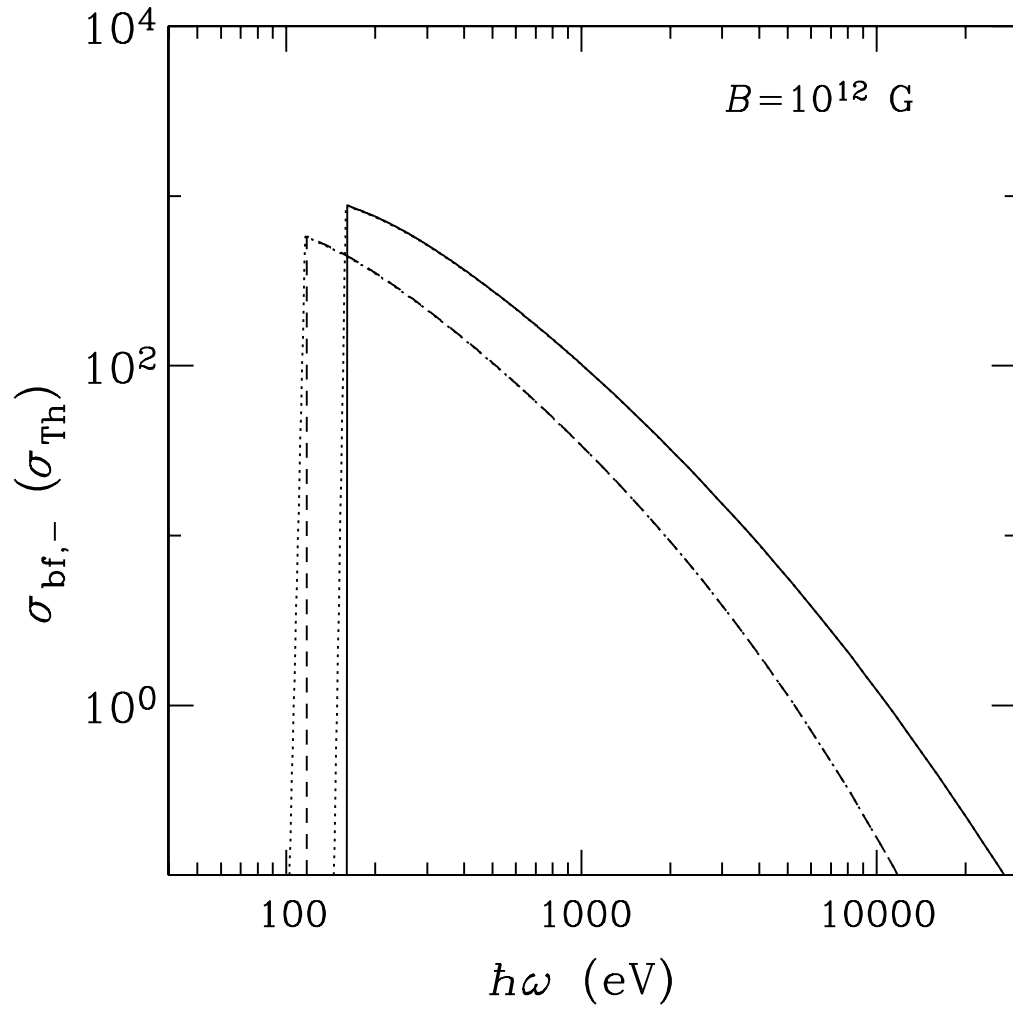


Figure 4.5: The same as in Fig. 4.4, but for  $\sigma_-$ .

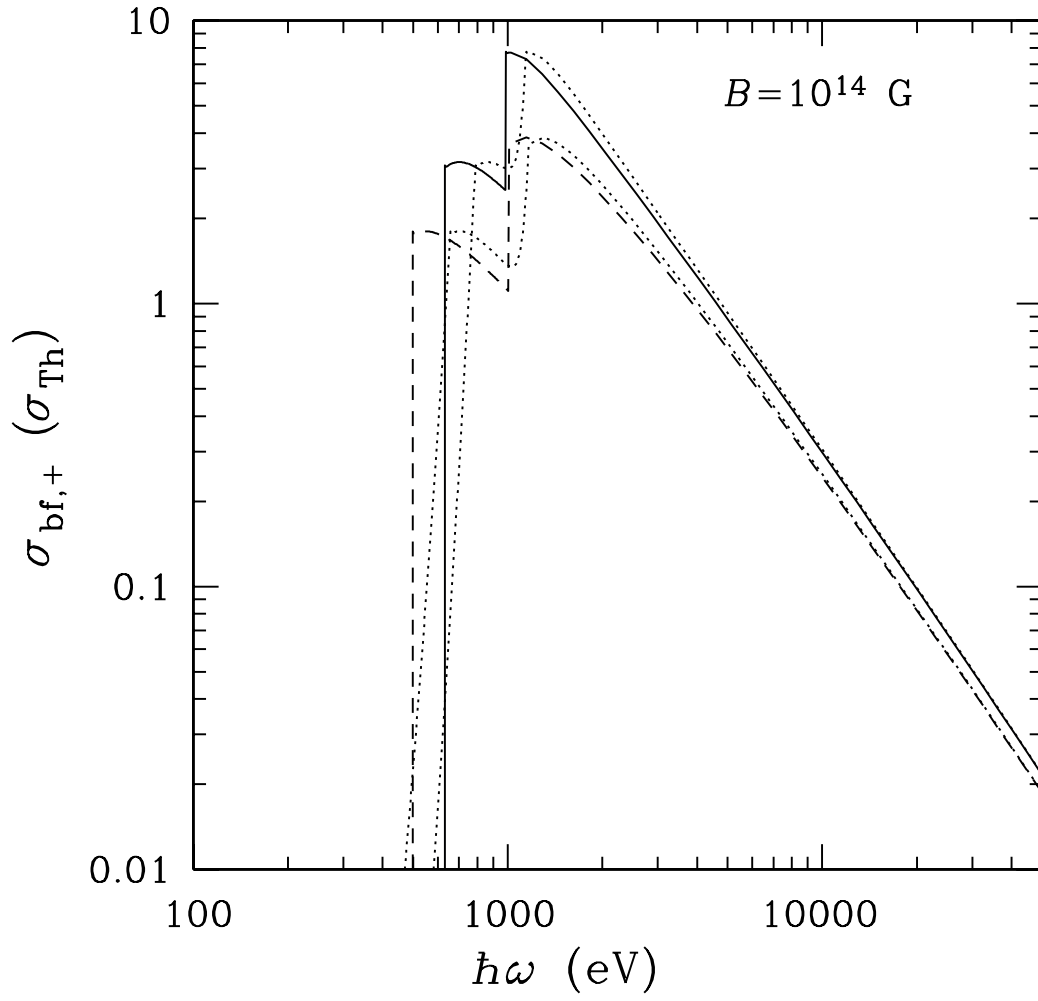


Figure 4.6: The same as in Fig. 4.4, but for  $B = 10^{14} \text{ G}$ .



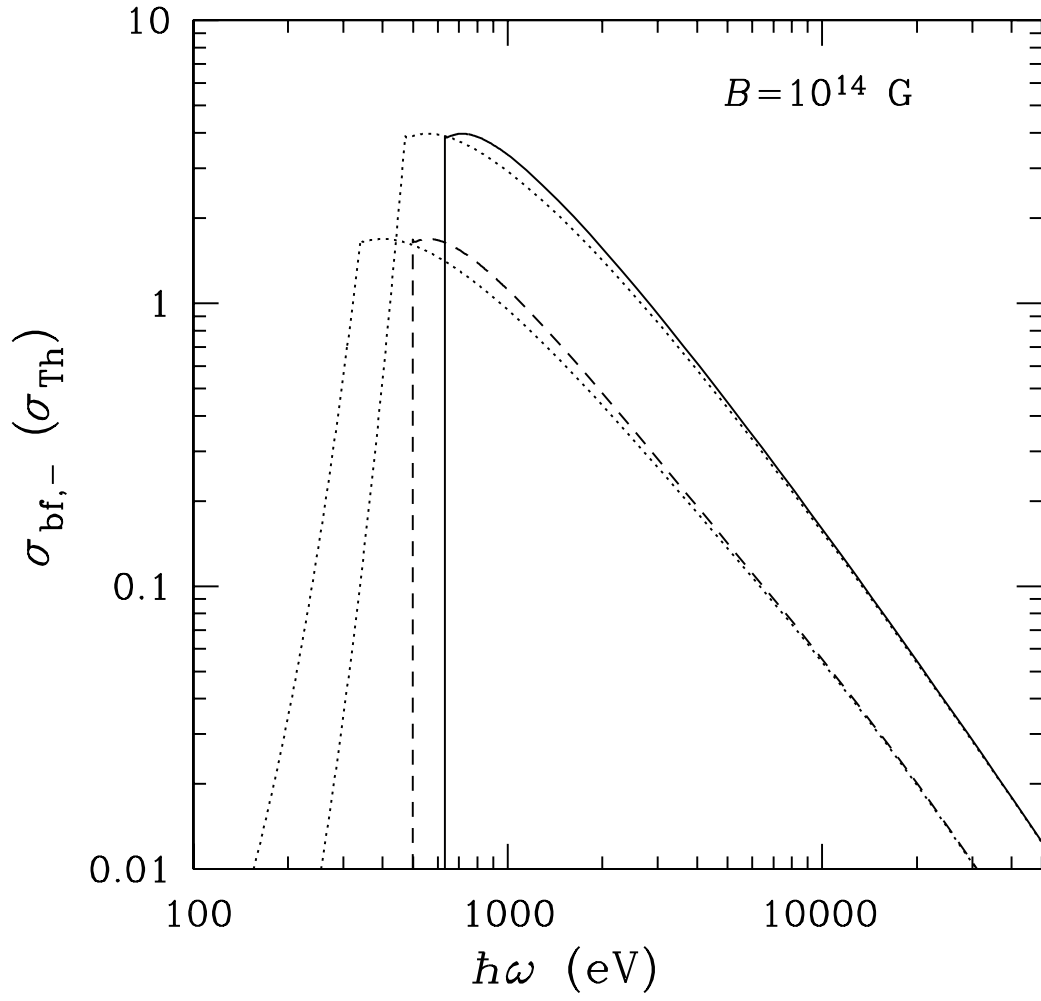


Figure 4.7: The same as in Fig. 4.6, but for  $\sigma_-$ .

& Schmelcher 2003a,b).

### 4.5.1 Non-moving helium atom

The state of motion of an atom can be described by pseudomomentum  $\mathbf{K}$ , which is a conserved vector since  $Q = 0$  (e.g., Vincke & Baye 1988; Schmelcher & Cederbaum 1991). Let us consider first the non-moving helium atom:  $K = 0$ .

According to Al-Hujaj & Schmelcher (2003a), there are trivial *normal mass corrections*, which consist in the appearance of reduced masses  $m_e/(1 \pm m_e/M_0)$  in  $H_3$ , and non-trivial *specific mass corrections*, which originate from the mass polarization operator.

The normal mass corrections for the total energy  $\mathcal{E}$  of the He state  $|m_1\nu_1, m_2\nu_2\rangle$  can be described as follows:

$$\mathcal{E}(M_0, B) = \frac{\mathcal{E}(\infty, (1 + m_e/M_0)^2 B)}{1 + m_e/M_0} + \hbar\Omega_{Be} \sum_j m_j, \quad (4.49)$$

where  $\Omega_{Be} = (m_e/M_0)\omega_{Be}$  (for He,  $\hbar\Omega_{Be} = 1.588B_{12}$  eV). The first term on the right-hand side describes the reduced mass transformation. The second term represents the energy shift due to conservation of the total  $z$  component of the angular momentum. Because of this shift, the states with sufficiently large values of  $m_1 + m_2$  become unbound (autoionizing, in analogy with the case of the H atom considered by Potekhin et al. 1997). This shift is also important for radiative transitions which change  $(m_1 + m_2)$  by  $\Delta m \neq 0$ : the transition energy  $\hbar\omega_{ba}$  is changed by  $\hbar\Omega_{Be}\Delta m$ . The dipole matrix elements  $M_{ba}$  are only slightly affected by the normal mass corrections, but the oscillator strengths are changed with changing  $\omega_{ba}$  according to Eq. (4.27). The energy shift also leads to the splitting of the photoionization

threshold by the same quantity  $\hbar\Omega_{Be}\Delta m$ , with  $\Delta m = 0, \pm 1$  depending on the polarization (in the dipole approximation). Clearly, these corrections must be taken into account, unless  $\Omega_{Be} \ll \omega_{ba}$  or  $\Delta m = 0$ , as illustrated in the last two columns of Table 4.1.

The specific mass corrections are more difficult to evaluate, but they can be neglected in the considered  $B$  range. Indeed, calculations by Al-Hujaj & Schmelcher (2003a) show that these corrections do not exceed 0.003 eV at  $B \leq 10^4 B_0$ .

#### 4.5.2 Moving helium atom

Eigenenergies and wave functions of a moving atom depend on its pseudomomentum  $\mathbf{K}$  perpendicular to the magnetic field. This dependence can be described by Hamiltonian components (e.g., Schmelcher & Cederbaum 1991)

$$H_1 + H_2 = \frac{K^2}{2M} + \sum_j \frac{e}{Mc} \mathbf{K} \cdot (\mathbf{B} \times \mathbf{r}_j), \quad (4.50)$$

where  $\sum_j$  is the sum over all electrons. The dependence on  $K_z$  is trivial, but the dependence on the perpendicular component  $\mathbf{K}_\perp$  is not. The energies depend on the absolute value  $K_\perp$ . For calculation of radiative transitions, it is important to take into account that the pseudomomentum of the atom in the initial and final state differ due to recoil:  $\mathbf{K}' = \mathbf{K} + \hbar\mathbf{q}$ . Effectively the recoil adds a term  $\propto \mathbf{q}$  into the interaction operator (cf. Potekhin et al. 1997; Potekhin & Pavlov 1997). The recoil should be neglected in the dipole approximation.

The atomic energy  $\mathcal{E}$  depends on  $K_\perp$  differently for different quantum states of the atom. In a real neutron star atmosphere, one should integrate the binding energies and cross sections over the  $K_\perp$ -distribution of the atoms, in order to

obtain the opacities.<sup>1</sup> Such integration leads to the specific magnetic broadening of spectral lines and ionization edges. Under the conditions typical for neutron star atmospheres, the magnetic broadening turns out to be much larger than the conventional Doppler and collisional broadenings (Pavlov & Potekhin 1995).

At present the binding energies and cross sections of a moving helium atom have not been calculated. However, we can approximately estimate the magnetic broadening for  $T \ll |(\Delta\mathcal{E})_{\min}|/k_B$ , where  $(\Delta\mathcal{E})_{\min}$  is the energy difference from a considered atomic level to the nearest level admixed by the perturbation due to atomic motion, and  $k_B$  is the Boltzmann constant. In this case, the  $K_{\perp}$ -dependence of  $\mathcal{E}$  can be approximated by the formula

$$\mathcal{E}(K_{\perp}) = \mathcal{E}(0) + \frac{K_{\perp}^2}{2M_{\perp}}, \quad (4.51)$$

where  $\mathcal{E}(0)$  is the energy in the infinite mass approximation and  $M_{\perp} = \frac{K_{\perp}}{\partial\mathcal{E}/\partial K_{\perp}}$  is an effective ‘transverse’ mass, whose value ( $M_{\perp} > M$ ) depends on the quantum state considered (e.g., Vincke & Baye 1988; Pavlov & Mészáros 1993).

Generally, at every value of  $K_{\perp}$  one has a different cross section  $\sigma(\omega, K_{\perp})$ . Assuming the equilibrium (Maxwell–Boltzmann) distribution of atomic velocities, the  $K_{\perp}$ -averaged cross section can be written as

$$\sigma(\omega) = \int_{\mathcal{E}_{\min}}^{\infty} \exp\left(\frac{\mathcal{E}(0) - \mathcal{E}(K_{\perp})}{k_B T}\right) \sigma(\omega, K_{\perp}) \frac{d\mathcal{E}(K_{\perp})}{k_B T}, \quad (4.52)$$

where  $\mathcal{E}_{\min} = -\hbar\omega$ .

The transitions that were dipole-forbidden for an atom at rest due to the conservation of the total  $z$ -projection of angular momentum become allowed for a moving atom. Therefore, the selection rule  $\Delta m = \lambda$  [Eqs. (4.30)–(4.32)] does not

---

<sup>1</sup>For the hydrogen atom, this has been done by Pavlov & Potekhin (1995) for bound-bound transitions and by Potekhin & Pavlov (1997) for bound-free transitions.

strictly hold, and we must write

$$\sigma(\omega, K_{\perp}) = \sum_{m'} \sigma_{m'}(\omega, K_{\perp}), \quad (4.53)$$

where the sum of partial cross sections is over all final quantum numbers  $m'$  (with  $m' \geq 0$  and  $m' \neq m_2$  for  $\Delta\nu = 0$ ) which are energetically allowed. For bound-bound transitions, this results in the splitting of an absorption line at a frequency  $\omega_{ba}$  in a multiplet at frequencies  $\omega_{ba} + \delta m \Omega_{Be} + (M_{\perp, m'}^{-1} - M_{\perp}^{-1}) K_{\perp}^2 / 2\hbar$ , where  $\delta m \equiv m' - m - \lambda$  and  $M_{\perp, m'}$  is the transverse mass of final states. For photoionization, we have the analogous splitting of the threshold. In particular, there appear bound-free transitions at frequencies  $\omega < \omega_{\text{thr}}$  – they correspond to  $\delta m < K_{\perp}^2 / (2M_{\perp} \hbar \Omega_{Be})$ . Here,  $\omega_{\text{thr}}$  is the threshold in the infinite ion mass approximation, and one should keep in mind that the considered perturbation theory is valid for  $K_{\perp}^2 / 2M_{\perp} \ll |(\Delta\mathcal{E})_{\text{min}}| < \hbar\omega_{\text{thr}}$ . According to Eq. (4.53),  $\sigma(\omega, K_{\perp})$  is notched at  $\omega < \omega_{\text{thr}}$ , with the cogs at partial thresholds  $\omega_{\text{thr}} + \delta m \Omega_{Be} - K_{\perp}^2 / (2M_{\perp} \hbar)$  (cf. Fig. 2 in Potekhin & Pavlov 1997).

Let us approximately evaluate the resulting envelope of the notched photoionization cross section (4.53), assuming that the ‘longitudinal’ matrix elements  $[\langle \dots \rangle]$  constructions in Eqs. (4.30)–(4.32) do not depend on  $K_{\perp}$ . The ‘transverse’ matrix elements can be evaluated following Potekhin & Pavlov (1997): in the perturbation approximation, they are proportional to  $|\xi|^{|\delta m|} e^{-|\xi|^2/2}$ , where  $|\xi|^2 = K_{\perp}^2 \rho_0^2 / (2\hbar^2)$ . Then

$$\begin{aligned} \sigma(\omega < \omega_{\text{thr}}, K_{\perp}) &\approx \sigma(\omega_{\text{thr}}, 0) \exp \left[ -\frac{M_{\perp}}{M} \frac{\omega_{\text{thr}} - \omega}{\Omega_{Be}} \right] \\ &\times \theta \left( \frac{K_{\perp}^2}{2M_{\perp}} - \hbar(\omega_{\text{thr}} - \omega) \right), \end{aligned} \quad (4.54)$$

where  $\theta(x)$  is the step function. A comparison of this approximation with numerical calculations for the hydrogen atom (Potekhin & Pavlov 1997) shows that it

gives the correct qualitative behavior of  $\sigma(\omega, K_\perp)$ . For a quantitative agreement, one should multiply the exponential argument by a numerical factor  $\sim 0.5\text{--}2$ , depending on the state and polarization. This numerical correction is likely due to the neglected  $K_\perp$ -dependence of the longitudinal matrix elements. We assume that this approximation can be used also for the helium atom. Using Eq. (4.52), we obtain

$$\sigma(\omega) \approx \sigma(\omega_{\text{thr}}) \exp \left[ -\frac{M_\perp}{M} \frac{\omega_{\text{thr}} - \omega}{\Omega_{Be}} - \frac{\hbar(\omega_{\text{thr}} - \omega)}{k_B T} \right] \quad (4.55)$$

for  $\omega < \omega_{\text{thr}}$ . Here the transverse mass  $M_\perp$  can be evaluated by treating the coupling Hamiltonian  $H_2$  as a perturbation, as was done by Pavlov & Mészáros (1993) for the H atom. Following this approach, retaining only the main perturbation terms according to the approximate orthogonality relation (4.33) and neglecting the difference between  $M$  and  $M_0$ , we obtain an estimate

$$\frac{M}{M_\perp} \approx 1 - \sum_{\lambda=\pm} \frac{\lambda}{2} \sum_{b(\Delta m=\lambda)} \frac{\omega_{Be} f_{ba}^\lambda / (2\omega_{ba})}{1 + \omega_{ba} / \Omega_{Be}}, \quad (4.56)$$

where  $|a\rangle$  is the considered bound state ( $|00, 10\rangle$  or  $|00, 20\rangle$  for the examples in Figs. 4.2–4.7) and  $|b\rangle$  are the final bound states to which  $\lambda = \pm$  transitions  $|a\rangle \rightarrow |b\rangle$  are allowed. According to Eq. (4.34), the numerator in Eq. (4.56) is close to  $m + 1$  for  $\lambda = +$  and to  $m$  for  $\lambda = -$ .

For the transitions from the ground state with polarization  $\lambda = -$ , which are strictly forbidden in the infinite ion mass approximation, using the same approximations as above we obtain the estimate  $\sigma_-(\omega) \propto \sigma_+(\omega) \hbar \Omega_{Be} k_B T / (k_B T + \hbar \Omega_{Be})^2$ .

Examples of the photoionization envelope approximation, as described in Eq. (4.55) above, are shown in Figs. 4.2–4.7. In Figs. 4.6 and 4.7 (for  $B = 10^{14}$  G), in addition to the magnetic broadening, we see a significant shift of the maximum, which originates from the last term in Eq. (4.49). Such shift is negligible in Figs. 4.4 and 4.5 because of the relatively small  $\Omega_{Be}$  value for  $B = 10^{12}$  G.

Finally, let us note that the Doppler and collisional broadening of spectral features in a strong magnetic field can be estimated, following Pavlov & Mészáros (1993), Pavlov & Potekhin (1995) and Rajagopal et al. (1997). The Doppler spectral broadening profile is

$$\phi_D(\omega) = \frac{1}{\sqrt{\pi}\Delta\omega_D} \exp\left[-\frac{(\omega - \omega_0)^2}{\Delta\omega_D^2}\right], \quad (4.57)$$

with

$$\Delta\omega_D = \frac{\omega_0}{c} \sqrt{\frac{2T}{M}} \left[ \cos^2 \theta_B + \frac{M_\perp}{M} \sin^2 \theta_B \right]^{-1/2}, \quad (4.58)$$

where  $\theta_B$  is the angle between the wave vector and  $\mathbf{B}$ . The collisional broadening is given by

$$\phi_{\text{coll}}(\omega) = \frac{\Lambda_{\text{coll}}}{2\pi} \frac{1}{(\omega - \omega_0)^2 + (\Lambda_{\text{coll}}/2)^2}, \quad (4.59)$$

with

$$\begin{aligned} \hbar\Lambda_{\text{coll}} &= 4.8n_e a_0 r_{\text{eff}}^2 \left( \frac{k_B T}{\text{Ryd}} \right)^{1/6} \\ &= 41.5 \frac{n_e}{10^{24} \text{ cm}^{-3}} T_6^{1/6} \left( \frac{r_{\text{eff}}}{a_0} \right)^2 \text{ eV}, \end{aligned} \quad (4.60)$$

where  $n_e$  is the electron number density and  $r_{\text{eff}}$  is an effective electron-atom interaction radius, which is about the quantum-mechanical size of the atom. The convolution of the Doppler, collisional and magnetic broadening profiles gives the total shape of the cross section. For bound-free transitions, the Doppler and collisional factors can be neglected, but for the bound-bound transitions they give the correct blue wings of the spectral features (cf. Pavlov & Potekhin 1995).

## 4.6 Conclusion

We have presented detailed numerical results and fitting formulae for the dominant radiative transitions (both bound-bound and bound-free) of He atoms in strong

magnetic fields in the range of  $10^{12} - 10^{14}$  G. These field strengths may be most appropriate for the identification of spectral lines observed in thermally emitting isolated neutron stars (see Sect. 4.1).

While most of our calculations are based on the infinite-nucleus-mass approximation, we have examined the effects of finite nucleus mass and atomic motion on the opacities. We found that for the field strengths considered in this chapter ( $B \lesssim 10^{14}$  G), these effects can be incorporated into the infinite-mass results to obtain acceptable He opacities for neutron star atmosphere modelling. For large field strengths, more accurate calculations of the energy levels and radiative transitions of a moving He atom will be needed in order to obtain reliable opacities.



CHAPTER 5

**CONDENSED SURFACES OF MAGNETIC NEUTRON STARS,  
THERMAL SURFACE EMISSION, AND PARTICLE  
ACCELERATION ABOVE PULSAR POLAR CAPS**

## **5.1 Introduction**

Recent observations of neutron stars have provided a wealth of information on these objects, but they have also raised many new questions. For example, with the advent of X-ray telescopes such as Chandra and XMM-Newton, detailed observations of the thermal radiation from the neutron star surface have become possible. These observations show that some nearby isolated neutron stars (e.g., RX J1856.5-3754) appear to have featureless, nearly blackbody spectra (Burwitz et al 2003; van Kerkwijk & Kaplan 2007). Radiation from a bare condensed surface (where the overlying atmosphere has negligible optical depth) has been invoked to explain this nearly perfect blackbody emission (e.g., Burwitz et al 2003; Mori & Ruderman 2003; Turolla et al. 2004; van Adelsberg et al. 2005; Perez-Azorin et al. 2006; Ho et al. 2007; but see Ruderman 2003 for an alternative view). However, whether surface condensation actually occurs depends on the cohesive properties of the surface matter (e.g., Lai 2001).

Equally puzzling are the observations of anomalous X-ray pulsars (AXPs) and soft gamma-ray repeaters (SGRs) (see Woods & Thompson 2005 for a review). Though these stars are believed to be magnetars, neutron stars with extremely strong magnetic fields ( $B \gtrsim 10^{14}$  G), they mostly show no pulsed radio emission (but see Camilo et al. 2006, 2007; Kramer et al. 2007) and their X-ray radiation is too strong to be powered by rotational energy loss. By contrast, several high-B

radio pulsars with inferred surface field strengths similar to those of magnetars have been discovered (e.g., Kaspi & McLaughlin 2005; Vranevsevic, Manchester, & Melrose 2007). A deeper understanding of the distinction between pulsars and magnetars requires further investigation of the mechanisms by which pulsars and magnetars radiate and of their magnetospheres where this emission originates. Theoretical models of pulsar and magnetar magnetospheres depend on the cohesive properties of the surface matter in strong magnetic fields (e.g., Ruderman & Sutherland 1975; Arons & Scharlemann 1979; Cheng & Ruderman 1980; Usov & Melrose 1996; Harding & Muslimov 1998; Gil, Melikidze, & Geppert 2003; Muslimov & Harding 2003; Beloborodov & Thompson 2007). For example, depending on how strongly bound the surface matter is, a charge-depleted acceleration zone (“vacuum gap”) above the polar cap of a pulsar may or may not form, and this will affect pulsar radio emission and other high-energy emission processes.

The cohesive property of the neutron star surface matter plays a key role in these and other neutron star processes and observed phenomena. The cohesive energy refers to the energy required to pull an atom out of the bulk condensed matter at zero pressure. A related (but distinct) quantity is the electron work function, the energy required to pull out an electron. For magnetized neutron star surfaces the cohesive energy and work function can be many times the corresponding terrestrial values, due to the strong magnetic fields threading the matter (e.g., Ruderman 1974; Lai 2001).

In Chapters 2 and 3, we carried out detailed, first-principle calculations of the cohesive properties of H, He, C, and Fe surfaces at field strengths between  $B = 10^{12}$  G to  $2 \times 10^{15}$  G. The main purpose of this chapter is to investigate several important astrophysical implications of these results (some preliminary

investigations were reported in Medin & Lai 2007). This chapter is organized as follows. In Section 5.2 we briefly summarize the key results (cohesive energy and work function values) of ML06a,b used in this chapter. In Section 5.3 we examine the possible formation of a bare neutron star surface, which directly affects the surface thermal emission. We find that the critical temperature below which a phase transition to the condensed state occurs is approximately given by  $kT_{\text{crit}} \sim 0.08Q_s$ , where  $Q_s$  is the cohesive energy of the surface. In Section 5.4 we consider the conditions for the formation of a polar vacuum gap in pulsars and magnetars. We find that neutron stars with rotation axis and magnetic moment given by  $\boldsymbol{\Omega} \cdot \mathbf{B}_p > 0$  are unable to form vacuum gaps (since the electrons which are required to fill the gaps can be easily supplied by the surface), but neutron stars with  $\boldsymbol{\Omega} \cdot \mathbf{B}_p < 0$  can form vacuum gaps provided that the surface temperature is less than  $kT_{\text{crit}} \sim 0.04Q_s$  (and that particle bombardment does not completely destroy the gap; see Section 5.5). Implications of our results for recent observations are discussed in Section 5.5.

This chapter and Chapter 6 are based on the published paper by Medin & Lai 2007 [Medin Z., Lai D., 2007, *Monthly Notices of the Royal Astronomical Society*, 382, 1833; ©2007. Blackwell Publishing. All rights reserved]. Sections of the paper are reprinted here and in Chapter 6 with minor changes, based on rights retained by the author.

## 5.2 Cohesive properties of condensed matter in strong magnetic fields

It is well-known that the properties of matter can be drastically modified by strong magnetic fields. The natural atomic unit for the magnetic field strength,  $B_0$ , is set by equating the electron cyclotron energy  $\hbar\omega_{Be} = \hbar(eB/m_e c) = 11.577 B_{12}$  keV, where  $B_{12} = B/(10^{12} \text{ G})$ , to the characteristic atomic energy  $e^2/a_0 = 2 \times 13.6 \text{ eV}$  (where  $a_0$  is the Bohr radius):

$$B_0 = \frac{m_e^2 e^3 c}{\hbar^3} = 2.3505 \times 10^9 \text{ G}. \quad (5.1)$$

For  $b = B/B_0 \gtrsim 1$ , the usual perturbative treatment of the magnetic effects on matter (e.g., Zeeman splitting of atomic energy levels) does not apply. Instead, the Coulomb forces act as a perturbation to the magnetic forces, and the electrons in an atom settle into the ground Landau level. Because of the extreme confinement of the electrons in the transverse direction (perpendicular to the field), the Coulomb force becomes much more effective in binding the electrons along the magnetic field direction. The atom attains a cylindrical structure. Moreover, it is possible for these elongated atoms to form molecular chains by covalent bonding along the field direction. Interactions between the linear chains can then lead to the formation of three-dimensional condensed matter (Ruderman 1974; Ruder et al. 1994; Lai 2001).

The basic properties of magnetized condensed matter can be estimated using the uniform electron gas model (e.g., Kadomtsev 1970). The energy per cell of a zero-pressure condensed matter is given by

$$\mathcal{E}_s \sim -120 Z^{9/5} B_{12}^{2/5} \text{ eV}, \quad (5.2)$$

and the corresponding condensation density is

$$\rho_s \sim 560 A Z^{-3/5} B_{12}^{6/5} \text{ g cm}^{-3}, \quad (5.3)$$

where  $Z$ ,  $A$  are the charge number and mass number of the ion (see Lai 2001 and references therein for further refinements to the uniform gas model). Although this simple model gives a reasonable estimate of the binding energy for the condensed state, it is not adequate for determining the cohesive property of the condensed matter. The cohesive energy is the (relatively small) difference between the atomic ground-state energy  $\mathcal{E}_a$  and the zero-pressure condensed matter energy  $\mathcal{E}_s$ , both increasing rapidly with  $B$ . Moreover, the electron Fermi energy (including both kinetic energy and Coulomb energy) in the uniform gas model,

$$\varepsilon_F = (3/5Z)\mathcal{E}_s \sim -73Z^{4/5}B_{12}^{2/5} \text{ eV}, \quad (5.4)$$

may not give a good scaling relation for the electron work function when detailed electron energy levels (bands) in the condensed matter are taken into account.

There have been few quantitative studies of infinite chains and zero-pressure condensed matter in strong magnetic fields. Earlier variational calculations (e.g., Flowers et al. 1977; Müller 1984) as well as calculations based on Thomas-Fermi type statistical models (e.g., Abrahams & Shapiro 1991; Fushiki et al. 1992), while useful in establishing scaling relations and providing approximate energies of the atoms and the condensed matter, are not adequate for obtaining reliable energy differences (cohesive energies). Quantitative results for the energies of infinite chains of hydrogen molecules  $\text{H}_\infty$  over a wide range of field strengths ( $B \gg B_0$ ) were presented in Lai et al. (1992) (using the Hartree-Fock method with the plane-wave approximation; see also Lai 2001 for some results for  $\text{He}_\infty$ ) and in Relovsky & Ruder (1996) (using density functional theory). For heavier elements such as C and Fe, the cohesive energies of one dimensional (1D) chains have only been

calculated at a few magnetic field strengths in the range of  $B = 10^{12}$ – $10^{13}$  G, using Hartree-Fock models (Neuhauser et al. 1987) and density functional theory (Jones 1985). There were some discrepancies between the results of these works, and some adopted a crude treatment for the band structure (Neuhauser et al. 1987). An approximate calculation of 3D condensed matter based on density functional theory was presented in Jones (1986).

Our calculations of atoms and small molecules (ML06a) and of infinite chains and condensed matter (ML06b) are based on a newly developed density functional theory code. Although the Hartree-Fock method is expected to be highly accurate in the strong field regime, it becomes increasingly impractical for many-electron systems as the magnetic field increases, since more and more Landau orbitals are occupied (even though electrons remain in the ground Landau level) and keeping track of the direct and exchange interactions between electrons in various orbitals becomes computationally rather tedious. Compared to previous density-functional theory calculations, we used an improved exchange-correlation function for highly magnetized electron gases, and we calibrated our density-functional code with previous results (when available) based on other methods. Most importantly, in our calculations of 1D condensed matter, we treated the band structure of electrons in different Landau orbitals self-consistently without adopting ad-hoc simplifications. This is important for obtaining reliable results for the condensed matter. Since each Landau orbital has its own energy band, the number of bands that need to be calculated increases with  $Z$  and  $B$ , making the computation increasingly complex for superstrong magnetic field strengths (e.g., the number of occupied bands for Fe chains at  $B = 2 \times 10^{15}$  G reaches 155; see Fig. 16 of ML06b). Our density-functional calculations allow us to obtain the energies of atoms and small molecules and the energy of condensed matter using the same method, thus providing reliable cohesive

energy and work function values for condensed surfaces of magnetic neutron stars.

In ML06a, we described our calculations for various atoms and molecules in magnetic fields ranging from  $10^{12}$  G to  $2 \times 10^{15}$  G for H, He, C, and Fe, representative of the most likely neutron star surface compositions. Numerical results of the ground-state energies are given for  $H_N$  (up to  $N = 10$ ),  $He_N$  (up to  $N = 8$ ),  $C_N$  (up to  $N = 5$ ), and  $Fe_N$  (up to  $N = 3$ ), as well as for various ionized atoms. In ML06b, we described our calculations for infinite chains for H, He, C, and Fe in that same magnetic field range. For relatively low field strengths, chain-chain interactions play an important role in the cohesion of three-dimensional (3D) condensed matter. An approximate calculation of 3D condensed matter is also presented in ML06b. Numerical results of the ground-state and cohesive energies, as well as the electron work function and the zero-pressure condensed matter density, are given in ML06b for  $H_\infty$  and  $H(3D)$ ,  $He_\infty$  and  $He(3D)$ ,  $C_\infty$  and  $C(3D)$ , and  $Fe_\infty$  and  $Fe(3D)$ .

Some numerical results from ML06a,b are provided in graphical form in Figs. 5.1, 5.2, 5.3, and 5.4 (see ML06a,b for approximate scaling relations for different field ranges based on numerical fits). Figure 5.1 shows the cohesive energies of condensed matter,  $Q_s = \mathcal{E}_1 - \mathcal{E}_s$ , and the molecular energy differences,  $\Delta\mathcal{E}_N = \mathcal{E}_N/N - \mathcal{E}_1$ , for He, Fig. 5.2 for C, and Fig. 5.3 for Fe; here  $\mathcal{E}_1$  is the atomic ground-state energy,  $\mathcal{E}_N$  is the ground-state energy of the  $He_N$ ,  $C_N$ , or  $Fe_N$  molecule, and  $\mathcal{E}_s$  is the energy per cell of the zero-pressure 3D condensed matter. Some relevant ionization energies for the atoms are also shown. Figure 5.4 shows the electron work functions  $\phi$  for condensed He, C, and Fe as a function of the field strength. We see that the work function increases much more slowly with  $B$  compared to the simple free electron gas model [see Eq. (5.4)], and the dependence on  $Z$  is also

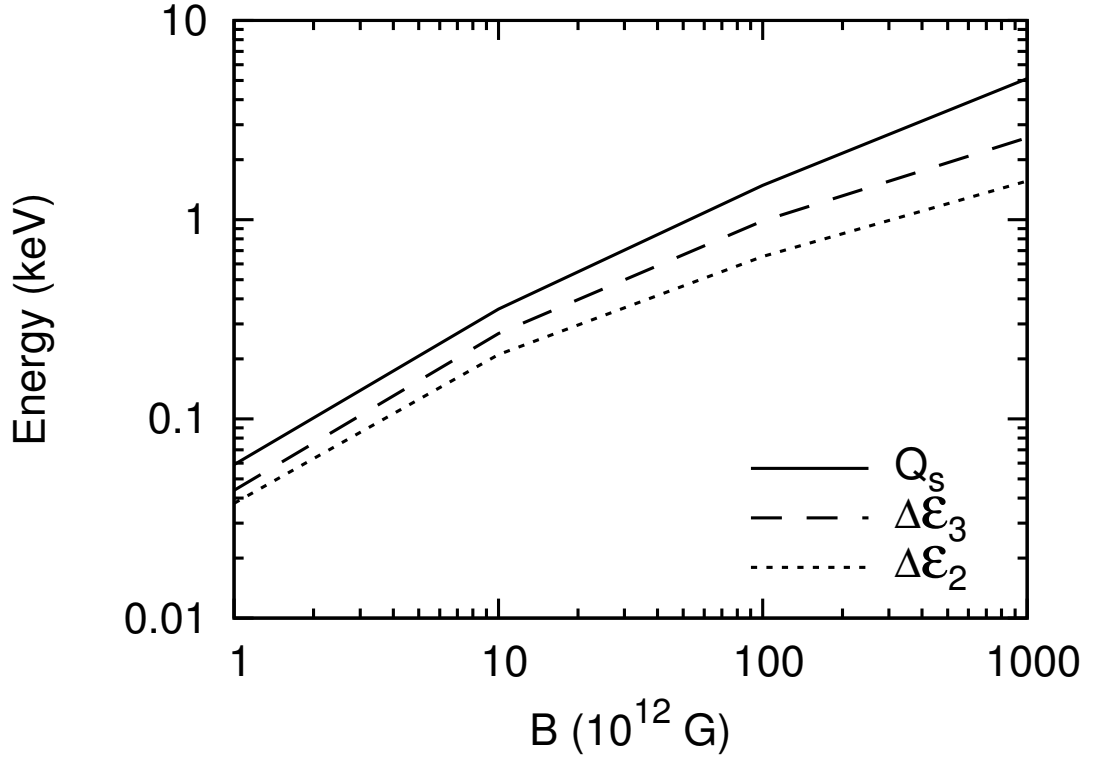


Figure 5.1: Cohesive energy  $Q_s = \mathcal{E}_1 - \mathcal{E}_s$  and molecular energy difference  $\Delta\mathcal{E}_N = \mathcal{E}_N/N - \mathcal{E}_1$  for helium as a function of the magnetic field strength.

weak. The results summarized here will be used in Section 5.3 and Section 5.4 below.

### 5.3 Condensation of neutron star surfaces in strong magnetic fields

As seen from Figs. 5.1, 5.2, and 5.3, the cohesive energies of condensed matter increase with magnetic field. We therefore expect that for sufficiently strong magnetic fields, there exists a critical temperature  $T_{\text{crit}}$  below which a first-order phase transition occurs between the condensate and the gaseous vapor. This has been



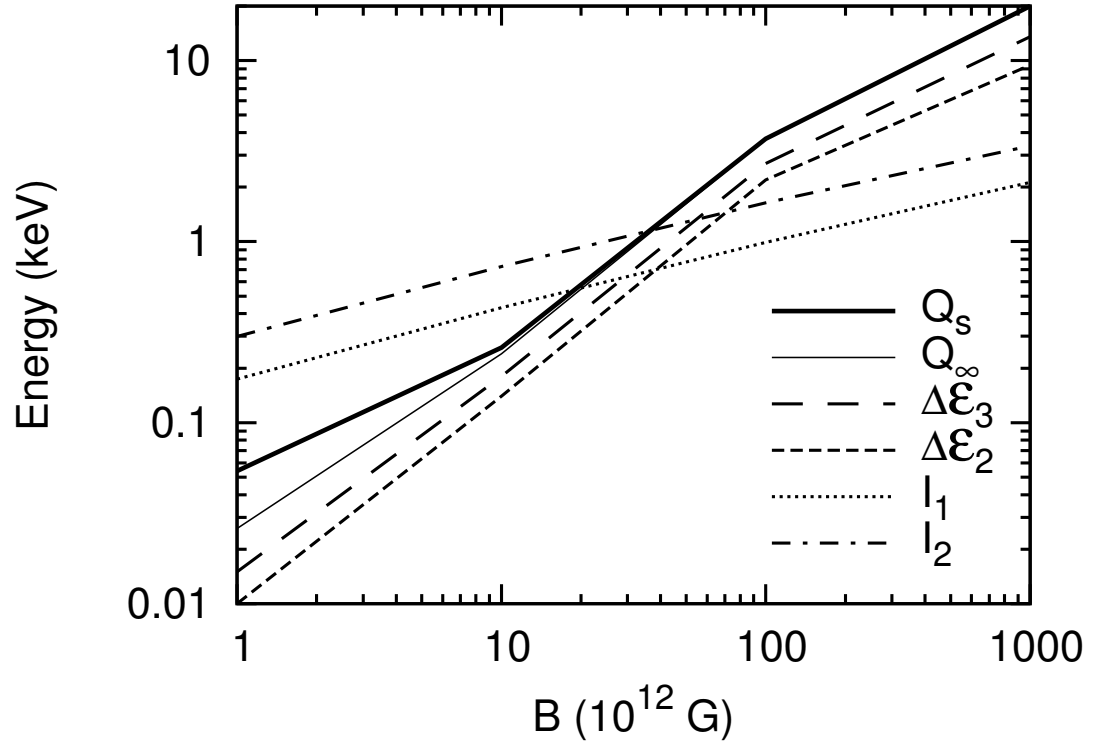


Figure 5.2: Cohesive energy  $Q_s = \mathcal{E}_1 - \mathcal{E}_s$  and molecular energy difference  $\Delta\mathcal{E}_N = \mathcal{E}_N/N - \mathcal{E}_1$  for carbon as a function of the magnetic field strength. The symbol  $Q_\infty$  represents the cohesive energy of a one-dimensional chain, and  $I_1$  and  $I_2$  are the first and second ionization energies of the C atom.

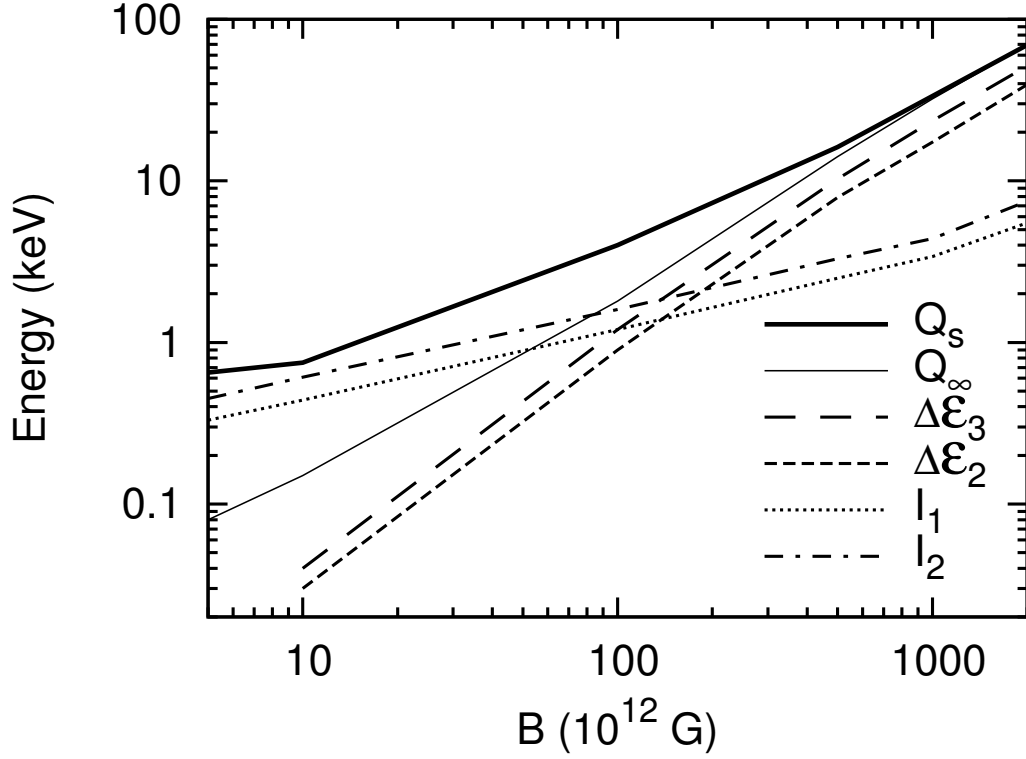


Figure 5.3: Cohesive energy  $Q_s = \mathcal{E}_1 - \mathcal{E}_s$  and molecular energy difference  $\Delta\mathcal{E}_N = \mathcal{E}_N/N - \mathcal{E}_1$  for iron as a function of the magnetic field strength. The symbol  $Q_\infty$  represents the cohesive energy of a one-dimensional chain, and  $I_1$  and  $I_2$  are the first and second ionization energies of the Fe atom. Below  $5 \times 10^{12}$  G, our results for  $Q_\infty$  and  $Q_s$  become unreliable as  $Q_\infty$  and  $Q_s$  become very small and approach numerical errors for  $\mathcal{E}_N$  and  $\mathcal{E}_s$ .

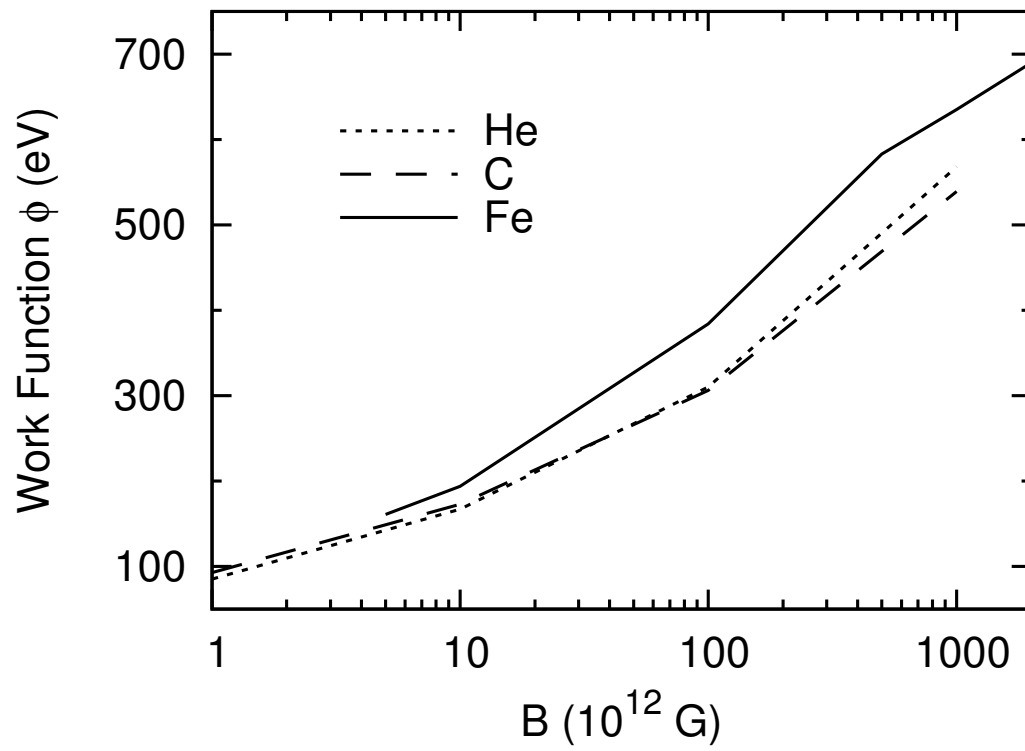


Figure 5.4: Numerical result for the electron work function as a function of the magnetic field strength, for He, C, and Fe infinite chains.

investigated in detail for hydrogen surfaces (see Lai & Salpeter 1997; Lai 2001), but not for other surface compositions. Here we consider the possibilities of such phase transitions of He, C, and Fe surfaces.

A precise calculation of the critical temperature  $T_{\text{crit}}$  is difficult. We can determine  $T_{\text{crit}}$  approximately by considering the equilibrium between the condensed phase (labeled “s”) and the gaseous phase (labeled “g”) in the ultrahigh field regime (where phase separation exists). The gaseous phase consists of a mixture of free electrons and bound ions, atoms, and molecules. Phase equilibrium requires the temperature, pressure and the chemical potentials of different species to satisfy the conditions (here we consider Fe as an example; He and C are similar)

$$P_s = P_g = [2n(\text{Fe}^+) + 3n(\text{Fe}^{2+}) + \cdots + n(\text{Fe}) + n(\text{Fe}_2) + n(\text{Fe}_3) + \cdots]kT, \quad (5.5)$$

$$\mu_s = \mu_e + \mu(\text{Fe}^+) = 2\mu_e + \mu(\text{Fe}^{2+}) = \cdots = \mu(\text{Fe}) = \frac{1}{2}\mu(\text{Fe}_2) = \frac{1}{3}\mu(\text{Fe}_3) = \cdots, \quad (5.6)$$

where we treat the gaseous phase as an ideal gas. The chemical potential of the condensed phase is given by

$$\mu_s = \mathcal{E}_s + P_s V_s \simeq \mathcal{E}_{s,0}, \quad (5.7)$$

where  $\mathcal{E}_s$  is the energy per cell of the condensate and  $\mathcal{E}_{s,0}$  is the energy per cell at zero-pressure (we will label this simply as  $\mathcal{E}_s$ ). We have assumed that the vapor pressure is sufficiently small so that the deviation from the zero-pressure state of the condensate is small; this is justified when the saturation vapor pressure  $P_{\text{sat}}$  is much less than the critical pressure  $P_{\text{crit}}$  for phase separation, or when the temperature is less than the critical temperature by a factor of a few.

For nondegenerate electrons in a strong magnetic field the number density is

related to  $\mu_e$  by

$$n_e \simeq \frac{1}{2\pi\rho_0^2} e^{\mu_e/kT} \sum_{n_L=0}^{\infty} g_{n_L} \exp\left(\frac{-n_L \hbar\omega_{Be}}{kT}\right) \int_{-\infty}^{\infty} \frac{dp_z}{h} \exp\left(\frac{-p_z^2}{2m_e kT}\right) \quad (5.8)$$

$$\simeq \frac{1}{2\pi\rho_0^2 \lambda_{Te}} e^{\mu_e/kT} \tanh^{-1}\left(\frac{\hbar\omega_{Be}}{2kT}\right) \quad (5.9)$$

$$\simeq \frac{1}{2\pi\rho_0^2 \lambda_{Te}} e^{\mu_e/kT}, \quad (5.10)$$

where  $g_{n_L} = 1$  for  $n_L = 0$  and  $g_{n_L} = 2$  for  $n_L > 0$  are the Landau degeneracies,  $\lambda_{Te} = (2\pi\hbar^2/m_e kT)^{1/2}$  is the electron thermal wavelength, and the last equality applies for  $kT \ll \hbar\omega_{Be}$ . The magnetic field length is  $\rho_0 = (\hbar c/eB)^{1/2}$ . For atomic, ionic, or molecular Fe the number density is given by

$$n(\text{Fe}_A) \simeq \frac{1}{h^3} e^{\mu_A/kT} \sum_i \exp\left(-\frac{\mathcal{E}_{A,i}}{kT}\right) \int d^3K \exp\left(\frac{-K^2}{2M_A kT}\right) \quad (5.11)$$

$$\simeq \frac{1}{\lambda_{TA}^3} \exp\left(-\frac{\mathcal{E}_A - \mu_A}{kT}\right) Z_{\text{int}}(\text{Fe}_A), \quad (5.12)$$

with the internal partition function

$$Z_{\text{int}}(\text{Fe}_A) = \sum_i \exp\left(-\frac{\Delta\mathcal{E}_{A,i}}{kT}\right). \quad (5.13)$$

and  $\Delta\mathcal{E}_{A,i} = \mathcal{E}_{A,i} - \mathcal{E}_A$ . Here, the subscript  $A$  represents the atomic, ionic, or molecular species whose number density we are calculating (e.g.,  $\text{Fe}_2$  or  $\text{Fe}^+$ ) and the sum  $\sum_i$  is over all excited states of that species. Also,  $\lambda_{Te} = (2\pi\hbar^2/M_A kT)^{1/2}$  is the Fe particle's thermal wavelength, where  $M_A = NAM$  is the total mass of the particle ( $N$  is the number of “atoms” in the molecule,  $A$  is the atomic mass number, and  $M = m_p + m_e$ ). The vector  $\mathbf{K}$  represents the center-of-mass momentum of the particle. Note that we have assumed here that the  $\text{Fe}_A$  particle moves across the field freely; this is a good approximation for large  $M_A$ . The internal partition function  $Z_{\text{int}}$  represents the effect of all excited states of the species on the total density; in this work we will use the approximation that this factor is the same for all species, and we will estimate the magnitude of this factor later in this section.

The equilibrium condition  $\mu_s = \mu(\text{Fe})$  for the process  $\text{Fe}_{s,\infty} + \text{Fe} = \text{Fe}_{s,\infty+1}$  yields the atomic density in the saturated vapor:

$$n(\text{Fe}) \simeq \left( \frac{AMkT}{2\pi\hbar^2} \right)^{3/2} \exp \left( -\frac{Q_s}{kT} \right) Z_{\text{int}}, \quad (5.14)$$

where  $Q_s = \mathcal{E}_1 - \mathcal{E}_s$  is the cohesive energy of the condensed Fe. The condition  $N\mu_s = \mu(\text{Fe}_N)$  for the process  $\text{Fe}_{s,\infty} + \text{Fe}_N = \text{Fe}_{s,\infty+N}$  yields the molecular density in the vapor:

$$n(\text{Fe}_N) \simeq \left( \frac{NAMkT}{2\pi\hbar^2} \right)^{3/2} \exp \left( -\frac{S_N}{kT} \right) Z_{\text{int}}, \quad (5.15)$$

where

$$S_N = \mathcal{E}_N - N\mathcal{E}_s = N[Q_s - (\mathcal{E}_1 - \mathcal{E}_N/N)] \quad (5.16)$$

is the “surface energy” and  $\mathcal{E}_N/N$  is the energy per ion in the molecule. The equilibrium condition  $\mu(\text{Fe}^{n+}) = \mu_e + \mu(\text{Fe}^{(n+1)+})$  for the process  $e + \text{Fe}^{n+} = \text{Fe}^{(n+1)+}$ , where  $\text{Fe}^{n+}$  is the  $n$ th ionized state of Fe, yields the vapor densities for the ions:

$$n(\text{Fe}^+)n_e \simeq \frac{b}{2\pi a_0^2} \sqrt{\frac{m_e kT}{2\pi\hbar^2}} \exp \left( -\frac{I_1}{kT} \right) n(\text{Fe}), \quad (5.17)$$

$$n(\text{Fe}^{2+})n_e \simeq \frac{b}{2\pi a_0^2} \sqrt{\frac{m_e kT}{2\pi\hbar^2}} \exp \left( -\frac{I_2}{kT} \right) n(\text{Fe}^+), \quad (5.18)$$

and so on. Here,  $b = B/B_0$  and  $a_0$  is the Bohr radius, and  $I_n = \mathcal{E}_{(n-1)+} - \mathcal{E}_{n+}$  represents the ionization energy of the  $n$ th ionized state of Fe (i.e., the amount of energy required to remove the  $n$ th electron from the atom when the first  $n - 1$  electrons have already been removed). The total electron density in the saturated vapor is

$$n_e = n(\text{Fe}^+) + 2n(\text{Fe}^{2+}) + \dots \quad (5.19)$$

The number densities of electrons [Eq. (5.19)] and ions [e.g., Eqs. (5.17) and (5.18)] must be found self-consistently, for all ion species that contribute significantly to the total vapor density. The total mass density in the vapor is calculated from the

number densities of all of the species discussed above, using the formula

$$\rho_g = AM \left[ n(\text{Fe}) + 2n(\text{Fe}_2) + \cdots + n(\text{Fe}^+) + n(\text{Fe}^{2+}) + \cdots \right]. \quad (5.20)$$

Figure 5.5 (for Fe) and Fig. 5.6 (for C) show the the densities of different atomic/molecular species in the saturated vapor in phase equilibrium with the condensed matter for different temperatures and field strengths. These are computed using the values of  $\mathcal{E}_N/N$ ,  $\mathcal{E}_s$ , and  $\mathcal{E}_{n+}$  presented in ML06a,b and depicted in Figs. 5.2 and 5.3. As expected, for sufficiently low temperatures, the total gas density in the vapor is much smaller than the condensation density, and thus phase separation is achieved. The critical temperature  $T_{\text{crit}}$ , below which phase separation between the condensate and the gaseous vapor occurs, is determined by the condition  $\rho_s = \rho_g$ ; the values of  $\rho_s$  we use are given in ML06b. We find that for Fe:

$$T_{\text{crit}} \simeq 6 \times 10^5, 7 \times 10^5, 3 \times 10^6, 10^7, 2 \times 10^7 \text{ K} \quad \text{for } B_{12} = 5, 10, 100, 500, 1000, \quad (5.21)$$

for C:

$$T_{\text{crit}} \simeq 9 \times 10^4, 3 \times 10^5, 3 \times 10^6, 2 \times 10^7 \text{ K} \quad \text{for } B_{12} = 1, 10, 100, 1000. \quad (5.22)$$

and for He:

$$T_{\text{crit}} \simeq 8 \times 10^4, 3 \times 10^5, 2 \times 10^6, 9 \times 10^6 \text{ K} \quad \text{for } B_{12} = 1, 10, 100, 1000. \quad (5.23)$$

In terms of the cohesive energy, these results can be approximated by

$$kT_{\text{crit}} \sim 0.08 Q_s. \quad (5.24)$$

Note that in our calculations for the iron vapor density at  $B_{12} = 5$ -500 we have estimated the magnitude of the internal partition function factor  $Z_{\text{int}}$ ; the

modified total density curves are marked on these figures as “ $\rho_g \times Z_{\text{int}}$ ”. To estimate  $Z_{\text{int}}$  we use Eq. (5.13) with a cutoff to the summation above some energy. For  $B_{12} = 5, 10, 100$ , and 500 we calculate or interpolate the energies for all excited states of atomic Fe with energy below this cutoff, in order to find  $Z_{\text{int}}$ . The energy cutoff is necessary because the highly excited states become unbound (ionized) due to finite pressure and should not be included in  $Z_{\text{int}}$  (otherwise  $Z_{\text{int}}$  would diverge). In principle, the cutoff is determined by requiring the effective size of the excited state to be smaller than the inter-particle space in the gas, which in turn depends on density. In practice, we choose the cutoff such that the highest excited state has a binding energy  $|\mathcal{E}_{A,i}|$  significantly smaller than the ground-state binding energy  $|\mathcal{E}_A|$  (typically 30% of it). As an approximation, we also assume that the internal partitions for  $\text{Fe}_N$  molecules and ions have the same  $Z_{\text{int}}$  as the Fe atom. Despite the crudeness of our calculation of  $Z_{\text{int}}$ , we see from Fig. 5.5 that the resulting  $T_{\text{crit}}$  is only reduced by a few tens of a percent from the  $T_{\text{crit}}$  value assuming  $Z_{\text{int}} = 1$ .

We note that our calculation of the saturated vapor density is very uncertain around  $T \sim T_{\text{crit}}$ , since Eqs. (5.14) – (5.18) are derived for  $\rho_g \ll \rho_s$  while the critical temperature of the saturated vapor density is found by setting  $\rho_s = \rho_g$ . However, since the vapor density decreases rapidly as  $T$  decreases, when the temperature is below  $T_{\text{crit}}/2$  (for example), the vapor density becomes much less than the condensation density and phase transition is unavoidable. When the temperature drops below a fraction of  $T_{\text{crit}}$ , the vapor density becomes so low that the optical depth of the vapor is negligible and the outermost layer of the neutron star then consists of condensed matter. The radiative properties of such condensed phase surfaces have been studied using a simplified treatment of the condensed matter (see van Adelsberg et al. 2005 and references therein).



Here we estimate the critical atmosphere density below which the optical depth of the vapor is negligible, following the method of Lai (2001). The key parameter is the photosphere density, the density at which the optical depth  $\tau = 2/3$ . When the atmospheric density is much less than this value, the vapor will be negligible and radiation will freely stream from the condensed surface. The photosphere density can be estimated by

$$\rho_{\text{ph}} \simeq 2/(3h\kappa_R), \quad (5.25)$$

where  $h \simeq kT_{\text{ph}}/(AMg)$  is the scale height,  $g$  is the gravitational acceleration, and  $\kappa_R$  is the Rosseland mean opacity. As a first approximation we will assume that the opacity is dominated by free-free absorption (in the presence of singly-ionized atoms), in which case the mean opacity is given by (Silant'ev & Yakovlev 1980)

$$\kappa_R \simeq 400 \left( \frac{kT}{\hbar\omega_{Be}} \right)^2 \kappa_R(0), \quad (5.26)$$

with  $\omega_{Be}$  the electron cyclotron frequency and  $\kappa_R(0)$  the zero-field opacity. Therefore, the critical atmosphere density is

$$\rho_{\text{crit}} \ll \rho_{\text{ph}} \simeq 0.9A^{1/2}g_{14}^{1/2}T_6B_{12} \text{ g/cm}^3, \quad (5.27)$$

where  $g_{14} = g/(10^{14} \text{ cm/s}^2)$ . Note that for the Fe and C atmospheres represented in Figs. 5.5 and 5.6,  $\rho_g \simeq \rho_{\text{ph}}$  when  $T \simeq T_{\text{crit}}/2$ ; therefore, if  $T \lesssim T_{\text{crit}}/2$  the atmosphere will have negligible optical depth.

## 5.4 Polar vacuum gap accelerators in pulsars and magnetars

A rotating, magnetized neutron star is surrounded by a magnetosphere filled with plasma. The plasma is assumed to be an excellent conductor, such that the charged

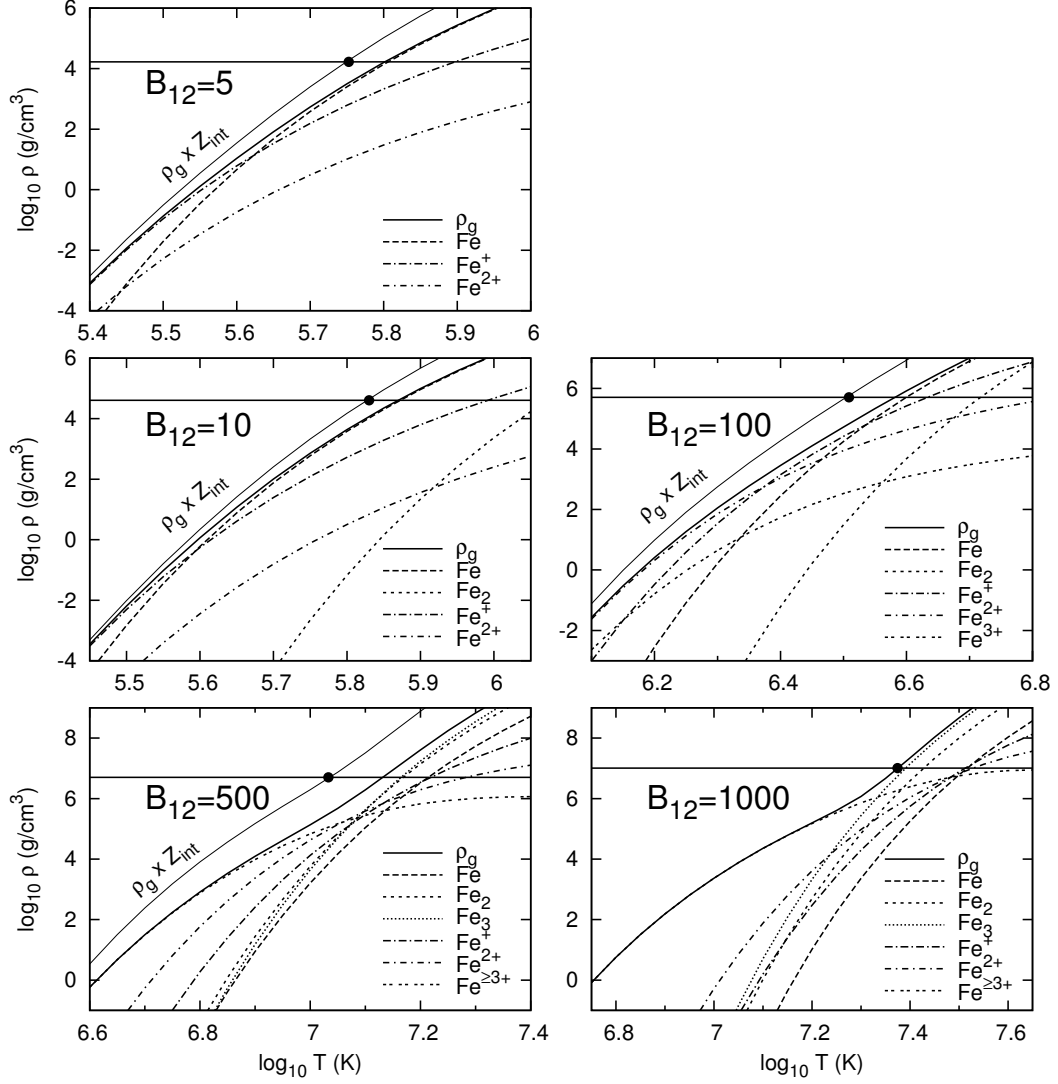


Figure 5.5: The mass densities of various atomic/ionic/molecular species and the total density ( $\rho_g$ ) of the vapor in phase equilibrium with the condensed iron surface. The five panels are for different field strengths,  $B_{12} = 5, 10, 100, 500, 1000$ . The horizontal lines give the densities of the condensed phase,  $\rho_s$  (ML06b). All the vapor density curves are calculated assuming  $Z_{\text{int}} = 1$ , except for the curve marked by “ $\rho_g \times Z_{\text{int}}$ ”, for which the total vapor density is calculated taking into account the nontrivial internal partition functions of various species. The critical temperature  $T_{\text{crit}}$  for phase separation is set by the condition  $\rho_g = \rho_s$  (marked on each plot by a filled circle).

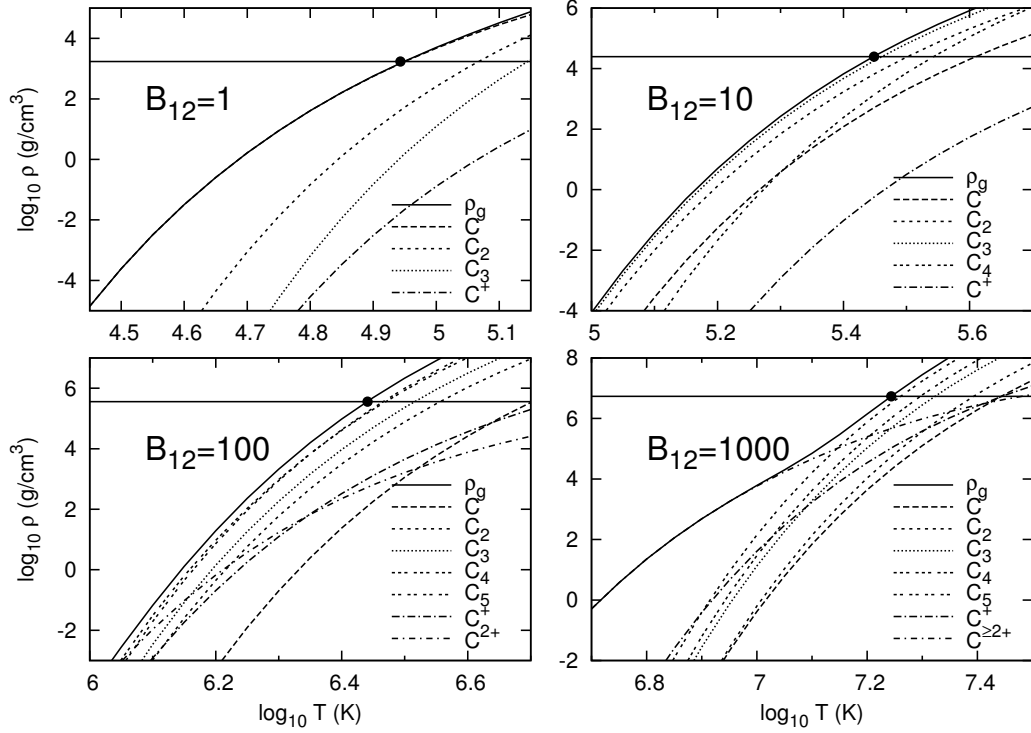


Figure 5.6: The mass densities of various atomic/ionic/molecular species and the total density ( $\rho_g$ ) of the vapor in phase equilibrium with the condensed carbon surface. The four panels are for different field strengths,  $B_{12} = 1, 10, 100, 1000$ . The horizontal lines give the densities of the condensed phase,  $\rho_s$ . All the vapor density curves are calculated assuming  $Z_{\text{int}} = 1$ . The critical temperature  $T_{\text{crit}}$  for phase separation is set by the condition  $\rho_g = \rho_s$  (marked on each plot by a filled circle).

particles move to screen out any electric field parallel to the local magnetic field. The corresponding charge density is given by (Goldreich & Julian 1969)

$$\rho_{GJ} \simeq -\frac{\boldsymbol{\Omega} \cdot \mathbf{B}}{2\pi c} \quad (5.28)$$

where  $\boldsymbol{\Omega}$  is the rotation rate of the neutron star.

The Goldreich-Julian density assumes that charged particles are always available. This may not be satisfied everywhere in the magnetosphere. In particular, charged particles traveling outward along the open field lines originating from the polar cap region of the neutron star will escape beyond the light cylinder. To maintain the required magnetosphere charge density these particles have to be replenished by the stellar surface. If the surface temperature and cohesive strength are such that the required particles are tightly bound to the stellar surface, those regions of the polar cap through which the charged particles are escaping will not be replenished. A vacuum gap will then develop just above the polar cap (e.g., Ruderman & Sutherland 1975; Cheng & Ruderman 1980; Usov & Melrose 1996; Zhang, Harding, & Muslimov 2000; Gil, Melikidze, & Geppert 2003). In this vacuum gap zone the parallel electric field is no longer screened and particles are accelerated across the gap until vacuum breakdown (via pair cascade) shorts out the gap. Such an acceleration region can have an important effect on neutron star emission processes. We note that in the absence of a vacuum gap, a polar gap acceleration zone based on space-charge-limited flow may still develop (e.g., Arons & Scharlemann 1979; Harding & Muslimov 1998; Muslimov & Harding 2003).

In this section we determine the conditions required for the vacuum gap to exist using our results summarized in Section 5.2. The cohesive energy and electron work function of the condensed neutron star surface are obviously the key factors. We examine the physics of particle emission from condensed surface in more detail

than considered previously.

### 5.4.1 Particle emission from condensed neutron star surfaces

We assume that the NS surface is in the condensed state, i.e., the surface temperature  $T$  is less than the critical temperature  $T_{\text{crit}}$  for phase separation (see Section 5.3). (If  $T > T_{\text{crit}}$ , the surface will be in gaseous phase and a vacuum gap will not form.) We shall see that in order for the surface not to emit too large a flux of charges to the magnetosphere (a necessary condition for the vacuum gap to exist), an even lower surface temperature will be required.

#### Electron emission

For neutron stars with  $\boldsymbol{\Omega} \cdot \mathbf{B}_p > 0$ , where  $\mathbf{B}_p$  is the magnetic field at the polar cap, the Goldreich-Julian charge density is negative at the polar cap, thus surface electron emission (often called thermionic emission in solid state physics; Ashcroft & Mermin 1976) is relevant. Let  $\mathcal{F}_e$  be the number flux of electrons emitted from the neutron star surface. The emitted electrons are accelerated to relativistic speed quickly, and thus the steady-state charge density is  $\rho_e = -e\mathcal{F}_e/c$ . For the vacuum gap to exist, we require  $|\rho_e| < |\rho_{\text{GJ}}|$ . (If  $|e\mathcal{F}_e/c| > |\rho_{\text{GJ}}|$ , the charges will be rearranged so that the charge density equals  $\rho_{\text{GJ}}$ .)

To calculate the electron emission flux from the condensed surface, we assume that these electrons behave like a free electron gas in a metal, where the energy barrier they must overcome is the work function of the metal. In a strong magnetic

field, the electron flux is given by

$$\mathcal{F}_e = \int_{p_{\min}}^{\infty} f(\epsilon) \frac{p_z}{m_e} \frac{1}{2\pi\rho_0^2} \frac{dp_z}{h}, \quad (5.29)$$

where  $p_{\min} = \sqrt{2m_e|U_0|}$ ,  $U_0$  is the potential energy of the electrons in the metal,  $\epsilon = p_z^2/(2m_e)$  is the electron kinetic energy, and

$$f(\epsilon) = \frac{1}{e^{(\epsilon - \mu'_e)/kT} + 1} \quad (5.30)$$

is the Fermi-Dirac distribution function with  $\mu'_e$  the electron chemical potential (excluding potential energy). Integrating this expression gives

$$\mathcal{F}_e = \frac{kT}{2\pi h \rho_0^2} \ln [1 + e^{-\phi/kT}] \simeq \frac{kT}{2\pi h \rho_0^2} e^{-\phi/kT}, \quad (5.31)$$

where  $\phi \equiv |U_0| - \mu'_e$  is the work function of the condensed matter and the second equality assumes  $\phi \gg kT$ . The steady-state charge density supplied by the surface is then

$$\rho_e = -\frac{e}{c} \mathcal{F}_e = \rho_{GJ} \exp(C_e - \phi/kT), \quad (5.32)$$

with

$$C_e = \ln \left( \frac{e}{c} \frac{kT}{2\pi h \rho_0^2 |\rho_{GJ}|} \right) \simeq 31 + \ln(P_0 T_6) \sim 30, \quad (5.33)$$

where  $T_6 = T/(10^6 \text{ K})$  and  $P_0$  is the spin period in units of 1 s. For a typical set of pulsar parameters (e.g.,  $P_0 = 1$  and  $T_6 = 0.5$ )  $C_e \sim 30$ , but  $C_e$  can range from 23 for millisecond pulsars to 35 for some magnetars. Note that the requirement  $\phi \gg kT$  is automatically satisfied here when  $|\rho_e|$  is less than  $|\rho_{GJ}|$ . The electron work function was calculated in ML06b and is depicted in Fig. 5.4.

## Ion emission

For neutron stars with  $\boldsymbol{\Omega} \cdot \mathbf{B}_p < 0$ , the Goldreich-Julian charge above the polar cap is positive, so we are interested in ion emission from the surface. Unlike the

electrons, which form a relatively free-moving gas within the condensed matter, the ions are bound to their lattice sites.<sup>1</sup> To escape from the surface, the ions must satisfy three conditions. First, they must be located on the surface of the lattice. Ions below the surface will encounter too much resistance in trying to move through another ion's cell. Second, they must have enough energy to escape as unbound ions. This binding energy that must be overcome will be labeled  $\mathcal{E}_B$ . Third, they must be thermally activated. The energy in the lattice is mostly transferred by conduction, so the ions must wait until they are bumped by atoms below to gain enough energy to escape.

Consider the emission of ions with charge  $Z_n e$  from the neutron star surface (e.g.,  $\text{Fe}^+$  would have  $Z_n = 1$ ). The rate of collisions between any two ions in the lattice is approximately equal to the lattice vibration frequency  $\nu_i$ , which can be estimated from

$$\nu_i = \frac{1}{2\pi} \left( \Omega_p^2 + \omega_{ci}^2 \right)^{1/2}, \quad (5.34)$$

where  $\Omega_p = (4\pi Z^2 e^2 n_i / m_i)^{1/2}$  is the ion plasma (angular) frequency and  $\omega_{ci} = ZeB/(m_i c)$  is the ion cyclotron frequency ( $m_i = Am_p$ ). Not all collisions will lead to ejection of ions from the surface, since an energy barrier  $\mathcal{E}_B$  must be overcome. Thus each surface ion has an effective emission rate of order

$$\chi = \nu_i e^{-\mathcal{E}_B/kT}. \quad (5.35)$$

The energy barrier  $\mathcal{E}_B$  for ejecting ions of charge  $Z_n e$  is equivalent to the energy required to release a neutral atom from the surface and ionize it, minus the energy gained by returning the electron to the surface (e.g., Tsong 1990). Thus

$$\mathcal{E}_B = Q_s + \sum_{i=1}^{Z_n} I_i - Z_n \phi, \quad (5.36)$$

---

<sup>1</sup>The freezing condition is easily satisfied for condensed matter of heavy elements (see van Adelsberg et al. 2005).

where  $Q_s > 0$  is the cohesive energy,  $I_i > 0$  is the  $i$ th ionization energy of the atom (so that  $\sum_{i=1}^{Z_n} I_i$  is the energy required to remove  $Z_n$  electrons from the atom), and  $\phi > 0$  is the electron work function. The surface density of ions is  $n_i r_i$ , where  $r_i$  is the mean spacing between ions in the solid. Thus the emission flux of  $Z_n$ -ions is

$$\mathcal{F}_i = \nu_i n_i r_i e^{-\mathcal{E}_B/kT}. \quad (5.37)$$

The steady-state  $Z_n$ -ion number density supplied by the surface is then

$$\rho_i = \frac{Z_n e}{c} \mathcal{F}_i = \rho_{GJ} \exp(C_i - \mathcal{E}_B/kT), \quad (5.38)$$

with

$$\begin{aligned} C_i &= \ln \left( \frac{Z_n e \nu_i n_i r_i}{c \rho_{GJ}} \right) \\ &\simeq 34 + \ln \left\{ Z_n Z A^{-1/2} n_{28}^{3/2} (r_i/a_0) B_{12}^{-1} P_0 \sqrt{1 + 5.2 \times 10^{-3} A^{-1} B_{12}^2 n_{28}^{-1}} \right\} \\ &\sim 27-33, \end{aligned} \quad (5.39)$$

where  $n_{28} = n_i/(10^{28} \text{ cm}^{-3})$ . For a typical set of pulsar parameters (e.g.,  $B_{12} = 1$  and  $P_0 = 1$ )  $C_i \sim 27$ , but  $C_i$  can be as large as 33 for magnetars with  $B_{12} = 1000$  and  $P_0 = 8$ .

All the quantities in  $\mathcal{E}_B$  were calculated in ML06b (see Figs. 5.2 and 5.3). We find that the emission of singly-ionized atoms ( $Z_n = 1$ ) is most efficient, as  $\mathcal{E}_B$  is significantly lower for  $Z_n = 1$  than for  $Z_n > 1$  ( $\sum_{i=1}^{Z_n} I_i$  grows much faster with  $Z_n$  than  $Z_n \phi$  does).

### Effect of electric field on charge emission

The discussion in Sections 5.4.1 and 5.4.1 includes only thermal emission of charged particles from the condensed surface. A strong electric field, of order  $E_s \sim \Omega B R/c$ ,



may be present. Since this electric field is much less than the characteristic field  $\sim e/r_i^2$  inside the condensed matter (where  $r_i$  is the mean particle separation), this field cannot directly rip charges off the surface. Nevertheless, the electric field may enhance the thermal emission of charge particles. We now estimate the magnitude of this effect.

In the presence of a vacuum gap, the electric field  $E_s$  at the stellar surface points outward ( $E_s > 0$ ) for stars with  $\mathbf{\Omega} \cdot \mathbf{B}_p < 0$  and inward ( $E_s < 0$ ) for stars with  $\mathbf{\Omega} \cdot \mathbf{B}_p > 0$ . A charge  $Q$  moved to some small height  $z$  above the surface gains a potential energy given by  $U = -Q^2/(4z) - QE_s z$ , where the first term is due to the interaction between the charge and the perfectly conducting metal surface, and the second term is due to the external field.<sup>2</sup> The potential reaches a maximum value

$$U_{\max} = -|Q|^{3/2}|E_s|^{1/2} \quad (5.40)$$

at the height  $z = |Q/4E_s|^{1/2}$ . Thus, compared to the  $E_s = 0$  case, the energy barrier for particle emission is now reduced by the amount  $U_{\max}$ .

Combining this consideration with the results of Sections 5.4.1 and 5.4.1, we find that steady-state charge density due to electron surface emission (for  $\mathbf{\Omega} \cdot \mathbf{B}_p > 0$  stars) is (cf. Jessner et al. 2001)

$$\rho_e = \rho_{GJ} \exp[C_e - (\phi - e^{3/2}|E_s|^{1/2})/kT], \quad (5.41)$$

and the steady-state charge density due to ion surface emission (for  $\mathbf{\Omega} \cdot \mathbf{B}_p < 0$  stars) is

$$\rho_i = \rho_{GJ} \exp[C_i - (\mathcal{E}_B - (Z_n e)^{3/2}|E_s|^{1/2})/kT]. \quad (5.42)$$

---

<sup>2</sup>In the vacuum gap, the electric field is not exactly uniform, but since the maximum  $U$  is attained at a rather small height compared to the gap thickness, this nonuniformity is unimportant for our consideration here.

For  $E_s \sim \Omega BR/c$ , we have  $e^{3/2}|E_s|^{1/2} \sim 10$  eV. This is typically much smaller than either  $\phi$  or  $\mathcal{E}_B$ .

### 5.4.2 Conditions for gap formation

No vacuum gap will form if the electrons or ions are able to fill the magnetosphere region above the polar cap with the required Goldreich-Julian density; i.e., the vacuum gap will cease to exist when  $\rho_e = \rho_{GJ}$  or  $\rho_i = \rho_{GJ}$ . From Eqs. (5.42) and (5.41) we can see that no polar gap will form if

$$\phi - e^{3/2}|E_s|^{1/2} < C_e kT \sim 3T_6 \text{ keV} \quad (5.43)$$

for a negative polar magnetosphere ( $\mathbf{\Omega} \cdot \mathbf{B}_p > 0$ ), and

$$\mathcal{E}_B - (Z_n e)^{3/2}|E_s|^{1/2} < C_i kT \sim 3T_6 \text{ keV} \quad (5.44)$$

for a positive polar magnetosphere ( $\mathbf{\Omega} \cdot \mathbf{B}_p < 0$ ). [For the exact expressions for  $C_e$  and  $C_i$  see Eqs. (5.33) and (5.39).]

For neutron stars in general, the electron work function  $\phi$  is much less than  $C_e kT \sim 3T_6$  keV (see Fig. 5.4), so electrons can easily escape from the condensed surface. No gap forms for a negative polar magnetosphere under neutron star surface conditions. (This is contrary to the conclusions of Usov & Melrose 1996 and Gil et al. 2003.) The ion binding energy  $\mathcal{E}_B$  [given by Eq. (5.36)], on the other hand, can be larger than  $C_i kT \sim 3T_6$  keV under certain neutron star surface conditions (see Figs. 5.1, 5.2, and 5.3). Ions can tightly bind to the condensed surface and a polar gap can form under these conditions. Figure 5.7 shows the critical temperature (determined by  $\mathcal{E}_B = C_i kT$ ) below which a vacuum gap can form for the Fe, C, and He surfaces.

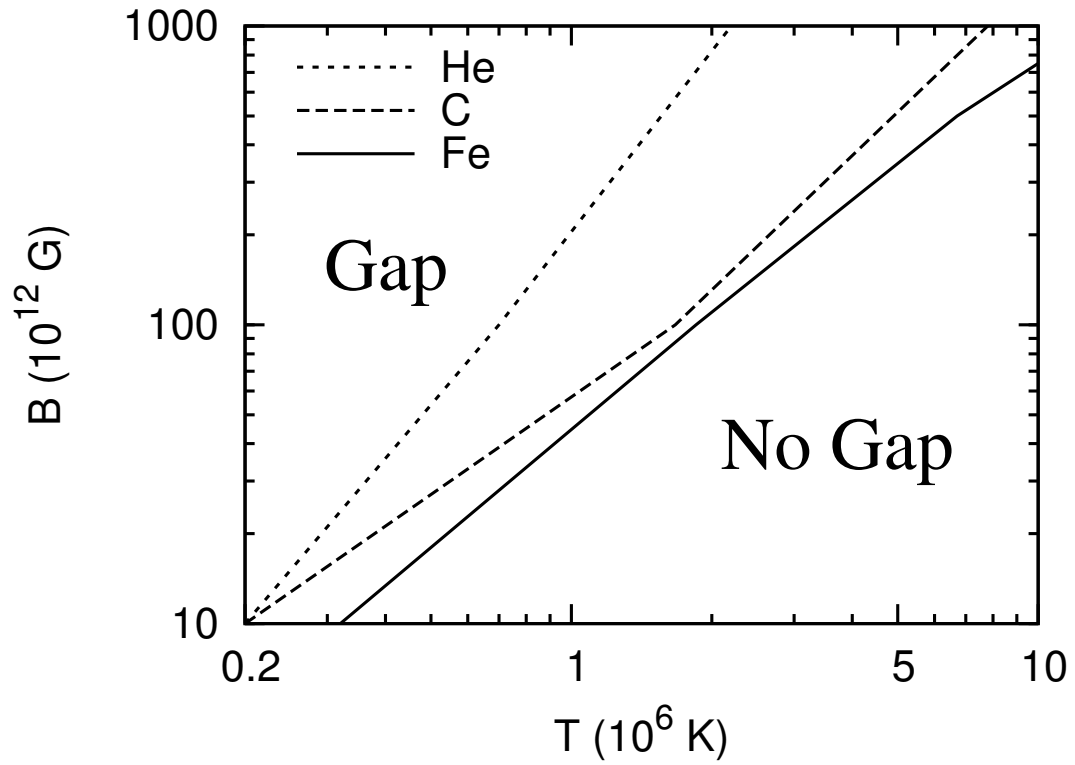


Figure 5.7: The condition for the formation of a vacuum gap above condensed helium, carbon, and iron neutron star surfaces, when the magnetosphere is positive over the poles ( $\boldsymbol{\Omega} \cdot \mathbf{B}_p < 0$ ).

## 5.5 Discussion

It is well known that a strong magnetic field increases the binding energy of individual atom and that of the zero-pressure condensed matter. Very approximately, for  $B \gg B_0$  [see Eq. (1)], the former increases as  $(\ln B)^2$  while the latter scales as  $B^{0.4}$ . Therefore one expects that the outermost layer of a neutron star may be in the condensed state when the magnetic field  $B$  is sufficiently strong and/or the surface temperature  $T$  is sufficiently low. Exactly under what conditions this occurs is an important question that entails quantitative calculations. In this chapter, using our recent results on the cohesive properties of magnetized condensed matter (Medin & Lai 2006a,b), we have established quantitatively the parameter regime (in  $B$  and  $T$  space) for which surface condensation occurs. Our calculations showed that there are a range of neutron star magnetic field strengths and surface temperatures where the condensed surface will have an important effect on radiation from these stars. For example, if the surface composition is Fe, then strong-field neutron stars ( $B \gtrsim 10^{13}$  G) with moderate ( $T \lesssim 10^6$  K) surface temperatures should have atmospheres/vapors that are effectively transparent to thermal radiation, so that the emission becomes that from a bare condensed surface. This may explain the nearly blackbody-like radiation spectrum observed from the nearby isolated neutron star RX J1856.5-3754 (e.g., Burwitz et al 2003; van Adelsberg et al. 2005; Ho et al. 2007).

We have also examined the conditions for the formation of a vacuum acceleration gap above the polar cap region of the neutron star. The inner acceleration gap model, first developed by Ruderman & Sutherland (1975), has provided a useful framework to understand numerous observations of radio pulsars. Most notably, the model naturally explains the phenomenon of drifting subpulses observed in

many pulsars (e.g., Backer 1976; Deshpande & Rankin 1999; Weltevrede et al. 2006) in terms of the  $\mathbf{E} \times \mathbf{B}$  circulation of plasma filaments produced by vacuum discharges. Partially screened gaps have also been studied (e.g., Cheng & Ruderman 1980; Gil et al. 2003, 2006). However, it has long been recognized that the original Ruderman & Sutherland model is problematic since the dipole magnetic field inferred from  $P, \dot{P}$  may not be strong enough to inhibit charge emission from the surface. Our calculations described in this chapter quantify the condition for vacuum gap formation (see Fig. 5.7). While this condition (i.e.,  $T$  is smaller than a critical value which depends on  $B$  and composition) may not be satisfied for most pulsars (unless one invokes surface magnetic fields much stronger than that inferred from  $P, \dot{P}$ ; see Gil et al. 2006 and references therein), it could well be satisfied for some neutron stars. In particular, the recently discovered high-B radio pulsars, having dipole surface magnetic fields in excess of  $10^{14}$  G and temperature about  $10^6$  K (e.g., Kaspi & Gavril 2004; Kaspi & McLaughlin 2005), may operate a vacuum gap accelerator. On the other hand, while magnetars have similar magnetic field strengths, their surface temperatures are about five times larger than those of high-B radio pulsars, and therefore may not have a vacuum gap. In this regard, it is interesting to note that most magnetars do not show radio emission (though this may be because the radio pulse is beamed away from us or the because their magnetosphere plasma “overwhelms” the radio pulses), and the two recently detected radio magnetars have rather different radio emission properties (e.g., the spectrum extends to high frequency and the radiation shows high degrees of linear polarization) compared to “normal” radio pulsars. We may therefore speculate that a key difference between magnetars and high-B radio pulsars is their difference in surface temperature. In any case, our gap formation condition (Fig. 5.7) suggests that the radio emission property of neutron stars may depend not only

on the magnetic field and rotation rate, but also on the surface temperature.

We note that our calculation of the requirements for vacuum gap formation assumes idealized conditions. A real neutron star polar cap may be immersed in a strong radiation field and suffer bombardment from high energy particles (e.g., Arons 1981; Beloborodov & Thompson 2007). The effective cohesive energy of the surface may be somewhat smaller than what we used in our chapter due to surface defects (Arons 2007, private communication). Whether the vacuum gap survives in realistic situations is unclear. It has been suggested that a partially screened gap is formed instead (Gil et al. 2003, 2006).

## PAIR CASCADES IN PULSAR MAGNETOSPHERES: POLAR GAP ACCELERATORS AND THE PULSAR DEATH LINE/BOUNDARY

### 6.1 Introduction

It has been known for over three decades that the magnetosphere of a pulsar is the source of its pulsed radio emission (Goldreich & Julian 1969; Sturrock 1971). What is less clear is how the mechanism for creating this radio emission works and why it shuts off under certain conditions, such as those in the magnetosphere of a magnetar. Of the dozen observed magnetars, only two show pulsed radio emission, and it is of a completely different nature than the emission from “standard” radio pulsars (e.g., the radio pulsations are transient and appear to be correlated with strong X-ray outbursts from the magnetars; see Camilo et al. 2007). In contrast, several radio pulsars with inferred surface field strengths similar to those of magnetars have been discovered (e.g., Kaspi & McLaughlin 2005; Vranevsevic et al. 2007). A deeper understanding of the various types of pulsars and their distinction from magnetars requires further investigation of the neutron star magnetosphere, where the radio and other pulsed emission originates.

A rotating, magnetized neutron star generates a strong electric field and leads to large voltage drops across the magnetosphere region. Particles accelerated across these drops reach energies of  $10^{12}$  eV or more and initiate cascades of pair production. More specifically, initiation of the pair cascade requires: (a) acceleration of charged particles by an electric field parallel to the magnetic field; (b) gamma ray emission by the accelerated particles moving along the magnetic field lines (either by curvature radiation or inverse Compton upscattering of surface photons); (c)

photon decay into pairs as the angle between the photon and the field line becomes sufficiently large. It is generally agreed that the highly-relativistic electron-positron plasma generated by the pair cascade is an essential ingredient for pulsar radio emission (e.g., Melrose 2004), though the exact mechanism for converting this plasma into coherent radio waves is not yet known. The large number of high energy photons generated by the cascade appear as pulsed emission in gamma-ray and X-ray pulsars; observations suggest that only the strongest cascades (largest potential drops) lead to detectable gamma ray pulses (e.g., Thompson 2004).

To initiate the cascade an acceleration region is required; the characteristics of this particle accelerator determine whether pulsar emission can operate or not (the so-called “pulsar death line”; e.g., Ruderman & Sutherland 1975; Arons 2000; Zhang et al. 2000; Hirschman & Arons 2001a). Depending on the boundary condition at the neutron star surface, there are two types of polar (“inner”) gap accelerators: If charged particles are strongly bound to the neutron star surface by cohesive forces, a vacuum gap develops directly above the surface, with height  $h$  much less than the stellar radius (Ruderman & Sutherland 1975); if charged particles can be freely extracted from the surface, a more extended space-charge-limited-flow (SCLF) type accelerator develops due to field line curvatures (Arons & Scharlemann 1979) and the relativistic frame dragging effect (e.g., Muslimov & Tsygan 1992). Because the cohesive strength of matter at  $B \sim 10^{12}$  G was thought to be negligible (based on the result of Neuhauser et al. 1987), most theoretical works in recent years have focused on the SCLF models (e.g., Arons 2000; Muslimov & Harding 2003, 2004). However, our results in Chapter 5 show that for sufficiently strong magnetic fields and/or low surface temperatures, a vacuum gap accelerator can form. Such a vacuum gap may be particularly relevant for the so-called high-B radio pulsars, which have inferred magnetic fields similar to those



of magnetars (e.g., Kaspi & McLaughlin 2005; Burgay et al. 2006). As discussed in Section 5.4, since electrons are weakly bound to the condensed stellar surface, such a vacuum gap is possible only for pulsars with  $\boldsymbol{\Omega} \cdot \mathbf{B}_p < 0$  (as suggested in the original Ruderman-Sutherland model). An “outer gap” accelerator can also form, in regions of the outer magnetosphere where  $\boldsymbol{\Omega} \cdot \mathbf{B}_p < 0$  changes sign along the open field lines (Cheng, Ho, & Ruderman 1986; Romani 1996). Charged particles pulled from the surface will be of the wrong sign to screen the electric field in these regions of the magnetosphere, so that a vacuum gap forms.

In this chapter we discuss the conditions under which an inner gap accelerator will be an effective generator of pulsar emission, both for the vacuum gap and SCLF type models. Here we restrict our analysis to the conditions for gap breakdown, a necessary but not sufficient ingredient for pair cascading and subsequent pulsar emission. (The full cascade will be discussed in Chapter 7.) From our analysis we derive pulsar “death lines”, or more precisely, “death boundaries”, boundaries in parameter space beyond which a pulsar cannot function. Our study makes two improvements over previous studies of inner gap accelerators and pulsar death lines (e.g., Ruderman & Sutherland 1975; Cheng & Ruderman 1980; Usov & Melrose 1996; Zhang et al. 1997 for vacuum gap accelerators; Arons & Scharlemann 1979; Muslimov & Tsygan 1992; Zhang et al. 2000; Hibschan & Arons 2001a; Harding & Muslimov 2002 for SCLF accelerators): we extend our discussion of the cascade physics to the magnetar field regime, and we use a more careful treatment of photon emission due to inverse Compton scattering in the gap.

This chapter is organized as follows. In Section 6.2 we discuss polar gap radiation mechanisms and the pulsar death line/boundary in the vacuum gap model. We find that when curvature radiation is the dominant radiation mechanism in the

gap, vacuum breakdown is possible for a large range of parameter space (in the  $P-\dot{P}$  diagram), but when inverse Compton scattering (either resonant or nonresonant) is the dominant radiation mechanism, vacuum breakdown is possible for only a very small range of parameter values. In Section 6.3 we discuss gap radiation mechanisms and the death boundary in the SCLF model. As with the vacuum gap case we find that gap breakdown is possible over a large range of parameter space when curvature radiation dominates but only a small range of parameter space when inverse Compton scattering dominates. We discuss our results in Section 6.4. Some technical details (on our treatment of inverse Compton scattering and vacuum gap electrodynamics of oblique rotators) are given in Appendix C.

## 6.2 Vacuum gap accelerators

### 6.2.1 Acceleration potential

When the temperature drops below the critical value given in Section 5.4, the charge density above the polar cap decreases quickly below  $\rho_{GJ}$ , and a vacuum gap results. In the vacuum region just above the surface ( $0 \leq z \ll R$ ), the parallel electric field satisfies the equation  $dE_{\parallel}/dz \simeq -4\pi\rho_{GJ}$ . The height of the gap  $h$  ( $\ll R$ ) is determined by vacuum breakdown due to pair cascade, which shorts out the electric field above the gap (i.e.,  $E_{\parallel} = 0$  for  $z \geq h$ ). Thus the electric field in the gap is

$$E_{\parallel} \simeq \frac{2\Omega B_p}{c}(h - z), \quad (6.1)$$

where  $B_p = b_d B_p^d$  is the actual magnetic field at the pole, and differs from the dipole field  $B_p^d$  by a factor  $b_d \geq 1$ . The potential drop across the gap is then

$$\Delta\Phi = \frac{\Omega B_p}{c} h^2 = b_d \frac{\Omega B_p^d}{c} h^2. \quad (6.2)$$

With this potential drop, the electrons and positrons can be accelerated to a Lorentz factor

$$\gamma_m = \frac{e\Delta\Phi}{m_e c^2} = 5.43 \times 10^6 \beta_Q h_3^2 P_0^{-1} = 1.23 \times 10^5 b_d B_{12} h_3^2 P_0^{-1}, \quad (6.3)$$

where  $\beta_Q = B_p/B_Q$  (with  $B_Q = m_e^2 c^3 / e \hbar = 4.414 \times 10^{13}$  G the QED field),  $B_{12} = B_p^d / (10^{12} \text{ G})$ ,  $h_3 = h / (10^3 \text{ cm})$  and  $P_0$  is the spin period in units of 1 s. The voltage drop across the gap can be no larger than the voltage drop across the polar cap region  $\Delta\Phi_{\max} \simeq (\Omega B_p / 2c) (r_{p+})^2 = (\Omega B_p^d / 2c) (r_{p+}^d)^2$ , where  $r_{p+} = r_{p+}^d / b_d^{1/2}$  is the radius of the polar cap through which a net positive current flows:

$$r_{p+}^d = \left(\frac{2}{3}\right)^{3/4} R \left(\frac{\Omega R}{c}\right)^{1/2}. \quad (6.4)$$

Thus the gap height is limited from above by

$$h_{\max} \simeq \frac{r_{p+}^d}{\sqrt{2b_d}} = 7.54 \times 10^3 b_d^{-1/2} P_0^{-1/2} \text{ cm}, \quad (6.5)$$

where we have adopted  $R = 10 \text{ km}$ .

The above equations are for an aligned rotator. For an oblique rotator (where the magnetic dipole axis is inclined relative to the rotation axis), the voltage drop across the polar cap region is larger, of order  $(\Omega B_p / 2c) R r_{p+}$ . But as discussed in Appendix C.1, the acceleration potential across the vacuum gap is still limited from above by  $\Delta\Phi_{\max} \sim (\Omega B_p / 2c) r_{p+}^2$ .

### 6.2.2 Requirements for gap breakdown

There are two requirements for the breakdown of a vacuum gap. First, the photons must be able to create electron-positron pairs within the gap, i.e., the mean free path of photon pair-production is less than the gap height:

$$l_{\text{ph}} < h. \quad (6.6)$$

Second, after being accelerated to large Lorentz factors the electrons and positrons must produce at least a few photons within the gap. If on average only one photon is emitted with the required energy for each electron-positron pair, for instance, then the number of charged particles produced in the gap will grow very slowly and the gap will not break down completely. Therefore, we must have

$$N_{\text{ph}} > \lambda, \quad (6.7)$$

where  $N_{\text{ph}}$  is the number of photons emitted within the gap by each electron or positron, and  $\lambda$  is a number of order 1–10.

### 6.2.3 Pair production

The threshold of pair production for a photon with energy  $\epsilon$  is

$$\frac{\epsilon}{2m_e c^2} \sin \theta > 1, \quad (6.8)$$

where  $\theta$  is the angle of intersection of the photon and the magnetic field. Suppose a photon is emitted at an angle  $\theta_e$ . After the photon travels a distance  $z$ , the intersection angle will grow as  $z/\mathcal{R}_c$ , where  $\mathcal{R}_c$  is the local radius of curvature of the polar magnetic field line. Thus the typical intersection angle (for a photon crossing the entire gap) is

$$\sin \theta \simeq \theta \simeq \frac{h}{\mathcal{R}_c} + \theta_e. \quad (6.9)$$

For a pure dipole field, the curvature radius is of order  $(Rc/\Omega)^{1/2} \simeq 10^8 P_0^{1/2}$  cm, but a more complex field topology at the polar cap could reduce  $\mathcal{R}_c$  to as small as the stellar radius.

In the weak-field regime, when the threshold condition is well-satisfied (so that the pairs are produced in highly excited Landau levels), the mean free path is given by (Erber 1966)

$$l_{\text{ph}} \simeq \frac{4.4a_0}{\beta_Q \sin \theta} \exp\left(\frac{4}{3\chi}\right), \quad \text{with } \chi = \frac{\epsilon}{2m_e c^2} \beta_Q \sin \theta, \quad (6.10)$$

where  $a_0 = \hbar^2/(m_e c^2)$  is the Bohr radius. The condition  $l_{\text{ph}} < h$  implies  $\chi \gtrsim 1/15$  for typical parameters (Ruderman & Sutherland 1975). For stronger magnetic fields ( $\beta_Q \gtrsim 0.1$ ), the pairs tend to be produced at lower Landau levels. Using the general expression for the pair production rate (e.g., Daugherty & Harding 1983), one can check that if the threshold condition Eq. (6.8) is satisfied, the pair-production optical depth across the gap would also be greater than unity [for  $\beta_Q = 0.1$ , the optical depth  $\tau$  is unity when  $\epsilon/(2m_e c^2) \sin \theta > 1.05$ , and by  $\beta_Q = 0.2$ ,  $\tau = 1$  when  $\epsilon/(2m_e c^2) \sin \theta > 1 + 10^{-7}$ ]. Thus for arbitrary field strengths, the condition  $l_{\text{ph}} < h$  leads to the constraint:

$$\frac{\epsilon}{2m_e c^2} \beta_Q \left( \frac{h}{\mathcal{R}_c} + \theta_e \right) \gtrsim \frac{1}{15} (1 + 15\beta_Q). \quad (6.11)$$

#### 6.2.4 Photon emission multiplicity and the pulsar death boundary

There are several possible photon emission mechanisms operating in the vacuum breakdown, each leading to a different death boundary. We consider them separately.

## Curvature radiation (CR)

The characteristic energy of a photon emitted through curvature radiation is  $\epsilon \sim (3/2)\gamma^3\hbar c/\mathcal{R}_c = 4.74 \times 10^9 \beta_Q^3 h_3^6 P_0^{-3} \mathcal{R}_6^{-1}$  eV, where  $\mathcal{R}_6 = \mathcal{R}_c/(10^6 \text{ cm})$ , and we have used  $\gamma \sim \gamma_m$  [Eq. (6.3)]. The emission angle is  $\theta_e \sim \gamma^{-1}$ , which is typically much less than  $h/\mathcal{R}_c$  (this can be easily checked *a posteriori*). Equation (6.11) then reduces to

$$h > h_{\min, \text{ph}} = 546 P_0^{3/7} \mathcal{R}_6^{2/7} \left( \frac{15\beta_Q + 1}{\beta_Q^4} \right)^{1/7} \text{ cm}. \quad (6.12)$$

The rate of energy loss of an electron or positron emitting curvature radiation is  $P_{\text{CR}} = 2e^2\gamma^4/(3c^3)(c^2/\mathcal{R}_c)^2$ , thus the number of photons emitted through curvature radiation by a single electron or positron across the gap is

$$N_{\text{ph}} \simeq \frac{P_{\text{CR}}}{\epsilon} \frac{h}{c} \simeq \frac{4}{9} \frac{e^2}{\hbar c} \frac{\gamma h}{\mathcal{R}_c} = 17.6 \beta_Q h_3^3 P_0^{-1} \mathcal{R}_6^{-1}. \quad (6.13)$$

The condition  $N_{\text{ph}} > \lambda$  [Eq. (6.7)] then gives

$$h \gtrsim h_{\min, \text{e}} = 384 \lambda^{1/3} \beta_Q^{-1/3} P_0^{1/3} \mathcal{R}_6^{1/3} \text{ cm}. \quad (6.14)$$

Thus the minimum gap height required for vacuum breakdown is  $h \simeq \max(h_{\min, \text{ph}}, h_{\min, \text{e}})$ .

Combining Eqs. (6.5), (6.12), and (6.14), we have

$$\max(h_{\min, \text{ph}}, h_{\min, \text{e}}) < h_{\max}. \quad (6.15)$$

This gives a necessary condition for pulsar emission and defines the pulsar “death line”. For all relevant parameter regimes,  $h_{\min, \text{ph}} > h_{\min, \text{e}}$ , and Eq. (6.15) simply becomes  $h_{\min, \text{ph}} < h_{\max}$ . The critical pulsar spin period is then

$$P_{\text{crit}} = 1.64 b_d^{1/13} B_{12}^{8/13} \mathcal{R}_6^{-4/13} (1 + 15\beta_Q)^{-2/13} \text{ s}, \quad (6.16)$$

where the dipole polar field is  $B_{12} = 2.0(P_0 \dot{P}_{15})^{1/2}$ , with  $\dot{P}_{15} = \dot{P}/(10^{-15} \text{ s s}^{-1})$ .

For  $\beta_Q \lesssim 1/15$  this is the same as the result of Ruderman & Sutherland (1975).

In Fig. 6.1, we show the death lines determined from Eq. (6.15) for the cases of  $\mathcal{R}_6 = 1$  and  $\mathcal{R}_6 = 100P_0^{1/2}$  (pure dipole field at the polar cap), with  $b_d = 1$ .

### Resonant inverse Compton scattering (RICS)

Here the high-energy photons in the cascade are produced by Compton upscatterings of thermal photons from the neutron star surface. Resonant scattering in strong magnetic fields (e.g., Herold 1979) can be thought of as resonant absorption (where the electron makes a transition from the ground Landau level to the first excited level) followed by radiative decay. Resonance occurs when the photon energy in the electron rest frame satisfies  $\epsilon' \simeq \epsilon_{Be} = \hbar(eB/m_e c) = \beta_Q m_e c^2$ . The resonant photon energy (in the “lab” frame) before scattering is  $\epsilon_i = \epsilon_{Be}/[\gamma(1 - \cos \theta_i)]$ , where  $\theta_i$  is the incident angle (the angle between the incident photon momentum and the electron velocity). After absorbing a photon, the electron Lorentz factor drops to  $\gamma_e = \gamma/(1 + 2\beta_Q)^{1/2}$ , and then radiatively decays isotropically in its rest frame. The characteristic photon energy after resonant scattering is therefore (e.g., Beloborodov & Thompson 2007)

$$\epsilon = \gamma \left( 1 - \frac{1}{\sqrt{1 + 2\beta_Q}} \right) m_e c^2, \quad (6.17)$$

with typical emission angle  $\theta_e \sim 1/\gamma_e$ . The condition  $l_{\text{ph}} < h$  [see Eq. (6.11)] becomes

$$\frac{\gamma}{2} \left( 1 - \frac{1}{\sqrt{1 + 2\beta_Q}} \right) \beta_Q \left( \frac{h}{\mathcal{R}_c} + \frac{\sqrt{1 + 2\beta_Q}}{\gamma} \right) \gtrsim \beta_Q + \frac{1}{15}. \quad (6.18)$$

For  $\beta_Q \gtrsim 4$  this condition is automatically satisfied, i.e., resonant ICS photons pair produce almost immediately upon being upscattered. For  $\beta_Q < 4$ , Eq. (6.18) puts a constraint on the gap height  $h$ . As we shall see below, most of the scatterings in the gap are done by electrons/positrons with  $\gamma \sim \min(\gamma_c, \gamma_m)$ , where  $\gamma_c = \epsilon_{Be}/kT$

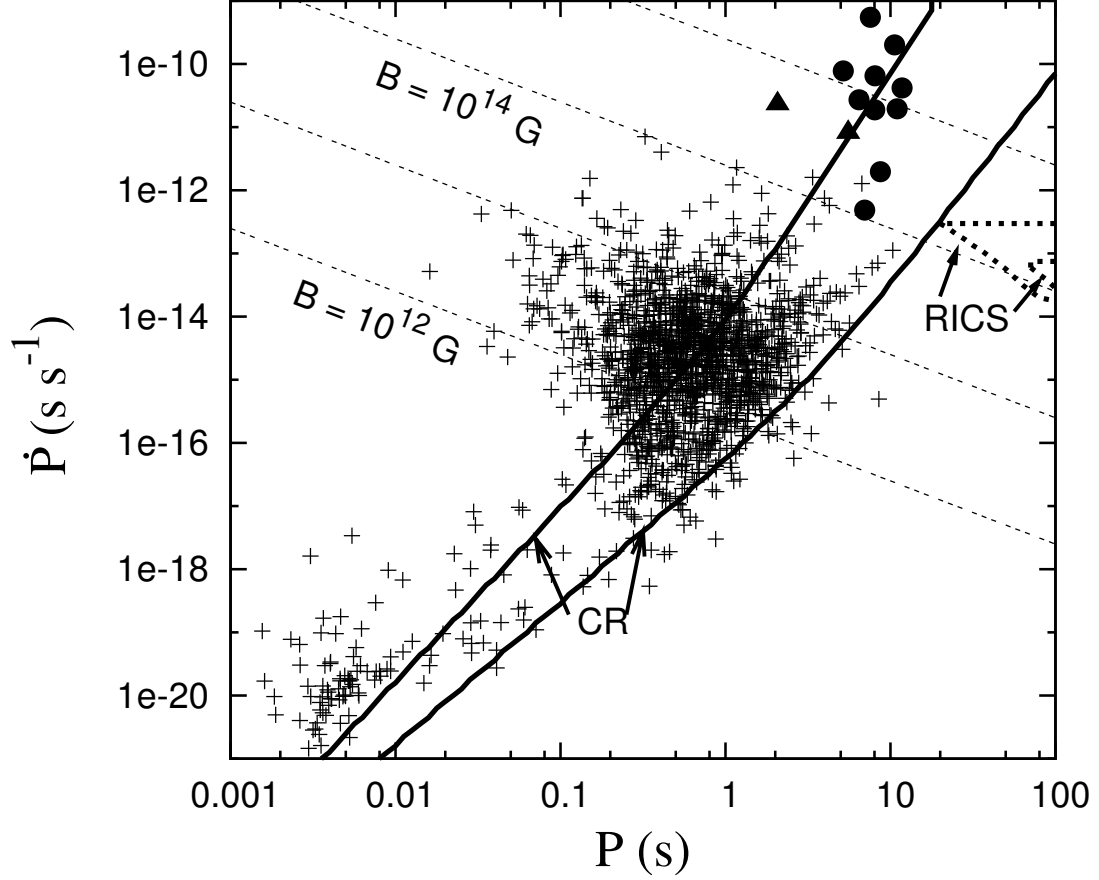


Figure 6.1: Pulsar death lines/boundaries for the CR and resonant ICS gap breakdown mechanisms. For curvature radiation, the lower line is for a magnetic field radius of curvature comparable to the stellar radius ( $\mathcal{R}_c \simeq R$ ) and the upper line is for a radius curvature given by the dipole formula ( $\mathcal{R}_6 = 100P_0^{1/2}$ ). For RICS, the large “box” is for  $\lambda = 1$  and the small box is for  $\lambda = 2$ ; both boxes are for a surface temperature of  $5 \times 10^6$  K. The unspecified neutron star parameters are taken to be unity (i.e., we set  $b_d = 1$  and for RICS  $\mathcal{R}_6 = 1$ ). The CR mechanism operates (and the pulsar is alive) above and to the left of the lines, and the RICS mechanism operates within the boxes. Radio/X-ray pulsars (ATNF catalog, <http://www.atnf.csiro.au/research/pulsar/psrcat>) are labeled by crosses, while magnetars (McGill catalog, <http://www.physics.mcgill.ca/~pulsar/magnetar/main.html>) are labeled by solid circles and the two radio magnetars are labeled by solid triangles.



(with  $T$  the surface blackbody temperature) and  $\gamma_m$  is the Lorentz factor of a fully-accelerated electron or positron [Eq. (6.3)]. For  $\gamma = \gamma_m$ , Eq. (6.18) yields

$$h \gtrsim h_{\min, \text{ph}}^{(1)} = 56.9 P_0^{1/3} \mathcal{R}_6^{1/3} f(\beta_Q)^{1/3} \text{ cm}, \quad (6.19)$$

where

$$f(\beta_Q) = \frac{\sqrt{1 + 2\beta_Q}}{\beta_Q} \left( \frac{2}{\sqrt{1 + 2\beta_Q} - 1} \frac{1 + 15\beta_Q}{15\beta_Q} - 1 \right). \quad (6.20)$$

For  $\gamma = \gamma_c$  we have

$$h \gtrsim h_{\min, \text{ph}}^{(2)} = 169 \mathcal{R}_6 T_6 f(\beta_Q) \text{ cm}. \quad (6.21)$$

Combining Eqs. (6.19) and (6.21), we find that the condition  $l_{\text{ph}} < h$  leads to

$$h \gtrsim h_{\min, \text{ph}} = \max(h_{\min, \text{ph}}^{(1)}, h_{\min, \text{ph}}^{(2)}). \quad (6.22)$$

The resonant cross section for inverse Compton scattering, in the rest frame of the electron before scattering, is

$$\sigma'_{\text{res}} \simeq 2\pi^2 \frac{e^2 \hbar}{m_e c} \delta(\epsilon' - \epsilon_{Be}), \quad (6.23)$$

where  $\epsilon' \sim \gamma \epsilon_i$ . This cross section is appropriate even for  $B_p > B_Q$ , since the resonant condition  $\epsilon' = \epsilon_{Be}$  holds regardless of field strength (cf. Gonthier et al. 2000). The ambient spectral photon number density near the polar cap is

$$\frac{dn_{\text{ph}}}{d\epsilon_i} = \frac{\epsilon_i^2 / (2\pi^2 \hbar^3 c^3)}{e^{\epsilon_i/kT} - 1} \quad (6.24)$$

(assuming a semi-isotropic distribution of photons). For concreteness, consider a positron produced at  $z = 0$  with initial Lorentz factor  $\gamma = 1$  and accelerated to  $\gamma = \gamma_m$  after crossing the full gap.<sup>1</sup> Neglecting the radiation reaction (see later),

---

<sup>1</sup>We can also consider the general situation where a positron (electron) is created at some location within the gap with initial Lorentz factor much less than  $\gamma_m$ , travels upwards (downwards) across the gap and get accelerated to a final Lorentz factor of order  $\gamma_m$ . This would give a similar result for  $N_{\text{ph}}$ .

we have  $\gamma - 1 = 2(\gamma_m - 1)(z/h - z^2/2h^2)$ . The number of photons upscattered through resonant ICS by the positron is given by (see Appendix C.2)

$$\begin{aligned}
N_{\text{ph}} &\simeq \int_0^h dz \int_0^\infty d\epsilon_i \frac{dn_{\text{ph}}}{d\epsilon_i} \sigma'_{\text{res}} \\
&\simeq \frac{\beta_Q^2}{2(\gamma_m - 1)} \frac{h}{a_0} \int_1^{\gamma_m} \frac{d\gamma}{\gamma^3 (e^{\epsilon_{Be}/kT\gamma} - 1)} \left(1 - \frac{\gamma - 1}{\gamma_m - 1}\right)^{-1/2} \\
&\simeq \frac{1}{2\gamma_m} \left(\frac{kT}{m_e c^2}\right)^2 \frac{h}{a_0} \int_{x_m}^{\epsilon_{Be}/(kT)} \frac{x dx}{(e^x - 1)(1 - x_m/x)^{1/2}} \quad (6.25)
\end{aligned}$$

where we have used  $\gamma_m \gg 1$  and

$$x_m = \frac{\epsilon_{Be}}{\gamma_m kT} = \frac{\gamma_c}{\gamma_m} = 1.09 \times 10^{-3} h_3^{-2} P_0 T_6^{-1}. \quad (6.26)$$

Note that the second equality of Eq. (6.25) gives

$$\frac{dN_{\text{ph}}}{d \ln \gamma} \simeq \beta_Q^2 \frac{h}{2\gamma_m a_0} \gamma^{-2} (e^{\gamma_c/\gamma} - 1)^{-1} (1 - \gamma/\gamma_m)^{-1/2}. \quad (6.27)$$

From this equation we see that for  $\gamma_c = \epsilon_{Be}/kT \lesssim \gamma_m$ ,  $dN_{\text{ph}}/d \ln \gamma$  peaks at  $\gamma \sim \gamma_c$ , with  $(dN_{\text{ph}}/d \ln \gamma)_{\gamma=\gamma_c} \sim N_{\text{ph}}$ , while for  $\gamma_c < \gamma \lesssim \gamma_m$ ,  $dN_{\text{ph}}/d \ln \gamma$  is of order  $(\gamma_c/\gamma)N_{\text{ph}}$ ; for  $\gamma_c \gtrsim \gamma_m$ ,  $dN_{\text{ph}}/d \ln \gamma \sim (\gamma/\gamma_m)N_{\text{ph}}$  peaks at  $\gamma \sim \gamma_m$ . Therefore, most of the scatterings in the gap are done by electrons/positrons with  $\gamma \sim \min(\gamma_c, \gamma_m)$ . Since we are interested in the regime  $\epsilon_{Be}/kT \gg 1$ , the integral in the last equality of Eq. (6.25) depends only on  $x_m$ , and for our purpose it can be approximated as  $(\pi^2/6)x_m(e^{x_m} - 1)^{-1}$ . This approximation reproduces the exact integral in the  $x_m \rightarrow 0$  limit. Thus we have

$$N_{\text{ph, res}} \simeq 2.45 \times 10^{-2} \beta_Q^{-1} T_6^{5/2} P_0^{1/2} F(x_m), \quad \text{with} \quad F(x_m) = \frac{x_m^{3/2}}{e^{x_m} - 1}. \quad (6.28)$$

The function  $F(x_m)$  peaks at  $x_m = 0.874$  with  $F_{\text{max}} = 0.585$ . Thus the condition  $N_{\text{ph}} > \lambda$  necessarily requires  $1.43 \times 10^{-2} \beta_Q^{-1} T_6^{5/2} P_0^{1/2} \gtrsim \lambda$ , or

$$\beta_Q \lesssim \beta_{Q, \text{crit}} = 1.43 \times 10^{-2} \lambda^{-1} T_6^{5/2} P_0^{1/2}. \quad (6.29)$$

For a given  $\beta_Q < \beta_{Q,\text{crit}}$ , the condition  $N_{\text{ph}} > \lambda$  is equivalent to  $F(x) > 0.585\beta_Q/\beta_{Q,\text{crit}}$ , which limits  $x_m$  to the range  $x_a < x_m < x_b$ , where  $x_{a,b}$  are determined by solving  $F(x_m) = 0.585\beta_Q/\beta_{Q,\text{crit}}$ . This condition then translates to the constraint on  $h$ :

$$h_{\text{min,e}} < h < h_{\text{max,e}} , \quad (6.30)$$

where

$$h_{\text{min,e}} = 33x_b^{-1/2}P_0^{1/2}T_6^{-1/2} \text{ cm} , \quad h_{\text{max,e}} = 33x_a^{-1/2}P_0^{1/2}T_6^{-1/2} \text{ cm}. \quad (6.31)$$

In summary, vacuum breakdown involving RICS requires

$$\beta_Q < \beta_{Q,\text{crit}} \quad \text{and} \quad \max(h_{\text{min,ph}}, h_{\text{min,e}}) < \min(h_{\text{max}}, h_{\text{max,e}}), \quad (6.32)$$

where  $\beta_{Q,\text{crit}}$ ,  $h_{\text{max}}$ ,  $h_{\text{min,ph}}$ ,  $h_{\text{min,e}}$ ,  $h_{\text{max,e}}$  are given by Eqs. (6.29), (6.5), (6.22) (note that  $h_{\text{min,ph}} = 0$  for  $\beta_Q \gtrsim 4$ ), and (6.31), respectively. In Fig. 6.1 we show the pulsar death boundary when RICS is most important for initiating a cascade in the vacuum gap, for the cases  $\lambda = 1$  and  $\lambda = 2$ , with  $b_d = 1$ ,  $\mathcal{R}_6 = 1$ , and  $T_6 = 5$ . Note that in Fig. 6.1 we have not plotted RICS death boundaries for the case of a dipole radius of curvature ( $\mathcal{R}_6 = 100P_0^{1/2}$ ) or a surface temperature  $T_6 \lesssim 1$ ; there are no regions of the  $P$ – $\dot{P}$  diagram where vacuum gap pair cascades are possible under these conditions.

The pulsar death boundary depicted in Fig. 6.1 can be understood as follows:

(i) a) The condition  $h_{\text{min,ph}}^{(1)} < h_{\text{max}}$  gives

$$\text{(Ia)} \quad P \lesssim 352 b_d^{-3/5} \mathcal{R}_6^{-2/5} f(\beta_Q)^{-2/5} \text{ s}, \quad (6.33)$$

where  $f(\beta_Q)$  is given by Eq. (6.20). This is shown as the long-dashed line labeled

(Ia) in Fig. 6.2. b) The condition  $h_{\text{min,ph}}^{(2)} < h_{\text{max}}$  gives

$$\text{(Ib)} \quad P \lesssim 1.99 \times 10^3 b_d^{-1} \mathcal{R}_6^{-2} T_6^{-2} f(\beta_Q)^{-2} \text{ s}. \quad (6.34)$$

This is shown as the short-dashed line labeled (Ib) in Fig. 6.2. This set of conditions, (Ia) and (Ib), is the usual requirement that photons emitted by an accelerated electron or positron in the gap must be able initiate pair production. (ii) a) For  $\beta_Q \ll \beta_{Q,\text{crit}}$ , we have  $x_a \simeq 0.342 (\beta_Q/\beta_{Q,\text{crit}})^2$ , and the condition  $h_{\text{min,ph}}^{(1)} < h_{\text{max,e}}$  then yields

$$(IIa) \quad P \gtrsim 593 \lambda^{3/2} \mathcal{R}_6^{1/2} T_6^{-3} \beta_Q^{3/2} f(\beta_Q)^{1/2} \text{ s.} \quad (6.35)$$

This is shown as the dotted line labeled (IIa) in Fig. 6.2. b) The condition  $h_{\text{min,ph}}^{(2)} < h_{\text{max,e}}$  yields

$$(IIb) \quad P \gtrsim 210 \lambda \mathcal{R}_6 T_6^{-1} f(\beta_Q) \text{ s.} \quad (6.36)$$

This is shown as the dot-long-dashed line labeled (IIb) in Fig. 6.2. This set of conditions, (IIa) and (IIb), together with  $\beta_Q \lesssim \beta_{Q,\text{crit}}$ , come from the requirement for efficient photon emission by RICS in the gap. (iii) The condition  $h_{\text{min,e}} < h_{\text{max}}$  gives

$$(III) \quad P \lesssim 228 b_d^{-1/2} T_6^{1/2} x_b^{1/2} \text{ s,} \quad \text{with } x_b \sim 0.874 + \ln \frac{\beta_{Q,\text{crit}}}{\beta_Q}. \quad (6.37)$$

This condition is shown as the dot-short-dashed line labeled (III) in Fig. 6.2. (iv) The condition  $\beta_Q > \beta_{Q,\text{crit}}$  gives Eq. (6.29) and is shown as the light solid line labeled (IV) in Fig. 6.2.

Previous studies of the the pulsar death conditions for vacuum gaps where RICS is the dominant photon emission mechanism have found that the RICS mechanism can lead to gap breakdown for a wide range of neutron star parameters (see, e.g., Zhang et al. 2000). This is contrary to our results, which show (see Figs. 6.1 and 6.2) that RICS is not a good mechanism for gap breakdown, except under very specific conditions (e.g., high surface temperatures and long rotation periods). The discrepancy arises because previous works did not calculate/estimate  $N_{\text{ph}}$  (the number of high energy photons produced as a positron/electron crosses the gap)

correctly. For example, it was implicitly assumed that photon production continues across the entire gap at the same rate as it does when  $\gamma \simeq \gamma_c$  (i.e., at the point of maximum RICS power loss) (Zhang et al. 2000). This assumption is invalid for  $\gamma > \gamma_c$ , as is discussed above:  $dN_{\text{ph}}/d\ln\gamma$  grows with increasing Lorentz factor until  $\gamma \sim \gamma_c$ , and then it decreases [see Eq. (6.27)]; therefore,  $dN_{\text{ph}}/d\gamma$  (which is directly related to the photon production rate  $\dot{N}_{\text{ph}}$ ) drops faster than  $\gamma^{-1}$  above  $\gamma \sim \gamma_c$ .

Note that the accelerating positron/electron is not radiation-reaction limited at  $\gamma \simeq \gamma_c$ , since the power loss due to RICS is significantly smaller than the power gain due to traversal across the potential drop. The power loss due to RICS is given by

$$P_{\text{loss}} = c \int_0^\infty d\epsilon_i \frac{dn_{\text{ph}}}{d\epsilon_i} \sigma'_{res}(\epsilon - \epsilon_i) \quad (6.38)$$

$$\simeq \frac{\beta_Q^2 c}{a_0} \left( 1 - \frac{1}{\sqrt{1 + 2\beta_Q}} \right) \frac{m_e c^2}{\gamma^2 (e^{\epsilon_{Be}/kT\gamma} - 1)}. \quad (6.39)$$

At the point of maximum RICS power loss (when  $\gamma = \gamma_c = \epsilon_{Be}/kT$ )

$$P_{\text{loss}}(\gamma = \gamma_c) \simeq \frac{c}{a_0} \left( 1 - \frac{1}{\sqrt{1 + 2\beta_Q}} \right) \left( \frac{kT}{m_e c^2} \right)^2 (e - 1)^{-1} m_e c^2 \quad (6.40)$$

$$\simeq 9.3 \times 10^{10} \left( 1 - \frac{1}{\sqrt{1 + 2\beta_Q}} \right) T_6^2 m_e c^2 \text{ s}^{-1} \quad (6.41)$$

(cf. Dermer 1990). The power gain due to acceleration across the gap is given by

$$P_{\text{gain}} = eE_{\parallel} c = \frac{2\Omega\beta_Q}{\alpha a_0} (h - z) m_e c^2 \quad (6.42)$$

(where  $\alpha = e^2/(\hbar c)$  is the fine structure constant). Thus

$$\left. \frac{P_{\text{gain}}}{P_{\text{loss}}} \right|_{\gamma=\gamma_c} \simeq 340 \left( \frac{h - z}{100 \text{ cm}} \right) P_0^{-1} T_6^{-2} \beta_Q \left( 1 - \frac{1}{\sqrt{1 + 2\beta_Q}} \right)^{-1}. \quad (6.43)$$

For most pulsar parameters,  $P_{\text{gain}} \gg P_{\text{loss}}$  [e.g., in order for  $\gamma$  to reach  $\gamma_c$  the gap height must be at least  $h = 33P_0^{1/2}T_6^{-1/2}$  cm; see Eq. (6.26) with  $x_m = 1$ ].

Therefore, there is no reason why  $\gamma$  should remain near  $\gamma_c$ , the point of maximum RICS photon emission, as was assumed in some earlier papers.

### Nonresonant inverse Compton scattering (NRICS)

The characteristic energy of a photon Compton-upscattered by an electron or positron of Lorentz factor  $\gamma$  is  $\epsilon \sim \gamma\epsilon'/(1+x)$ , where  $x = \epsilon'/m_e c^2$ ,  $\epsilon' \sim \gamma\epsilon_i$ , and  $\epsilon_i$  is the initial seed photon energy; the pitch angle of the scattered photon is of order  $\theta_e \sim (1+x)/\gamma$ . In the vacuum gap, most the scatterings are by electrons/positrons with  $\gamma \sim \gamma_m$  on seed photons with initial energy  $\epsilon_i \sim 2.82kT$  (see below). Substituting

$$\epsilon \sim \frac{\gamma_m \epsilon'_m}{1+x_m}, \quad \text{with} \quad x_m = \frac{\epsilon'_m}{m_e c^2} = \frac{2.82kT\gamma_m}{m_e c^2} \quad (6.44)$$

into Eq. (6.11) (which results from the requirement  $l_{\text{ph}} < h$ ), we find

$$\frac{\gamma_m}{2} \left( \frac{x_m}{1+x_m} \right) \beta_Q \left( \frac{h}{\mathcal{R}_c} + \frac{1+x_m}{\gamma_m} \right) > \beta_Q + \frac{1}{15}. \quad (6.45)$$

Using Eq. (6.3), this becomes

$$0.0415\beta_Q^{-1/2}P_0^{1/2}T_6^{-3/2}\mathcal{R}_6^{-1}\frac{x_m^{5/2}}{1+x_m} + x_m > 2 \left( 1 + \frac{1}{15\beta_Q} \right). \quad (6.46)$$

The gap height is related to  $x_m$  by

$$h = 19.7x_m^{1/2}\beta_Q^{-1/2}P_0^{1/2}T_6^{-1/2} \text{ cm}. \quad (6.47)$$

The solution to Eq. (6.46) yields  $x_m > x_{\text{min}}$ , and thus the constraint on the gap height from  $l_{\text{ph}} < h$  is

$$h \gtrsim h_{\text{min,ph}} = 19.7x_{\text{min}}^{1/2}\beta_Q^{-1/2}P_0^{1/2}T_6^{-1/2} \text{ cm}. \quad (6.48)$$

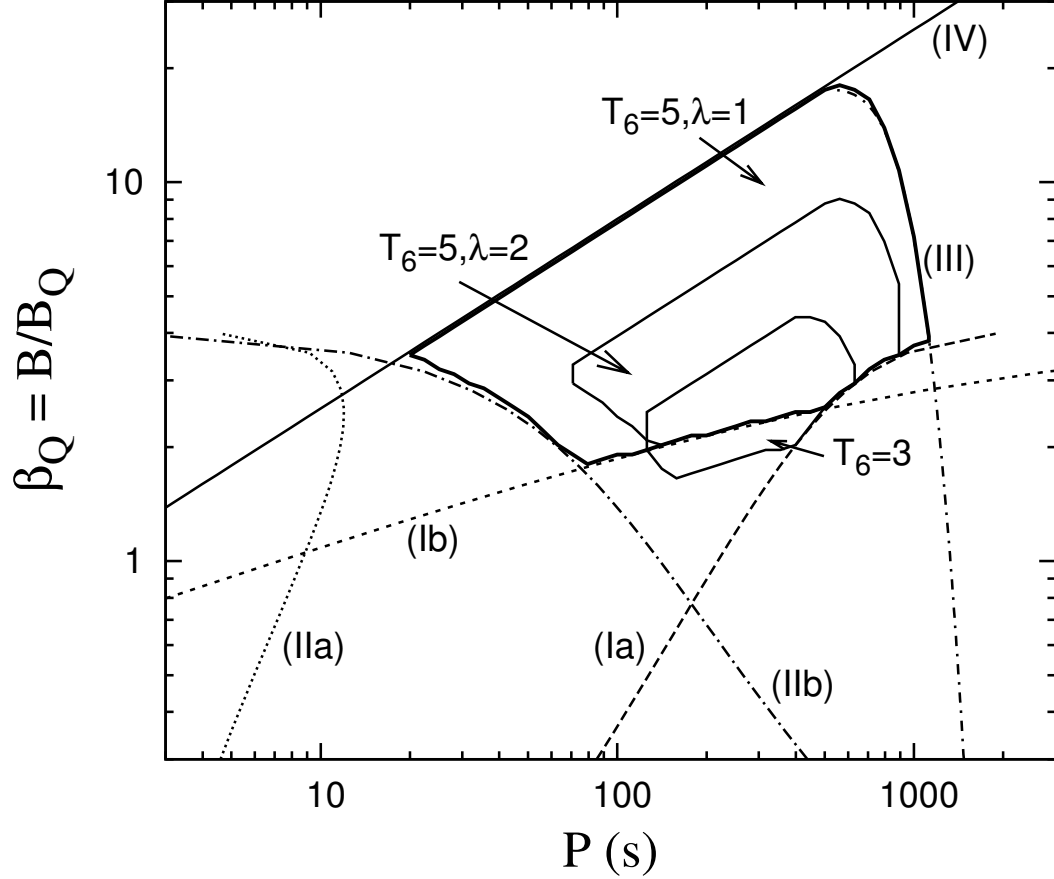


Figure 6.2: The pulsar death boundaries when the resonant ICS mechanism is most important for initiating a cascade, plotted as a function of the dimensionless magnetic field strength  $\beta_Q = B/B_Q$  and the period  $P$ . The boundaries are shown for surface temperature  $T = 5 \times 10^6$  K and parameter  $\lambda = 1$  (the largest, bold, enclosed region),  $T = 5 \times 10^6$  K and  $\lambda = 2$  (the mid-sized enclosed region) and  $T = 3 \times 10^6$  K and  $\lambda = 1$  (the smallest enclosed region). The critical lines defining the edges of the region for  $T_6 = 5, \lambda = 1$  are also shown. Each critical line (I)–(IV) is determined by one of Eqs. (6.33)–(6.37) and (6.29), as discussed in Section 6.2.4.

The nonresonant part of the ICS cross section, in the rest frame of the electron before scattering, is approximately given by

$$\sigma'(\epsilon') \simeq \sigma_T \left( \frac{\epsilon'}{\epsilon' + \epsilon_{Be}} \right)^2 f_{\text{KN}}(x) = \sigma_T \left( \frac{x}{x + \beta_Q} \right)^2 f_{\text{KN}}(x), \quad (6.49)$$

where  $\sigma_T$  is the Thomson cross-section,  $x = \epsilon'/(m_e c^2)$ , and

$$f_{\text{KN}}(x) = \frac{3}{4} \left[ \frac{1+x}{x^3} \left\{ \frac{2x(1+x)}{1+2x} - \ln(1+2x) \right\} + \frac{1}{2x} \ln(1+2x) - \frac{1+3x}{(1+2x)^2} \right] \quad (6.50)$$

is the Klein-Nishina suppression factor [ $f_{\text{KN}} \simeq 1 - 2x$  for  $x \ll 1$  and  $f_{\text{KN}} \simeq (3/8x)(\ln 2x + 1/2)$  for  $x \gg 1$ ]. This agrees well with the calculated NR cross sections in strong magnetic fields (e.g., Gonthier et al. 2000).

The number of scatterings per unit length by an electron or positron is

$$\frac{dN_{\text{ph}}}{dz} \simeq \int_0^\infty d\epsilon_i \frac{dn_{\text{ph}}}{d\epsilon_i} \sigma'(\gamma\epsilon_i) \sim 0.12 \left( \frac{kT}{\hbar c} \right)^3 \sigma'(2.82kT\gamma), \quad (6.51)$$

where in the second equality we have used the fact that  $dn_{\text{ph}}/d\ln\epsilon_i$  peaks at  $\epsilon_i = 2.82kT$ , while  $\sigma'(\epsilon')$  varies more slowly with  $\epsilon'$ . Similar to Section 6.2.4, consider a positron produced at  $z = 0$  with initial Lorentz factor  $\gamma = 1$  and accelerated to  $\gamma = \gamma_m$  after crossing the full gap. The number of scatterings produced by the positron is given by

$$N_{\text{ph}} \simeq \frac{h}{2\gamma_m} \int_1^{\gamma_m} \frac{d\gamma}{\sqrt{1 - \gamma/\gamma_m}} \frac{dN_{\text{ph}}}{dz}. \quad (6.52)$$

Clearly, most of the scatterings are by positrons/electrons with  $\gamma \sim \gamma_m$ , producing photons with energy  $2.82kT\gamma_m^2/(1+x_m)$  [see Eq. (6.44)]. The number of photons scattered by  $\gamma = (0.7-1)\gamma_m$  electrons/positrons is

$$\begin{aligned} N_{\text{ph}} &\sim \frac{h}{2} \left( \frac{dN_{\text{ph}}}{dz} \right)_{\gamma=\gamma_m} \simeq 0.059 h \left( \frac{kT}{\hbar c} \right)^3 \sigma_T \left( \frac{x_m}{x_m + \beta_Q} \right)^2 f_{\text{KN}}(x_m) \\ &\simeq 6.6 \times 10^{-5} \beta_Q^{-1/2} T_6^{5/2} P_0^{1/2} F(x_m, \beta_Q), \end{aligned} \quad (6.53)$$



where

$$F(x_m, \beta_Q) = \frac{x_m^{5/2}}{(x_m + \beta_Q)^2} f_{\text{KN}}(x_m). \quad (6.54)$$

Now consider the vacuum breakdown condition  $N_{\text{ph}} > \lambda$ . For a given  $\beta_Q$ , the function  $F(x_m, \beta_Q)$  has a maximum  $F_{\text{max}}(\beta_Q)$  (this maximum is approximately achieved at  $x_m \sim 2.24 + 3\beta_Q$ ). Then  $N_{\text{ph}} > \lambda$  requires

$$P \gtrsim P_{\text{crit}}(\beta_Q) = 2.3 \times 10^8 \lambda^2 T_6^{-5} \beta_Q F_{\text{max}}(\beta_Q)^{-2} \text{ s}. \quad (6.55)$$

When this is satisfied, we additionally require

$$\frac{F(x_m, \beta_Q)}{F_{\text{max}}(\beta_Q)} > \left[ \frac{P}{P_{\text{crit}}(\beta_Q)} \right]^{-1/2}, \quad (6.56)$$

which yields the solution  $x_a < x_m < x_b$ . In terms of the gap height, we have

$$h_{\text{min,e}} < h < h_{\text{max,e}}, \quad (6.57)$$

where

$$h_{\text{min,e}} = 19.7 x_a^{1/2} \beta_Q^{-1/2} P_0^{1/2} T_6^{-1/2} \text{ cm}, \quad (6.58)$$

When the neutron star surface temperature  $T_6 \leq 5$  there are no values of  $\beta_Q$  or  $P$  for which NRICS can initiate a cascade in the vacuum gap. (Only when  $T_6 \gtrsim 9$  are there any  $\beta_Q, P$  values which permit an NRICS-initiated cascade, and even at these high temperatures the allowed range of  $\beta_Q$  and  $P$  values is very small and atypical of neutron stars.) Therefore, no pulsar death boundaries appear for the NRICS process in Fig. 6.1.

## 6.3 Space-charge-limited flow (SCLF) accelerators

### 6.3.1 Acceleration potential

If charged particles can be freely extracted from the surface such that a vacuum gap never forms, a SCLF type accelerator develops. In the SCLF gap zone charged particles fully screen the parallel electric field at the surface but are prevented from fully screening the electric field at larger heights, due either to magnetic field line curvatures (as first discussed by Arons & Scharlemann 1979) or relativistic frame dragging effects (as first discussed by Muslimov & Tsygan (1992)). In the following analysis we will only consider the effects of frame dragging on the acceleration potential, because they are typically 50-100 times stronger than any effects due to field line curvature. For simplicity we will also assume that the pulsars are oriented with  $\mathbf{\Omega} \cdot \mathbf{B}_p > 0$ , so that electrons, not ions, are accelerated away from the surface.

A general, approximate solution to the SCLF potential due to frame dragging was given by Muslimov & Tsygan (1992). We will adopt a simplified potential for our analysis (cf. Hirschman & Arons 2001a):

At low altitudes the potential as a function of height  $h$  is

$$\Phi \simeq \frac{3\kappa_g \Omega B_p}{2c} \left( \frac{\Omega R}{c} \right)^{1/2} h^2, \quad (6.59)$$

where

$$\kappa_g = \frac{2GI}{c^2 R^3} \simeq 0.15. \quad (6.60)$$

Note that we will use  $\kappa_g = 0.15$  throughout this chapter. At high altitudes the potential becomes

$$\Phi \simeq \frac{\kappa_g \Omega^2 B_p R^3}{2c^2} (1 - \eta^{-3}) \simeq \frac{3\kappa_g \Omega^2 B_p R^2}{2c^2} h, \quad (6.61)$$

where  $\eta = r/R$  and the second equality is valid for  $h \ll R$ . These potentials intersect at  $h \simeq r_p \simeq R\sqrt{\Omega R/c}$ , or at a Lorentz factor of

$$\gamma_1 = \frac{e\Delta\Phi(r_p)}{m_e c^2} = 3.70 \times 10^6 \beta_Q P_0^{-5/2}. \quad (6.62)$$

With the high altitude potential, the electrons and positrons can be accelerated to a Lorentz factor

$$\gamma(h) = \frac{e\Delta\Phi}{m_e c^2} = 2.56 \times 10^5 \beta_Q h_3 P_0^{-2} \quad (6.63)$$

for  $h \ll R$ . The maximum potential drop is

$$\Delta\Phi_{\max} = \frac{\kappa_g \Omega^2 B_p R^3}{2c^2}, \quad (6.64)$$

and the maximum Lorentz factor is

$$\gamma_{\max} = \frac{e\Delta\Phi}{m_e c^2} = 8.53 \times 10^7 \beta_Q P_0^{-2}. \quad (6.65)$$

In this chapter we use the following simplified potential model:  $\Phi$  is given by Eq. (6.59) for  $h < r_p$  and given by the second equality of Eq. (6.61) for  $r_p < h < h_{\max}$ . Therefore we have

$$h_{\max} = \frac{R}{3}. \quad (6.66)$$

The above formulae do not take into account the boundary conditions at the “pair formation front”, the height at which the multiplicity of pairs produced is enough to screen the potential (the point of gap breakdown). The parallel electric field must be zero at this height, which can significantly reduce the strength of the accelerating electric field as a function of height (analogous to Eq. 6.1 of the vacuum gap case). In the following analysis, we will not consider this complication.

### 6.3.2 Requirements for gap breakdown

The requirements for the breakdown of a SCLF gap are the same as for a vacuum gap [see Eqs. (6.6) and (6.7)], except that the minimum number of photons that must be produced per particle is approximately 0.1: at large height the charge deficit between the actual magnetosphere density and the Goldreich-Julian charge density is of order  $\kappa_g \simeq 0.15$  (see, e.g., Hirschman & Arons 2001b); to screen the gap enough photons must be created that the charged particles they decay into can account for this deficit. For our analysis of SCLF death boundaries we adopt the more stringent requirement  $\lambda = 1$ . In our analysis of the full cascade (see Chapter 7) we have found that ICS-initiated cascades produce an extremely low multiplicity of secondary particles, making this more stringent requirement a necessity [while for curvature radiation-initiated cascades so many photons are produced per primary particle that Eq. (6.7) is non-binding for either  $\lambda = 0.1$  or  $\lambda = 1$ ].

### 6.3.3 Pair production

The physics of photon decay into pairs is independent of the acceleration model used, and so the pair production equations from our vacuum gap model [Eqs. (6.8)–(6.11)] apply here as well. Because the relevant heights are restricted to be less than  $h_{\max} = R/3$ , the variation of  $\beta_Q$  as a function of height can be neglected here and in the following analysis.

Note that regardless of photon energy and magnetic field strength, Eq. (6.11) as written can always be solved with a large enough value of  $h$ ; but if the equation

is replaced by its  $h \gtrsim R$  equivalent (with the substitution  $\beta_Q \rightarrow \beta_Q \eta^{-3}$ )

$$\frac{\epsilon}{2m_e c^2} \beta_Q (1 + h/R)^{-3} \frac{h}{\mathcal{R}_c} \gtrsim \frac{1}{15} [1 + 15\beta_Q (1 + h/R)^{-3}], \quad (6.67)$$

this does not work — if Eq. (6.67) is not true for  $h \simeq R/2$ , it will not be true for any value of  $h$  (cf. Hirschman & Arons 2001b). This lends validity to our semi-arbitrary choice of  $h_{\max} = R/3$  [Eq. (6.66)].

### 6.3.4 Photon emission multiplicity and the pulsar death boundary

There are several possible photon emission mechanisms operating in the SCLF breakdown, each leading to a different death boundary. We consider them separately.

#### Curvature radiation (CR)

The characteristic energy of a photon emitted through curvature radiation is  $\epsilon \sim (3/2)\gamma^3 \hbar c / \mathcal{R}_c = 7.95 \times 10^4 \beta_Q^3 h_3^3 P_0^{-6} \mathcal{R}_6^{-1}$  eV, where we have used  $\gamma \sim \gamma(h)$  [Eq. (6.63)]. The low altitude maximum Lorentz factor,  $\gamma_1$  [Eq. (6.62)], is unimportant here. The emission angle is  $\theta_e \sim \gamma^{-1}$ , which is typically much less than  $h/\mathcal{R}_c$  (this can be easily checked *a posteriori*). Equation (6.11) then reduces to

$$h > h_{\min, \text{ph}} = 3.42 \times 10^3 P_0^{3/2} \mathcal{R}_6^{1/2} \frac{(15\beta_Q + 1)^{1/4}}{\beta_Q} \text{ cm}. \quad (6.68)$$

The rate of energy loss of an electron or positron emitting curvature radiation is  $P_{\text{CR}} = 2e^2 \gamma^4 / (3c^3) (c^2 / \mathcal{R}_c)^2$ , thus the number of photons emitted through curvature

radiation by a single electron or positron across the gap is

$$N_{\text{ph}} \simeq \frac{P_{\text{CR}}}{\epsilon} \frac{h}{c} \simeq \frac{4}{9} \frac{e^2}{\hbar c} \frac{\gamma h}{\mathcal{R}_c} = 0.830 \beta_Q h_3^2 P_0^{-2} \mathcal{R}_6^{-1}. \quad (6.69)$$

The condition  $N_{\text{ph}} > \lambda$  [Eq. (6.7)] then gives

$$h \gtrsim h_{\text{min,e}} = 1.10 \times 10^3 \lambda^{1/2} \beta_Q^{-1/2} P_0 \mathcal{R}_6^{1/2} \text{ cm}. \quad (6.70)$$

Thus the minimum gap height required for vacuum breakdown is  $h \simeq \max(h_{\text{min,ph}}, h_{\text{min,e}})$ .

Combining Eqs. (6.66), (6.68), and (6.70), we have

$$\max(h_{\text{min,ph}}, h_{\text{min,e}}) < h_{\text{max}}. \quad (6.71)$$

This gives a necessary condition for pulsar emission and defines the pulsar “death line”. For all relevant parameter regimes,  $h_{\text{min,ph}} > h_{\text{min,e}}$ , and Eq. (6.71) simply becomes  $h_{\text{min,ph}} < h_{\text{max}}$ . The critical pulsar spin period is then

$$P_{\text{crit}} = 1.70 b_d^{2/3} B_{12}^{2/3} \mathcal{R}_6^{-1/3} (1 + 15\beta_Q)^{-1/6} \text{ s}, \quad (6.72)$$

where the dipole polar field is  $B_{12} = 2.0(P_0 \dot{P}_{15})^{1/2}$ , with  $\dot{P}_{15} = \dot{P}/(10^{-15} \text{ s s}^{-1})$ .

In Fig. 6.3 we show the pulsar death boundary when curvature radiation is most important for initiating a cascade in the SCLF gap.

## Resonant inverse Compton scattering (RICS)

The characteristic photon energy after resonant scattering is

$$\epsilon = \gamma \left( 1 - \frac{1}{\sqrt{1 + 2\beta_Q}} \right) m_e c^2, \quad (6.73)$$

with typical emission angle  $\theta_e \sim 1/\gamma_e$ . The condition  $l_{\text{ph}} < h$  [see Eq. (6.6)]

becomes

$$\frac{\gamma}{2} \left( 1 - \frac{1}{\sqrt{1 + 2\beta_Q}} \right) \beta_Q \left( \frac{h}{\mathcal{R}_c} + \frac{\sqrt{1 + 2\beta_Q}}{\gamma} \right) \gtrsim \beta_Q + \frac{1}{15}. \quad (6.74)$$

For  $\beta_Q \gtrsim 4$  this condition is automatically satisfied, i.e., resonant ICS photons pair produce almost immediately upon being upscattered. For  $\beta_Q < 4$ , Eq. (6.74) puts a constraint on the gap height  $h$ . As we shall see below, most of the scatterings in the gap are done by electrons/positrons with  $\gamma \sim \min(\gamma_c, \gamma(h))$ , where  $\gamma_c = \epsilon_{Be}/kT$  (with  $T$  the surface blackbody temperature) and  $\gamma(h)$  is the Lorentz factor of a fully-accelerated electron or positron [Eq. (6.63)]. Note that the low altitude maximum gamma factor,  $\gamma_1$  [Eq. (6.62)], does not enter here. For  $\gamma(h) < \gamma_c$ , Eq. (6.74) yields

$$h \gtrsim h_{\min, \text{ph}}^{(1)} = 62.5 P_0 \mathcal{R}_6^{1/2} f(\beta_Q)^{1/2} \text{ cm}, \quad (6.75)$$

where

$$f(\beta_Q) = \frac{\sqrt{1+2\beta_Q}}{\beta_Q} \left( \frac{2}{\sqrt{1+2\beta_Q}-1} \frac{1+15\beta_Q}{15\beta_Q} - 1 \right). \quad (6.76)$$

For  $\gamma(h) > \gamma_c$  we have

$$h \gtrsim h_{\min, \text{ph}}^{(2)} = 169 \mathcal{R}_6 T_6 f(\beta_Q) \text{ cm}. \quad (6.77)$$

Combining Eqs. (6.75) and (6.77), we find that the condition  $l_{\text{ph}} < h$  leads to

$$h \gtrsim h_{\min, \text{ph}} = \max(h_{\min, \text{ph}}^{(1)}, h_{\min, \text{ph}}^{(2)}). \quad (6.78)$$

The resonant cross section for inverse Compton scattering, in the rest frame of the electron before scattering, is

$$\sigma'_{\text{res}} \simeq 2\pi^2 \frac{e^2 \hbar}{m_e c} \delta(\epsilon' - \epsilon_{Be}), \quad (6.79)$$

where  $\epsilon' \sim \gamma \epsilon_i$ . This cross section is appropriate even for  $B_p > B_Q$ , since the resonant condition  $\epsilon' = \epsilon_{Be}$  holds regardless of field strength. The ambient spectral photon number number density near the polar cap is

$$\frac{dn_{\text{ph}}}{d\epsilon_i} = \frac{\epsilon_i^2 / (2\pi^2 \hbar^3 c^3)}{e^{\epsilon_i/kT} - 1} \quad (6.80)$$

(assuming a semi-isotropic distribution of photons). For concreteness, consider an electron produced at  $z = 0$  with initial Lorentz factor  $\gamma = 1$  and accelerated to  $\gamma = \gamma_{\max}$  after reaching height  $h_{\max}$ . Neglecting the radiation reaction (see later), we have

$$\gamma - 1 = (\gamma_1 - 1) \frac{h^2}{h_1^2}, \quad h < h_1 \equiv r_p, \quad (6.81)$$

$$\gamma - \gamma_1 = (\gamma_{\max} - \gamma_1) \frac{h - h_1}{h_{\max} - h_1}, \quad h_1 < h < h_{\max}. \quad (6.82)$$

The number of photons upscattered through resonant ICS by the electron is given by

$$\begin{aligned} N_{\text{ph}} &\simeq \int_0^{h_{\max}} dz \int_0^\infty d\epsilon_i \frac{dn_{\text{ph}}}{d\epsilon_i} \sigma'_{\text{res}} \\ &\simeq \frac{\beta_Q^2}{2(\gamma_1 - 1)} \frac{r_p}{a_0} \int_1^{\gamma_1} \frac{d\gamma}{\gamma^3 (e^{\epsilon_{Be}/kT\gamma} - 1)} \sqrt{\frac{\gamma_1 - 1}{\gamma - 1}} \\ &\quad + \frac{\beta_Q^2}{(\gamma_{\max} - \gamma_1)} \frac{h_{\max} - h_1}{a_0} \int_{\gamma_1}^{\gamma_{\max}} \frac{d\gamma}{\gamma^3 (e^{\epsilon_{Be}/kT\gamma} - 1)}, \end{aligned} \quad (6.83)$$

where we have used  $\gamma_1, \gamma_{\max} \gg 1$ . Defining

$$x = \frac{\epsilon_{Be}}{\gamma kT}, \quad (6.84)$$

$$x_1 = \frac{\epsilon_{Be}}{\gamma_1 kT} = \frac{\gamma_c}{\gamma_1} = 1.61 \times 10^{-3} P_0^{5/2} T_6^{-1}, \quad (6.85)$$

$$x_m = \frac{\epsilon_{Be}}{\gamma_{\max} kT} = \frac{\gamma_c}{\gamma_{\max}} = 6.97 \times 10^{-5} P_0^2 T_6^{-1}, \quad (6.86)$$

we have

$$N_{\text{ph}} \simeq \frac{1}{2\gamma_1 \sqrt{x_1}} \left( \frac{kT}{m_e c^2} \right)^2 \frac{r_p}{a_0} \int_{x_1}^{\epsilon_{Be}/(kT)} \frac{x^{3/2} dx}{(e^x - 1)} + \frac{1}{\gamma_{\max}} \left( \frac{kT}{m_e c^2} \right)^2 \frac{h_{\max}}{a_0} \int_{x_m}^{x_1} \frac{x dx}{(e^x - 1)}. \quad (6.87)$$

Note that only one of these terms will actually matter; if  $\gamma_c \lesssim \gamma_1$ , the first term will be important, and if  $\gamma_c \gtrsim \gamma_1$  [which only occurs for large periods and low temperatures; see Eq. (6.85)], the second term will be important. Since we are interested in the regime  $\gamma_c = \epsilon_{Be}/kT \gg 1$ , the first integral in Eq. (6.87) depends only on  $x_1$ , and for our purpose it can be approximated as  $\frac{3\sqrt{\pi}}{4} \zeta\left(\frac{5}{2}\right) x_1 (e^{x_1} - 1)^{-1} \simeq$



$1.783x_1(e^{x_1} - 1)^{-1}$ . Also, for  $\gamma_c \gg \gamma_1$ , the second integral in Eq. (6.87) depends only on  $x_m$ , and for our purpose it can be approximated as  $(\pi^2/6)x_m(e^{x_m} - 1)^{-1}$ . These approximations reproduce the exact integrals in the  $x_1, x_m \rightarrow 0$  limit. Thus we have

$$N_{\text{ph, res}} \simeq 0.465\beta_Q^{-1}T_6^{5/2}P_0^{1/2}F(x_1) + 0.0344\beta_Q^{-1}T_6^2P_0^2F(x_m), \quad \text{with} \quad F(x) = \frac{x}{e^x - 1}. \quad (6.88)$$

Thus the condition  $N_{\text{ph}} > \lambda$  necessarily requires

$$\beta_Q \lesssim \beta_{Q, \text{crit}} = 0.465\lambda^{-1}T_6^{5/2}P_0^{1/2}F(x_1) + 0.0344\lambda^{-1}T_6^2P_0^2F(x_m). \quad (6.89)$$

In summary, RICS-initiated cascades are possible only when

$$\beta_Q < \beta_{Q, \text{crit}} \quad \text{and} \quad h_{\text{min, ph}} < h_{\text{max}}, \quad (6.90)$$

where  $\beta_{Q, \text{crit}}$ ,  $h_{\text{max}}$ ,  $h_{\text{min, ph}}$  are given by Eqs. (6.89), (6.66), and (6.78) (note that  $h_{\text{min, ph}} = 0$  for  $\beta_Q \gtrsim 4$ ), respectively. In Fig. 6.3 we show the pulsar death boundary when RICS is most important for initiating a cascade in the SCLF gap.

The pulsar death boundary depicted in Fig. 6.3 can be understood as follows:

(i) a) The condition  $h_{\text{min, ph}}^{(1)} < h_{\text{max}}$  gives

$$P \lesssim 5.33 \times 10^3 \mathcal{R}_6^{-1/2} f(\beta_Q)^{-1/2} \text{ s}; \quad (6.91)$$

for a dipole field curvature ( $\mathcal{R}_6 \simeq 100P_0^{1/2}$ ) this is

$$(Ia) \quad P \lesssim 152 f(\beta_Q)^{-2/5} \text{ s}, \quad (6.92)$$

where  $f(\beta_Q)$  is given by Eq. (6.76). This is shown as the short-dashed line labeled

(Ia) in Fig. 6.4. b) The condition  $h_{\text{min, ph}}^{(2)} < h_{\text{max}}$  gives

$$f(\beta_Q) \lesssim 1.97 \times 10^3 \mathcal{R}_6^{-1} T_6^{-1}; \quad (6.93)$$

for a dipole field curvature this is

$$(Ib) \quad P \lesssim 388 T_6^{-2} f(\beta_Q)^{-2}. \quad (6.94)$$

This is shown as the dotted line labeled (Ib) in Fig. 6.2. This set of conditions, (Ia) and (Ib), is the usual requirement that photons emitted by an accelerated electron or positron in the gap must be able initiate pair production. (ii) The condition  $N_{\text{ph}} > \lambda$  or  $\beta_Q > \beta_{Q,\text{crit}}$  gives Eq. (6.89). To show the contribution of the low altitude region versus the high altitude region to the total photon multiplicity, this requirement has been divided into two conditions,

$$(IIa) \quad \beta_Q \lesssim \beta_{Q,\text{low}} = 0.465 \lambda^{-1} T_6^{5/2} P_0^{3/4} F(x_1), \quad (6.95)$$

which is shown as the light solid line labeled (IIa) in Fig. 6.4, and

$$(IIb) \quad \beta_Q \lesssim \beta_{Q,\text{high}} = 0.0344 \lambda^{-1} T_6^2 P_0^2 F(x_m), \quad (6.96)$$

which is shown as the long-dashed line labeled (IIb) in Fig. 6.4 [see Eq. (6.89)].

Note that in the SCLF model the accelerating electron/positron can be radiation-reaction limited at  $\gamma \simeq \gamma_c$  for some pulsar parameters: The power loss due to RICS is given by

$$P_{\text{loss}} = c \int_0^\infty d\epsilon_i \frac{dn_{\text{ph}}}{d\epsilon_i} \sigma'_{\text{res}}(\epsilon - \epsilon_i) \quad (6.97)$$

$$\simeq \frac{\beta_Q^2 c}{a_0} \left( 1 - \frac{1}{\sqrt{1 + 2\beta_Q}} \right) \frac{m_e c^2}{\gamma^2 (e^{\epsilon_{Be}/kT\gamma} - 1)}. \quad (6.98)$$

At the point of maximum RICS power loss (when  $\gamma = \gamma_c = \epsilon_{Be}/kT$ )

$$P_{\text{loss}}(\gamma = \gamma_c) \simeq \frac{c}{a_0} \left( 1 - \frac{1}{\sqrt{1 + 2\beta_Q}} \right) \left( \frac{kT}{m_e c^2} \right)^2 (e - 1)^{-1} m_e c^2 \quad (6.99)$$

$$\simeq 9.3 \times 10^{10} \left( 1 - \frac{1}{\sqrt{1 + 2\beta_Q}} \right) T_6^2 m_e c^2 \text{ s}^{-1}. \quad (6.100)$$

The power gain due to acceleration across the gap is given by

$$P_{\text{gain}} = eE_{\parallel}c = \frac{3\kappa_g\Omega\beta_Q}{\alpha a_0} \sqrt{\frac{\Omega R}{c}} z m_e c^2 \quad (6.101)$$

for  $\gamma < \gamma_1$ , or

$$P_{\text{gain}} = eE_{\parallel}c = \frac{3\kappa_g\Omega R\beta_Q}{2\alpha a_0} \left(\frac{\Omega R}{c}\right) m_e c^2 \quad (6.102)$$

for  $\gamma > \gamma_1$ . Since  $z(\gamma_c) = x_1^{1/2} r_p = 788 T_6^{-1/2} P_0^{3/4}$  cm, we have

$$\left. \frac{P_{\text{gain}}}{P_{\text{loss}}} \right|_{\gamma=\gamma_c} \simeq 8.8 P_0^{-3/4} T_6^{-5/2} \beta_Q \left(1 - \frac{1}{\sqrt{1+2\beta_Q}}\right)^{-1}, \quad (6.103)$$

for  $P_0 < 6.96 T_6^{1/3}$ , or

$$\left. \frac{P_{\text{gain}}}{P_{\text{loss}}} \right|_{\gamma=\gamma_c} \simeq 80 P_0^{-2} T_6^{-2} \beta_Q \left(1 - \frac{1}{\sqrt{1+2\beta_Q}}\right)^{-1}. \quad (6.104)$$

for  $P_0 > 6.96 T_6^{1/3}$ . For most pulsar parameters,  $P_{\text{gain}} \gg P_{\text{loss}}$ . But for large  $P, T$  ( $P \gtrsim 5$  s or  $T \gtrsim 3 \times 10^6$  K),  $P_{\text{gain}} \lesssim P_{\text{loss}}$ . In these cases, the accelerating particle will be radiation-reaction limited and will remain near the point of maximum RICS photon emission for an extended length of time. Incorporating the radiation-reaction effect into our model would change our results (Fig. 6.3) very little, however, as most pulsars with parameters conducive to this effect already satisfy  $N_{\text{ph}} > \lambda$  [Eq. (6.7)].

### Nonresonant inverse Compton scattering (NRICS)

The characteristic energy of a photon Compton-upscattered by an electron or positron of Lorenz factor  $\gamma$  is  $\epsilon \sim \gamma \epsilon' / (1 + x)$ , where  $x = \epsilon' / m_e c^2$ ,  $\epsilon' \sim \gamma \epsilon_i$ , and  $\epsilon_i$  is the initial seed photon energy; the pitch angle of the scattered photon is of order  $\theta_e \sim (1 + x) / \gamma$ . In the SCLF gap, most the scatterings are by electrons/positrons with  $\gamma \sim \gamma(h)$  on seed photons with initial energy  $\epsilon_i \sim 2.82 kT$ .

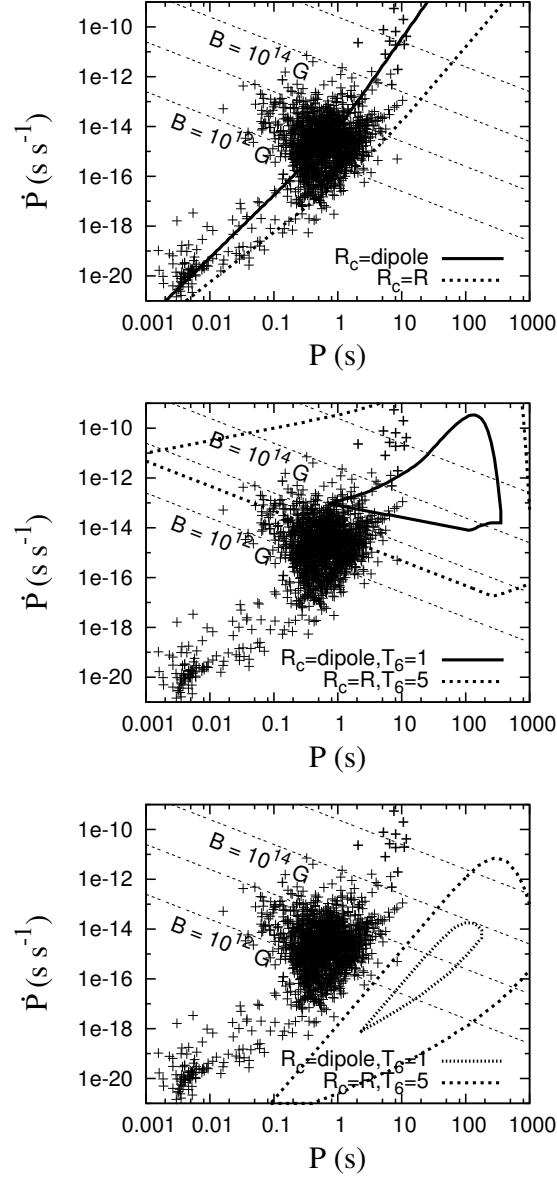


Figure 6.3: Death boundaries for the SCLF model, at  $\mathcal{R}_c = R, T_6 = 5$  and  $\mathcal{R}_c = 10^8 P_0^{1/2}, T_6 = 1$ . The upper panel is for cascades initiated by curvature radiation, the middle for cascades initiated by RICS, and lower for cascades initiated by NRICS. All boundaries have  $\lambda = 1$  except the  $\mathcal{R}_c = 10^8 P_0^{1/2}, T_6 = 1$  boundary for the NRICS (bottom) panel, which has  $\lambda = 0.1$  (because there are no allowed  $P$ - $\dot{P}$  values for  $\lambda = 1$  in this case).

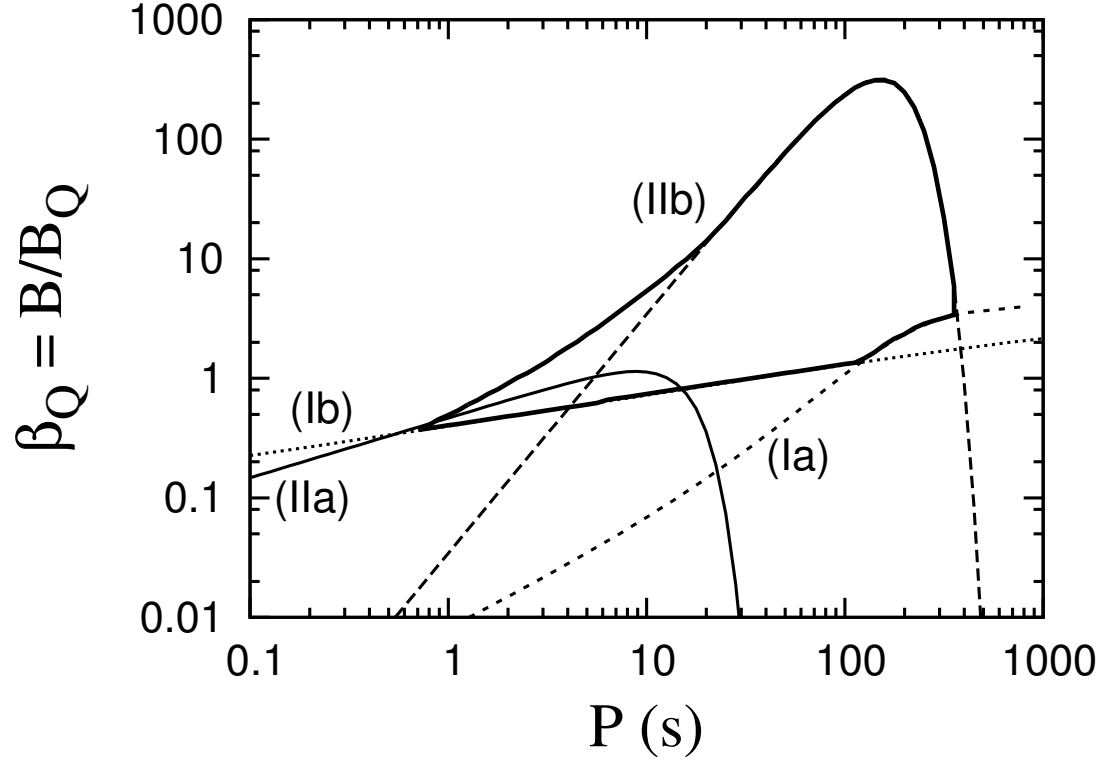


Figure 6.4: The pulsar death boundaries for the SCLF model, when the resonant ICS mechanism is most important for initiating a cascade, plotted as a function of the dimensionless magnetic field strength  $\beta_Q = B/B_Q$  and the period  $P$ . The boundaries are shown for surface temperature  $T = 1 \times 10^6$  K, dipole curvature ( $\mathcal{R}_6 = 100P_0^{1/2}$ ), and parameter  $\lambda = 1$  (the bold, enclosed region). Each critical line (Ia)–(IIb) is determined by one of Eqs. (6.92), (6.94), and (6.89).

Substituting

$$\epsilon \sim \frac{\gamma(h)\epsilon'_m}{1+x_m}, \quad \text{with} \quad x_m = \frac{\epsilon'_m}{m_e c^2} = \frac{2.82kT\gamma(h)}{m_e c^2} \quad (6.105)$$

into Eq. (6.6) (which results from the requirement  $l_{\text{ph}} < h$ ), we find

$$\frac{\gamma(h)}{2} \left( \frac{x_m}{1+x_m} \right) \beta_Q \left( \frac{h}{\mathcal{R}_c} + \frac{1+x_m}{\gamma(h)} \right) > \beta_Q + \frac{1}{15}. \quad (6.106)$$

Using Eq. (6.63) (again,  $\gamma_1$  doesn't matter here), this becomes

$$0.0174\beta_Q^{-1}P_0^2T_6^{-2}\mathcal{R}_6^{-1}\frac{x_m^3}{1+x_m} + x_m > 2 \left( 1 + \frac{1}{15\beta_Q} \right). \quad (6.107)$$

The gap height is related to  $x_m$  by

$$h = 8.23x_m\beta_Q^{-1}P_0^2T_6^{-1} \text{ cm}. \quad (6.108)$$

The solution to Eq. (6.107) yields  $x_m > x_{\text{min}}$ , and thus the constraint on the gap height from  $l_{\text{ph}} < h$  is

$$h \gtrsim h_{\text{min,ph}} = 8.23x_m\beta_Q^{-1}P_0^2T_6^{-1} \text{ cm}. \quad (6.109)$$

The nonresonant part of the ICS cross section, in the rest frame of the electron before scattering, is approximately given by

$$\sigma'(\epsilon') \simeq \sigma_T \left( \frac{\epsilon'}{\epsilon' + \epsilon_{Be}} \right)^2 f_{\text{KN}}(x) = \sigma_T \left( \frac{x}{x + \beta_Q} \right)^2 f_{\text{KN}}(x), \quad (6.110)$$

where  $\sigma_T$  is the Thomson cross-section,  $x = \epsilon'/(m_e c^2)$ , and

$$f_{\text{KN}}(x) = \frac{3}{4} \left[ \frac{1+x}{x^3} \left\{ \frac{2x(1+x)}{1+2x} - \ln(1+2x) \right\} + \frac{1}{2x} \ln(1+2x) - \frac{1+3x}{(1+2x)^2} \right] \quad (6.111)$$

is the Klein-Nishina suppression factor [ $f_{\text{KN}} \simeq 1 - 2x$  for  $x \ll 1$  and  $f_{\text{KN}} \simeq (3/8x)(\ln 2x + 1/2)$  for  $x \gg 1$ ]. This agrees well with the calculated NR cross sections in strong magnetic fields.

The number of scatterings per unit length by an electron or positron is

$$\frac{dN_{\text{ph}}}{dz} \simeq \int_0^\infty d\epsilon_i \frac{dn_{\text{ph}}}{d\epsilon_i} \sigma'(\gamma\epsilon_i) \sim 0.12 \left( \frac{kT}{\hbar c} \right)^3 \sigma'(2.82kT\gamma), \quad (6.112)$$

where in the second equality we have used the fact that  $dn_{\text{ph}}/d\ln\epsilon_i$  peaks at  $\epsilon_i = 2.82kT$ , while  $\sigma'(\epsilon')$  varies more slowly with  $\epsilon'$ . Similar to the RICS section, consider a positron produced at  $z = 0$  with initial Lorentz factor  $\gamma = 1$  and accelerated to  $\gamma = \gamma(h)$  after crossing the full gap. The number of scatterings produced by the positron is given by

$$N_{\text{ph}} \simeq \frac{r_p}{2\gamma_1} \int_1^{\gamma_1} \frac{d\gamma}{\sqrt{\gamma/\gamma_1}} \frac{dN_{\text{ph}}}{dz} + \frac{h_{\text{max}}}{\gamma_{\text{max}}} \int_{\gamma_1}^{\gamma_{\text{max}}} d\gamma \frac{dN_{\text{ph}}}{dz}. \quad (6.113)$$

As with the vacuum gap case, these integrals are well-fit (i.e., within a factor of a few) over the relevant  $\gamma$  range (up to  $\sim 10^6$ ) by  $\gamma \frac{dN_{\text{ph}}}{dz}$ . (We can treat  $\frac{dN_{\text{ph}}}{dz}$  as approximately constant over the drop.) In this approximation both the low-altitude and high-altitude terms have the same form, within a factor of two, so they can be combined. We then have that the number of photons scattered by high-energy electrons/positrons is

$$\begin{aligned} N_{\text{ph}} &\sim \frac{h}{2} \left( \frac{dN_{\text{ph}}}{dz} \right)_{\gamma=\gamma(h)} \simeq 0.059 h \left( \frac{kT}{\hbar c} \right)^3 \sigma_T \left( \frac{x_m}{x_m + \beta_Q} \right)^2 f_{\text{KN}}(x_m) \\ &\simeq 2.7 \times 10^{-5} \beta_Q^{-1} T_6^2 P_0^2 x_m F(x_m, \beta_Q), \end{aligned} \quad (6.114)$$

where

$$F(x_m, \beta_Q) = \frac{x_m^2}{(x_m + \beta_Q)^2} f_{\text{KN}}(x_m). \quad (6.115)$$

Using  $N_{\text{ph}} > \lambda$  and

$$x_{\text{max}} = x_m(h_{\text{max}}) = 4.05 \times 10^4 \beta_Q P_0^{-2} T_6 \quad (6.116)$$

(since  $N_{\text{ph}}$  increases with  $h$ ), we obtain the photon multiplicity requirement for NRICS-dominated cascades:

$$F(x_{\text{max}}, \beta_Q) \gtrsim 0.914 \lambda T_6^{-3}. \quad (6.117)$$

In Fig. 6.3 we show the pulsar death boundary when RICS is most important for initiating a cascade in the SCLF gap.

The pulsar death boundary depicted in Fig. 6.3 can be understood as follows:

(i) a) Eq. (6.107) places a lower bound on  $x_m$ , so to obtain a boundary condition from this equation we can set  $x_m = x_{\max}$  [Eq. (6.116)]. For  $x_{\max} \gg 1$  Eq. (6.107) can be written

$$0.0174\beta_Q^{-1}P_0^2T_6^{-2}\mathcal{R}_6^{-1}x_{\max}^2 \gtrsim 2 \left(1 + \frac{1}{15\beta_Q}\right). \quad (6.118)$$

The condition  $h_{\min,\text{ph}} < h_{\max}$  then gives

$$P \lesssim 1.46 \times 10^4 \mathcal{R}_6^{-1/2} \frac{\beta_Q}{\sqrt{15\beta_Q + 1}} \text{ s}; \quad (6.119)$$

for a dipole field curvature ( $\mathcal{R}_c \simeq 100P_0^{1/2}$ ) this is

$$(Ia) \quad P \lesssim 340 \left( \frac{\beta_Q^2}{15\beta_Q + 1} \right)^{2/5} \text{ s}. \quad (6.120)$$

This is shown as the short-dashed line labeled (Ia) in Fig. 6.5. b) For  $x_{\max} \sim 1$  Eq. (6.107) can be written

$$x_{\max} \gtrsim 2 \left(1 + \frac{1}{15\beta_Q}\right). \quad (6.121)$$

The condition  $h_{\min,\text{ph}} < h_{\max}$  then gives

$$(Ib) \quad P \lesssim 551 T_6^{1/2} \frac{\beta_Q}{\sqrt{15\beta_Q + 1}} \text{ s}, \quad (6.122)$$

This is shown as the dotted line labeled (Ib) in Fig. 6.5. This set of conditions, (Ia) and (Ib), is the usual requirement that photons emitted by an accelerated electron or positron in the gap must be able initiate pair production.

(ii) The condition  $N_{\text{ph}} > \lambda$  gives Eq. (6.117). For  $T_6 \sim 1\text{--}5$ ,  $\lambda \sim 0.1\text{--}1$  we have  $F(x_{\max}, \beta_Q) \gtrsim 0.005\text{--}0.05$ . In this range we can use the approximation  $f_{\text{KN}}(x_{\max}) \sim$



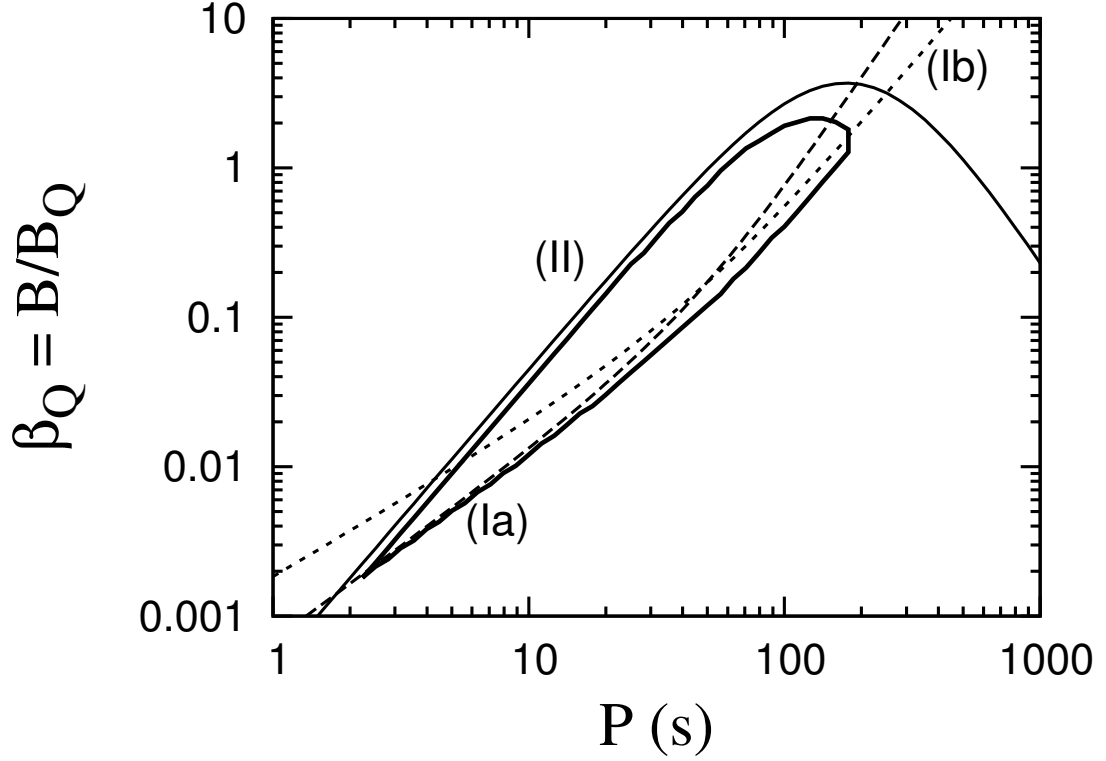


Figure 6.5: The pulsar death boundaries for the SCLF model, when the non-resonant ICS mechanism is most important for initiating a cascade, plotted as a function of the dimensionless magnetic field strength  $\beta_Q = B/B_Q$  and the period  $P$ . The boundaries are shown for surface temperature  $T = 1 \times 10^6$  K, dipole curvature ( $\mathcal{R}_6 = 100P_0^{1/2}$ ), and parameter  $\lambda = 0.1$  (the bold, enclosed region). Each critical line (Ia)–(II) is determined by one of Eqs. (6.120), (6.122), and (6.123). (Note that there are no allowed regions for NRICS-dominated cascades when  $T_6 = 1$ ,  $\mathcal{R}_6 = 100P_0^{1/2}$  for  $\lambda \gtrsim 0.3$ .)

$1.1x_{\max}^{-6/7}$ . We then have the condition

$$(II) \quad \beta_Q \lesssim 3.06 \times 10^{-5} \lambda^{-7/6} \frac{P_0^2 T_6^{5/2}}{(1 + 2.47 \times 10^{-5} P_0^2 T_6^{-1})^{7/3}}. \quad (6.123)$$

which is shown as the light solid line labeled (II) in Fig. 6.5.

Previous studies of the the pulsar death conditions for SCLF gaps where RICS or NRICS is the dominant photon emission mechanism have found that these mechanisms can lead to gap breakdown for a wide range of neutron star parameters (see, e.g., Zhang et al. 2000; Hirschman & Arons 2001a; Harding & Muslimov

2002). This is contrary to our results, which show (see Figs. 6.3, 6.4, and 6.5) that RICS and NRICS, while more relevant than in the vacuum gap case, are not good mechanisms for gap breakdown except under specific conditions (e.g., high surface fields and temperatures for RICS and long rotation periods for NRICS). There are a variety of reasons for the discrepancies, as no two models take the same approach or yield the same results; in most cases, however, the discrepancies can be traced to the previous work ignoring or miscalculating the second gap breakdown condition, Eq. 6.7. For example, in some works the total number of photons produced as an electron/positron crosses the gap is greatly overestimated (as discussed in Section 6.2; see (Zhang et al. 2000; Harding & Muslimov 2002)). Hirschman & Arons (2001a) find, as we do, that RICS is a very ineffective method for gap breakdown unless  $B \gtrsim 10^{13}$  G. However, they find a large region of effectiveness for NRICS that we do not find, because they rely on the secondary cascade of synchrotron radiation to provide the necessary photon multiplicity  $\lambda$ . As we will discuss in Chapter 7, such a cascade will either: result in a very low final plasma density (as is pointed out in Hirschman & Arons 2001b); or, for  $B \gtrsim 3 \times 10^{12}$  G, not occur, because the synchrotron emission process is suppressed.

## 6.4 Discussion

We have considered the conditions for pair cascades in two inner acceleration gap models, the vacuum gap model and the space-charge-limited-flow gap model. Our results from Chapter 5 show that while SCLF accelerators operate in most pulsars, a vacuum gap may form above the polar caps of some pulsars. In addition, even if a vacuum gap cannot form due to heavy bombardment of the cap, a partially screened gap may form instead (Gil et al. 2003, 2006). With small modifications

[e.g., the potential drop given by Eq. (6.2) is reduced], our discussion of pair cascades in the vacuum gap can be easily generalized to the case of a partially screened gap.

In the vacuum gap case (Section 6.2) we find that pair cascades initiated by curvature radiation can account for most pulsars in the  $P-\dot{P}$  diagram, but significant field line curvature near the stellar surface is needed. Although such field curvature is possible for some pulsars, it is unlikely to occur for all of them. For a pure dipole magnetic field, only about half of all pulsars can be explained by a curvature radiation-initiated cascade. Contrary to previous works (e.g., Zhang et al. 2000), we find that inverse Compton scatterings (resonant or not) are not efficient in producing vacuum breakdown via pair cascade.

We obtain similar results in the SCLF gap case (Section 6.3). The death lines for cascades initiated by curvature radiation have nearly the same shape and position on the  $P-\dot{P}$  diagram as in the vacuum gap case, both for dipole and for stronger field line curvatures. While such cascades can account for most pulsars, cascades initiated by resonant inverse Compton scatterings can only account for pulsars with high surface fields and temperatures, and cascades initiated by non-resonant inverse Compton scatterings can only account for the very oldest (non-recycled) pulsars.

For both our vacuum gap and SCLF gap models there are regions of the  $P-\dot{P}$  diagram where gap breakdown via pair cascade is possible but no pulsars have been observed (see Figs. 6.1 and 6.3). These occur at long rotation periods, for gaps where RICS or NRICS is the dominant photon emission mechanism. It may be that pulsars do exist with these parameters (rotation periods longer than 10 seconds), but that because of their long periods they are too difficult to observe. More likely,

however, is that gap breakdown occurs but the resulting pair plasma is too diffuse to generate coherent radio emission; as will be discussed in Chapter 7, cascades initiated by inverse Compton scatterings produce an extremely low multiplicity of secondary particles.

The recent detection of the radio emission from two AXPs (Camilo et al. 2006, 2007) is of great interest. The emission appears to be triggered by X-ray outbursts of usually quiescent magnetars. This may be due to a rearrangement of the surface magnetic field, which makes pair cascades possible. We note that the occurrence of pair cascades depends strongly on the field line geometry/curvature; our study of pair cascades in the context of inner gap accelerators serves as an illustration of this point.

## CHAPTER 7

# PAIR CASCADES IN PULSAR MAGNETOSPHERES: PLASMA DISTRIBUTIONS AND PHOTON SPECTRA

## 7.1 Introduction

The pair cascade in the magnetosphere of a pulsar has long been considered an essential ingredient for its nonthermal emission, from radio to gamma ray (Sturrock 1971; Ruderman & Sutherland 1975; Melrose 2004; Thompson 2004; Wang & Lai 2007). The pair cascade involves several steps: (i) acceleration of primary particles by an electric field parallel to the magnetic field; (ii) gamma ray emission by the accelerated particles moving along the magnetic field lines (either by curvature radiation or inverse Compton upscattering of surface photons); (iii) photon decay into electron-positron pairs as the angle between the photon and the field line becomes sufficiently large; (iv) gamma ray emission by the newly-created particles as they lose their transverse energy through synchrotron emission; (v) further pair production and gamma ray emission via steps iii and iv. In Chapter 6 we investigated the magnetosphere acceleration zone (“gap”) where the cascade originates, and derived the conditions of cascade-induced gap breakdown and the related pulsar death boundary. In this chapter we present simulations of the full pair cascade from onset to completion, using the results of Chapter 6 to estimate the inputs for the cascade simulation (e.g., initial particle energy). We use our simulation to generate the spectra of the final photons and the energy distribution of the secondary plasma produced by the cascade. Additionally, we use our simulation to further constrain the pulsar death boundaries derived in Chapter 6. For example, for a particular neutron star enough pairs may be produced in the polar cap

acceleration zone such that the accelerating electric field is screened (step iii of the cascade). However, if these pairs are too weak to sustain the cascade through high-energy synchrotron emission (step iv), the secondary plasma density will be too small to generate coherent radio emission. According to the gap breakdown criteria of Chapter 6 only, such a neutron star would be erroneously classified as a “live” pulsar.

There have been only a few publications devoted to full simulations of the pair cascade in pulsar magnetospheres. For moderate-strength magnetospheres ( $B \lesssim 3 \times 10^{12}$  G), significant progress has been made. Daugherty & Harding (1982) present numerical simulations of cascades initiated by electrons emitting photons through curvature radiation, for a dipole magnetic field geometry with field strengths up to  $B = 5 \times 10^{12}$  G and rotation periods  $P = 0.033$ -1 s; Daugherty & Harding (1996) present simulations of the gamma ray emission from the entire pulsar cap, using a simplified acceleration model and for Vela-like pulsar parameters ( $B = 3 \times 10^{12}$  G and  $P = 0.089$  s). Sturmer, Dermer, & Michel (1995) present a similar simulation to that of Daugherty & Harding, but for cascades initiated by electrons upscattering photons through the inverse Compton process (again for Vela-like parameters). Hirschman & Arons (2001b) develop a semi-analytic model of the cascade, both for curvature radiation-initiated and inverse Compton scattering-initiated cascades, applicable for  $B \lesssim 3 \times 10^{12}$  G. Cascades occurring in the outer magnetosphere, due to “outer gap” accelerators (Cheng et al. 1986), have also been simulated, by Romani (1996) for Vela- and Crab-like ( $B = 4 \times 10^{12}$  G and  $P = 0.033$  s) parameters.

However, for superstrong magnetospheres ( $B \gtrsim B_Q = 4.414 \times 10^{13}$  G) only limited aspects of the full cascades have been studied. For example, Arendt &

Eilek (2002) simulate the cascade for  $B \leq 10^{13}$  G and  $P = 0.033$  s (for both a pure dipole and a more complex field geometry), but with the simplification that all photons radiated by the primary particle are emitted from the surface. Baring & Harding (2001) (see also Harding, Baring, & Gonthier 1997) use this same simplification to study the effects of photon splitting on the cascade for field strengths up to  $B = 2 \times 10^{14}$  G.

Motivated by this lack of full cascade results for the superstrong field regime, and in light of the unexplained differences between the observed emission properties of high-field radio pulsars and magnetars (see Chapter 6), we simulate the full pair cascade for magnetic field strengths up to  $10^{15}$  G. In our simulation we consider several important factors that affect high-field cascades, including photon splitting, pair creation in low Landau levels, photon polarization modes ( $\perp$  or  $\parallel$ ), and resonant inverse Compton scattering. The outline of the chapter is as follows. In Section 7.2 we summarize the relevant results of our magnetosphere acceleration model (see Sections 6.2 and 6.3; see also Medin & Lai 2007b). In Section 7.3 we describe the numerical simulation we use to generate plasma distributions and photon spectra. Both electron/positron- and photon-initiated cascades are discussed. In Section 7.4 we present our results for a wide range of parameters (surface magnetic fields  $B = 10^{12}$  G, rotation periods 0.033-5 s, surface temperatures  $T = 10^6$  K and  $5 \times 10^6$  K, and pure dipole and more complex field geometries). Our results suggest that pulsar death boundaries are actually far smaller than derived in Chapter 6, particularly for cascades initiated by resonant and nonresonant inverse Compton scattering. Our results also show that photon splitting, while important for the suppression of synchrotron emission near the stellar surface, has very little effect on the overall pair cascade. This is a qualitatively different result than was previously found (e.g., Baring & Harding 2001), which arises because previous works

ignored the contributions of high-altitude photon emission and pair production to the final cascade spectra. We conclude this chapter in Section 7.5. Some technical details (on our treatment of inverse Compton scattering, attenuation coefficients for pair creation, and electron levels) are given in Appendix D.

## 7.2 Acceleration models for the primary particle

In Chapter 6 we described the conditions for cascade-induced gap breakdown, both for vacuum and space-charge-limited-flow (SCLF) accelerators (see Section 6.2 and Section 6.3, respectively). For each gap model we derived the minimum condition for initiating pair cascades, when the dominant mechanism for photon emission was curvature radiation, resonant inverse Compton scattering (RICS), or nonresonant inverse Compton scattering (NRICS). We adapt these results for use as input parameters in our cascade simulation.

In our cascade simulation (described in Section 7.3) we do not include an actual acceleration region. Instead, we model the effect of this region by giving the primary electron<sup>1</sup> (the electron that initiates the cascade) a large initial energy (Lorentz factor)  $\gamma_0$ . Ideally the value we should use for  $\gamma_0$  in our simulation is the energy the electron would have obtained if it had crossed the entire gap,  $\gamma_m$  (see Sections 6.2 and 6.3). This parameter is shown in Fig. 7.1 for SCLF accelerators; we do not show our results of  $\gamma_m$  for vacuum gap accelerators, as they are either within a factor of three of the SCLF values (for curvature radiation-dominated cascades) or irrelevant (for RICS- and NRICS-dominated cascades, since these types of cascades lead to few or no “live” pulsars in the vacuum gap model). Note

---

<sup>1</sup>For simplicity we will assume that the pulsar is aligned such that  $\boldsymbol{\Omega} \cdot \mathbf{B}_p > 0$ .



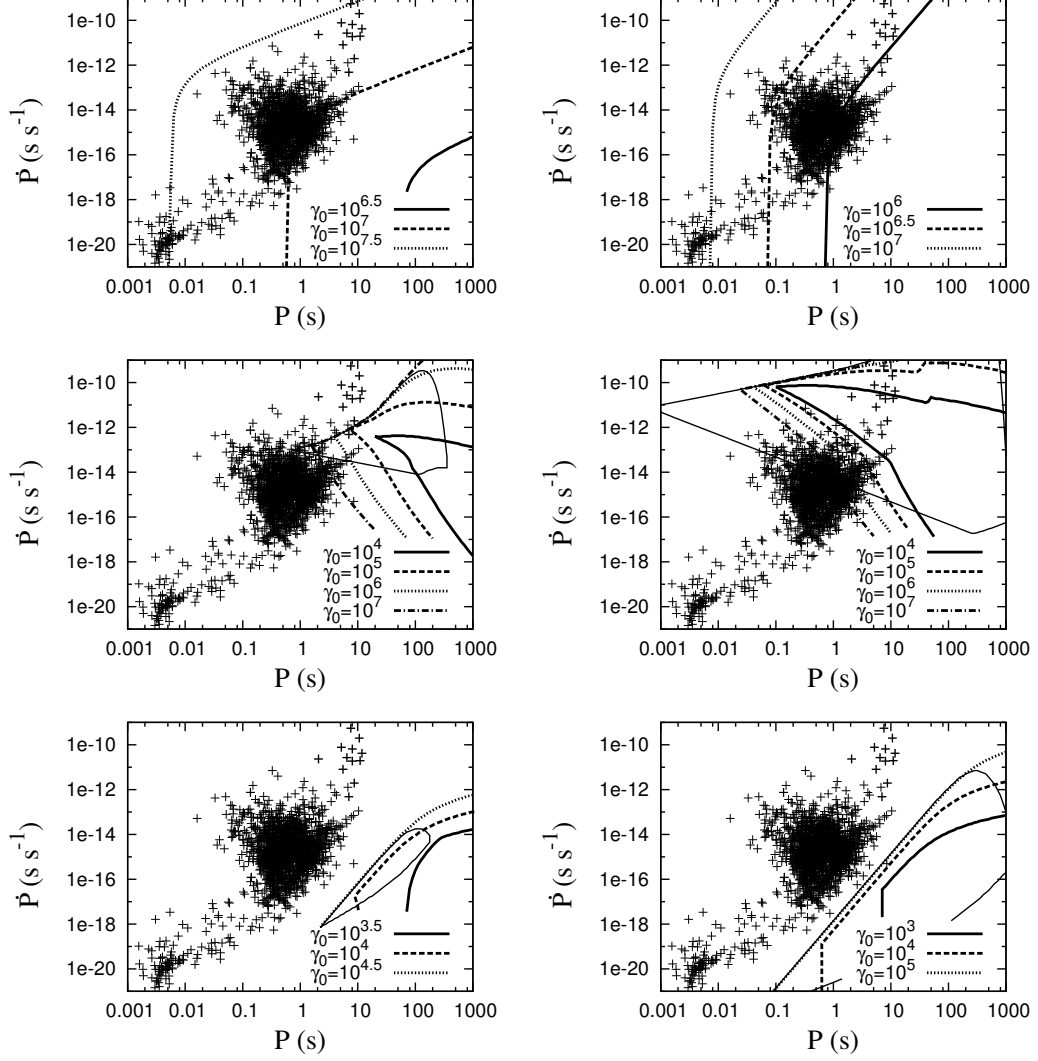


Figure 7.1: SCLF Lorentz factor contours for cascades initiated by curvature radiation (top), RICS (middle), and NRICS (bottom), for a dipole radius of curvature and warm surface ( $T_6 = 1$ ) (left) and a multipole radius of curvature ( $\mathcal{R}_c = R \simeq 10$  km) and hot surface ( $T_6 = 5$ ) (right). The light solid lines in the middle and bottom panels show the RICS and NRICS death boundaries for the conditions given (as derived in Sections 6.2 and 6.3).

that we do not always use  $\gamma_0 = \gamma_m$  in our simulation (we often want to compare cascade results when only one parameter, such as magnetic field strength, has changed), but we use  $\gamma_0 \sim \gamma_m$  whenever appropriate.

For RICS-initiated cascades, the primary electron makes very little contribution to the total cascade once it has reached full energy,  $\gamma_m$ . Instead, most of the first generation of cascade photons are upscattered by the primary electron when  $\gamma \sim \gamma_c = \epsilon_{Be}/kT$ . Therefore, we get a better picture of the final spectra by starting the simulation with a single photon rather than a single electron. The appropriate initial parameter for the simulation of RICS-initiated cascades is the typical energy of a photon upscattered by the primary electron, given by [Eq. (6.73) of Section 6.3.4 with  $\gamma = \gamma_c = \epsilon_{Be}/kT$ ]:

$$\epsilon_0 = \beta_Q \left( 1 - \frac{1}{\sqrt{1 + 2\beta_Q}} \right) \left( \frac{m_e c^2}{kT} \right) m_e c^2, \quad (7.1)$$

where  $\beta_Q = B_p/B_Q$ . In order to compare the relative strength of this cascade to the cascade initiated by a single electron (as occurs in the curvature radiation case), we must multiply the results (the total number and energy distributions of the photons and electrons) by the number of first-generation photons produced by the primary electron. This is given by Eqs. (6.85), (6.86), and (6.88) of Section 6.3.4:

$$N_{\text{ph,res}} \simeq 0.465 \beta_Q^{-1} T_6^{5/2} P_0^{1/2} F(x_1) + 0.0344 \beta_Q^{-1} T_6^2 P_0^2 F(x_m), \quad \text{with} \quad F(x) = \frac{x}{e^x - 1}, \quad (7.2)$$

where  $P_0$  is the spin period in units of 1 s,  $T_6 = T/(10^6 \text{ K})$ ,  $x_1 = 1.61 \times 10^{-3} P_0^{5/2} T_6^{-1}$ , and  $x_m = 6.97 \times 10^{-5} P_0^2 T_6^{-1}$ .

### 7.3 Simulation of the pair cascade: Physics ingredients and methods

The general picture of our cascade simulation is sketched in Fig. 7.2. At the start of the simulation, an electron with initial Lorentz factor  $\gamma_0 \sim 10^7$  travels outward from the stellar surface along the last open field line. As it travels it emits high-energy photons through curvature radiation or inverse Compton upscattering. The simulation tracks these photons as they propagate from the point of emission out through the magnetosphere, until they decay into electron-positron pairs through magnetic pair production or escape to infinity. In the superstrong field regime, the photon (if it has the correct polarization; see later) also has a finite probability of splitting into two photons before pair production, in which case we follow the two daughter photons in a similar way. The electron-positron pairs created by these photons are tracked as they radiate away their transverse momenta through synchrotron radiation and then gradually lose their forward momenta through inverse Compton scattering (ICS). Subsequent generations of photons and pairs are also tracked, in a recursive manner, and the total numbers and energies of photons and pairs that escape the magnetosphere are recorded. We track the pairs and the photons until they reach a height comparable to the light cylinder radius; while in general there is no discernible pair production above  $r \sim 10R$ , where  $r$  is the altitude of the cascade (measured from the center of the star) and  $R$  is the stellar radius, curvature radiation continues up to very high altitudes (albeit very weakly, with  $\epsilon \lesssim 10$  MeV near the light cylinder).

Note that we use a simplified treatment of the acceleration region (see Chapter 6) in our simulation, in that the primary electron is imparted with a large energy at the stellar surface and experiences no further acceleration. This intro-

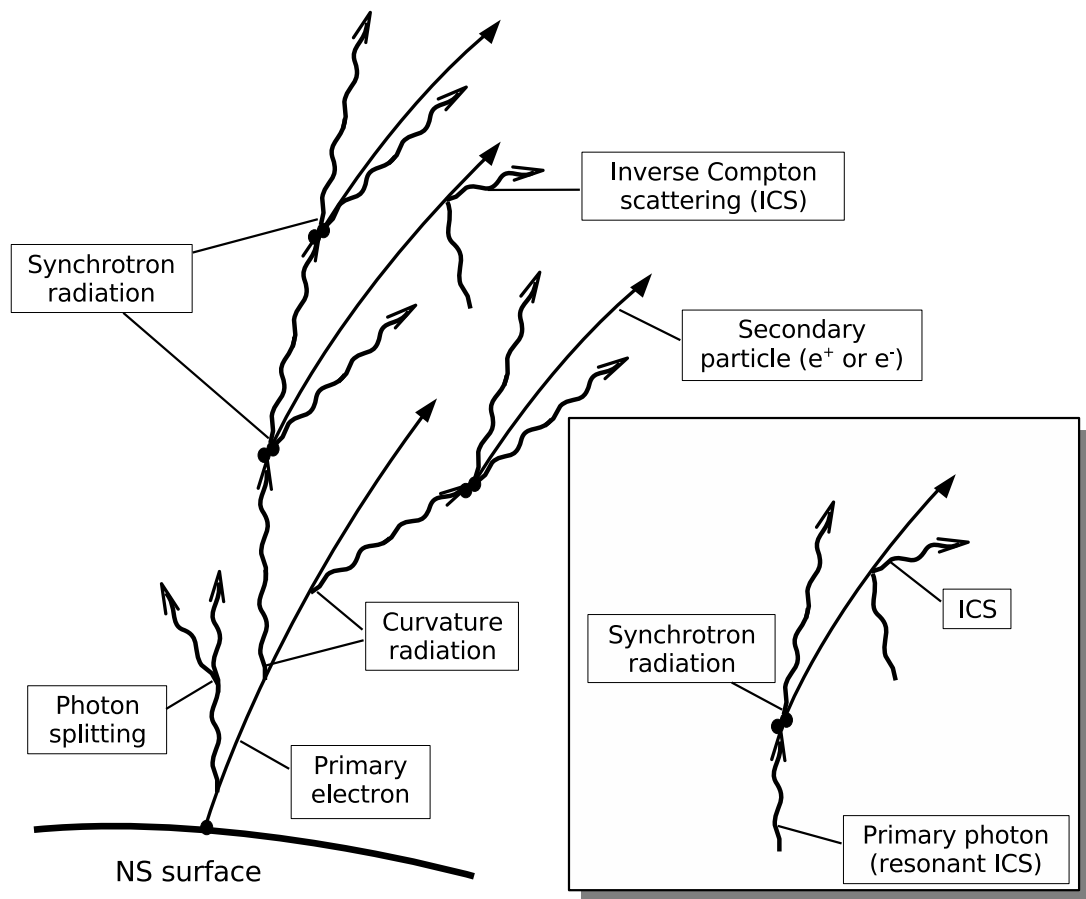


Figure 7.2: A schematic diagram showing the magnetosphere pair cascade, from initiation by a high-energy electron to completion. Photon splitting is also shown. The inset shows the beginning of a cascade “initiated” by a photon upscattered through the inverse Compton process.

duces two errors into the cascade calculation: First, the height at which the full energy ( $\gamma_0$ ) cascade begins is lower in our simulation than in reality. This will tend to overestimate the strength of the cascade, because of the stronger and more curved field lines near the surface (see Section 7.4). The difference, though, is small, since at worst the error in height is  $h_{\max} = R/3$  and for most pulsars will be much smaller than this. Second, the simplification ignores the contribution to the cascade by photons emitted before the primary electron reaches full energy ( $\gamma < \gamma_0$ ), which will tend to underestimate the strength of the cascade. For primary electrons emitting photons through curvature radiation the error is small, as the number and energies of photons emitted grows rapidly with the electron energy  $\gamma$  (Daugherty & Harding 1982 find similar results). However, for primary electrons upscattering photons through the ICS process the error can be very large, since far more photons are upscattered by the electron at energy  $\gamma \sim \gamma_c = \epsilon_{Be}/KT$  (see Sections 6.2 and 6.3) than at full energy  $\gamma_0$ . We therefore also run a second version of the simulation to track and record the cascade of particles initiated by a primary photon, rather than a primary electron. When combined with the results from Chapter 6 (see Section 7.2) on the number and peak energy of photons produced in the inner gap accelerator, this simulation gives a better picture of the final cascade due to inner accelerators dominated by ICS emission than does our “full energy” cascade simulation.

The input parameters for our simulation are the initial energy of the electron ( $\gamma_0 \sim 10^3$ - $10^7$ ; see Section 7.2), its initial position (in most cases, the intersection of the last open field line with the stellar surface), the general pulsar parameters (surface magnetic field strength  $B = 10^{12}$ - $10^{15}$  G, rotation period  $P = 0.33$ -5 s, and surface temperature  $T = 10^6$  K or  $5 \times 10^6$  K), and the geometry of the magnetic field (dipolar or strongly curved). For the second version of the simulation, where

the cascade is initiated by a photon, the additional parameters are the primary photon energy ( $\epsilon_0 \sim 10^2$ - $10^6$  MeV; Section 7.2) and the emission angle, or the angle between the photon propagation direction and the magnetic field at the point of emission (of order  $1/\gamma \sim 10^{-7}$ - $10^{-3}$ ).

In each run of the simulation, the magnetic field structure is given by one of two topologies: (i) a pure dipole field geometry; or (ii) a more complex field geometry near the polar cap which gradually reverts to dipole at higher altitudes (a “multipole” field geometry). Modeling the dipole field geometry is straightforward (see, e.g., von Hoensbroech et al. 1998), but there is no obviously correct way to model the geometry for the multipole field case. There are two features of a multipole field geometry that have a strong effect on the pair cascade dynamics and must be incorporated into our model: First, the radius of curvature  $\mathcal{R}_c$  is much stronger than dipole (we choose  $\mathcal{R}_c = R$ , the stellar radius) near the surface of the star. This leads to a much larger number and peak energy of photons emitted through curvature radiation than in the dipole field case. Second, as a photon propagates through the magnetosphere the angle between the photon and the field grows as  $\Delta\theta \sim s/\mathcal{R}_c = s/R$ , where  $s$  is the distance traveled by the photon from the point of emission. This leads to a much more rapid decay of photons into pairs than in the dipole case. The integration of these two features into our model is discussed in the relevant subsections below (Section 7.3.1 and Section 7.3.2, respectively). Note that Arendt & Eilek (2002) consider the first aspect of a multipole field geometry in their model (that  $\mathcal{R}_c = R$ ) but ignore the second. In all of the simulation runs we assume that the magnetic field strength varies as in the dipole case,

$$B(r, \theta) = B_p \left( \frac{R}{r} \right)^3 \frac{3 \cos^2 \theta + 1}{4}, \quad (7.3)$$

and do not account for any amplification of the field strength near the surface

caused by the complex topology.

For simplicity we consider an axially symmetric cascade in which all photons are emitted and travel in the plane defined by the local magnetic field line. Both the photons and the electrons/positrons are tracked in the “corotating” frame (the frame rotating with the star), and any bending of the photon path due to rotation is ignored (this is expected to be valid since the cascade takes place far inside the light cylinder). With this approximation the particle positions and trajectories are defined only in terms of  $r$  and  $\theta$  in our simulation. We justify this approximation below (Sections 7.3.1 and 7.3.2). As an additional simplification we ignore any effects of general relativity on the photon trajectory.

The cascade simulation can naturally be divided into three parts: (i) the propagation and photon emission of the primary electron; (ii) photon propagation, pair production, and splitting; and (iii) the propagation and photon emission of the secondary pairs. Each of these aspects of the simulation is described in a separate subsection below. At the end of this section, cascades initiated by primary photons are discussed.

### 7.3.1 Propagation and photon emission of the primary electron

The primary electron starts at the position  $r_0, \theta_0$  (typically the location of the last open field line at the stellar surface,  $r_0 = R$  and  $\theta_0 = \theta_c = \sqrt{\frac{R}{r_{\text{LC}}}}$ ) with the initial energy (Lorentz factor)  $\gamma_0$ , and moves outward along the field line in a stepwise fashion. The lengths of the steps  $\Delta s(r)$  are chosen so that a uniform amount of

energy  $\Delta\gamma$  (we choose  $\sim 0.01\gamma_0$ ) is lost by the electron in each step:

$$\Delta s(r) \simeq \Delta\gamma \frac{d\gamma}{ds}; \quad (7.4)$$

for an electron emitting curvature radiation,

$$\frac{d\gamma}{ds} = \frac{2}{3}\gamma^4 \frac{\alpha^2 a_0}{\mathcal{R}_c^2}, \quad (7.5)$$

where  $\alpha = e^2/(\hbar c)$  is the fine structure constant and  $a_0$  is the Bohr radius. Note that for a multipole radius of curvature we use  $\mathcal{R}_c = R$ .

As the electron moves a distance  $\Delta s$  along the field it emits photons with energies divided into discrete bins (our simulation uses  $\sim 50$  bins). The energy in each bin,  $\epsilon$ , is a constant multiple of  $\epsilon_{\text{CR}} = 3\gamma^3\hbar c/(2\mathcal{R}_c)$ , the characteristic energy of curvature photons. The number of photons in a given energy bin emitted in one step is given by the classical spectrum of curvature radiation (e.g., Jackson 1998),

$$\Delta N_\epsilon \simeq \Delta\epsilon \frac{dN}{d\epsilon} \simeq \frac{\sqrt{3}}{2\pi} \frac{\alpha \Delta s}{\mathcal{R}_c} \frac{\gamma \Delta\epsilon}{\epsilon} F\left(\frac{\epsilon}{\epsilon_{\text{CR}}}\right), \quad (7.6)$$

where  $\Delta\epsilon$  is the spacing between energy bins and  $F(x) = x \int_x^\infty K_{5/3}(t) dt$  (and the values of  $\mathcal{R}_c$  and  $\gamma$  used are averages over the interval  $\Delta s$ ).

The photons are emitted in the direction tangent to the field line at the current location of the electron,  $(r, \theta)$ . For a dipole field geometry the angle between the emitted photon and the magnetic dipole axis is given by

$$\chi(\theta) = \theta + \arctan(\tan \theta/2) \quad (7.7)$$

(see Fig. 7.3). There is an additional contribution to the emission angle of  $\sim 1/\gamma$ , due to relativistic beaming. In reality this beaming angle is in a random direction; however, for our two-dimensional approximation it can only be in the plane of the magnetic field. The actual emission angle is given by the sum of these two angles:

$$\Theta_{\text{ph}} = \chi + \frac{1}{\gamma} \cos \phi \quad (7.8)$$



where  $\phi$  is a random angle between 0 and  $2\pi$ . We also use Eq. (7.8) for simulation runs with a multipole field geometry. While technically the direction of photon emission should change with changing field geometries, in practice the photon propagation direction has little effect on the overall cascade (as long as it points generally outward) and so for simplicity we use the same formula. What matters for the cascade is how the angle between the photon and the magnetic field changes as the photon travels. As is discussed in Section 7.3.2, we artificially force this angle to change more rapidly with distance than in the dipole case, to account for the effect of the stronger field line curvature.

Note that ignoring the three-dimensional aspect of the photon emission introduces an error in the emission angle of order  $1/\gamma$ . This affects the point at which the photon decays in our simulation, since photon decay depends strongly on the intersection angle between the photon and the magnetic field (see below, Section 7.3.2). However, as the photon propagates through the magnetosphere these errors (which are on the order of  $1/\gamma \sim 10^{-7}$  for curvature radiation and  $10^{-3}$  for ICS) quickly become negligible in comparison to the photon-magnetic field intersection angle, which grows like  $s_{\text{ph}}/\mathcal{R}_c$  (and so reaches the angle  $1/\gamma$  by  $s_{\text{ph}} \sim 10^{-5}R$  for curvature and  $\sim 0.1R$  for ICS).

The total energy lost over the step is

$$\sum_{\epsilon} \epsilon \Delta N_{\epsilon} \simeq \Delta \gamma m_e c^2. \quad (7.9)$$

Only one photon is tracked for each energy bin  $\epsilon$  at each step  $\Delta s$ , so the photon is given a weighting factor  $\Delta N_{\epsilon}$ . In addition to its initial position [the position of the electron at the point of emission,  $(r, \theta)$ ] and propagation direction ( $\Theta_{\text{ph}}$ ), the photon has a polarization direction. For curvature radiation the polarization fraction is between 50% and 100% polarized parallel to the magnetic field curva-

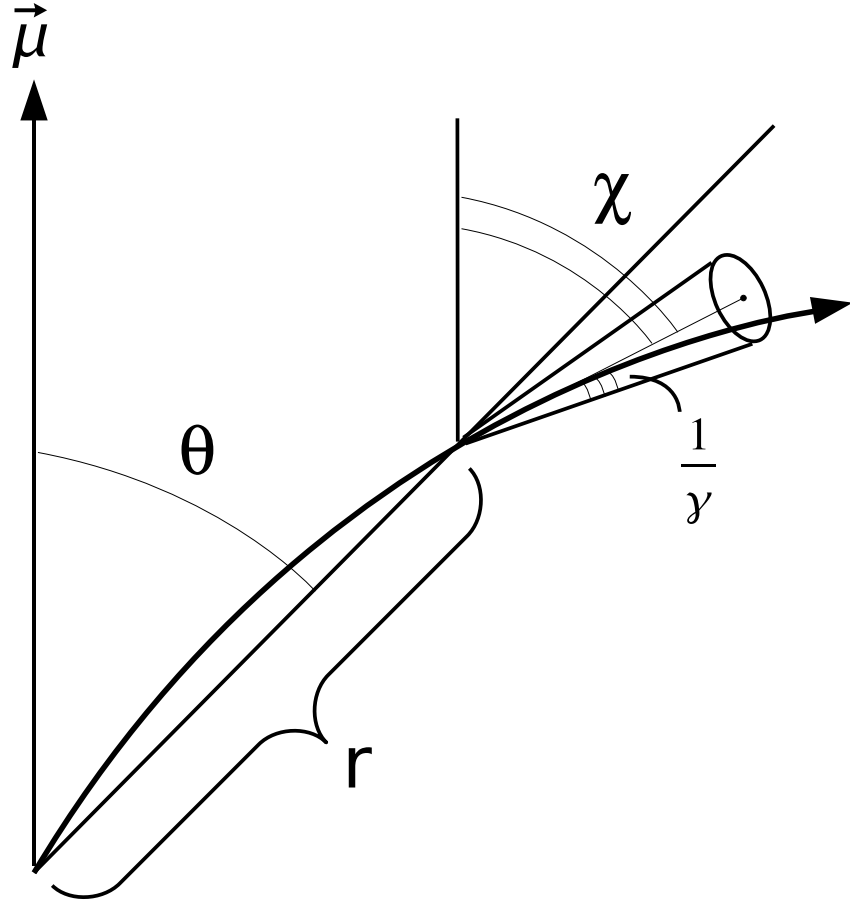


Figure 7.3: A schematic diagram for deriving the photon emission angle. The direction of the magnetic dipole axis is given by  $\vec{\mu}$ . The electron (positron) follows the curved field line to the point  $(r, \theta)$ , then emits a photon in a cone of width  $1/\gamma$  inclined with respect to the magnetic axis by an angle  $\chi$ .

ture (see Rybicki & Lightman 1979); therefore we randomly assign the photon a polarization with a weighting of one  $\perp$  to every seven  $\parallel$  photons, corresponding to a 75% parallel polarization.

### 7.3.2 Photon propagation, pair production, and splitting

The photon is emitted/scattered with energy  $\epsilon$  and polarization  $\parallel$  or  $\perp$  (and weighting factor  $\Delta N_\epsilon$ ). It propagates in a straight line from the point of emission, at an angle  $\Theta_{\text{ph}}$  with respect to the magnetic dipole axis. It has an optical depth to pair production,  $\tau$ , and to photon splitting,  $\tau_{\text{sp}}$ , both of which are set to zero at the moment of the photon's creation.

Note that in the corotating frame (which is the frame we are working in for most of our simulation; but see Section 7.3.3) the photon path is actually bent; the deviation grows as  $s_{\text{ph}}\Omega/c$ , where  $s_{\text{ph}}$  is the distance traveled (outward) by the photon from the point of emission (cf. Harding et al. 1978). Like the beaming angle (Section 7.3.1), this bending affects the photon-magnetic field intersection angle and the point of photon decay in our simulation. However, the total intersection angle grows much faster with photon distance  $s_{\text{ph}}$  than the deviation does ( $s_{\text{ph}}/\mathcal{R}_c$  versus  $s_{\text{ph}}\Omega/c = s_{\text{ph}}/r_{\text{LC}}$ , or a factor of  $\sqrt{r_{\text{LC}}/R} \simeq 100P_0^{1/2}$  larger), so we can safely ignore this deviation.

In each step the photon moves a short distance through the magnetosphere,  $\Delta s_{\text{ph}} [\simeq 0.05r_{\text{ph}}, \text{ where } (r_{\text{ph}}, \theta_{\text{ph}}) \text{ refers to the current position of the photon}]$ . At the new position the change in the optical depth for pair production,  $\Delta\tau$ , and for photon splitting,  $\Delta\tau_{\text{sp}}$ , are calculated:

$$\Delta\tau \simeq \Delta s R'_{\parallel, \perp} \sin \psi, \quad (7.10)$$

$$\Delta\tau_{\text{sp}} \simeq \Delta s R'_{\parallel,\perp}{}^{\text{sp}} \sin \psi, \quad (7.11)$$

where  $\psi$  is the angle of intersection between the photon and the local magnetic field and  $R'$  is the attenuation coefficient in the frame where the photon is propagating perpendicular to the local magnetic field, for  $\parallel$  and  $\perp$  polarized photons.

For a dipole field geometry the intersection angle is given by

$$\psi = \chi(\theta_{\text{ph}}) - \Theta_{\text{ph}}, \quad (7.12)$$

where  $\Theta_{\text{ph}}$  is given by Eq. (7.8) and  $\chi(\theta_{\text{ph}})$  is the angle between the magnetic axis and the magnetic field at the current location of the photon [Eq. (7.7)]; see Fig. 7.4 for a sketch. For a multipole geometry we set

$$\tan \psi = \frac{s_{\text{ph}}}{R}. \quad (7.13)$$

This approximation has the advantage of accounting for the effect of a strong field curvature on the photon propagation without requiring knowledge of the actual field topology.

As was discussed in Chapter 6, for photons propagating in “weak” magnetic fields ( $\beta_Q \lesssim 0.1$ ) it is valid to use the asymptotic attenuation coefficient for pair production,

$$R'_{\parallel,\perp} \simeq \frac{0.23}{a_0} \beta_Q \exp\left(-\frac{4}{3x\beta_Q}\right), \quad (7.14)$$

where

$$x = \frac{\epsilon'}{2m_e c^2} = \frac{\epsilon}{2m_e c^2} \sin \psi \quad (7.15)$$

and Eq. (7.14) applies for both polarizations. For stronger fields, however, pairs are produced in low Landau levels, and the quantum attenuation coefficients must be used (see Daugherty & Harding 1983). In Appendix D we find that the critical magnetic field strength separating these two regimes is  $B_{\text{crit}} \simeq 3 \times 10^{12}$  G

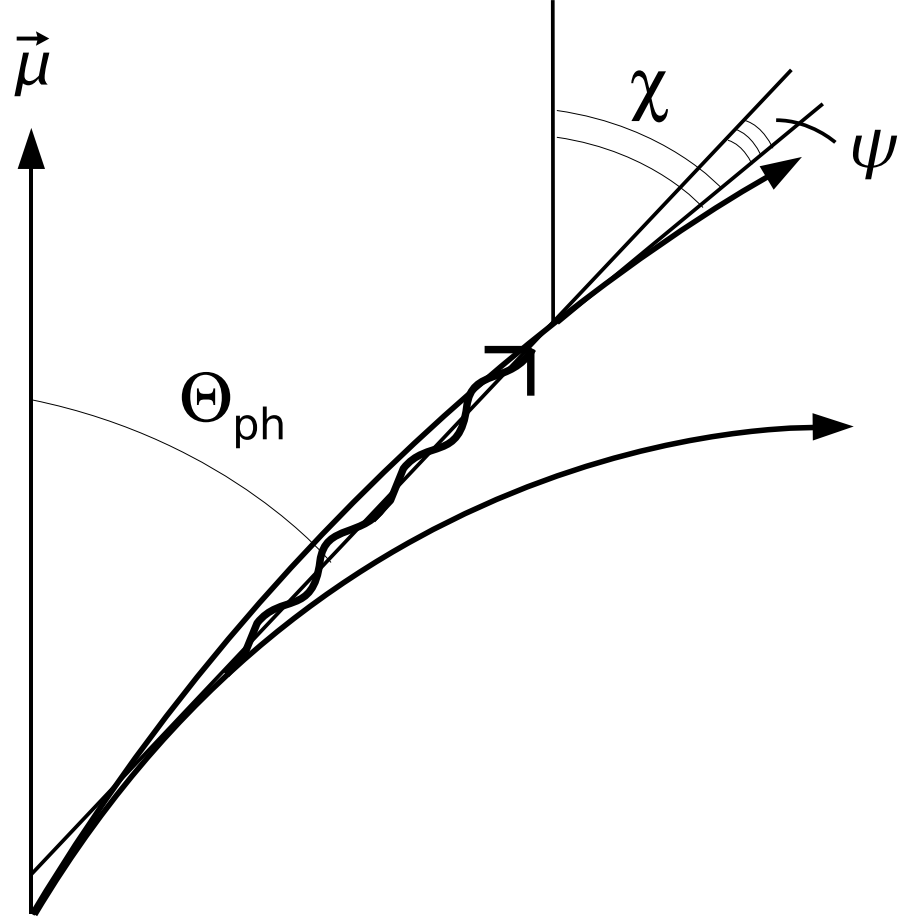


Figure 7.4: A schematic diagram for deriving the angle between the photon and the magnetic field,  $\psi$ . The direction of the magnetic dipole axis is given by  $\vec{\mu}$ . The photon propagates through the magnetosphere with angle  $\Theta_{\text{ph}}$  with respect to the magnetic axis [see Eq. (7.8)]. The local magnetic field makes an angle  $\chi$  with respect to the magnetic axis [Eq. (7.7)].

[Eq. (D.20)]. We also find that the boundary between the two regimes is very sharp: pairs are either created at or near threshold (Landau levels  $n \leq 2$ ) for  $B \gtrsim B_{\text{crit}}$  or in high Landau levels for  $B \lesssim B_{\text{crit}}$ , with very few electrons/positrons created in intermediate Landau levels. Therefore, in our simulation we only consider the first three attenuation coefficients for  $\parallel$ -polarized photons and the first two attenuation coefficients for  $\perp$ -polarized photons [up to  $x = 0.5(1 + \sqrt{1 + 6\beta_Q})$ , the point where one particle is created in the  $n = 2$  Landau level and the other is created in the  $n = 0$  Landau level]. These attenuation coefficients are given in Appendix D.2, Eqs. (D.8)–(D.12). If the photon propagates far enough into the magnetosphere that a higher attenuation coefficient is needed, the asymptotic attenuation coefficient, Eq. (7.14), is used instead. The attenuation coefficients for both polarizations of pair production and the asymptotic value are plotted in Fig. 7.5.

For photon splitting the attenuation coefficient is given by

$$R'_{\perp \rightarrow \parallel \parallel}^{\text{sp}} \simeq \frac{\alpha^2}{60\pi^2 a_0} \left(\frac{26}{315}\right)^2 x^5 \begin{cases} \beta_Q^6, & \beta_Q < 1, \\ 1, & \beta_Q \geq 1 \end{cases} \quad (7.16)$$

for  $\perp$  polarization and

$$R'_{\parallel}^{\text{sp}} = 0 \quad (7.17)$$

for  $\parallel$  polarization; the only allowed photon splitting process is  $\perp \rightarrow \parallel \parallel$  (Adler 1971; Usov 2002). Note that, to compare with previous works, we later relax this restriction and allow both  $\perp$  and  $\parallel$  modes to split (as suggested by Baring & Harding 2001); in this case we used Eq. (7.16) as an approximate attenuation coefficient for both. The  $\perp \rightarrow \parallel \parallel$  attenuation coefficient for photon splitting is plotted in Fig. 7.5 for  $\beta_Q = 1$ . Because the attenuation coefficient  $R'_{\perp \rightarrow \parallel \parallel}^{\text{sp}}$  drops rapidly with field strength for  $\beta_Q < 1$  [see Eq. (7.16)], photon splitting is unimportant for  $\beta_Q \lesssim 0.5$  (Baring & Harding 2001). However, for perpendicular-polarized photons propa-

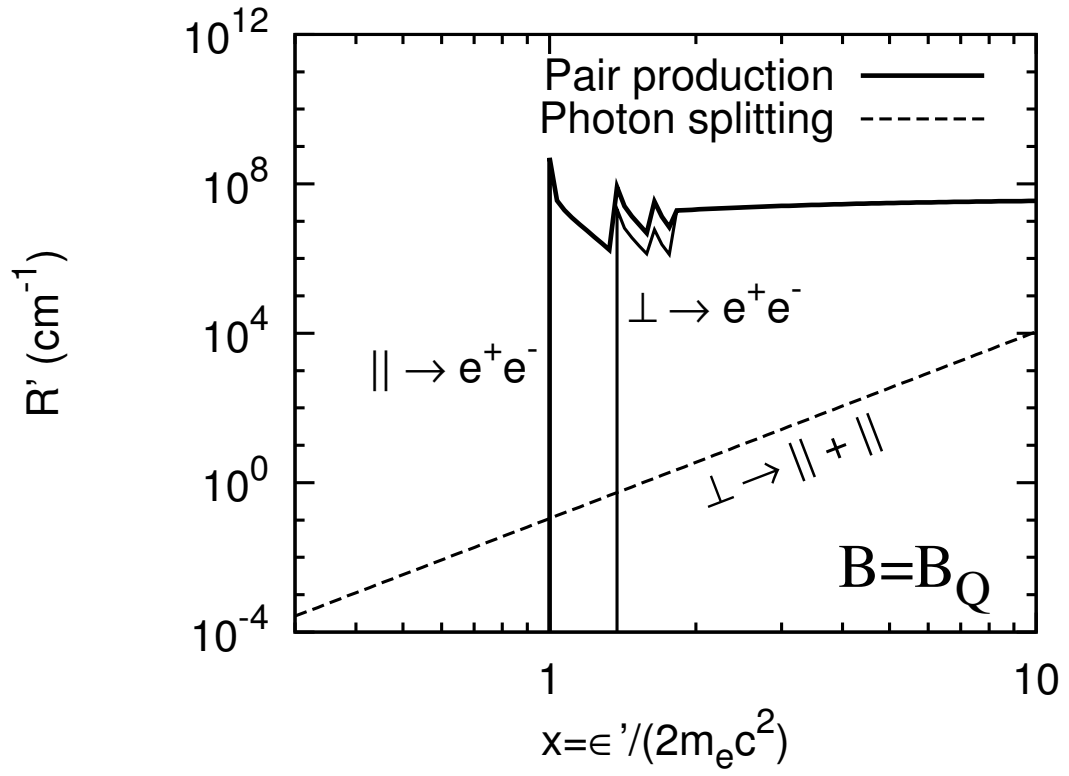


Figure 7.5: Attenuation in the frame where the photon is traveling perpendicular to the magnetic field, for both photon splitting (labeled by  $\perp \rightarrow \parallel + \parallel$ ) and pair production (labeled by  $\parallel \rightarrow e^+e^-$  and  $\perp \rightarrow e^+e^-$ ). The magnetic field strength is  $B = B_Q = 4.414 \times 10^{13}$  G.

gating in superstrong fields  $\beta_Q \gtrsim 0.5$ , photon splitting is the dominant attenuation process. Even though above threshold [ $x \geq 0.5(1 + \sqrt{1 + 2\beta_Q})$ ] the attenuation coefficient for photon splitting is much smaller than that for pair production (see Fig. 7.5), in superstrong fields the photon splits before reaching threshold.

Whenever  $\tau \geq 1$  or  $\tau_{\text{sp}} \geq 1$  the photon is destroyed. While technically the photon should only be destroyed with probability  $1 - \exp(-\tau)$ , in practice once either  $\tau$  reaches unity it grows so dramatically with distance  $s_{\text{ph}}$  that the probability of photon destruction above  $\tau = 1$  is nearly unity anyway. If  $\tau_{\text{sp}} \geq 1$  the photon splits into two. As a simplification we assume that each photon takes half of the energy of the parent photon. Rather than tracking two new photons we halve the energy of the original photon, double the number of photons it represents ( $\Delta N_\epsilon$ ), and reset both optical depth values ( $\tau_{\text{sp}}$  and  $\tau$ ) to zero. Because  $\perp \rightarrow \parallel$  is the only allowed photon splitting process, the daughter photons are now  $\parallel$ -polarized and can not split again. If  $\tau \geq 1$  the photon creates an electron-positron pair. If the photon has reached a height in the magnetosphere such that the asymptotic version of the attenuation coefficient is applicable (i.e., at low fields) the electron and positron are both created with half the energy of the photon ( $\mathcal{E} = 0.5\epsilon$ ) and traveling in the same direction as the photon (the pitch angle  $\Psi = \psi$ ). Such an approximation is valid as long as  $x\beta_Q \lesssim 0.1$  (see Daugherty & Harding 1983), which according to Eq. (6.11) is always true for  $B \lesssim 3 \times 10^{12}$  G. If the photon does not reach this asymptotic limit (i.e., at high fields) the electron and positron are created in low Landau levels as close to the threshold as possible, with energies and pitch angles given in Appendix D.3 [Eqs. (D.23) and (D.24), respectively].



### 7.3.3 Propagation and photon emission of the secondary electrons and positrons

In the corotating frame the secondary electron (or positron) is created with initial energy  $\gamma_{0,s}$  and pitch angle  $\vartheta_0$  or Landau level  $n$  (and weighting  $\Delta N_\epsilon$ ). (We use the subscript ‘s’ here for the initial electron/positron energy  $\gamma_0$  to distinguish it from the initial energy for the primary electron.) For the purpose of tracking the synchrotron emission from the electron it is easier to work in the frame in which the electron has no momentum along the magnetic field direction and only moves transverse to the field in a circular motion. We hereafter refer to this frame as the “circular motion” frame. In this frame the electron’s initial energy is given by

$$\gamma_\perp = \sqrt{\gamma_{0,s}^2 \sin^2 \Psi + \cos^2 \Psi} = \sqrt{1 + 2\beta_Q n}. \quad (7.18)$$

For synchrotron radiation the emission rates are extremely large:

$$P_{\text{synch}} = \frac{2e^2}{3c^3} \gamma^2 \omega_{Be}^2 v^2 \sin^2 \Psi \gtrsim 4 \times 10^{18} \beta_Q^2 m_e c^2 \text{ s}^{-1}. \quad (7.19)$$

We therefore assume for the simulation that the electron loses all of its perpendicular momentum  $p_\perp$  “instantaneously” due to synchrotron radiation, before moving from its initial position (cf. Daugherty & Harding 1982). In the “circular motion” frame the photons are assumed to be emitted perpendicular to the magnetic field so that no kick is imparted to the electron; with this approximation the frame corresponding to circular motion of the electron does not change over the course of the synchrotron emission process. The final energy of the electron after  $p_\perp = 0$  is given by

$$\gamma_\parallel = \gamma_{0,s} / \gamma_\perp. \quad (7.20)$$

Unlike curvature photons, each synchrotron photon carries an energy comparable to the “transverse” energy of the parent electron. Therefore, in the synchrotron

part of the simulation the electron emits one photon per step, rather than a large number of photons at many different energies as was done in the curvature radiation part. (Note that to generate smooth photon distributions we sometimes use energy bins as in the curvature case, but with each bin representing a fraction of a photon.) If the electron is created in a high Landau level,  $n > 2$ , the energy of the photon is chosen randomly, but with a weighting based on the asymptotic synchrotron spectrum<sup>2</sup> (e.g., Sokolov & Ternov 1968; Harding & Preece 1987)

$$\frac{d^2 N}{dt d\epsilon_{\perp}} = \frac{\sqrt{3} \alpha \omega_{Be}}{2\pi \epsilon_{\perp}} \left[ f F\left(\frac{\epsilon_{\perp}}{f \epsilon_{SR}}\right) + \left(\frac{\epsilon_{\perp}}{\gamma_{\perp}}\right)^2 G\left(\frac{\epsilon_{\perp}}{f \epsilon_{SR}}\right) \right]. \quad (7.21)$$

where  $\epsilon_{\perp}$  is the photon energy in the circular motion frame,  $\epsilon_{SR} = 3\gamma_{\perp}^2 \hbar \omega_{Be}/2$  is the characteristic energy of the synchrotron photons,  $\omega_{Be}$  is the electron cyclotron frequency,  $f = 1 - \epsilon_{\perp}/(\gamma_{\perp} m_e c^2)$  is the fraction of the electron's energy remaining after photon emission,  $F(x) = x \int_x^{\infty} K_{5/3}(t) dt$ , and  $G(x) = x K_{2/3}(x)$ . If  $n = 1$ , the energy of the photon is that required to lower the electron to its ground state:  $\epsilon_{\perp} = m_e c^2 (\sqrt{1 + 2\beta_Q} - 1)$ . If  $n = 2$ , the energy of the photon could be that required to lower the electron to its ground state or the first excited state, depending on the transition. We do not calculate the exact transition rates for the  $n = 2$  state here. Instead, we use the following simplified formalism, based on the results of Herold et al. (1982) (see also Harding & Preece 1987): If  $\beta_Q \gtrsim 1$  the energy of the photon is chosen to be that required to lower the electron to its ground state,  $\epsilon_{\perp} = m_e c^2 (\sqrt{1 + 4\beta_Q} - 1)$ . If  $\beta_Q < 1$  the energy of the photon is randomly chosen to be that required to lower the electron to either the ground state, 50% of the

---

<sup>2</sup>This expression differs from classical synchrotron spectrum (e.g., Rybicki & Lightman 1979) in two ways: First, a factor of  $f = 1 - \epsilon_{\perp}/(\gamma_{\perp} m_e c^2)$  appears in several places throughout Eq. (7.21); when the photon energy is equal to the electron energy ( $\epsilon_{\perp} = \gamma_{\perp} m_e c^2$  or  $f = 0$ ) the asymptotic expression goes to zero. Second, a term containing the function  $G(x)$  appears in Eq. (7.21). While a term containing  $G(x)$  appears in the classical expressions for the radiation spectra of both perpendicular- and parallel-polarized photons, in the classical expression for the total radiation spectra these terms cancel and  $G(x)$  disappears. However, when the quantum effect of the electron spin is considered there is an asymmetry between the perpendicular and parallel polarizations such that the  $G(x)$  term remains.

time, or the first excited state  $[\epsilon_{\perp} = m_e c^2 (\sqrt{1 + 4\beta_Q} - \sqrt{1 + 2\beta_Q})]$ , 50% of the time.

The energy of the photon is transformed into the “lab” frame of the neutron star (the corotating frame) using

$$\epsilon = \gamma_{\parallel} \epsilon_{\perp} . \quad (7.22)$$

Because the photon is emitted in a random direction perpendicular to the magnetic field in the “circular motion” frame, in the neutron star frame the angle of emission is approximately given by

$$\Theta_{\text{ph}} = \chi + (\Psi + 1/\gamma_{\parallel}) \cos(\phi) , \quad (7.23)$$

where  $\phi$  is a random angle between 0 and  $2\pi$ ,  $\chi$  is given by Eq. (7.7), and the pitch angle is given by Eq. (7.18):

$$\Psi = \arcsin \left( \sqrt{\frac{\gamma_{\perp}^2 - 1}{\gamma_{0,s}^2 - 1}} \right) . \quad (7.24)$$

For synchrotron radiation the polarization fraction is between 50% and 100% polarized **perpendicular** to the magnetic field (which is the opposite situation from that for curvature radiation; see Rybicki & Lightman 1979). Therefore we randomly assign the photon a polarization with a weighting of one  $\parallel$  to every seven  $\perp$  photons (corresponding to a 75% perpendicular polarization). After the photon is emitted the energy of the electron is reduced by the amount  $\Delta\gamma_{\perp} = \epsilon_{\perp}/(m_e c^2)$  and the synchrotron process is repeated. This continues until  $\gamma_{\perp} = 1$ , i.e., the electron is in the ground Landau level.

Once the electron (or positron) loses all of its perpendicular momentum, it moves along the magnetic field line and upscatters RICS photons. In each step one RICS photon is scattered. The length of the path the electron travels along

the field in each step,  $\Delta s$ , is chosen such that one RICS photon is scattered per step,  $\Delta N_{\text{RICS}} = 1$ . Since

$$\Delta s \simeq \frac{c \Delta N_{\text{RICS}}}{dN_{\text{RICS}}/dt}, \quad (7.25)$$

we have [Appendix D.1, Eq. (D.7)]

$$\Delta s \simeq \left[ \frac{\beta_Q^2}{\gamma^2 \beta a_0} \int_{\gamma(1-\beta)}^{\gamma(1-\beta x_{\min})} \frac{dy}{e^{\epsilon_{Be}/(ykT)} - 1} \right]^{-1}, \quad (7.26)$$

where  $y = \gamma(1 - \beta x)$ ,  $x_{\min} \simeq \cos[\arctan(R_{th}/z)]$ , and  $z = r - R$ . The mean energy of the scattered photon is

$$\epsilon = \gamma \left( 1 - \frac{1}{\sqrt{1 + 2\beta_Q}} \right) m_e c^2, \quad (7.27)$$

and the energy loss is given by

$$\epsilon \Delta N_{\text{RICS}} = \epsilon. \quad (7.28)$$

### 7.3.4 Cascades initiated by a primary photon

For our simulation, the only difference between a photon that is initiating a cascade and one that is emitted/scattered by an electron or positron (Section 7.3.2) is that for a photon initiating a cascade the initial conditions must be provided at the beginning of the simulation. The photon is usually injected into the magnetosphere at the stellar surface, though at high fields a more interesting cascade results if the photon is injected higher up (e.g.,  $r = 3R$ ; see Section 7.4). The photon is injected tangent to the magnetic field, as we find almost no difference in the final photon spectra/pair plasma if we add a beaming angle  $1/\gamma \sim 10^{-7}$ - $10^{-3}$ . At high fields ( $B \gtrsim 3 \times 10^{12}$  G; see Section 7.3.2 and Appendix D.2) the photon is given a perpendicular polarization to generate the largest possible cascade; at low fields ( $B \lesssim 3 \times 10^{12}$  G) the polarization does not matter as pairs are not being created in low Landau levels.

## 7.4 Results

In this section we present our results for photon- and electron-initiated cascades (Sections 7.4.1 and 7.4.2, respectively). We present our results for photon-initiated cascades first, as they are simpler and aid us in our discussion of the results for the full cascade (initiated by an electron). Our main results are the final photon spectra and pair plasma distributions presented in each subsection for various input parameters (surface temperature, surface field strength, rotation period, initial energy and injection radius of the particle, whether or not ICS operates, and which photon polarization modes are allowed to split). While most previous works on pair cascades present photon and pair spectra as functions of differential number counts  $dN/dE$  versus energy  $E$  (e.g., Daugherty & Harding 1982; Hirschman & Arons 2001b; Arendt & Eilek 2002), where  $E$  represents the energy of the photon  $\epsilon$  or the electron/positron  $\mathcal{E}$ , we plot  $dN/d\ln E$  versus energy in order to show on a log-log plot the approximate number of photons or electrons at any energy.

### 7.4.1 Photon-initiated cascades

Our results for photon-initiated cascades are presented in Figs. 7.6–7.8. Note that due to the discrete nature of the synchrotron and ICS emission the spectra should be very coarse; we have smoothed the spectra by allowing the electrons to emit fractions of a photon, rather than an entire photon, in each step. At all field strengths we find that the peak energies of the photons and electrons produced in the cascades are approximately given by

$$\epsilon \sim 0.2\mathcal{R}_6 \text{ MeV} \tag{7.29}$$

and

$$\mathcal{E} \sim 2\mathcal{R}_6 \text{ MeV} \quad (7.30)$$

respectively, where  $\mathcal{R}_6 = \mathcal{R}_c/(10^6 \text{ cm})$  is the local radius of curvature of the magnetic field (see Figs. 7.6 and 7.8). At moderate fields ( $B \lesssim 3 \times 10^{12} \text{ G}$ ; Section 7.3.2 and Appendix D.2) we find that cascades are initiated by photons with  $\epsilon \gtrsim 10^4 \text{ MeV}$  for dipole geometries or  $\epsilon \gtrsim 10^2 \text{ MeV}$  for multipole geometries; below these energies the primary photons do not produce pairs within the magnetosphere. Strong cascades (cascades with a second generation of pair production) occur when  $\epsilon \gtrsim 10^5 \text{ MeV}$  for dipole geometries or  $\epsilon \gtrsim 10^3 \text{ MeV}$  for multipole geometries. For the moderate and strong cascades the multiplicities of photons and electrons produced are given by

$$N_\epsilon \sim \frac{\epsilon_0}{5 \text{ MeV}} \mathcal{R}_6^{-1} \quad (7.31)$$

and

$$N_{\mathcal{E}} \sim \frac{\epsilon_0}{100 \text{ MeV}} \mathcal{R}_6^{-1} \quad (7.32)$$

respectively, where  $\epsilon_0$  is the primary photon energy. Therefore, for a given primary photon energy, cascades in multipole geometries are a factor of  $\sim 100P_0^{1/2}$  times larger in multiplicity but  $\sim 100P_0^{1/2}$  times lower in peak energy than those in dipole geometries. Figures 7.6 and 7.7 show the spectra for photon-initiated cascades at  $B = 10^{12} \text{ G}$ .

At high fields ( $B \gtrsim 3 \times 10^{12} \text{ G}$ ), if we “turn off” inverse Compton scattering (ICS) by the secondary electrons and positrons we find that cascades are very weak at all energies and field geometries; if the primary photon is parallel polarized, there will be no cascade at all. This is because the electrons and positrons produced by the primary photon are near or at threshold (Landau levels  $n < 2$ ) and so will not emit synchrotron radiation to sustain the cascade. With the ICS process operating

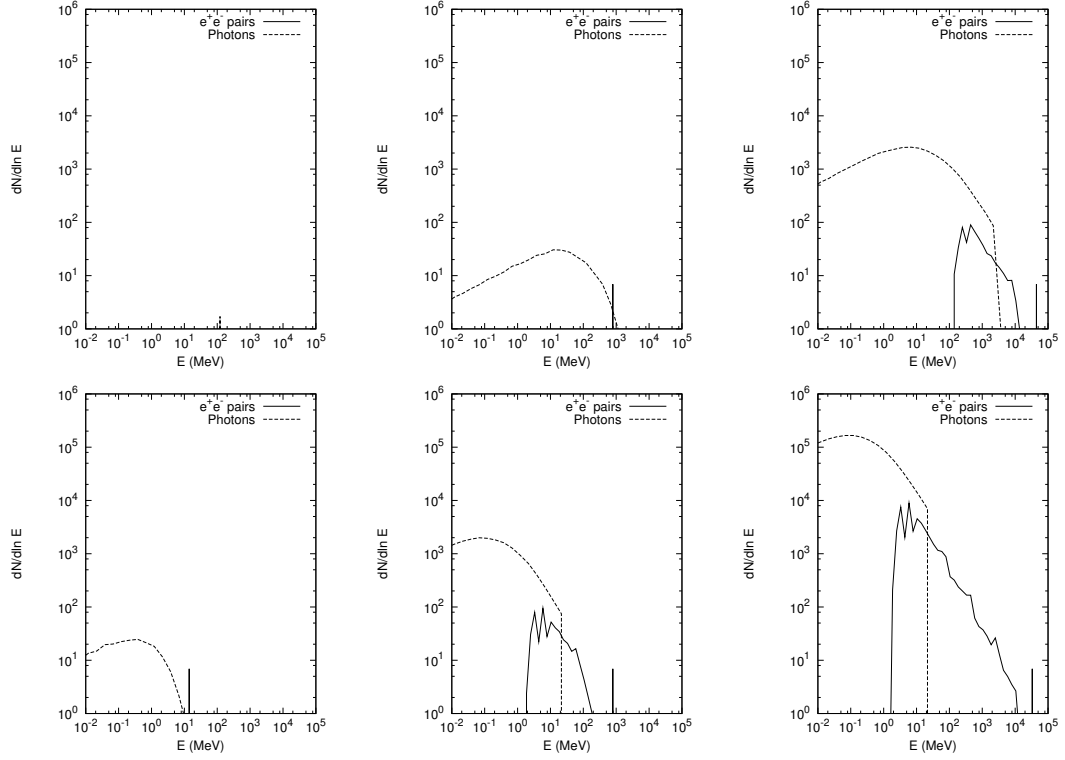


Figure 7.6: Final photon spectra and plasma distributions of photon-initiated cascade, for  $B_{12} = 1$  and  $P_0 = 1$ . The primary photon energy is  $10^2$  MeV (left-most panels),  $10^4$  MeV (middle), or  $10^6$  MeV (right), and the field geometry is dipole (top) or multipole ( $\mathcal{R}_c = R$ ) (bottom). The spike in every panel except the first represents the final energies of the first generation of pairs (one electron and one positron). The spike in the first panel represents the primary photon, which does not initiate a cascade for these parameters.

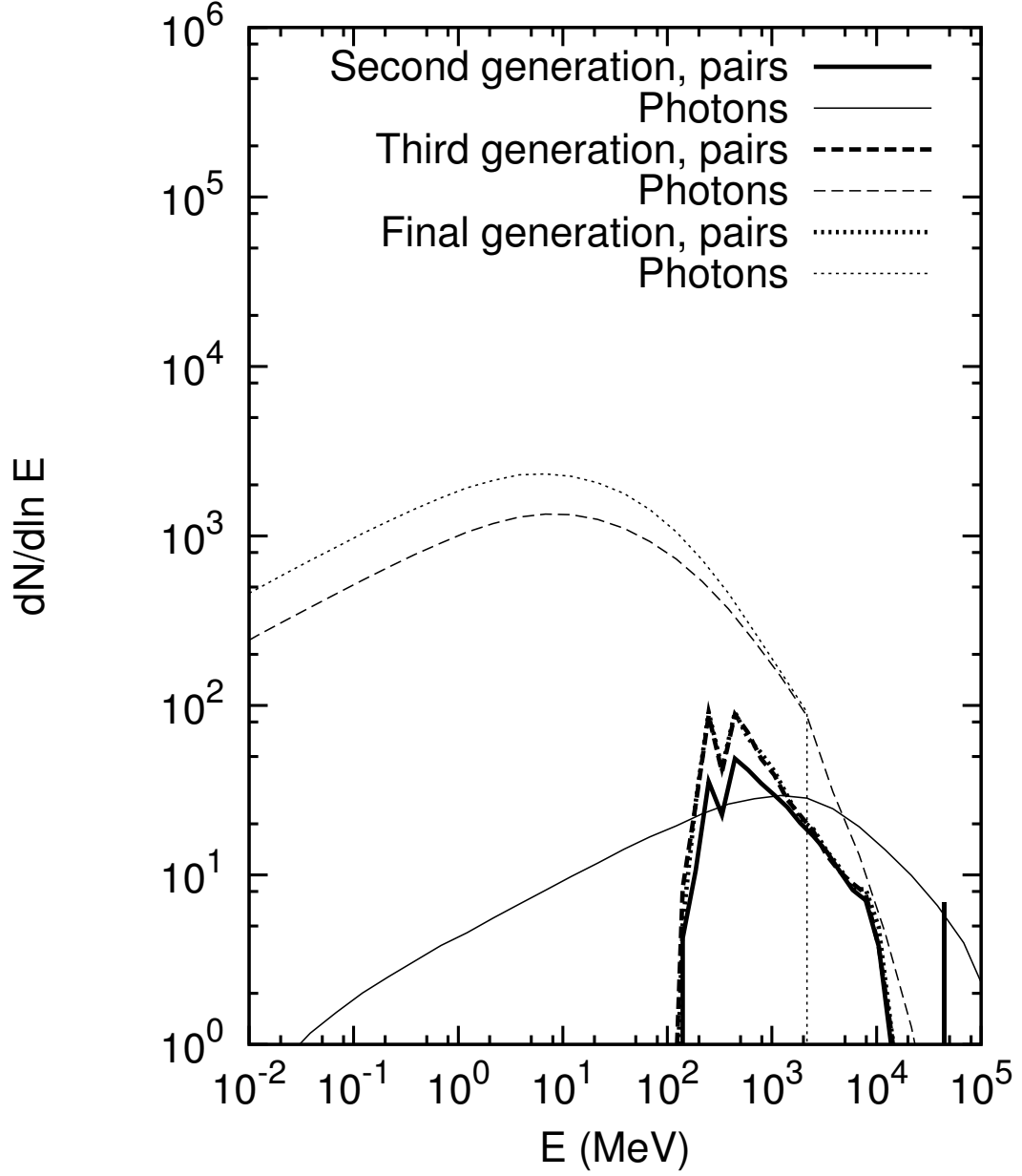


Figure 7.7: Cumulative spectra of successive generations of  $e^+e^-$  pair production and photon emission, for photon-initiated cascades. The thick lines represent the pair plasma distributions and the thin lines represent the photon spectra. Here the primary photon energy is  $10^6$  MeV and the field geometry is dipole, with  $B_{12} = 1$  and  $P_0 = 1$ .



there will be a moderate cascade in most cases, provided that the electrons are at low enough energies for this process to work efficiently ( $\mathcal{E} \lesssim \beta_Q m_e c^2 / (kT)$ ). For primary photons injected at a height  $r \gtrsim 2R$  above the surface, the background of thermal photons from the surface is too weak for ICS to assist in the propagation of the cascade. However, for these primary photons the cascade will actually be stronger than for primary photons injected near the surface, because the local magnetic field strength has dropped by a factor of  $(r/R)^3$ ; if  $B_p(R/r)^3 \lesssim 3 \times 10^{12}$  G, where  $B_p$  is the surface magnetic field strength, the cascade will be similar in behavior to the weak-field cascades discussed above. Figure 7.8 shows spectra for photon-initiated cascades at  $B = B_Q = 4.414 \times 10^{13}$  G.

#### 7.4.2 Electron-initiated cascades

Our results for electron-initiated cascades are presented in Figs. 7.12–7.18 and Table 7.1. We find that the densest and most energetic pair plasmas are produced for neutron stars with strong surface fields, short rotation periods, and multipole field geometries. The amplitudes of the photon spectra and plasma distributions increase rapidly with the initial energy of the primary electron; large initial energies also tend to come from stars with strong fields and rapid rotation (Fig. 7.1). Figures 7.9–7.11 show our results for a variety of magnetic field strengths, periods, and initial electron energies.

Figure 7.12 shows the photon energy distribution in the frame in which each photon is traveling perpendicular to the magnetic field, for various heights above the star. Note that when the local magnetic field [given by  $B \simeq B_p(R/r)^3$ , where  $B_p$  is the surface magnetic field at the pole] is greater than about  $3 \times 10^{12}$  G, there are no photons in the spectra with  $\epsilon' = \epsilon \sin \psi > 2m_e c^2$ ; as we saw in Section 7.3.2,

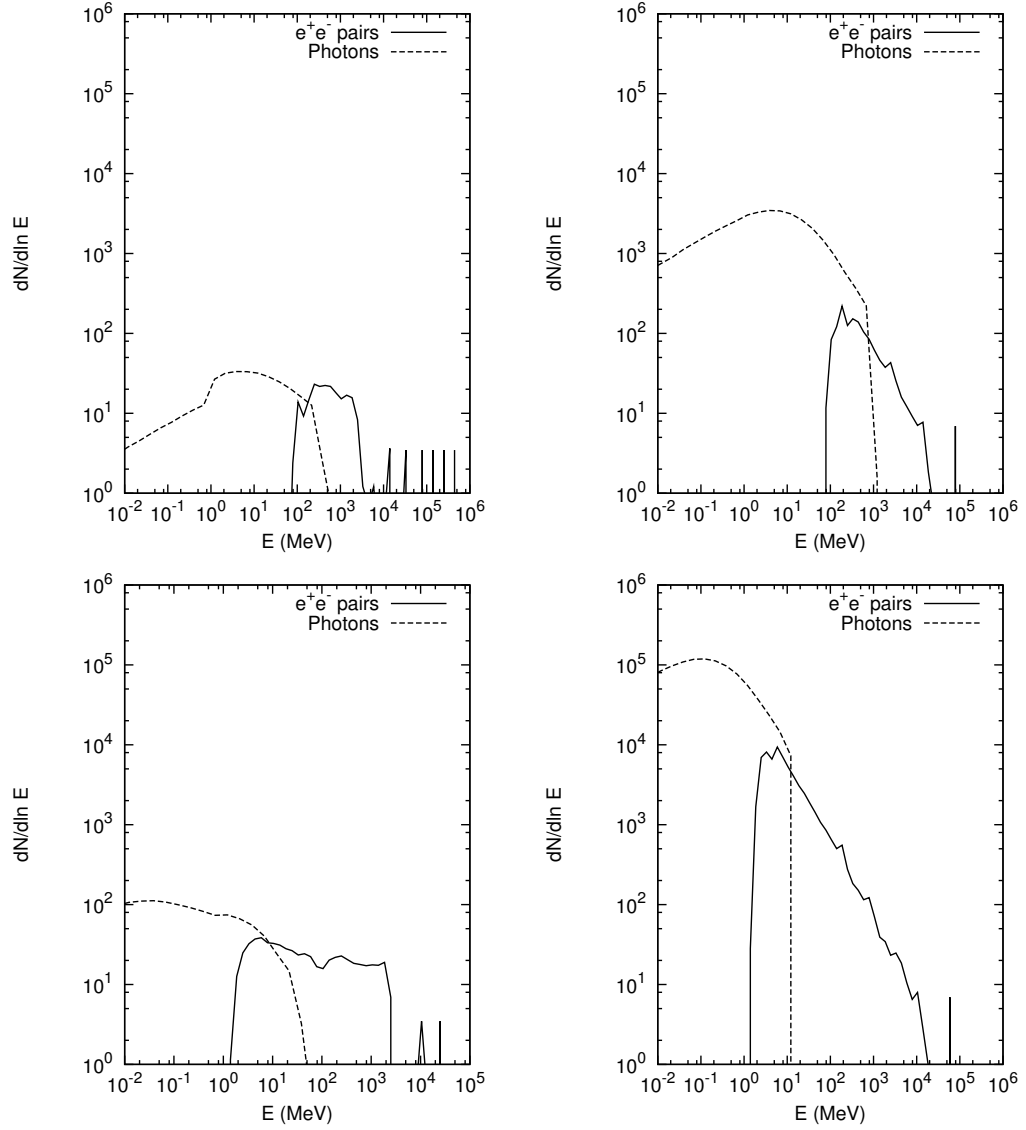


Figure 7.8: Final photon spectra and plasma distributions of photon-initiated cascades, for  $B = B_Q$  and  $P_0 = 1$ . The primary photon energy is  $10^6$  MeV, the injection radius is  $r_0 = R$  (left-most panels) or  $r_0 = 3R$  (right), and the field geometry is dipole (top) or multipole ( $\mathcal{R}_c = R$ ) (bottom). The spikes in the plasma distributions represent individual electrons or positrons or electron-positron pairs. The spectra in the left-most panels are of cascades where all photons are polarized perpendicular to the field; for random polarizations the cascades are generally much smaller. All of the cascades shown here include ICS secondary effects.

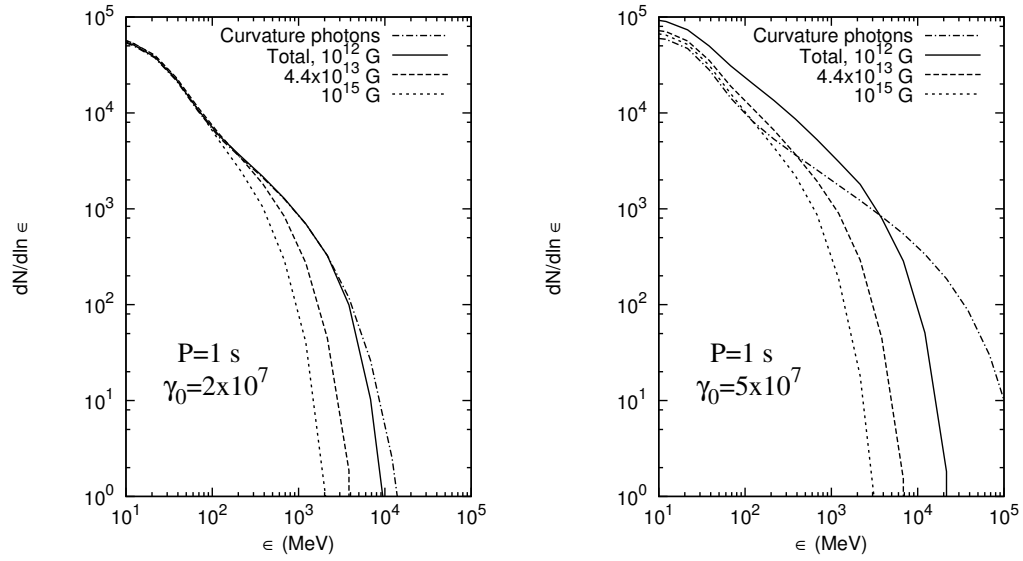


Figure 7.9: Photon spectra for polar magnetic field strengths  $B_p = 10^{12}$  G,  $B_Q = 4.414 \times 10^{13}$  G (the critical quantum magnetic field strength), and  $10^{15}$  G. Here, the period is  $P = 1$  s, the magnetic field is dipole, and the primary electron travels along the last open field line. The curve labeled “Curvature photons” in each panel (the dot-dashed line) shows the curvature radiation generated by the primary electron, which is the same for all field strengths. The other curves show the final photon spectra after pair production and synchrotron emission. In the first panel the initial Lorentz factor of the primary electron is  $\gamma_0 = 2 \times 10^7$ , in the second  $\gamma_0 = 5 \times 10^7$ .

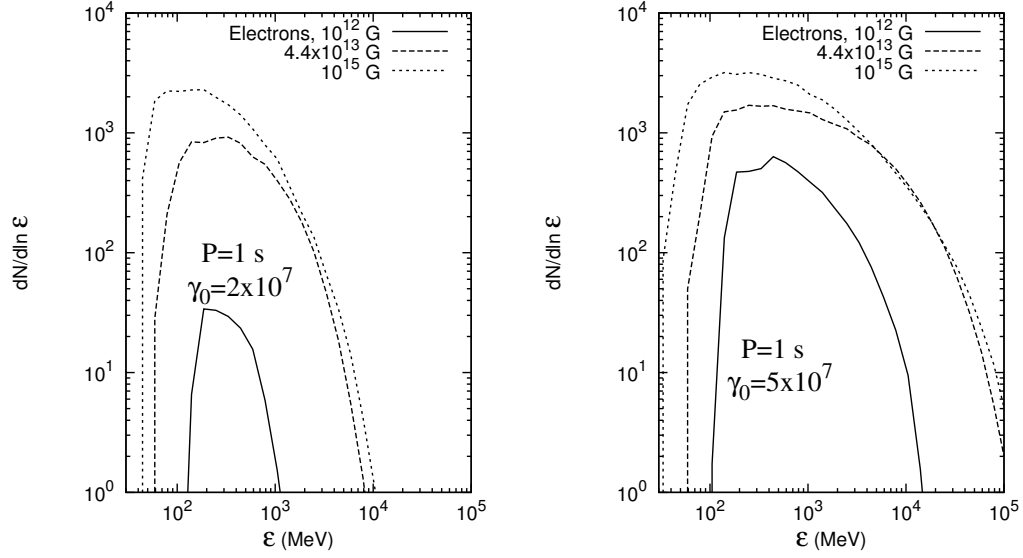


Figure 7.10: Pair plasma distributions for polar magnetic field strengths  $B_p = 10^{12}$  G,  $B_Q = 4.414 \times 10^{13}$  G (the critical quantum magnetic field strength), and  $10^{15}$  G. Here, the period is  $P = 1$  s, the magnetic field is dipole, and the primary electron travels along the last open field line. In the first panel the initial Lorentz factor of the primary electron is  $\gamma_0 = 2 \times 10^7$ , in the second  $\gamma_0 = 5 \times 10^7$ .

for  $B \gtrsim 3 \times 10^{12}$  G photons pair produce almost immediately upon reaching the threshold condition ( $\epsilon' = 2m_e c^2$ ).

Figure 7.13 shows the photon and electron/positron number distributions as a function of height above the star, for surface magnetic field strengths  $B = 10^{12}$  G,  $4.414 \times 10^{13}$  G, and  $10^{15}$  G. The curves representing the number distributions of curvature radiation photons are the same in each case, since the spectrum of curvature radiation given by Eq. (7.6) does not depend on magnetic field strength. Electron-positron pairs are produced with almost 100% efficiency (i.e., one pair is created for each curvature photon) until  $B$  drops below about  $3 \times 10^{12}$  G; they are then produced with moderate efficiency until  $B$  drops below about  $10^{11}$  G (the exact value depends on the initial electron energy  $\gamma_0$ ), at which point no more pairs are produced. Note that while curvature radiation dominates the overall photon distribution, there is a flurry of synchrotron radiation between  $B = 3 \times 10^{12}$  G,

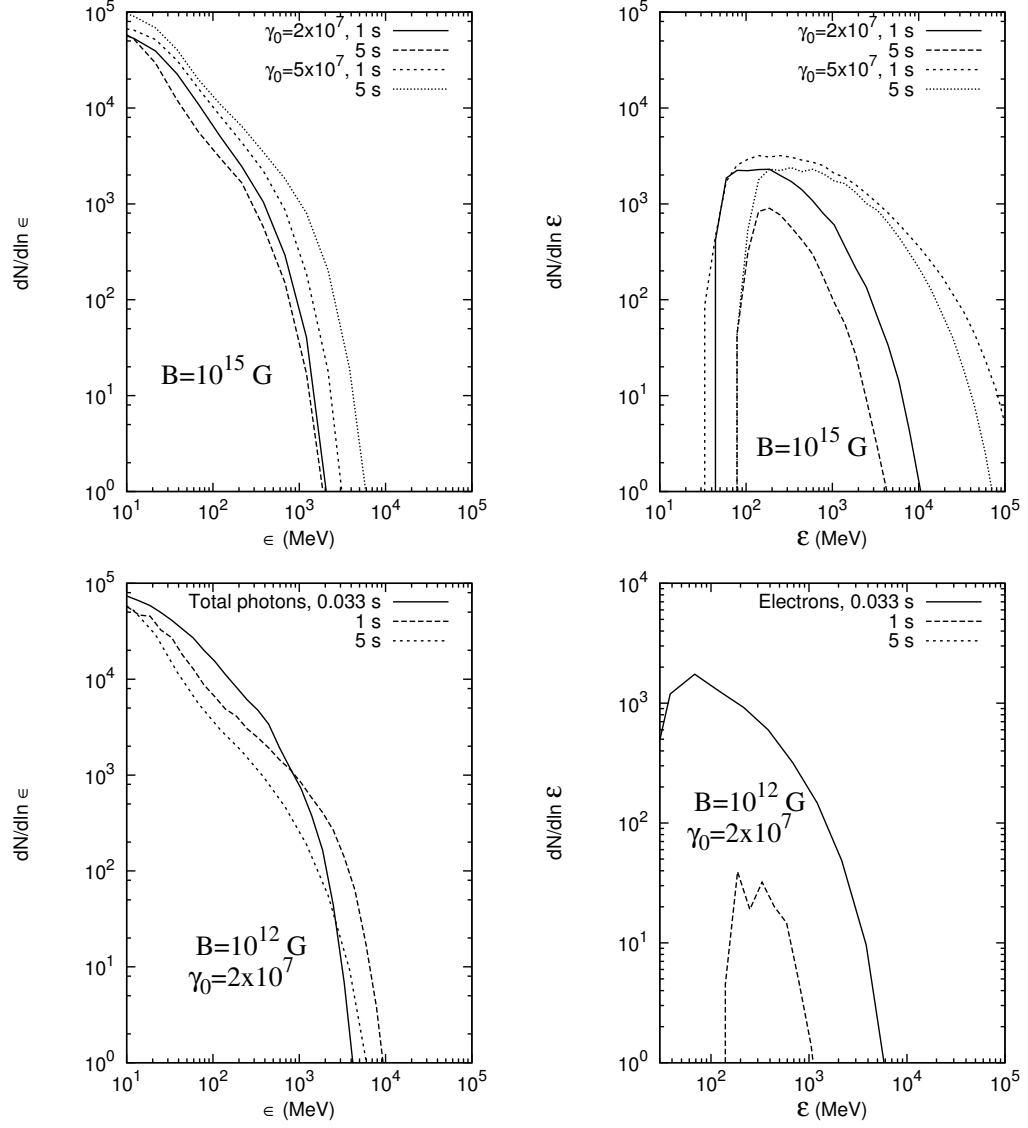


Figure 7.11: Photon spectra and plasma distributions for various stellar periods. The spectra for  $B = 10^{15}$  G are on the top; the spectra for  $B = 10^{12}$  G are on the bottom; the photon spectra are on the left; the pair spectra are on the right.

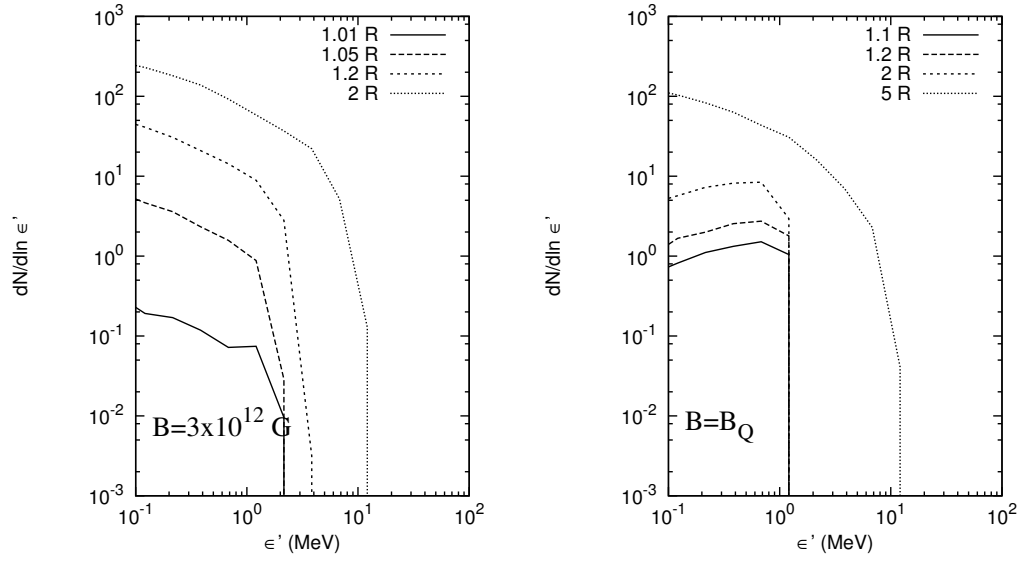


Figure 7.12: Photon energy distribution  $\epsilon' = \epsilon \sin \psi$  at different heights above the star, where  $\epsilon'$  is the photon energy in the frame in which the photon is traveling perpendicular to the magnetic field and  $\psi$  is the angle between the photon and the local magnetic field. The stellar surface is located at  $r = R$ . The left panel shows the spectrum at  $B = 3 \times 10^{12} \text{ G}$ ; the right panel shows the spectrum at  $B = B_Q = 4.414 \times 10^{13} \text{ G}$ . Every photon that passes a given height is recorded in the spectrum for that height. The initial electron Lorentz factor is  $\gamma_0 = 5 \times 10^7$ .

the point at which electrons and positrons are created in high Landau levels, and  $B \sim 10^{11}$  G, the point at which electron-positron pairs are no longer created.

Figures 7.14 and 7.15 show photon spectra and plasma distributions at different heights above the star. These spectra are generated by recording the parameters of any photon or electron/positron which crosses a given height, say  $r = 2R$ . For a given initial electron energy  $\gamma_0$ , the spectra all exhibit similar trends with height as long as the local field is greater than about  $3 \times 10^{12}$  G. For example, the numbers and peak energies of the cascade photons and electrons/positrons which pass  $r = 2R$  in a star with  $B_p = B_Q$  are approximately the same as those which pass  $r = 2R$  in a star with  $B = 10^{15}$  G; however, the numbers and energies are different passing  $r = 5R$ , since the local field of the  $B_p = B_Q$  star is now  $B = 3 \times 10^{11}$  G (see Fig. 7.14).

Table 7.1 shows the final photon and electron/positron energies and multiplicities for various magnetic field strengths, with  $\gamma_0 = 5 \times 10^7$  and  $P_0 = 1$ . Note that while the total number of photons does not change much with field strength (as curvature radiation, which is independent of  $B$ , dominates the total multiplicity of photons produced; see Fig. 7.13), the total energy of the photons changes dramatically with field strength. A much larger fraction of the total photon energy is converted in to pair production at high fields, resulting in a larger number and total energy of electron-positron pairs. Fig. 7.16 shows the final electron multiplicities as a function of  $\gamma_0$ , for various field strengths and periods. Note that multiplicity drops off precipitously with decreasing  $\gamma_0$ ; if indeed a dense ( $\rho \gg \rho_{GJ}$ ) pair plasma is necessary to generate the observed radio emission from rotation-powered pulsars (as is suggested by, e.g., Melrose 2004; Thompson 2004), then  $\gamma_0$  can not be much less than  $5 \times 10^6$  (a number which varies slightly with field strength and rotation

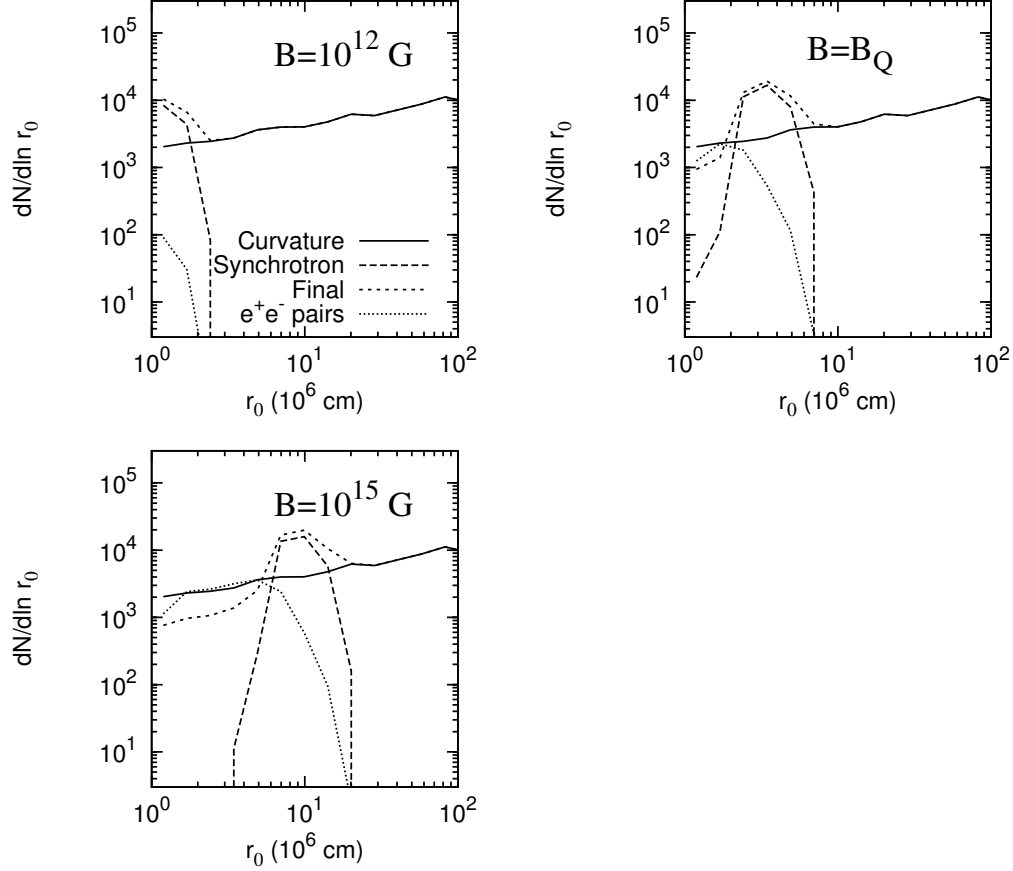


Figure 7.13: Photon and electron/positron number distributions as a function of radius, for  $\gamma_0 = 2 \times 10^7$ ,  $P_0 = 1$ , and  $B_{12} = 1$  (top left panel),  $B_{12} = 44.14$  (top right), and  $B_{12} = 1000$  (bottom). For a given particle (photon, electron, or positron), the radius  $r_0$  is the radius where the particle is created, so that  $dN/d\ln r_0$  is a measure of how many particles are created at the point  $r_0$ . The curve labeled “Curvature” shows where the curvature radiation photons are emitted by the primary electron (which continues in a similar manner beyond the graph out to  $r = r_{LC}$ ), “Synchrotron” shows where the synchrotron photons are emitted by the secondary electrons/positrons, “Final” shows where the photons that escape the magnetosphere are created (any photon that avoids destruction through pair production or photon splitting), and “ $e^+e^-$  pairs” shows where the electrons and positrons are created.



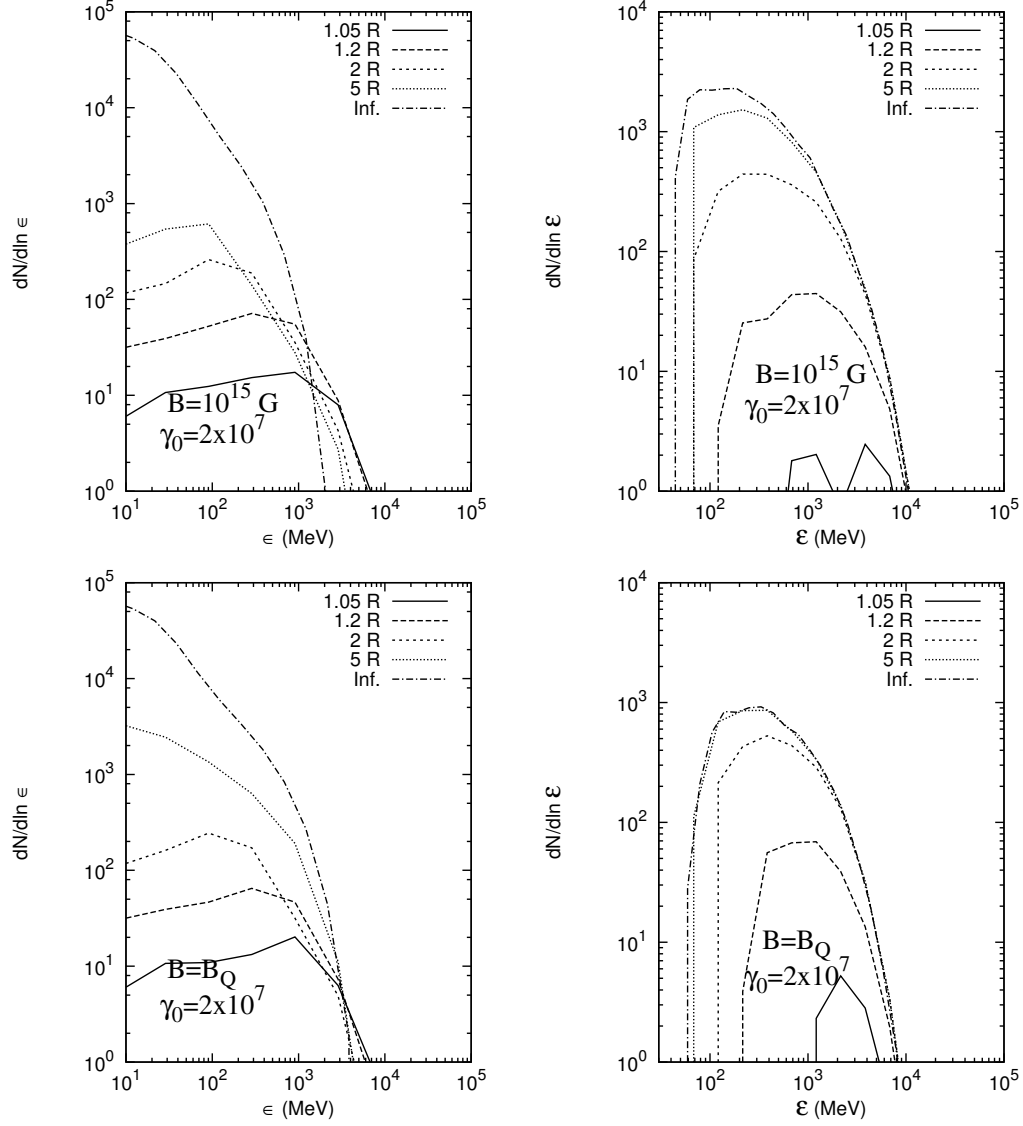


Figure 7.14: Photon spectra and plasma distributions at different heights above the star, where the stellar surface is at  $r = R$ . Here,  $\gamma_0 = 2 \times 10^7$ . The photon spectra are shown in the left-most panels; the pair spectra are shown in the right-most panels; the spectra for  $B = 10^{15}$  G are on the top; the spectra for  $B = B_Q = 4.414 \times 10^{13}$  G are on the bottom. Every photon or electron/positron that passes a given height is recorded in the spectrum for that height.

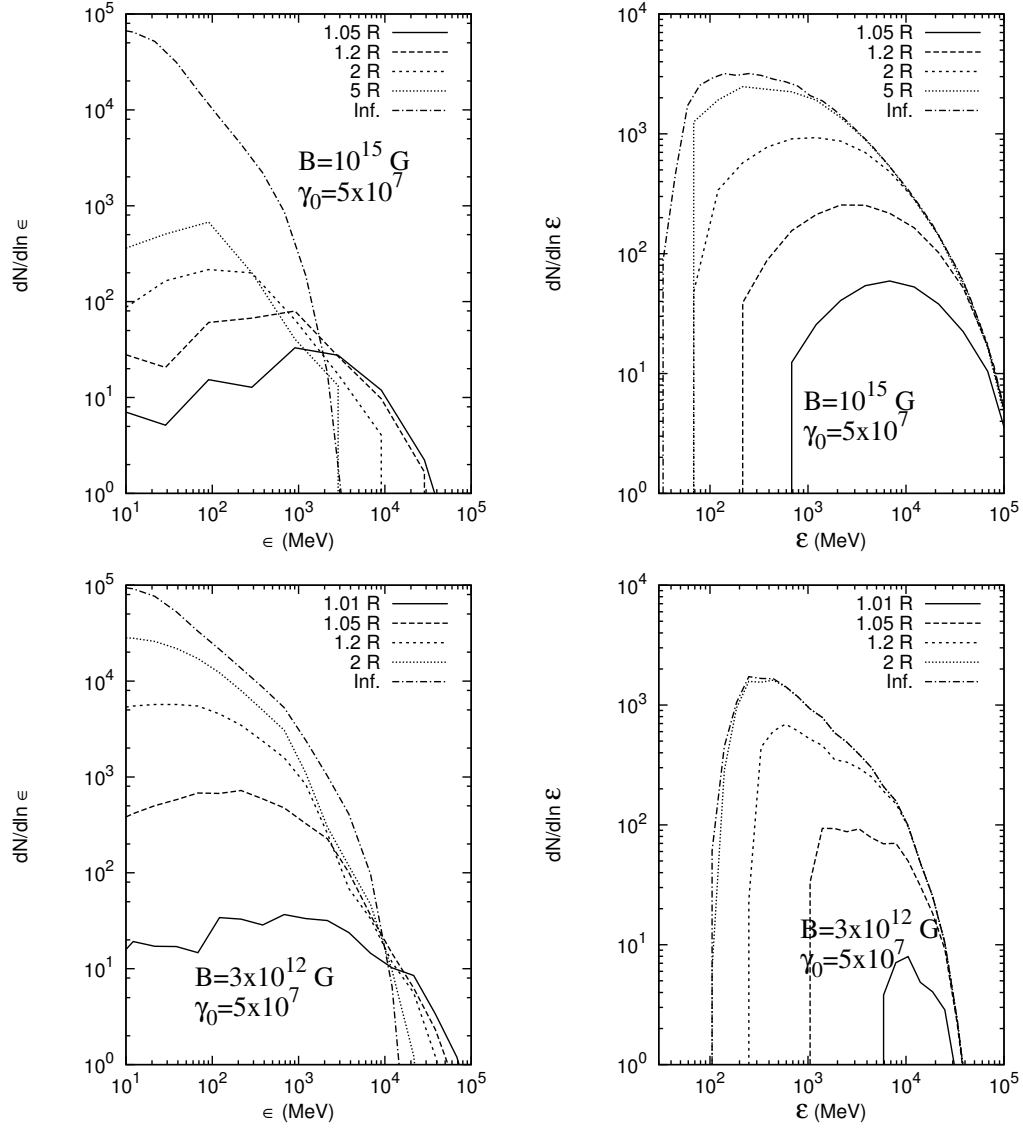


Figure 7.15: Same as for Fig. 7.14, but with  $\gamma_0 = 5 \times 10^7$ . The spectra for  $B = 10^{15}$  G are on the top; the spectra for  $B = 3 \times 10^{12}$  G are on the bottom.

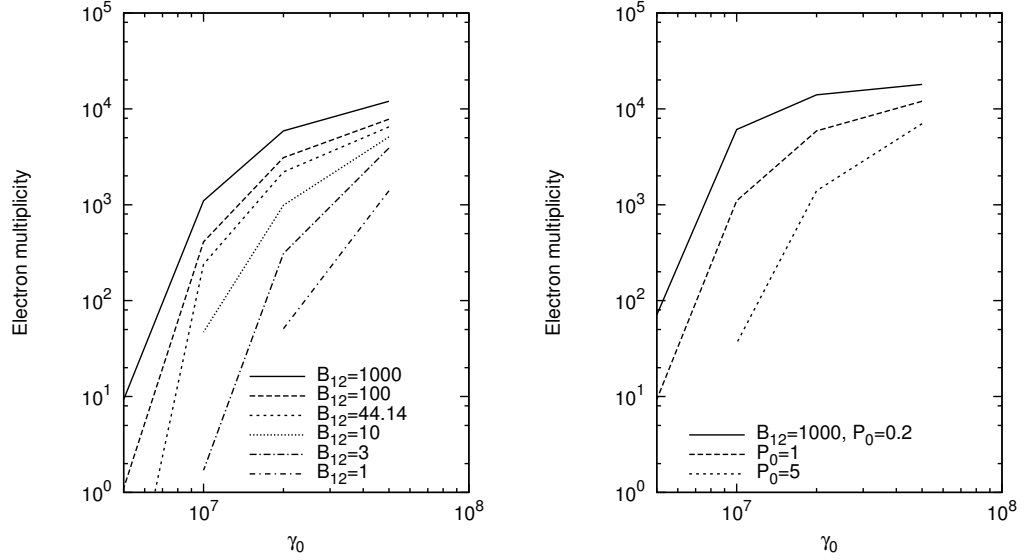


Figure 7.16: Final electron/positron multiplicity as a function of the initial energy of the primary electron  $\gamma_0$ , for  $P_0 = 1$  at several different  $B$  fields (left panel) and for  $B_{12} = 1000$  at several different periods (right panel).

period).

### 7.4.3 Photon splitting

Photon splitting makes a large difference if photons with both parallel and perpendicular polarizations are allowed to split, but only a slight difference if only  $\perp \rightarrow \parallel$  photon splitting is allowed (see Fig. 7.17). Note that regardless of which splitting modes are allowed, the photon spectra and plasma distributions remain more-or-less intact, such that photon splitting by itself will prevent a neutron star from generating gamma-ray or radio pulsed emission.

Table 7.1: Final photon and electron energies, in units of MeV, for various surface magnetic field strengths, with  $P = 1$  s,  $\theta_0 = \theta_c$ , and  $\gamma_0 = 5 \times 10^7$ . When the primary electron reaches  $r_\perp = r_{\text{LC}}$ , the simulation stops and the electron's remaining energy is  $E = 5 \times 10^6$  MeV.

$B_p$ ( $\times 10^{12}$ G)	Curvature radiation (MeV)	Final photons (MeV)	Electrons/positrons (MeV)	# of photons	# of electrons
1	$2.1 \times 10^7$	$1.9 \times 10^7$	$1.3 \times 10^6$	$6.6 \times 10^5$	$1.4 \times 10^3$
3	$2.1 \times 10^7$	$1.6 \times 10^7$	$4.5 \times 10^6$	$6.4 \times 10^5$	$3.9 \times 10^3$
10	$2.1 \times 10^7$	$1.1 \times 10^7$	$1.0 \times 10^7$	$5.3 \times 10^5$	$5.1 \times 10^3$
44.14	$2.1 \times 10^7$	$7.6 \times 10^6$	$1.3 \times 10^7$	$4.8 \times 10^5$	$6.5 \times 10^3$
100	$2.1 \times 10^7$	$6.7 \times 10^6$	$1.4 \times 10^7$	$4.6 \times 10^5$	$7.8 \times 10^3$
1000	$2.1 \times 10^7$	$5.1 \times 10^6$	$1.5 \times 10^7$	$4.4 \times 10^5$	$1.2 \times 10^4$

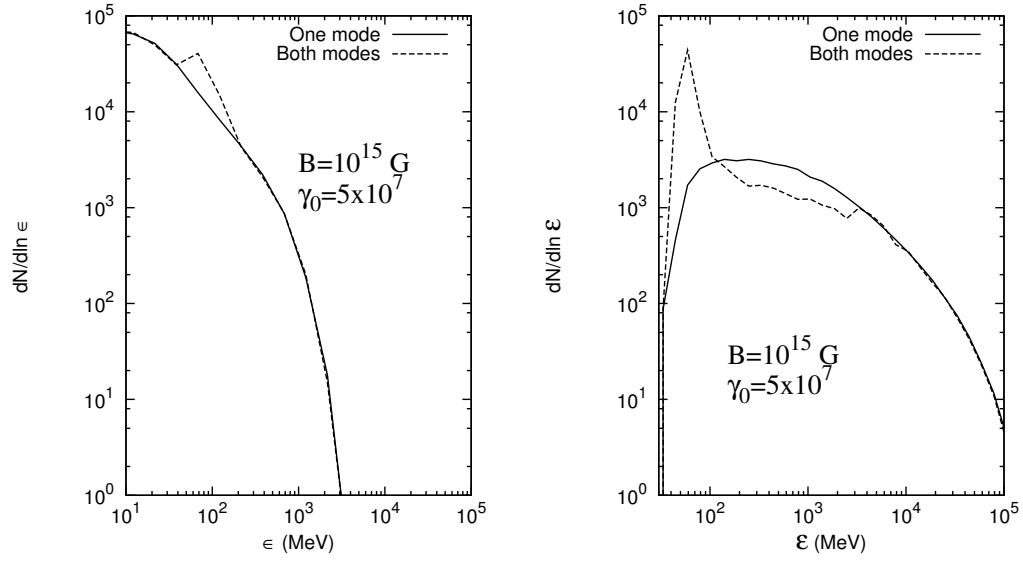


Figure 7.17: The effect of photon splitting on the final photon spectra and plasma distributions. The photon spectra are shown in the left panel; the plasma energy distributions are shown in the right panel. The magnetic field strength is  $B = 10^{15}$  G. In each panel the spectrum when only photons with perpendicular polarizations are allowed to split (with  $\perp \rightarrow \parallel \parallel$ ) is plotted along with the spectrum when photons of both polarizations are allowed to split. The spectrum when photon splitting is “turned off” in the simulation is indistinguishable from the spectrum when  $\perp \rightarrow \parallel \parallel$  is allowed, within the error of the Monte Carlo calculation.

#### 7.4.4 Inverse Compton scattering (ICS)

As was shown in Section 7.4.1, ICS increases the effectiveness of the cascade near the stellar surface but has very little effect for  $r \gtrsim 2R$ . In addition, because the photons scattered by the ICS process have mean energy  $\epsilon_0 = 3.04 \times 10^3 T_6^{-1} \beta_Q (1 - 1/\sqrt{1 + 2\beta_Q})$  MeV, ICS photons are generally weak compared to other cascade photons and only affect the cascade when  $B \gtrsim B_Q$ . Our method for generating ICS scattered photons is described in Appendix D.1. We plot our results in Fig. 7.18. To generate the figure we use two ‘thermal cap’ models: one where the thermal cap has a temperature of  $T = 3 \times 10^5$  K and a radius of  $R$  (i.e., the size of the star) for a stronger ICS effect, and one where the thermal cap has a temperature of  $T = 10^6$  K and a radius of  $R\theta_c$  (i.e., the size of the polar cap) for a weaker ICS effect.

### 7.5 Discussions

We have presented simulations of pair cascades in the neutron star magnetosphere, for strong magnetic fields ranging from  $B = 10^{12}$  G to  $10^{15}$  G. Our results, presented in various tables and figures, show that pair cascades initiated by curvature radiation can account for most pulsars in the  $P-\dot{P}$  diagram, but significant field line curvature near the stellar surface is needed. Contrary to previous works (e.g., Hibschan & Arons 2001b; Arendt & Eilek 2002), we find that inverse Compton scatterings (resonant or not) are not efficient generators of pulsar radio emission, and that the allowed (“alive”) regions of the pulsar death boundaries are even smaller than is shown in Figs. 6.1 and 6.3. Resonant inverse Compton scatterings may even make the death boundaries for curvature-radiation initiated cascades

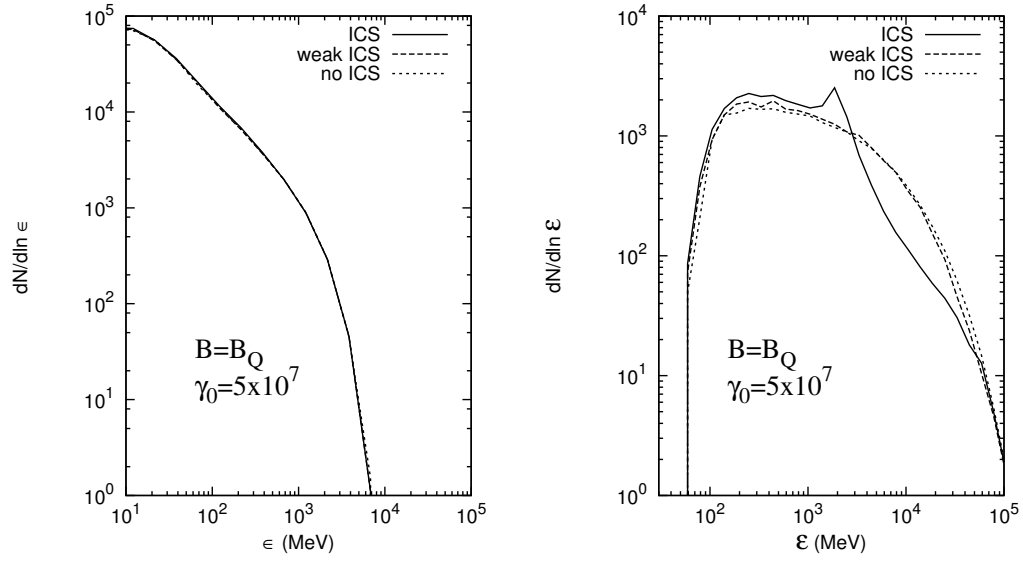


Figure 7.18: The effect of resonant inverse Compton scattering on the final photon spectra and plasma distributions. The photon spectra are shown in the left panel; the plasma energy distributions are shown in the right panel. The magnetic field strength is  $B = B_Q$ . For the curves labeled “ICS” the ‘thermal cap’ has a temperature of  $T = 3 \times 10^5$  K and a radius of  $R$  (i.e., the size of the star); for the curves labeled “weak ICS” the thermal cap has a temperature of  $T = 10^6$  K and a radius of  $R\theta_c$  (i.e., the size of the polar cap).

smaller, by prematurely shorting out the gap before electrons can reach the Lorentz factors necessary for efficient curvature radiation. Our results for RICS-initiated cascades differ from those of Arendt & Eilek (2002) because the previous work greatly overestimates the magnitude of the RICS spectrum in the relevant energy range (a primary electron with  $\gamma_0 \sim 10^3$ - $10^5$ ): to estimate the spectrum these authors adopt the same scaling as is given in Daugherty & Harding (1989) for the spectrum at the point of peak power loss ( $\gamma_0 \sim \epsilon_{Be}/kT \simeq 135$  for  $B = 10^{12}$  G), and additionally normalize the spectrum such that the electron loses all of its energy to the photons; however, at high energies the RICS spectrum is much shallower in slope than at its peak and very little of the primary electron’s initial energy is lost. While we find similar results to those of Hibschan & Arons (2001b), that RICS- and NRICS-initiated cascades produce a very low multiplicity of secondary particles ( $\lambda \sim 0.1$ -1 secondary electrons and positrons for every primary electron), we reach the opposite conclusions. Hibschan & Arons (2001b) suggest that any pulsar is alive if it has a “pair formation front” (the height at which the multiplicity of pairs produced is enough to screen the potential); we suggest that pulsars with  $\lambda \sim 0.1$ -1 are dead even though they have pair formation fronts, because the resulting plasma is not dense enough to generate coherent radio emission. Indeed, there is hardly a reason to require that a cascade forms if the resulting plasma density is lower than the ambient Goldreich-Julian charge density, as would be the case if  $\lambda \sim 0.1$ . Additionally, we find that the synchrotron emission mechanism is suppressed for  $B \gtrsim 3 \times 10^{12}$  G, such that NRICS-initiated cascades at these field strengths can not even reach  $\lambda \sim 0.1$ . In addition to our results for RICS and NRICS cascades, we find that photon splitting, while important near the stellar surface, has very little effect on the final photon and pair spectra (contrary to, e.g., Baring & Harding 2001).



The high-energy photon spectra generated by our simulation agree with observations of gamma-ray pulsars in several respects. First, not surprisingly, cascades initiated in magnetospheres with the strongest voltage drops (those in neutron stars with strong surface fields and rapid rotation) generate the largest multiplicity of gamma rays; all of the gamma-ray pulsars detected so far have very large characteristic voltage drops (e.g., Arons 1996; Thompson 2004). Second, our results (e.g., Fig. 7.9) show high-energy cutoffs in the photon spectra which decrease with magnetic field strength and which occur at around  $10^3$ - $10^4$  MeV for dipole field geometries; this trend and these cutoff values are observed in the six of the seven confirmed gamma-ray pulsars (Thompson 2004). The one exception is B1509-58, which has a high-energy cutoff at around 10 MeV; this very low cutoff energy could be explained by a multipole field geometry, which tends to give energy cutoffs a factor of 10-100 times lower than those for dipole field geometries. Third, to first order our gamma-ray spectra agree in shape and amplitude with observed spectra of gamma-ray pulsars, when properly normalized. Our results for the photon spectrum generated by a single electron emitted from the stellar surface can be converted into a total photon flux coming from the polar cap, by multiplying by the electron flux from the surface,

$$\mathcal{F}_e = \frac{\rho_{\text{GJC}}}{e} = \frac{\beta_Q}{\alpha^3 a_0^2} \frac{\Omega}{2\pi} = 9.19 \times 10^{22} \beta_Q P_0^{-1} \text{ cm}^{-2} \text{ s}^{-1} \quad (7.33)$$

(see Section 5.4.1). This flux can then be converted into an observed flux by multiplying by the factor  $(R/d)^2$ , where  $d$  is the distance to the pulsar. We stress that this is only a first-order approximation; an accurate model of the phase-averaged photon spectrum must account for the change in polar cap viewing angle with phase and the geometry of the beam. Figure 7.19 shows the comparison between the observed phase-averaged spectrum and the spectrum from our first-order model, for the case of PSR B1055-52. We use the parameters  $d = 0.72$  kpc,

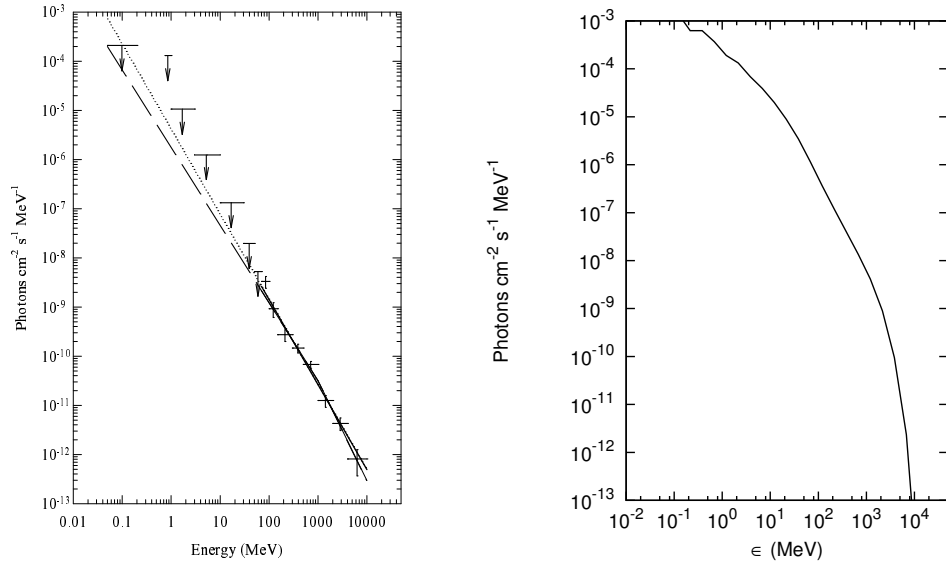


Figure 7.19: The observed phase-averaged gamma ray spectrum for PSR B1055-52, from Thompson et al. (1999) (left panel), along with the ‘model fit’ from our simulation (right panel).

$P = 0.197$  s,  $\dot{P} = 5.83 \times 10^{-15}$  s s $^{-1}$ , and polar cap field strength  $B_p = 6.32 \times 10^{19} \sqrt{P_0 \dot{P}}$  G =  $2.14 \times 10^{12}$  G (Thompson 2004), and assume that  $R = 10$  km,  $\gamma_0 = 2 \times 10^7$ , and  $\theta_0 = \sqrt{R\Omega/c}$ .

The recently-launched Gamma-ray Large Area Space Telescope (GLAST) will greatly improve the quantity and quality of observations from gamma-ray pulsars. GLAST has a sensitivity 30 times larger than that of its predecessor, the Compton Gamma Ray Observatory (CGRO), which could allow it to detect 30 to 100 gamma-ray pulsars (compared to the 7 confirmed and 3 candidate gamma-ray pulsars seen by CGRO) (Thompson 2008). In addition, GLAST will extend the observed spectra of these pulsars out to 300 GeV (compared to the upper limit of 10-30 GeV for CGRO). With this detection range GLAST will be able to discrim-

inate between polar gap models (such as the one used here and in Chapter 6) and outer gap models (e.g., Romani 1996; Zhang & Cheng 1997), as these two models predict photon spectra that are similar in shape for  $\epsilon < 10$  GeV but which diverge at higher energies (the spectra are much steeper for the polar cap models than for the outer gap models; see Thompson 2008 for a comparison).

## APPENDIX A

### CHAPTER 2 APPENDIX

#### A.1 Numerical method

##### A.1.1 Evaluating the integrals in the Kohn-Sham equations

The two most computation-intensive terms in the Kohn-Sham equations [Eq. (3.35)] are the ion-electron interaction term and the direct electron-electron interaction term:

$$V_{Ze,m}(z) = \int d\mathbf{r}_\perp \frac{|W_m|^2(\rho)}{|\mathbf{r} - \mathbf{z}_j|} \quad (\text{A.1})$$

and

$$V_{ee,m}(z) = \iint d\mathbf{r}_\perp d\mathbf{r}' \frac{|W_m|^2(\rho) n(\mathbf{r}')}{|\mathbf{r} - \mathbf{r}'|}. \quad (\text{A.2})$$

Equation (A.1), together with the exchange-correlation term,  $\int d\mathbf{r}_\perp |W_m|^2(\rho) \mu_{\text{exc}}(n)$ , can be integrated by a standard quadrature algorithm, such as Romberg integration (Press et al. 1992). Equation (A.2), however, is more complicated and its evaluation is the rate-limiting step in the entire energy calculation. The integral is over four variables ( $\rho$ ,  $\rho'$ ,  $z'$ , and  $\phi$  or  $\phi - \phi'$ ), so it requires some simplification to become tractable. To simplify the integral we use the identity (see, e.g., Jackson 1998)

$$\frac{1}{|\mathbf{r} - \mathbf{r}'|} = \sum_{n=-\infty}^{\infty} \int_0^{\infty} dq e^{in(\phi-\phi')} J_n(q\rho) J_n(q\rho') e^{-q|z-z'|}, \quad (\text{A.3})$$

where  $J_n(z)$  is the  $n$ th order Bessel function of the first kind. Then

$$V_{ee}(\mathbf{r}) = \int d\mathbf{r}' \frac{n(\mathbf{r}')}{|\mathbf{r} - \mathbf{r}'|}$$

$$= 2\pi \int_{-\infty}^{\infty} dz' \int_0^{\infty} dq J_0(q\rho) \left[ \int_0^{\infty} \rho' d\rho' n(\rho', z') J_0(q\rho') \right] \exp(-q|z - z'|), \quad (\text{A.4})$$

and

$$\begin{aligned} V_{ee,m}(z) &= \int d\mathbf{r}_{\perp} |W_m|^2(\rho) V_{ee}(\mathbf{r}) \\ &= 4\pi^2 \int_{-\infty}^{\infty} dz' \int_0^{\infty} dq \left[ \int_0^{\infty} \rho d\rho |W_m|^2(\rho) J_0(q\rho) \right] \times \\ &\quad \left[ \int_0^{\infty} \rho' d\rho' n(\rho', z') J_0(q\rho') \right] \exp(-q|z - z'|). \end{aligned} \quad (\text{A.5})$$

Using Eq. (2.11) for the electron density distribution, Eq. (A.5) becomes

$$V_{ee,m}(z) = \sum_{m'\nu'} \int_{-\infty}^{\infty} dz' |f_{m'\nu'}(z')|^2 \int_0^{\infty} dq G_m(q) G_{m'}(q) \exp(-q|z - z'|), \quad (\text{A.6})$$

where

$$\begin{aligned} G_m(q) &= 2\pi \int_0^{\infty} \rho d\rho |W_m|^2(\rho) J_0(q\rho) \\ &= \exp(-q^2/2) L_m(q^2/2), \end{aligned} \quad (\text{A.7})$$

and

$$L_m(x) = \frac{e^x}{m!} \frac{d^m}{dx^m} (x^m e^{-x}) \quad (\text{A.8})$$

is the Laguerre polynomial of order  $m$ . These polynomials can be calculated using the recurrence relation

$$mL_m(x) = (2m - 1 - x)L_{m-1}(x) - (m - 1)L_{m-2}(x), \quad (\text{A.9})$$

with  $L_0(x) = 1$  and  $L_1(x) = 1 - x$ .

Using the method outlined above the original four-dimensional integral in Eq. (A.2) reduces to a two-dimensional integral. Once a value for  $z$  is specified, the integral can be evaluated using a quadrature algorithm (such as the Romberg integration method).

### A.1.2 Solving the differential equations and total energy

The Kohn-Sham equations [Eq. (3.35)] are solved on a grid in  $z$ . Because of symmetry we only need to consider  $z \geq 0$ , with  $z = 0$  at the center of the molecule. The number and spacing of the  $z$  grid points determine how accurately the equations can be solved. In this chapter we have attempted to calculate ground-state energies to better than 0.1% numerical accuracy. This requires approximately (depending on  $Z$  and  $B$ ) 133 grid points for a single atom calculation, plus 66 more for each additional atom in the molecule, or a total of  $\approx 66 * (N + 1)$  points for an  $N$ -atom molecule. The grid spacing is chosen to be constant from the center out to the outermost ion, then exponentially increasing as the potential decays to zero. The maximum  $z$  value for the grid is chosen such that the amplitude of all of the electron wave functions  $f_{m\nu}$  at that point is less than  $5 \times 10^{-3}$ .

For integration with respect to  $\rho$ ,  $\rho'$ , or  $q$  (e.g., when calculating the direct electron-electron interaction term), our 0.1%-accuracy goal for the energy values requires an accuracy of approximately  $10^{-5}$  in the integral. A variable-step-size integration routine is used for each such integral, where the number of points in the integration grid is increased until the error in the integration is within the desired accuracy.

Solving the Kohn-Sham equations requires two boundary conditions for each  $(m\nu)$  orbital. The first is that  $f_{m\nu}(z)$  vanishes exponentially for large  $z$ . Because the  $f_{m\nu}(z)$  wave functions must be symmetric or anti-symmetric about the center of the molecule, there is a second boundary condition: wave functions with an even number of nodes have an extremum at the center and wave functions with an odd number of nodes have a node at the center; i.e.,  $f'_{m\nu}(0) = 0$  for even  $\nu$  and  $f_{m\nu}(0) = 0$  for odd  $\nu$ . In practice, we integrate Eq. (3.35) from the large- $z$

edge of the  $z$  grid and “shoot” toward  $z = 0$ , adjusting  $\varepsilon_{m\nu}$  until the boundary condition at the center is satisfied. One final step must be taken to ensure that we have obtained the desired energy and wave function shape, which is to count the number of nodes in the wave function. For each  $(m\nu)$  orbital there is only one wave function shape that satisfies the required boundary conditions and has the correct number of nodes  $\nu$  (e.g., the shape of each orbital in Fig. 2.4, however complicated-looking, is uniquely determined).

To determine the electronic structure of an atom or molecule self-consistently, a trial set of wave functions is first used to calculate the potential as a function of  $z$ , and that potential is used to calculate a new set of wave functions. These new wave functions are then used to find a new potential, and the process is repeated until consistency is reached. In practice, we find that  $f_{m\nu}(z) = 0$  works well as the trial wave function, and rapid convergence can be achieved: four or five iterations for atoms and no more than 20 iterations for the largest and most complex molecules. To prevent overcorrection from one iteration to the next, the actual potential used for each iteration is a combination of the newly-generated potential and the old potential from the previous iteration (the weighting used is roughly 30% old, 70% new).

## A.2 Correlation energy

As was mentioned in Section 3, the form of the correlation energy has very little effect on the relative energy between atom and molecule (or between different states of the same molecule). This holds true even if the calculations are done in the extreme case where the correlation energy term is set to zero. As an example,

consider the energy of the  $\text{C}_2$  molecule at  $B = 10^{15}$  G. Using the correlation energy of Skudlarski and Vignale [Eq. (3.31)], we find the C atom has energy  $\mathcal{E}_a = -41\,330$  eV and the  $\text{C}_2$  molecule has energy per atom  $\mathcal{E}_m = -50\,760$  eV, so that the relative energy is  $\Delta E = 9430$  eV. Using the correlation energy of Jones [Eq. (2.33)], we find  $\mathcal{E}_a = -44\,420$  eV and  $\mathcal{E}_m = -53\,840$  eV, so that  $\Delta E = 9420$  eV. Without any correlation term at all,  $\mathcal{E}_a = -38\,600$  eV and  $\mathcal{E}_m = -47\,960$  eV, so that  $\Delta E = 9360$  eV. As another example of the relative unimportance of the correlation term, two other works using density-functional calculations, Jones (1985); Relovsky & Ruder (1996), find very similar cohesive energy (i.e., infinite chain) results even though they use two very different correlation energy terms. For example, at  $B = 5 \times 10^{12}$  G they both find a cohesive energy of 220 eV for  $\text{He}_\infty$ .

We make one final comment about the accuracy of our chosen correlation energy term, the Skudlarski-Vignale expression Eq. (3.31). Jones (1985) found an empirical expression for the correlation energy at high  $B$  [Eq. (2.33)], and then checked its accuracy using the fact that the self-interaction of an occupied, self-consistent orbital should be zero, i.e.,

$$\mathcal{E}_{\text{dir}}[n_{m\nu}] + \mathcal{E}_{\text{exc}}[n_{m\nu}] = 0, \quad (\text{A.10})$$

where  $n_{m\nu} = |\Psi_{m\nu}(\mathbf{r})|^2$  is the number density of electrons in the  $(m\nu)$  orbital. Performing such a test on the Skudlarski-Vignale expression, we find that the error in Eq. (A.10) is of order 5–20% for  $B_{12} = 1$  and up to 20–30% for  $B_{12} = 1000$  for the elements and molecules considered here. Testing Jones’s expression, we find it does as well and sometimes better at  $B_{12} = 1$ , but at large fields it does considerably worse, up to 60–100% error for  $B_{12} = 1000$ . For example, for  $\text{He}_2$  at  $B_{12} = 1000$  the Skudlarski-Vignale correlation function satisfies Eq. (A.10) to within 23% but Jones’s expression satisfies Eq. (A.10) only to within 63%. Thus,



the Skudlarski-Vignale correlation function adopted in this chapter is much more accurate than Jones's expression for a wide range of field strengths.

## APPENDIX B

### CHAPTER 3 APPENDIX

#### B.1 Technical details and numerical method

##### B.1.1 Evaluating the integrals in the Kohn-Sham equations

The most computation-intensive term in the modified Kohn-Sham equations [Eqs. (3.35) and (3.41)] is the direct electron-electron interaction term

$$V_{ee,m}(z) = \iint_{|z'| < a(N_Q+1/2)} d\mathbf{r}_\perp d\mathbf{r}' \frac{|W_m|^2(\rho) n(\mathbf{r}')}{|\mathbf{r} - \mathbf{r}'|}. \quad (\text{B.1})$$

The evaluation of this term is the rate-limiting step in the entire energy calculation. The integral is over four variables ( $\rho$ ,  $\rho'$ ,  $z'$ , and  $\phi$  or  $\phi - \phi'$ ), so it requires some simplification to become tractable. To simplify the integral we use the identity (e.g., Jackson 1998)

$$\frac{1}{|\mathbf{r} - \mathbf{r}'|} = \sum_{n=-\infty}^{\infty} \int_0^{\infty} dq e^{in(\phi-\phi')} J_n(q\rho) J_n(q\rho') e^{-q|z-z'|}, \quad (\text{B.2})$$

where  $J_n(z)$  is the  $n$ th order Bessel function of the first kind. Then

$$V_{ee}(\mathbf{r}) = \int_{|z'| < a(N_Q+1/2)} d\mathbf{r}' \frac{n(\mathbf{r}')}{|\mathbf{r} - \mathbf{r}'|} \quad (\text{B.3})$$

$$= 2\pi \int_{-a(N_Q+1/2)}^{a(N_Q+1/2)} dz' \int_0^{\infty} dq J_0(q\rho) \times \left[ \int_0^{\infty} \rho' d\rho' n(\rho', z') J_0(q\rho') \right] \exp(-q|z - z'|), \quad (\text{B.4})$$

and

$$V_{ee,m}(z) = \int d\mathbf{r}_\perp |W_m|^2(\rho) V_{ee}(\mathbf{r}) \quad (\text{B.5})$$

$$\begin{aligned}
&= 4\pi^2 \int_{-a(N_Q+1/2)}^{a(N_Q+1/2)} dz' \int_0^\infty dq \left[ \int_0^\infty \rho d\rho |W_m|^2(\rho) J_0(q\rho) \right] \times \\
&\quad \left[ \int_0^\infty \rho' d\rho' n(\rho', z') J_0(q\rho') \right] \exp(-q|z - z'|). \quad (\text{B.6})
\end{aligned}$$

Using Eq. (2.11) for the electron density distribution, Eq. (B.6) becomes

$$V_{ee,m}(z) = \sum_{m'\nu'} \int_{-a(N_Q+1/2)}^{a(N_Q+1/2)} dz' \bar{f}_{m'\nu'}^2(z') \int_0^\infty dq G_m(q) G_{m'}(q) \exp(-q|z - z'|), \quad (\text{B.7})$$

where

$$G_m(q) = 2\pi \int_0^\infty \rho d\rho |W_m|^2(\rho) J_0(q\rho) \quad (\text{B.8})$$

$$= \exp(-q^2/2) L_m(q^2/2), \quad (\text{B.9})$$

and

$$L_m(x) = \frac{e^x}{m!} \frac{d^m}{dx^m} (x^m e^{-x}) \quad (\text{B.10})$$

is the Laguerre polynomial of order  $m$ . These polynomials can be calculated using the recurrence relation

$$mL_m(x) = (2m - 1 - x)L_{m-1}(x) - (m - 1)L_{m-2}(x), \quad (\text{B.11})$$

with  $L_0(x) = 1$  and  $L_1(x) = 1 - x$ .

Using the method outlined above the original four-dimensional integral in Eq. (B.1) reduces to a two-dimensional integral. Once a value for  $z$  is specified, the integral can be evaluated using a quadrature algorithm [such as the Romberg integration method Press et al. 1992].

### B.1.2 Evaluating the integrals in the calculation of 3D condensed matter

For the 3D condensed matter calculation, we simplify the energy integrals of the nearest-neighbor interactions in a way similar to that for the infinite chain cal-

ulation. To do this, we require Eq. (B.2) and one additional identity of Bessel functions:

$$J_0(q\sqrt{a^2 + b^2 - 2ab\cos\theta}) = \sum_{n=-\infty}^{\infty} e^{in\theta} J_n(qa) J_n(qb). \quad (\text{B.12})$$

With these equations the ion-electron nearest-neighbor energy term [Eq. (3.65)] becomes

$$\mathcal{E}_{eZ,\text{nn}}[n] = -Ze^2 \int_{|z|<a/2} d\mathbf{r} \frac{n(\mathbf{r})}{|\mathbf{r} - \mathbf{r}_{\text{nn}}|} \quad (\text{B.13})$$

$$= -Ze^2 2\pi \int_{-a/2}^{a/2} dz \int_0^\infty dq J_0(2Rq) \times \left[ \int_0^\infty \rho d\rho n(\rho, z) J_0(q\rho) \right] \exp(-q|z - a/2|) \quad (\text{B.14})$$

$$= -Ze^2 \sum_{m\nu} \int_{-a/2}^{a/2} dz \bar{f}_{m\nu}^2(z) \int_0^\infty dq J_0(2Rq) G_m(q) \exp(-q|z - a/2|). \quad (\text{B.15})$$

The electron-electron energy term [Eq. (3.66)] becomes

$$\mathcal{E}_{\text{dir},\text{nn}}[n] = \frac{e^2}{2} \iint_{|z|<a/2, |z'|<a/2} d\mathbf{r} d\mathbf{r}' \frac{n(\mathbf{r})n(\mathbf{r}')}{|\mathbf{r} - (\mathbf{r}' + \mathbf{r}_{\text{nn}})|} \quad (\text{B.16})$$

$$= \frac{e^2}{2} 2\pi \int_{-a/2}^{a/2} dz \int_{-a/2}^{a/2} dz' \int_0^\infty \rho' d\rho' n(\rho', z') \int_0^{2\pi} d\phi' \times \int_0^\infty dq J_0(q|\mathbf{r}'_\perp + \mathbf{r}_{\perp,\text{nn}}|) \left[ \int_0^\infty \rho d\rho n(\rho, z) J_0(q\rho) \right] e^{-q|z - z' - a/2|}, \quad (\text{B.17})$$

where  $\theta$  is the angle of  $\mathbf{r}'_\perp + \mathbf{r}_{\perp,\text{nn}}$  in the  $(\rho, \phi, z)$  cylindrical coordinate system  $\Rightarrow$

$$\mathcal{E}_{\text{dir},\text{nn}}[n] = \frac{e^2}{2} 4\pi^2 \int_{-a/2}^{a/2} dz \int_{-a/2}^{a/2} dz' \int_0^\infty dq J_0(2Rq) \left[ \int_0^\infty \rho d\rho n(\rho, z) J_0(q\rho) \right] \times \left[ \int_0^\infty \rho' d\rho' n(\rho', z') J_0(q\rho') \right] e^{-q|z - z' - a/2|} \quad (\text{B.18})$$

$$= \frac{e^2}{2} \sum_{m\nu, m'\nu'} \int_{-a/2}^{a/2} dz \bar{f}_{m\nu}^2(z) \int_{-a/2}^{a/2} dz' \bar{f}_{m'\nu'}^2(z') \times \int_0^\infty dq J_0(2Rq) G_m(q) G'_m(q) \exp(-q|z - z' - a/2|). \quad (\text{B.19})$$

Notice that the infinite chain expression for the nearest-neighbor electron-electron interaction energy is recovered when  $R = 0$  and  $a/2$  is replaced by  $\pm a$ .

### B.1.3 Solving the differential equations and the total energy self-consistently

The Kohn-Sham equations [Eqs. (3.35) and (3.41)] are solved on a grid in  $z$ . Because of symmetry we only need to consider  $z \geq 0$ , with  $z = 0$  coincident with an ion. The number and spacing of the  $z$  grid points determine how accurately the equations can be solved. In this chapter we have attempted to calculate ground-state chain energies to better than 0.1% numerical accuracy. This requires approximately (depending on  $Z$  and  $B$ ) 33 grid points for each unit cell and 3 cells (for  $N_Q = 1$  there are three cells that require exact treatment: the cell under consideration  $z \in [-a/2, a/2]$  and its nearest neighbors; the rest of the cells enter the calculation only through their quadrupole moments). The grid spacing is chosen to be constant from the center out to the edge of the cell. The shape of the wave function is found within one cell and then copied to the other cells.

For integration with respect to  $\rho$ ,  $\rho'$ , or  $q$  (e.g., when calculating the direct electron-electron interaction term), our goal of 0.1% accuracy for the total energy requires an accuracy of approximately  $10^{-5}$  in the integral. A variable-step-size integration routine is used for each such integral, where the number of points in the integration grid is increased until the error in the integration is within the desired accuracy.

We discussed the boundary conditions for the wave function solutions to the Kohn-Sham equations (see Section 3.3.3). The only other requirement we have for these wave functions is that the magnitude of each wave function has the correct number ( $\nu$ ) of nodes per cell (see Fig. 3.2). In practice, to find  $f_{m\nu 0}(z)$  and  $f_{m\nu\pi/a}(z)$  we integrate Eqs. (3.36) and (3.41) from one edge of the  $z$  grid

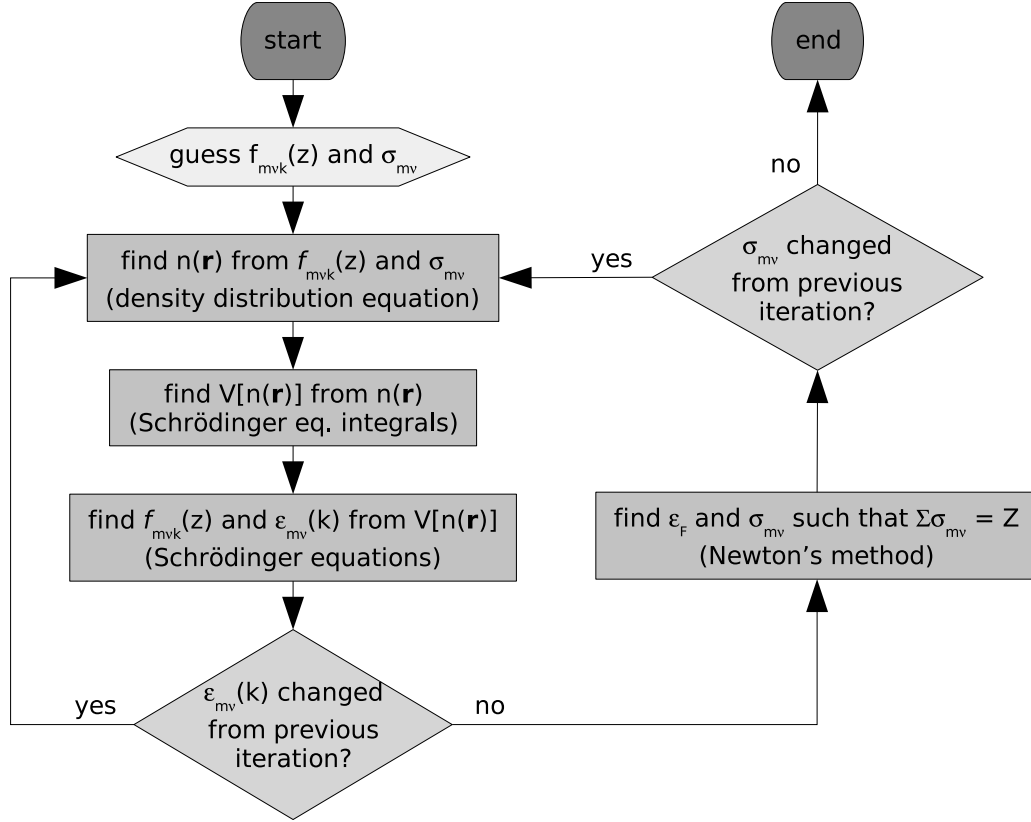


Figure B.1: Flowchart of our procedure for finding  $f_{mvk}(z)$ ,  $\varepsilon_{mv}(k)$ , and  $\sigma_{mv}$  self-consistently.

(e.g.,  $z = a/2$ ) and shoot toward the center ( $z = 0$ ), adjusting  $\varepsilon_{mv}(k = 0)$  and  $\varepsilon_{mv}(\pi/a)$  until the correct boundary condition is satisfied. For the other  $k$  values with energies between these two extremes, we use the given energy to find a wave function and calculate the  $k$  that solves the boundary condition Eq. (3.51), as discussed in Section 3.3.3.

Our procedure for finding  $f_{mvk}(z)$ ,  $\varepsilon_{mv}(k)$ , and  $\sigma_{mv}$  self-consistently is shown in Fig. B.1.3. There are two parts: (i) determining the longitudinal wave functions  $f_{mvk}$  and periodic potential self-consistently, and (ii) determining the electron level occupations  $\sigma_{mv}$  self-consistently.

To determine the  $f_{mvk}$  wave functions self-consistently, a trial set of wave func-

tions and  $\sigma_{m\nu}$  values is first used to calculate the potential as a function of  $z$ , and that potential is used to calculate a new set of wave functions. These new wave functions are then used to find a new potential, and the process is repeated until consistency is reached. In practice, we find that  $f_{m\nu k}(z) = 0$  works well as the trial wave function and a linear spread of  $\sigma_{m\nu}$  from  $\sigma_{0\nu} = 1$  to  $\sigma_{n_m\nu} = 0$  works well for the trial  $\sigma$  values. Convergence can be achieved in four or five iterations. To prevent overcorrection from one iteration to the next, the actual potential used for each iteration is a combination of the newly-generated potential and the old potential from the previous iteration (the weighting used is roughly 30% old, 70% new).

To determine the  $\sigma_{m\nu}$  level occupations self-consistently, we first find the wave functions and eigenvalues  $\varepsilon_{m\nu}(k)$  as a function of  $k$  self-consistently as described above. With this information, and given a Fermi level energy  $\varepsilon_F$ , we can calculate new  $\sigma$  values, using the equations in Section 3. The Fermi level energy is adjusted until  $\sum \sigma_{m\nu} = Z$  using Newton's method. These new  $\sigma_{m\nu}$  values are used to re-calculate the wave functions self-consistently. This process is repeated until self-consistency is reached, which is typically after about three (for hydrogen at  $10^{12}$  G) to twelve (for iron at  $2 \times 10^{15}$  G) full iterations.

## APPENDIX C

### CHAPTER 6 APPENDIX

#### C.1 Maximum potential drop for an oblique rotator

For an oblique rotator, with the magnetic inclination angle  $i$  much larger than the polar cap angular size  $r_p/R$ , the voltage drop across the polar cap is of order  $(\Omega B_p/c)Rr_p \sin i$ , which is a factor of  $R/r_p$  larger than the aligned case. Here we show explicitly that the maximum potential drop across the height of the vacuum gap is still of order  $(\Omega B_p/c)r_p^2$ .

We will be working in the “lab” frame, where the star rotates with respect to the observer. For simplicity we approximate the vacuum gap to be a cylinder of radius  $r_p$  and height  $h \ll R$ ; see Fig. C.1. In reality the bases of the cylinder are not exactly circular for an oblique rotator, but this does not affect our conclusion. The gap is small compared to the stellar radius and we can treat it locally, using a Cartesian coordinate system:  $z$  along the gap height and  $x, y$  for the distance from the pole (with  $\hat{x}$  being principally along  $\hat{\theta}$  and  $\hat{y}$  along  $\hat{\phi}$ ;  $\hat{\theta}$  points in the direction from the rotational pole to the magnetic pole). The magnetic field in the cylinder is approximately uniform,  $\mathbf{B} = -B_p \hat{z}$ .

The electric potential inside the cylindrical gap satisfies  $\nabla^2 \Phi = 0$ . The potential at the base and on the walls of the cylinder can be found from  $\mathbf{E} = -c^{-1}[(\boldsymbol{\Omega} \times \mathbf{r}) \times \mathbf{B}]$ . At the top of the cylinder, the potential satisfies  $E_z = -\partial\Phi/\partial z = 0$ . With these boundary conditions the potential within the cylinder is completely determined.

Without solving the complete potential problem, here we only consider the



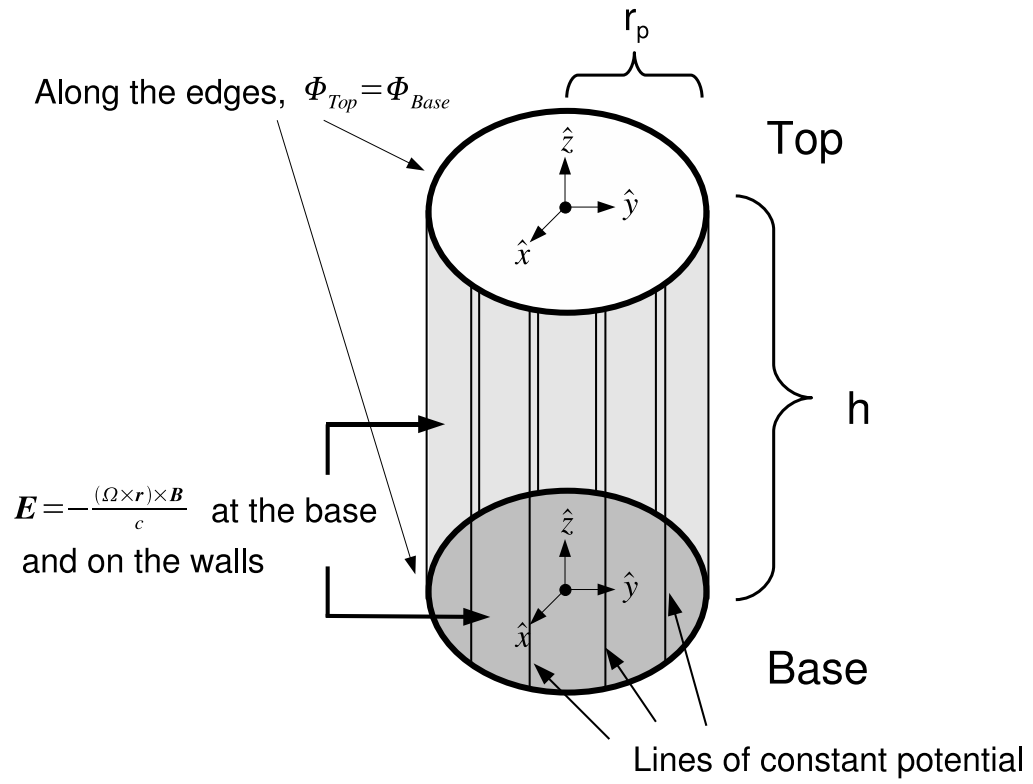


Figure C.1: A schematic diagram showing the polar gap structure in the cylindrical approximation.

potential at the top of the cylinder in the limit of  $h \gg r_p$  (but  $h \ll R$ ); this corresponds to the maximum potential drop across the gap. In this limit, the electric field on the top satisfies not only  $E_z = 0$  but also  $dE_z/dz = 0$ . Thus the Laplace equation below the top of the cylinder becomes

$$\frac{d^2\Phi}{dx^2} + \frac{d^2\Phi}{dy^2} = 0. \quad (\text{C.1})$$

To lowest order in  $x/R$  and  $y/R$  the electric field below the base of the cylinder is given by

$$\mathbf{E} = -\frac{(\mathbf{\Omega} \times \mathbf{r}) \times \mathbf{B}}{c} \simeq \frac{\Omega B_p R}{c} \left[ \left( \sin i + \cos i \frac{x}{R} \right) \hat{x} + \cos i \frac{y}{R} \hat{y} \right]. \quad (\text{C.2})$$

The potential at the base of the cylinder is therefore (using  $\mathbf{E} = -\nabla\Phi$  and renormalizing such that the potential is zero at the pole)

$$\Phi_{\text{base}} = -\frac{\Omega B_p R^2}{c} \left[ \sin i \frac{x}{R} + \cos i \left( \frac{x^2}{2R^2} + \frac{y^2}{2R^2} \right) \right]. \quad (\text{C.3})$$

Since  $E_z = 0$  on the cylindrical wall, the potential on the wall is also given by Eq. (C.3). The potential at the top of the cylinder must solve Eq. (C.1) and match the potential on the wall along the upper edge. For a circular polar cap boundary, given by  $x^2 + y^2 = r_p^2$ , the potential at the top is then

$$\Phi_{\text{top}} = -\frac{\Omega B_p R^2}{c} \left[ \sin i \frac{x}{R} + \cos i \frac{r_p^2}{2R^2} \right]. \quad (\text{C.4})$$

From Eqs. (C.3) and (C.4), we find that at the magnetic pole,  $|\Phi_{\text{top}} - \Phi_{\text{base}}| \simeq (\Omega B_p r_p^2 / 2c) \cos i$ , which is the value of the aligned case multiplied by  $\cos i$ . Figure C.2 compares the potential at the base and top of the cylindrical gap along the  $x$  axis. We see that although there is a large potential drop across the polar cap, the potential difference between the top and the base is smaller.

Alternatively, we may examine the problem in the rotating frame, in which the potential inside the vacuum gap satisfies the equation  $\nabla^2\Phi = 4\pi\rho_{\text{GJ}}$ , where  $\rho_{\text{GJ}}$

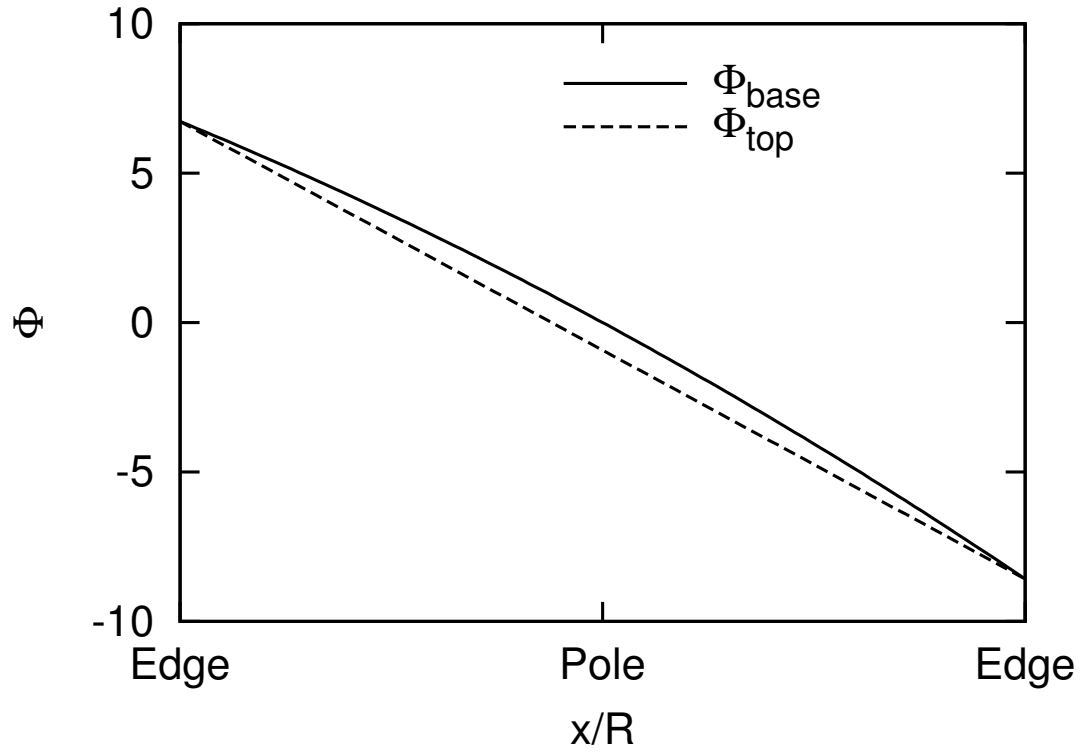


Figure C.2: Potential along the  $\hat{x}$  ( $\sim \hat{\theta}$ ) direction, through the magnetic pole, both at the stellar surface and at the top of the vacuum gap, for an oblique rotator. The magnetic inclination angle is chosen to be  $i = \pi/8$ . The potential is measured in units of  $\Omega B_p r_p^2 / 2c$ , the value of the maximum potential drop for an aligned rotator case.

is the Goldreich-Julian charge density. The potential at the base and on the wall of the cylinder is  $\Phi = 0$  (since the electric field is zero there). At the top of the cylinder, we have  $\partial\Phi/\partial z = 0$ . These boundary conditions completely determine the potential inside the cylinder. For  $h \ll r_p$ , we expect the potential drop along the  $z$ -axis,  $\Delta\Phi$ , to grow as  $h^2$ . But when  $h$  becomes larger than  $r_p$ , the potential drop  $\Delta\Phi$  will saturate to  $(\Omega B_p r_p^2 / 2c) \cos i$ , similar to the aligned case.

## C.2 Scattering rate calculation

In the neutron star rest frame (“lab” frame), the electron (positron) is embedded in a radiation field with specific intensity  $I_{\epsilon_i}(\hat{\Omega}_i)$ . In the electron rest frame,

$$I'_{\epsilon'}(\hat{\Omega}') = \left(\frac{\epsilon'}{\epsilon_i}\right)^3 I_{\epsilon_i}(\hat{\Omega}_i), \quad (\text{C.5})$$

where  $\epsilon'$  and  $\epsilon_i$  are related by a Lorentz transformation:  $\epsilon' = \epsilon_i \gamma (1 - \beta \cos \theta_i)$ .

For a photon coming in along the  $\hat{\Omega}'$  direction, the total scattering cross section is  $\sigma' = \int d\Omega'_1 \left(\frac{d\sigma}{d\Omega'_1}\right)_{\hat{\Omega}' \rightarrow \hat{\Omega}'_1}$ , which in general depends on  $\hat{\Omega}'$  and  $\epsilon'$ . The scattering rate in the electron rest frame is

$$\frac{dN}{dt'} = \int d\Omega' \int d\epsilon' \frac{I'_{\epsilon'}}{\epsilon'} \sigma'. \quad (\text{C.6})$$

In the lab frame the scattering rate is  $dN/dt = \gamma^{-1}(dN/dt')$  (e.g., Rybicki & Lightman 1979). Using  $d\Omega'/d\Omega_i = (\epsilon_i/\epsilon')^2$  and Eq. (C.5) we have

$$\frac{dN}{dt} = \int d\Omega_i \int d\epsilon_i (1 - \beta \cos \theta_i) \frac{I_{\epsilon_i}}{\epsilon_i} \sigma'. \quad (\text{C.7})$$

Neglecting the angle dependence of  $\sigma'$  and assuming that the radiation field  $I_{\epsilon_i}$  is semi-isotropic, this becomes

$$\frac{dN}{dt} \simeq c \int d\epsilon_i \frac{dn_{\text{ph}}}{d\epsilon_i} \sigma', \quad (\text{C.8})$$

which is the same as Eq. (6.25).

APPENDIX D  
CHAPTER 7 APPENDIX

## D.1 Resonant inverse Compton scattering

To determine the photon scattering rate for the resonant inverse Compton process we use the simplified model of an electron positioned directly above the pole and traveling radially outward (see Fig. D.1).

$$\epsilon' = \gamma\epsilon_i(1 - \beta \cos \theta_i). \quad (\text{D.1})$$

$$\sigma'_{\text{res}} \simeq 2\pi^2 \frac{e^2 \hbar}{m_e c} \delta(\epsilon' - \epsilon_{Be}). \quad (\text{D.2})$$

$$\tan \theta_{i,\text{crit}} = R_{\text{th}}/z. \quad (\text{D.3})$$

[Note that  $\theta_{i,\text{crit}}$  can be no larger than  $\arcsin(R/r)$ .]

$$I_{\epsilon_i}(\theta_i; r) = \begin{cases} B_{\epsilon_i}(T) = \frac{\epsilon_i^3/(4\pi^3 \hbar^3 c^2)}{e^{\epsilon_i/kT} - 1}, & \theta_i < \theta_{i,\text{crit}}, \\ 0, & \text{otherwise.} \end{cases} \quad (\text{D.4})$$

$$\frac{dN_{\text{ph}}}{dt} = \int d\Omega_i \int d\epsilon_i (1 - \beta \cos \theta_i) \left( \frac{I_{\epsilon_i}}{\epsilon_i} \right) \sigma'_{\text{res}} \quad (\text{D.5})$$

$$= \frac{2\pi^2 e^2 \hbar}{m_e c \gamma} \int_{\theta_i < \theta_{i,\text{crit}}} d\Omega_i \left( \frac{B_{\epsilon_i}}{\epsilon_i} \right)_{\epsilon_i = \epsilon_{Be}/[\gamma(1 - \beta \cos \theta_i)]} \quad (\text{D.6})$$

$$= \frac{c}{\gamma^3 a_0} \left( \frac{\epsilon_{Be}}{m_e c^2} \right)^2 \int_{\cos \theta_{i,\text{crit}}}^1 \frac{dx/(1 - \beta x)^2}{e^{\epsilon_{Be}/[\gamma(1 - \beta x)kT]} - 1}. \quad (\text{D.7})$$

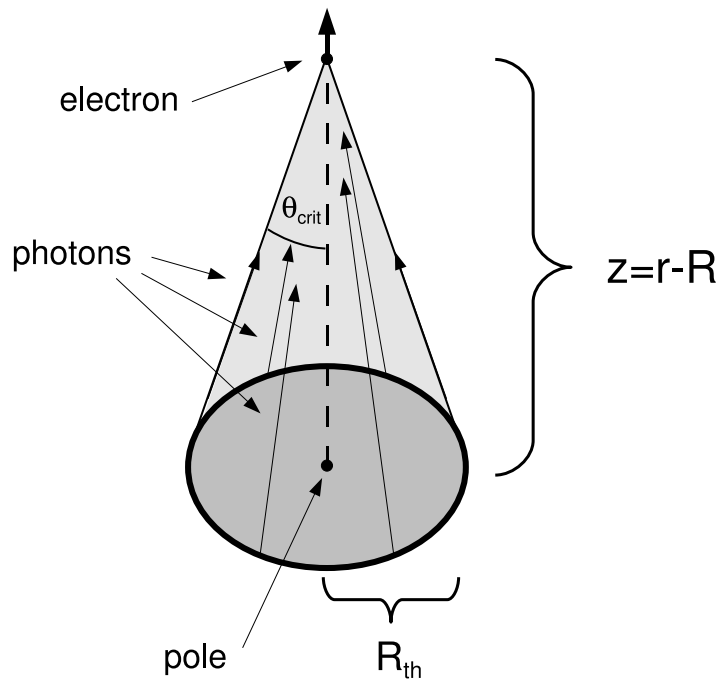


Figure D.1: Simplified picture of the ICS effect on the electron. The electron is assumed to be directly above the pole traveling radially outward.

## D.2 Photon attenuation and the optical depth for pair production

In the frame where the photon is traveling perpendicular to the local magnetic field direction (the “perpendicular” frame), the first five attenuation coefficients (the coefficients with the lowest threshold energies) for the photon are (Daugherty & Harding 1983)

$$R'_{\parallel,00} = \frac{1}{2a_0} \frac{\beta_Q}{x^2 \sqrt{x^2 - 1}} e^{-2x^2/\beta_Q}, \quad (\text{D.8})$$

$$R'_{\parallel,10} = 2 \times \frac{1}{2a_0} \frac{2 + \beta_Q - \frac{\beta_Q^2}{4x^2}}{\sqrt{x^2 - 1 - \beta_Q + \frac{\beta_Q^2}{4x^2}}} e^{-2x^2/\beta_Q}, \quad (\text{D.9})$$

$$R'_{\parallel,20} = 2 \times \frac{1}{2a_0} \frac{2x^2}{\beta_Q} \frac{1 + \beta_Q - \frac{\beta_Q^2}{2x^2}}{\sqrt{x^2 - 1 - 2\beta_Q + \frac{\beta_Q^2}{x^2}}} e^{-2x^2/\beta_Q}, \quad (\text{D.10})$$

$$R'_{\perp,10} = 2 \times \frac{1}{2a_0} \frac{\beta_Q}{2x^2} \frac{2x^2 - \beta_Q}{\sqrt{x^2 - 1 - \beta_Q + \frac{\beta_Q^2}{4x^2}}} e^{-2x^2/\beta_Q}, \quad (\text{D.11})$$

$$R'_{\perp,20} = 2 \times \frac{1}{2a_0} \frac{x^2 - \beta_Q}{\sqrt{x^2 - 1 - 2\beta_Q + \frac{\beta_Q^2}{x^2}}} e^{-2x^2/\beta_Q}. \quad (\text{D.12})$$

where  $\xi = 2x^2/\beta_Q$  and  $x = \frac{\epsilon}{2m_e c^2} \sin \psi$  [Eq. (7.15)]. In the above equations  $R'_{\parallel,jk}$  is the attenuation coefficient for parallel polarizations and  $R'_{\perp,jk}$  is the attenuation coefficient for perpendicular polarizations of the photon, and  $j$  and  $k$  are the Landau levels of the electron and positron produced by the photon.

Below, we examine the conditions for pair production by a parallel-polarized photon (the analysis is similar for a perpendicular-polarized photon and yields the same result). Our goal is to determine when pairs are created in low Landau levels and when they are created in high Landau levels. We find that above a critical magnetic field strength  $B_{\text{crit}} \simeq 3 \times 10^{12}$  G, the electrons and positrons are created at or near threshold (Landau levels  $n \lesssim 2$ ).

The optical depth for pair production, in the neutron star (“lab”) frame, is

$$\tau = \int_0^s ds R(s) = \int_0^{s'} ds' R'(s') \sin \psi, \quad (\text{D.13})$$

where  $s$  is the distance traveled by the photon ( $s$  in the lab frame and  $s'$  in the perpendicular frame) and  $\psi$  is the photon-magnetic field intersection angle. We assume here that  $\psi \ll 1$ , which is valid since most photons that can pair produce will do so long before the angle  $\psi$  approaches unity (only photons near threshold,  $\epsilon \simeq 2m_e c^2$ , must wait until  $\psi \sim 1$  to pair produce). In this limit

$$\sin \psi \simeq \frac{s}{\mathcal{R}_c}, \quad (\text{D.14})$$

so that  $x$  and  $s$  are related by

$$x = \frac{s}{\mathcal{R}_c} \frac{\epsilon}{2m_e c^2}. \quad (\text{D.15})$$

For  $x < 1$ , the photon cannot pair produce, so  $R'(s') = 0$ . For  $1 < x < 0.5(1 + \sqrt{1 + 2\beta_Q})$ ,  $R'(s') = R'_{\parallel,00}(s')$ . We define  $s'_{00}$  to be distance traveled by the photon to reach the first threshold  $x = 1$ , and  $s'_{01}$  to be the distance traveled by the photon to reach the second threshold  $x = 0.5(1 + \sqrt{1 + 2\beta_Q})$ . The optical depth to reach the second threshold for pair production is therefore

$$\tau_{01} = \int_{s_{00}}^{s_{01}} ds R_{\parallel,00}(s) \quad (\text{D.16})$$

$$= \frac{\beta_Q}{2a_0} \left( \frac{2m_e c^2}{\epsilon} \right)^2 R_c \int_1^{\frac{1+\sqrt{1+2\beta_Q}}{2}} \frac{dx}{x\sqrt{x^2-1}} e^{-2x^2/\beta_Q} \quad (\text{D.17})$$

$$= 9.87 \times 10^{11} \left( \frac{R_c}{10^8 \text{ cm}} \right) \left( \frac{100 \text{ MeV}}{\epsilon} \right)^2 F(\beta_Q), \quad (\text{D.18})$$

where

$$F(\beta_Q) = \beta_Q \int_1^{\frac{1+\sqrt{1+2\beta_Q}}{2}} \frac{dx}{x\sqrt{x^2-1}} e^{-2x^2/\beta_Q}. \quad (\text{D.19})$$

We plot  $\tau_{01}$  as a function of magnetic field strength in Fig. D.2, for  $\epsilon = 100 \text{ MeV}$  and  $R_c = 10^8 \text{ cm}$ .



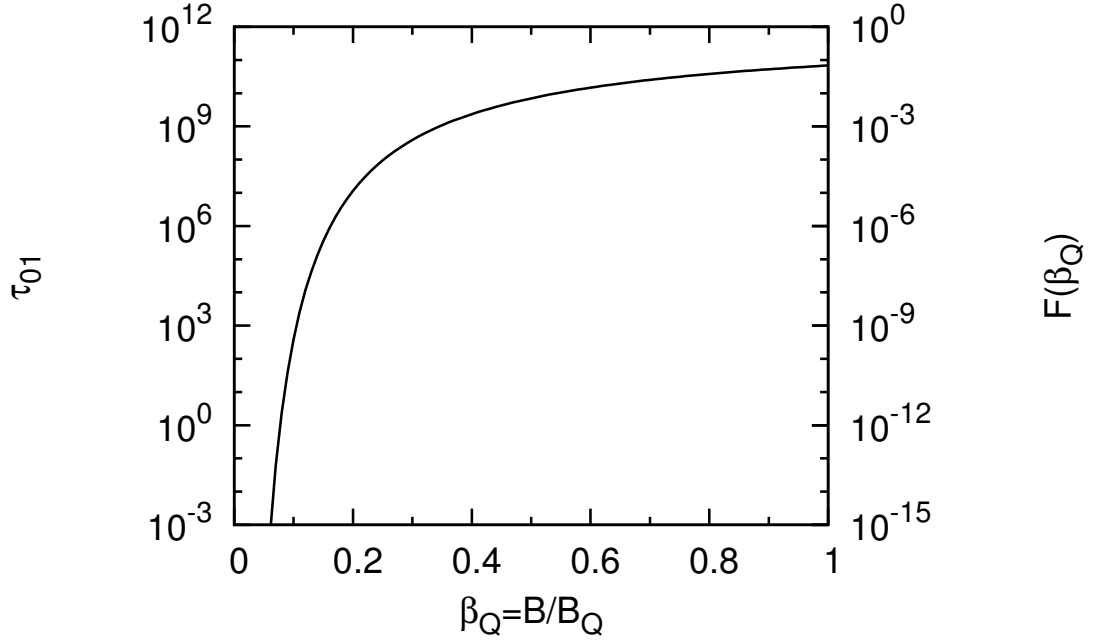


Figure D.2: Plot of  $F(\beta_Q)$  as given by Eq. (D.19) (right axis) and the optical depth to reach the second threshold for pair production,  $\tau_{01}$ , as a function of  $\beta_Q$ , for  $\epsilon = 100$  MeV and  $R_c = 10^8$  cm (left axis).

From Eq. (D.18) we see that pair production occurs at threshold ( $\tau_{01} \geq 1$ ) when

$$B \gtrsim B_{\text{crit}} = 3 \times 10^{12} \text{ G}. \quad (\text{D.20})$$

Because of the steep dependence of  $\tau$  on  $B$  for  $B \sim 3 \times 10^{12}$  G, the value of  $B_{\text{crit}}$  does not change much for different cascade parameters (photon energy  $\epsilon$  and curvature radius  $R_c$ ). For example,  $B_{\text{crit}} = 3 \times 10^{12}$  G for  $\epsilon = 100$  MeV and  $R_c = 10^8$  cm (see Fig. D.2), and  $B_{\text{crit}} = 7 \times 10^{12}$  G for  $\epsilon = 10^4$  MeV and  $R_c = 10^6$  cm. Eq. (D.18) also shows that for  $B \lesssim B_{\text{crit}}$ , the optical depth  $\tau_{01}$  is much less than unity. The same result is found for the optical depth from the second to the third threshold, and for higher thresholds. The pair production process can therefore be divided into two regimes: for  $B \lesssim B_{\text{crit}}$ , photons must travel large distances before pair producing, at which point the pairs will be in high Landau levels; for  $B \gtrsim B_{\text{crit}}$ , photons pair produce almost immediately upon reaching threshold ( $x = 1$ ), so that

the pairs will be in low Landau levels.

### D.3 Electron levels

In the frame where the photon is traveling perpendicular to the local magnetic field direction, the momentum along the field of an electron (or positron) created by this photon is given by

$$p'_z = m_e c \sqrt{x^2 - 1 - (j+k)\beta_Q + (j-k)^2 \frac{\beta_Q^2}{4x^2}}, \quad (\text{D.21})$$

and its energy is given by

$$\mathcal{E}'_j = m_e c^2 \sqrt{x^2 + (j-k)\beta_Q + (j-k)^2 \frac{\beta_Q^2}{4x^2}}, \quad (\text{D.22})$$

where  $j$  and  $k$  are the Landau levels of the electron and positron produced by the photon (or vice versa). In the neutron star (“lab”) frame, the energies of the electron and positron are given by

$$\mathcal{E} = \frac{1}{\sin \psi} (\mathcal{E}' \pm p'_z c \cos \psi), \quad (\text{D.23})$$

with one particle being randomly assigned ‘+’ and the other ‘−’. The electron’s pitch angle  $\Psi$  is given by

$$\sin \Psi = \frac{p_\perp}{p} = \sqrt{\frac{2\beta_Q j}{\mathcal{E}^2/m_e^2 - 1}}. \quad (\text{D.24})$$

## BIBLIOGRAPHY

- Abrahams A. M., Shapiro S. L., 1991, ApJ, 382, 233.
- Adler S. L., 1971, Ann. Phys., 67, 599.
- Al-Hujaj O.-A., Schmelcher P., 2003a, Phys. Rev. A, 67, 023403.
- Al-Hujaj O.-A., Schmelcher P., 2003b, Phys. Rev. A, 68, 053403.
- Al-Hujaj O.-A., Schmelcher P., 2004, Phys. Rev. A, 70, 023411.
- Al-Hujaj O.-A., Schmelcher P., 2004, Phys. Rev. A, 70, 033411.
- Arendt P. N., Eilek J. A., 2002, ApJ, 581, 451.
- Armstrong B. M., Nicholls R. W., 1972, Emission, Absorption, and Transfer of Radiation in Heated Atmospheres. Pergamon, Oxford.
- Arons J., 1981, ApJ, 248, 1099.
- Arons J., 1996, A&A, 120, 49.
- Arons J., 2000, in Kramer M., Wex N., Wielebinski N., eds, Proc. IAU Colloq. 177, Pulsar Astronomy - 2000 and Beyond. ASP, San Francisco, p.449.
- Arons J., Scharlemann E. T., 1979, ApJ, 231, 854.
- Ashcroft N. W., Mermin N. D., 1976, Solid State Physics. Saunders College, Philadelphia.
- Backer D. C., 1976, ApJ, 209, 895.
- Baring M. G., Harding A. K., 2001, ApJ, 547, 929.
- Baye D., Vincke M., 1990, Phys. Rev. A, 42, 391.

- Beloborodov A. M., Thompson C., 2007, *ApJ*, 657, 967.
- Bezchastnov V. G., Pavlov G. G., Ventura J., 1998, *Phys. Rev. A*, 58, 180
- Burgay M. et al., 2006, *MNRAS*, 372, 410.
- Burwitz V., Haberl F., Neuhäuser R., Predehl P., Trümper J., Zavlin V. E., 2003, *A&A*, 399, 1109.
- Camilo F. et al., 2006, *Nature*, 442, 892.
- Camilo F., Ransom S. M., Halpern J. P., Reynolds J., 2007, *ApJ*, 666, 93.
- Chandrasekhar S., 1945, *ApJ*, 102, 223.
- Chang P., Arras P., Bildsten L., 2004, *ApJ*, 616, L147.
- Chen Z. H., Goldman S. P., 1992, *Phys. Rev. A*, 45, 1722.
- Cheng A. F., Ruderman M. A., 1980, *ApJ*, 235, 576.
- Cheng K. S., Ho C., Ruderman, M., 1986, *ApJ*, 300, 500.
- Cohen R., Lodenguai J., Ruderman, M., 1970, *Phys. Rev. Lett.*, 25, 467.
- Danz R. W., Glasser M. L., 1971, *Phys. Rev. B*, 4, 94.
- Daugherty J. K., Harding A. K., 1982, *ApJ*, 252, 337.
- Daugherty J. K., Harding A. K., 1983, *ApJ*, 273, 761.
- Daugherty J. K., Harding A. K., 1989, *ApJ*, 336, 861.
- Daugherty J. K., Harding A. K., 1996, *ApJ*, 458, 278.
- De Luca A., Mereghetti S., Caraveo P. A., Moroni M., Mignani R. P., Bignami G. F., 2004, *A&A*, 418, 625.

- Demeur M., Heenen P. H., Godefroid M., 1994, Phys. Rev. A, 49, 176.
- Dermer C. D., 1990, ApJ, 360, 197.
- Deshpande A. A., Rankin J. M., 1999, ApJ, 524, 1008.
- Duncan R. C., Thompson C., 1992, ApJ, 392, L9.
- Erber T., 1966, Rev. Mod. Phys., 38, 626..
- Flowers E. G. et al., 1977, ApJ, 215, 291.
- Fushiki I., Gudmundsson E. H., Pethick C. J., 1989, ApJ, 342, 958.
- Fushiki I., Gudmundsson E. H., Pethick C. J., Yngvason J., 1992, Ann. Phys., 216, 29.
- Gil J., Melikidze G. I., Geppert U., 2003, A&A, 407, 315.
- Gil J., Melikidze G. I., Zhang B., 2006, ApJ, 650, 1048.
- Goldreich P., Julian W. H., 1969, ApJ, 157, 869.
- Gonthier P. L., Harding A. K., Baring M. G., Costello R. M., Mercer C. L., 2000, ApJ, 540, 907.
- Haberl F., 2005, in Briel U. G., Sembay S., Read A., eds, Proc. of XMM-Newton EPIC Consortium Meeting, MPE Report 288, Garching, p. 39.
- Haberl F., 2006, Ap&SS, 308, 181.
- Haberl F., Schwobe A. D., Hambaryan V., Hasinger G., Motch C., 2003, A&A, 403, L19.
- Haberl F., Turolla R., de Vries C. P., Zane S., Vink J., Me'ndez M., Verbunt F., 2006, A&A, 451, L17.

- Harding A. K., Baring M. G., Gonthier P. L., 1997, *ApJ*, 476, 246.
- Harding A. K., Lai D., 2006, *Rep. Prog. Phys.*, 69, 2631.
- Harding A. K., Muslimov A. G., 1998, *ApJ*, 508, 328.
- Harding A. K., Muslimov A. G., 2002, *ApJ*, 568, 862.
- Harding A. K., Preece R., 1987, *ApJ*, 319, 939.
- Harding A. L., Tadamaru E., Esposito L. W., 1978, *ApJ*, 225, 226.
- Herold H., 1979, *Phys. Rev. D*, 19, 2868.
- Herold H., Ruder H., Wunner G., 1982, *A&A*, 115, 90.
- Hirschman J. A., Arons. J., 2001, *ApJ*, 554, 624.
- Hirschman J. A., Arons. J., 2001, *ApJ*, 560, 871.
- Ho W. C. G., Lai D., 2001, *MNRAS*, 327, 1081.
- Ho W. C. G., Lai D., 2003, *MNRAS*, 338, 233.
- Ho W. C. G., Lai D., 2004, *ApJ*, 607, 420.
- Ho W. C. G., Kaplan D. L., Chang P., van Adelsberg M., Potekhin A. Y., 2007, *MNRAS*, 375, 821.
- Ho W. C. G., Lai D., Potekhin A. Y., Chabrier G., 2003, *ApJ*, 599, 1293.
- Hohenberg P., Kohn W., 1964, *Phys. Rev.*, 136, 864.
- Ivanov M. V., 1994, *J. Phys. B*, 27, 4513.
- Ivanov M. V., Schmelcher P., 2000, *Phys. Rev. A*, 61, 022505.

- Jackson J. D., 1998, *Classical Electrodynamics*, 3rd edition. Wiley, New York.
- Jessner A., Lesch H., Kunzl T., 2001, *MNRAS*, 547, 959.
- Jones R. O., Gunnarsson O., 1989, *Rev. Mod. Phys.*, 61, 689.
- Jones P. B., 1985, *MNRAS*, 216, 503.
- Jones P. B., 1986, *MNRAS*, 218, 477.
- Jones M. D., Ortiz G., Ceperley D. M., 1999, *Phys. Rev. A*, 59, 2875.
- Kössl D., Wolff R. G., Müller E., Hillebrandt W., 1988, *A&A*, 205, 347.
- Kadomtsev B. B., 1970, *Zh. Eksp. Teor. Fiz.*, 58, 1765 [1970, *Sov. Phys. JETP*, 31, 945].
- Kadomtsev B. B., Kudryavtsev V. S., 1971, *Zh. Eksp. Teor. Fiz. Pis'ma Red.* 13, 61 [1971, *Sov. Phys. JETP*, 13, 42].
- Kaspi V. M., Gavriil F. P., 2004, *Nuc. Phys. B Proc. Suppl.*, 132, 456.
- Kaspi V. M., McLaughlin M. A., 2005, *ApJ*, 618, 41.
- Kaspi V. M., Roberts M., Harding A. K., 2006, in Lewin W., van der Klis M., eds, *Compact Stellar X-ray Sources*. Cambridge Univ. Press, Cambridge, p. 279.
- Kohn W., Sham L. J., 1965, *Phys. Rev.*, 140, 1133.
- Kramer M., Stappers B. W., Jessner A., Lyne A. G., Jordan C. A., 2007, *MNRAS*, 377, 107.
- Lai D., 2001, *Rev. Mod. Phys.*, 73, 629.
- Lai D., Ho W. C. G., 2002, *ApJ*, 566, 373.

- Lai D., Ho W. C. G., 2003, ApJ, 588, 962.
- Lai D., Salpeter E. E., 1996, Phys. Rev. A, 53, 152.
- Lai D., Salpeter E. E., 1997, ApJ, 491, 270.
- Lai D., Salpeter E. E., Shapiro S. L., 1992, Phys. Rev. A, 45, 4832.
- Landau L. D., Lifshitz E. M., 1977, Quantum Mechanics. Pergamon, Oxford.
- Lieb E. H., Solovej J. P., Yngvason J., 1994, Commun. Pure Appl. Math., 47, 513.
- Lieb E. H., Solovej J. P., Yngvason J., 1994, Commun. Math. Phys. 161, 77.
- Manchester R. N., Hobbs G. B., Teoh A., Hobbs, M., 2005, AJ, 129, 1993.
- Medin Z., Lai D., 2006, Phys. Rev. A, 74, 062507 [ML06a].
- Medin Z., Lai D., 2006, Phys. Rev. A, 74, 062508 [ML06b].
- Medin Z., Lai D., 2007, Adv. Space Res., 40, 1466.
- Medin Z., Lai D., 2007, MNRAS, 382, 1833.
- Medin Z., Lai D., Potekhin A. Y., 2008, MNRAS, 383, 161.
- Melrose D., 2004, in Camilo F., Gaensler B. M., eds, Proc. IAU Symp. 218, Young Neutron Stars and Their Environments. ASP, San Francisco, p.349.
- Mészáros P., 1992, High-Energy Radiation From Magnetized Neutron Stars. University of Chicago, Chicago.
- Miller M. C., Neuhauser D., 1991, MNRAS, 253, 107.
- Mori K., Chonko J. C., Hailey C. J., 2005, ApJ, 631, 1082.
- Mori K., Hailey C. J., 2002, ApJ, 564, 914.



- Mori K., Ho W. C. G., 2007, MNRAS, 377, 905.
- Mori K., Ruderman M., 2003, ApJ, 592, L95.
- Mueller R. O., Rau A. R. P., Spruch L., 1971, Phys. Rev. Lett., 26, 1136.
- Müller E., 1984, A&A, 130, 415.
- Muslimov A. G., Harding A. K., 2003, ApJ, 588, 430.
- Muslimov A. G., Harding A. K., 2004, ApJ, 606, 1143.
- Muslimov A. G., Tsygan A. I., 1992, MNRAS, 255, 61.
- Neuhauser D., Langanke K., Koonin S. E., 1986, Phys. Rev. A, 33, 2084.
- Neuhauser D., Koonin S. E., Langanke K., 1987, Phys. Rev. A, 36, 4163.
- Ortiz G., Jones M. D., Ceperley D. M., 1995, Phys. Rev. A, 52, R3405.
- Pavlov G. G., Bezchastnov V. G., 2005, ApJ, 635, L61.
- Pavlov G. G., Mészáros P., 1993, ApJ, 416, 752.
- Pavlov G. G., Potekhin A. Y., 1995, ApJ, 450, 883.
- Perez-Azorin J. F., Miralles J. A., Pans J. A., 2006, A&A, 451, 1009.
- Potekhin A. Y., 1994, J. Phys. B, 27, 1073.
- Potekhin A. Y., 1998, J. Phys. B, 31, 49.
- Potekhin A. Y., Chabrier G. 2003, ApJ, 585, 955.
- Potekhin A. Y., Chabrier G., 2004, ApJ, 600, 317.
- Potekhin A. Y., Chabrier G., Lai D., Ho W. C. G., van Adelsberg M., 2006, J. Phys. A: Math. Gen., 39, 4453.

- Potekhin A. Y., Chabrier G., Shibano Y. A., 1999, *Phys. Rev. E*, 60, 2193 (Erratum: 2001, *Phys. Rev. E*, 63, 01990).
- Potekhin A. Y., Lai D., Chabrier G., Ho W. C. G., 2004, *ApJ*, 612, 1034.
- Potekhin A. Y., Pavlov G. G., 1993, *ApJ*, 407, 330.
- Potekhin A. Y., Pavlov G. G., 1997, *ApJ*, 483, 414.
- Potekhin A. Y., Pavlov G. G., Ventura J., 1997, *A&A*, 317, 618.
- Pröschel P., Rösner W., Wunner G., Ruder H., Herold H., 1982, *J. Phys. B*, 15, 1959.
- Press W. H., Teukolsky S. A., Vetterling W. T., Flannery B. P., 1992, *Numerical recipes in C. The art of scientific computing*, 2nd edition. Cambridge University, Cambridge.
- Rajagopal M., Romani R., Miller M. C., 1997, *ApJ*, 479, 347.
- Romani R. W., 1996, *ApJ*, 470, 469.
- Reisenegger A., Prieto J. P., Benguria R., Lai D., Araya P. A., 2005, in de Gouveia Dal Pino E. M., Lugones G., Lazarian A., eds, *Magnetic Fields in the Universe*, AIP Conf. Proc. No. 784. AIP, New York, p. 263.
- Relovsky B. M., Ruder H., 1996, *Phys. Rev. A*, 53, 4068.
- Ruder H., Wunner G., Herold H., Geyer F., 1994, *Atoms in Strong Magnetic Fields*. Springer-Verlag, Berlin.
- Ruderman M., 1971, *Phys. Rev. Lett.*, 27, 1306.
- Ruderman M., 1974, in Hansen C. J., ed, *Proc. IAU Symp. 53, Physics of Dense Matter*. Reidel, Dordrecht-Holland/Boston, p.117.

- Ruderman M., 2003, preprint (astro-ph/0310777).
- Ruderman M. A., Sutherland P. G., 1975, *ApJ*, 196, 51.
- Rybicki G. B., Lightman A. P., 1979, *Radiative Processes in Astrophysics*. Wiley-Interscience, New York.
- Sanwal D., Pavlov G. G., Zavlin V. E., Teter M. A., 2002, *ApJ*, 574, L61.
- Schmelcher P., Cederbaum L. S., 1991, *Phys. Rev. A*, 43, 287.
- Schmelcher P., Detmer T., Cederbaum L. S., 2001, *Phys. Rev. A*, 64, 023410.
- Schmelcher P., Ivanov M. V., Becken W., 1999, *Phys. Rev. A*, 59, 3424.
- Scrinzi A., 1998, *Phys. Rev. A*, 58, 3879
- Shibanov Yu. A., Pavlov G. G., Zavlin V. E., Ventura J., 1992, *A&A*, 266, 313.
- Silant'ev N. A., Yakovlev D. G., 1980, *Astrophys. Space Sci.*, 71, 45.
- Skudlarski P., Vignale G., 1993, *Phys. Rev. B*, 48, 8547.
- Sokolov A. A., Ternov I. M., 1968, *Synchrotron Radiation*, Pergamon, New York.
- Sokolov A. A., Ternov I. M., 1986, *Radiation from Relativistic Electrons*, 2nd rev. ed. AIP, New York.
- Steinberg M., Ortner J., 1998, *Phys. Rev. B*, 58, 15460.
- Sturmer S. J., Dermer C. D., Michel F. C., 1995, *ApJ*, 445, 736.
- Sturrock P. A., 1971, *ApJ*, 164, 529.
- Thompson C., Duncan R. C., 1995, *MNRAS*, 275, 255.
- Thompson C., Duncan R. C., 1996, *ApJ*, 473, 332.

- Thompson, D. J. et al., 1999, *ApJ*, 516, 297.
- Thompson, D. J., 2004, in Cheng K. S., Romero G. E., eds, *Cosmic Gamma-Ray Sources*. Kluwer, Dordrecht, p. 149.
- Thompson, D. J., 2008, in *40 Years of Pulsars: Millisecond Pulsars, Magnetars, and More*. AIP Conf. Proc. No. 983. AIP, New York, p. 56.
- Thurner G., Körbel H., Braun M., Herold H., Ruder H., Wunner G., 1993, *J. Phys. B*, 26, 4719.
- Tsong T. T., 1990, *Atom-Probe Field Ion Microscopy: Field Ion Emission and Surfaces and Interfaces at Atomic Resolution*. Cambridge University, Cambridge.
- Turbiner A. V., Guevara N. L., 2006, *Phys. Rev. A*, 74, 063419
- Turolla R., Zane S., Drake J. J., 2004, *ApJ*, 603, 265.
- Usov V. V., 2002, *ApJ*, 572, L87.
- Usov V. V., Melrose D. B., 1996, *ApJ*, 464, 306.
- van Adelsberg M., Lai D., 2006, *MNRAS*, 373, 1495.
- van Adelsberg M., Lai D., Potekhin A. Y., Arras P., 2005, *ApJ*, 628, 902.
- van Kerkwijk M. H., Kaplan D. L., 2007, *Ap&SS*, 308, 191.
- van Kerkwijk M. H., Kaplan D. L., Durant M., Kulkarni S. R., Paerels F., 2004, *ApJ*, 608, 432.
- von Hoensbroech A., Lesch H., Kunzl T., 1998, *A&A*, 336, 209.
- Vignale G., Rasolt M., 1987, *Phys. Rev. Lett.*, 59, 2360.
- Vignale G., Rasolt M., 1988, *Phys. Rev. B*, 37, 10685.

- Vincke M., Baye D., 1988, J. Phys. B., 21, 2407.
- Vincke M., Baye D., 1989, J. Phys. B., 22, 2089.
- Vranevsevic N., Manchester R. N., Melrose D. B., 2006, in Becker W., Huang H. H., eds, Proc. WE-Heraeus Seminar 363, Neutron Stars and Pulsars. MPE Report 291, p.88.
- Wagner U. et al., 2004, Phys. Rev. E, 70, 026401.
- Wang C., Lai D., 2007, MNRAS, 377, 1095.
- Weltevrede P., Edwards R. T., Stappers B. W., 2006, ChJAS, 6, 13.
- Woods P. M., Thompson C., 2005, in Lewin W. H. G., van der Klis M., eds, Compact Stellar X-ray Sources. Cambridge University, Cambridge.
- Yakovlev D. G., Pethick C. J., 2004, Ann. Rev. Astron. Astrophys., 42, 169.
- Zane S., Turolla R., Stella L., Treves A., 2001, ApJ, 560, 384.
- Zane S., Cropper M., Turolla R., Zampieri L., Chierigato M., Drake J. J., Treves A., 2005, ApJ, 627, 397.
- Zhang B., Harding A. K., Muslimov A. G., 2000, ApJ, 531, L135.
- Zhang B., Qiao G. J., Lin W. P., Han J. L., 1997, ApJ, 478, 313.
- Zhang L., Cheng K. S., 1997, ApJ, 487, 370.